PRECISION ENGINEERING CENTER

2009 ANNUAL REPORT
VOLUME XXVII
March 2010

Sponsors:

3M Corporation
Lexmark International, Inc.
Vistakon, Johnson & Johnson Vision Care Inc.
Lockheed Martin
National Science Foundation

Faculty:

Thomas Dow, Editor
Jeffrey Eischen
Ronald Scattergood
William Roberts

Graduate Students:

David Brehl
Qunyi Chen
Timothy Kennedy
Erik Zdanowicz
Brandon Lane
Meirong Shi
Joseph Scroggins
Scott Steinmetz
John Sayres

Staff:

Kenneth Garrard
Monica Ramanath
Alexander Sohn

Consultants:

Karl Falter
Amir Pirzadeh
David Youden

Table of Contents

Summary i

Design

1. Polaris 3D Error Compensation 1
   Alex Sohn
2. Polaris 3D Operation and Control 21
   Kenneth Garrard
3. Design of a Fast Long Range Actuator - Flora II 47
   Erik Zdanowicz, Jeffrey Eischen, Thomas Dow

Fabrication

4. Diamond Tool Wear Improvements with Elliptical Vibration Assisted Machining 67
   Brandon Lane, Thomas Dow, Ronald Scattergood
5. Diamond Tool Wear in Orthogonal Cutting of 6061 AL, 1215 Steel and 416 Stainless Steel 89
   Meirong Shi, Thomas Dow and Ronald Scattergood
6. Integrated Prescan Optics for Laser Printers 107
   Alexander Sohn, Kenneth Garrard
7. Fabrication and Testing of an Air Amplifier as a Focusing Device for Electrospray Ionization Mass Spectrometry 119
   Guillaume Robichaud, Thomas Dow, Alex Sohn

Metrology

8. Diamond Tool Centering for Cylindrical Turning 135
   Alex Sohn

Control

10. Design of a Miniature Pulsejet Engine 143
    John Sayres, Joseph Scroggins, Scott Steinmetz, William Roberts, Thomas Dow

Personnel 167

Graduates of the PEC 177

Academic Program 185

Publications 191

1 POLARIS 3D ERROR COMPENSATION

Alex Sohn
Precision Engineering Center Staff

The Spherical Profilometer Polaris 3D uses a unique arrangement of axes to measure optical surfaces in a spherical coordinate system. It is an evolution of the earlier 2D version with the addition of movable part axes. With more axes, however, come more errors including axis errors due to imperfections in the individual axes, their mounting and their relative alignments. Since a combination of axes that could achieve the ultimate accuracy goal over the measurement volume would be prohibitively expensive, the strategy in this case has become to measure all repeatable axis and alignment errors and to compensate the resulting measurement data for these errors. Compensation techniques as well as measurement and alignment strategies have been developed for this unique geometry.

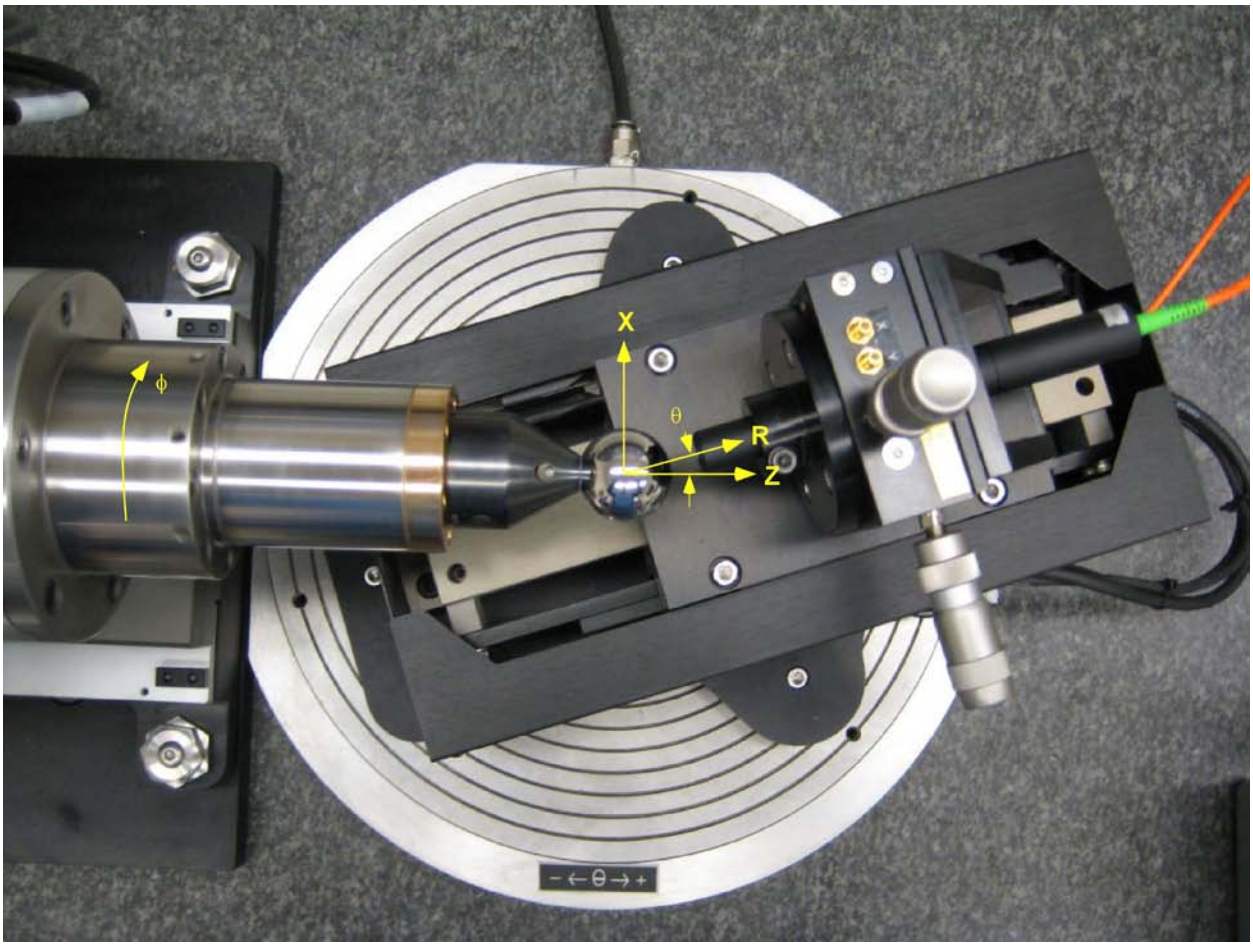

1.1 INTRODUCTION

The Polaris 3D spherical profilometer relies on the accuracy of its constituent axes and their alignment to produce an accurate measurement. There are, however, errors in these axes that will translate into measurement errors in a part. By putting all of the error components in terms of the measurement system spherical (R, θ, ϕ) coordinates, the errors can be subtracted from any axis coordinates.

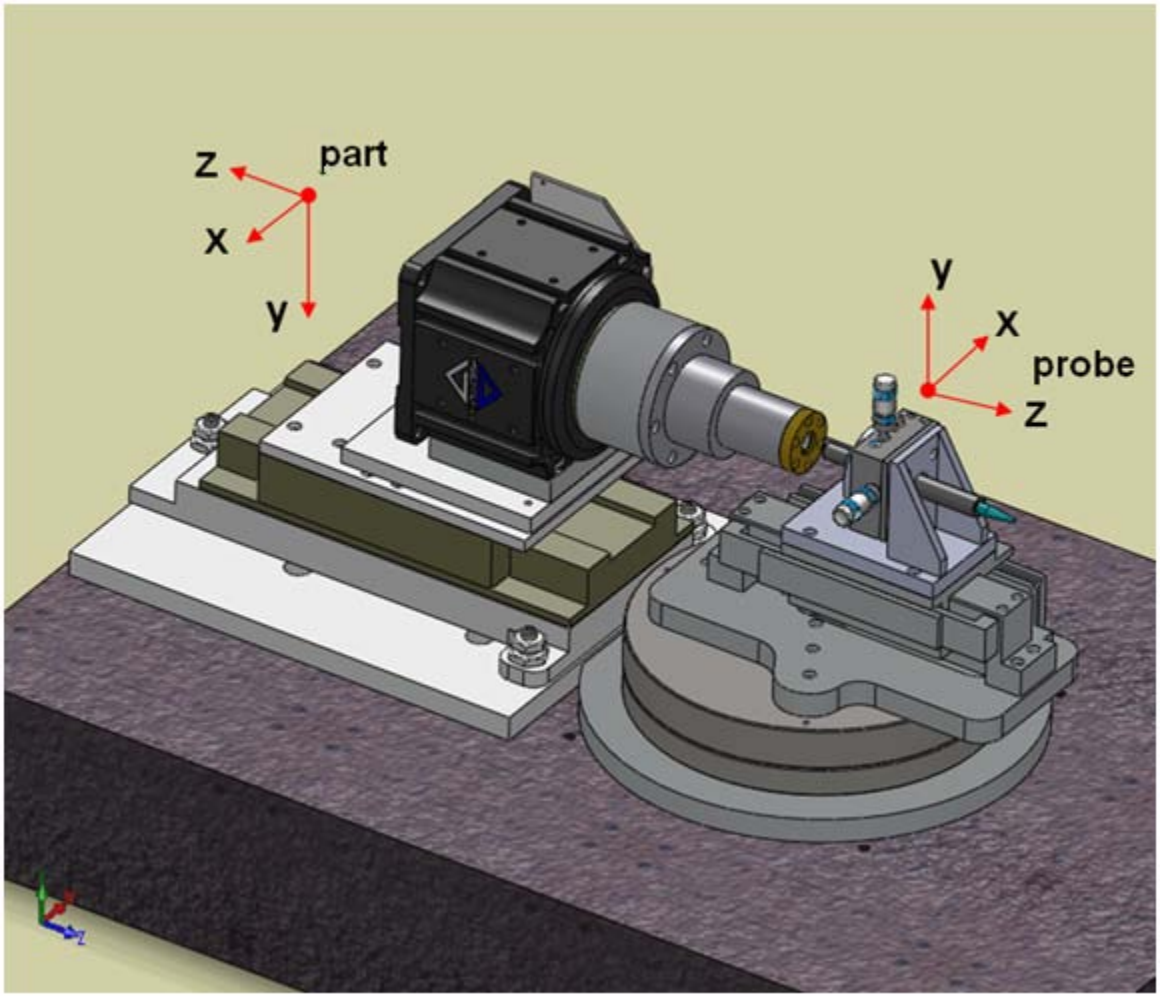

Figure 1. Polaris 3D with the part and probe coordinate systems shown.

1.2 Coordinate System Definitions

Three coordinate systems are used:

1. Cartesian: X, Y, and Z with origin at the θ-axis centerline in the X/Z plane and the probe measurement point in Y.

2. Spherical: R, θ and ϕ with origin at intersection of the θ-axis centerline and the probe center axis at θ = 0.
3. Probe: ρ, τ and y

The three coordinate systems have a fixed relationship in which transformations between them can be made at any time using the equations shown in Table 1 with definition in Figure 2.
Global coordinate definitions are all with respect to probe position. Part coordinates are the inverse of probe coordinates as shown in Figure 1. Hence, all measurements of R and θ-axis errors are performed in the probe coordinate system and all Z and ϕ–axis measurements are performed in the part coordinate system. Rotations are all in the same coordinate system as the translational errors with rotational axes along the translation axes. Definitions of the rotational errors are:

- Z-roll is rotation about the part z-axis
- Z-pitch is rotation about the part x-axis
- Z-yaw is rotation about the part y-axis
- ϕ–axis x-tilt is rotation about the part y-axis
- ϕ–axis y-tilt is rotation about the part x-axis
- R-roll is rotation about the probe ρ–axis
- R-pitch is rotation about the probe τ–axis
- R-yaw is rotation about the probe y-axis

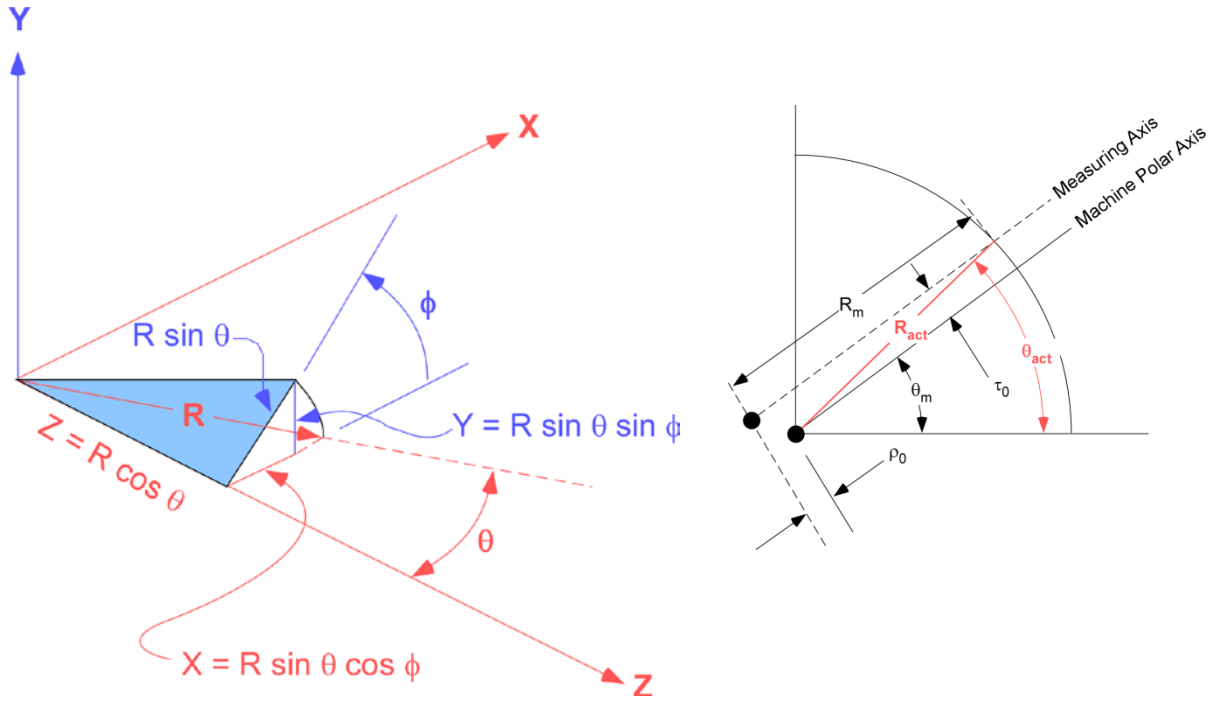

Figure 2. Coordinate systems of measuring machine (left) and probe misalignment (right)

Table 1. The relationships between the three coordinate systems

Spherical to Cartesian: $X = R\sin\theta\sin\phi$ $Y = R\sin\theta\cos\phi$ $Z = R\cos\theta$	**Cartesian to Spherical:** $R = \sqrt{X^2+Y^2+Z^2}$ $\theta = \arccos\frac{Z}{\sqrt{X^2+Y^2+Z^2}}$ $\phi = \arctan\frac{Y}{X}$
Spherical to Probe: $\rho = -R$ $\tau = R\tan\theta$ $y = R\sin\theta\cos\phi$	**Probe to Spherical:** $R = -\rho$ $\theta = \arctan\left(\frac{\tau}{\rho}\right)$ $\phi = \arctan-\frac{y\sqrt{1-\frac{\tau}{\rho}}}{\tau}$
Cartesian to Probe: $\rho = -\sqrt{X^2+Z^2}$ $\tau = \sqrt{Z^2\left(\frac{Z^2}{X^2}+1\right)}$ $y = Y$	**Probe to Cartesian:** $X = -\frac{\tau}{\sqrt{1-\frac{\tau}{\rho}}}$ $Z = \sqrt{Z^2\left(\frac{Z^2}{X^2}+1\right)}$ $Y = y$
Cartesian to Probe with θ : $\rho = -X\sin\theta + Z\cos\theta$ $\tau = X\cos\theta + Z\sin\theta$ $y = Y$	**Probe to Cartesian with θ:** $X = \tau\cos\theta - \rho\sin\theta$ $Z = \tau\sin\theta + \rho\cos\theta$ $Y = y$

1.2 ERROR COMPENSATION

1.2.1 IDENTIFYING AXIS ERRORS

The significant errors that cannot be completely removed by physical alignment fall into two categories, axis errors and alignment errors:

Axis Errors

- R- axis
  - ✓ Pitch (e_{RP})
  - ✓ Yaw (e_{RY})

- ✓ τ-straightness ($S_{R\tau}$)
- ✓ Y-straightness (S_{RY})

- θ-axis
  - ✓ Radial spindle error in ρ ($S_{\theta\rho}$)
- ϕ-axis
  - ✓ Axial spindle error ($S_{\phi Z}$)
  - ✓ Radial spindle error in x ($S_{\phi X}$)
  - ✓ Radial spindle error in y ($S_{\phi Y}$)
  - ✓ Tilt error in x ($e_{\phi X}$)
  - ✓ Tilt error in y ($e_{\phi Y}$)
- Z-axis
  - ✓ Pitch (e_{ZP})
  - ✓ Yaw (e_{ZY})
  - ✓ X-straightness (S_{ZX})
  - ✓ Y-straightness (S_{ZY})

In addition to these axis errors, scale errors also exist, though these are compensated in the axis scaling terms of the axis definitions and will be ignored for the purposes of this discussion.

Alignment Errors

- ρ-alignment of probe to θ-axis origin
- τ- alignment of probe to θ-axis origin
- y- alignment of probe to ϕ-axis origin
- ϕ/θ-alignment (in the x-direction)
- ϕ /Z-parallelism in the x- and y-directions
- R/Z parallelism in y and x

In the case of the alignment errors, it is easier to separate them into errors of the R/θ-axis stack (probe holder) and those of the Z/ϕ-axis stack (part holder). R/θ-errors are defined in terms of probe coordinates in the ρ, τ, and y directions whereas Z/ϕ-errors are defined in terms of x, y and z directions. Error components in the same directions are then combined and these error components are then corrected for their contributions in the measurement (R, θ, ϕ) coordinate system.

1.2.3 AXIS AND ALIGNMENT ERROR ANALYSIS

X-components

ϕ Radial Spindle Error in x($S_{\phi X}$)

$S_{\phi X}(\phi)$ is the radial spindle error of the ϕ-axis measured in the x-direction at the origin of the measurement coordinate system (R=0) at a fixed Z-position ($Z=Z_{m1}$). This error is fit to a 6^{th} degree Fourier series using Matlab from measured data using a reference ball with reversal to remove ball error. This error is purely a function of ϕ-axis position. ($S_{\phi X}$) is the total spindle x-error at $R\cos\theta+Z=Z_m$.

ϕ Tilt Error in x($e_{\phi X}$)

$e_{\phi X}(\phi)$ us the tilt spindle error of the ϕ-axis measured in the x-direction. Tilt error is measured as the difference in spindle error between two balls separate by a distance of l. The ratio of the difference between the readings at any given ϕ to l is the tilt.

ϕ Total spindle x-error($t_{\phi X}$)

The total spindle x-error $t_{\phi X}(R)$ is then:

$$t_{\phi X}=S_{\phi X}(\phi)+e_{\phi X}(\phi)*(R\cos\theta+Z- Z_m) \quad (1)$$

Z X-straightness(S_{ZX})

X-straightness $S_{ZX}(Z)$ is given by a 6^{th} order polynomial fit to straightness measurement data acquired with the probe at the measurement coordinate system origin(R=0) at absolute Z-position (Z=0).

Z Yaw (e_{ZY})

Z-yaw $e_{ZY}(Z)$ is given by a 6^{th} order polynomial fit to Yaw measurement data. Yaw data is acquired with two probes separated by a known distance whose displacement difference divided by their separation gives the yaw slope

Z Total x-error(e_{ZX})

The x-component of the Z-axis errorr is given by

$$e_{ZX}(Z, R)= S_{ZX}(Z) +e_{ZY}(Z)* (R\cos\theta+Z) \quad (2)$$

ϕ/θ-alignment ($e_{x\phi}$)

ϕ/θ-alignment is measured using the tilted flat or sphere at a given Z_{m3}. It is a constant expressed as $e_{x\phi}$.

ϕ /Z-parallelism in the x-direction($e_{\gamma x}$)

γ_x is the slope of the angle formed between the Z-axis and ϕ–axis in the x-direction and is measured on a test cylinder and essentially gives the variation of $e_{x\phi}$ as a function of Z-axis position. The error is entered as a slope (in µrad) whose contribution to the combined error is the product of that slope times the distance from the origin

$$e_{\gamma x}(Z)= \gamma_x*(Z) \quad (3)$$

Combined x-errors (e_x)

The combination of all x-errors is:

$$e_x (R, \phi, Z) =S_{\phi X}(\phi)+e_{\phi X}(\phi)*(R\cos\theta+Z- Z_m) +S_{ZX}(Z) +e_{ZY}(Z)* (R\cos\theta+Z)+ e_{x\phi.}+ \gamma_x*(Z) \quad (4)$$

Error correction

The relationship between the combined x-errors e_x and axis coordinates is shown in Figure 3. Once the error has been e_x measured, the new R-coordinate of any point is:

$$R_x' = \sqrt{R^2 + e_x^2 + 2Re_x sin\theta} \tag{5}$$

And the new θ coordinate is

$$\theta_x' = \sin^{-1}\left(\frac{R_x'^2 - R^2 + e_x^2}{-2R_x' e_x}\right) \tag{6}$$

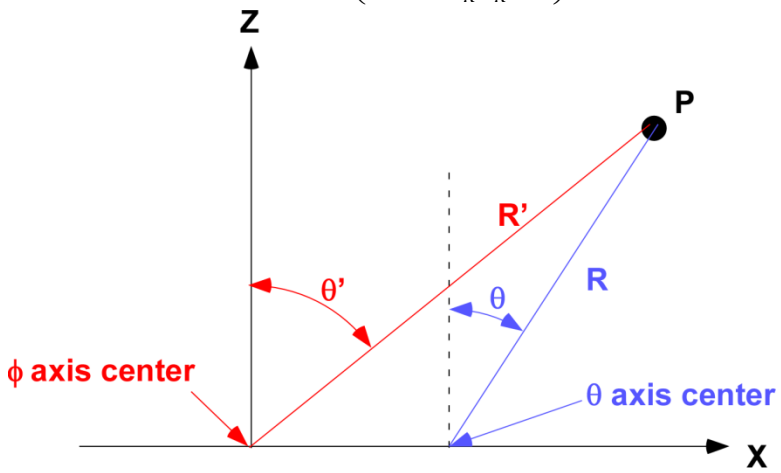

Figure 3. Schematic showing position of a point ***p*** relative to the θ-axis center of rotation and the ideal intersection of the ϕ-axis center of rotation intersected with the θ-axis (primed system) offset by the combined error e_x in the x-direction.

y-components

ϕ Radial Spindle Error in y($S_{\phi y}$)

$S_{\phi y}(\phi)$ is the radial spindle error of the ϕ-axis measured in the y-direction at the origin of the measurement coordinate system (R=0) at a fixed Z-position (Z=0). This error is fit to a 6th degree fourier series using matlab from measured data using a reference ball and reversal. This error is purely a function of ϕ-axis position. ($S_{\phi y}$) is the total spindle y-error at Rcosθ+Z =Z_m.

ϕ Tilt Error in y($e_{\phi y}$)

$e_{\phi y}(\phi)$ us the tilt spindle error of the ϕ-axis measured in the y-direction. Tilt error is measured as the difference in spindle error between two balls separated by a distance of l. The ratio of the difference between the readings at any given ϕ to l is the tilt.

ϕ Total spindle y-error($t_{\phi y}$)

The total spindle x-error $t_{\phi y}(R)$ is then:

$$t_{\phi y} = S_{\phi y}(\phi) + e_{\phi y}(\phi) * (R\cos\theta + Z - Z_m) \tag{7}$$

where Z_m is the z-axis offset used in measurement (z_offset).

Z Y-straightness(S_{ZY})

X-straightness $S_{ZY}(Z)$ is given by a 6th order polynomial fit to straightness measurement data acquired with the probe at the measurement coordinate system origin(R=0) at Z=0.

Z Pitch (e_{ZP})

Z-yaw $e_{ZP}(Z)$ is given by a 6th order polynomial fit to Pitch measurement data. Yaw data is acquired with two probes separated by a known distance whose displacement difference divided by their separation gives the yaw slope.

Z Total y-error (e_{ZY})

The y-component of the Z-axis errorr is given by

$$e_{ZY}(Z, R)= S_{ZY}(Z) +e_{ZP}(Z)* (R\cos\theta+Z) \quad (8)$$

R Y-straightness(S_{RY})

R-straightness $S_{RY}(R)$ is given by a 6th order polynomial fit to straightness measurement data acquired with the probe at the measurement coordinate system origin and R=0

Y-alignment of probe to ϕ-axis($e_{y\phi}$)

ϕ/θ-alignment is measured using the tilted flat at Z_{m3}. It is a constant expressed as $e_{y\phi.}$

ϕ /Z-parallelism in the y-direction($e_{\gamma y}$)

$\gamma_{\phi y}$ is the slope of the angle formed between the Z-axis and ϕ–axis in the y-direction and is measured on a test cylinder and essentially gives the variation of $e_{y\phi}$ as a function of Z-axis position. The error is entered as a slope whose contribution to the combined error is the product of that slope times the distance from the origin.

$$e_{\gamma y}(Z)= \gamma_{\phi y}*(Z) \quad (9)$$

R/Z-parallelism in the y-direction(e_{Ry})

γ_{Ry} is the slope of the angle formed between the Z-axis and ϕ–axis in the y-direction and is measured on a test cylinder and essentially gives the variation of $e_{y\phi}$ as a function of Z-axis position. The error is entered as a slope whose contribution to the combined error is the product of that slope times the distance from Z=0.

$$e_{Ry}(Z)= \gamma_{Ry}*(R-Z) \quad (10)$$

Combined y-errors (e_y)

The combination of all y-errors is:

$$e_y (R, \phi, Z)= -S_{\phi y}(\phi)-e_{\phi y}(\phi)*(R\cos\theta+Z- Z_m) -S_{Zy}(Z) -e_{ZP}(Z)* (R\cos\theta+Z)+ S_{RY}(R) + e_{y\phi} .- \gamma_{\phi y}*(Z)+ \gamma_{Ry}*(R-Z) \quad (11)$$

The predominant influence of y-errors is on ϕ–axis position.

$$\phi_y ' = \phi + \tan^{-1}\left(\frac{e_y}{R}\right) \quad (12)$$

However, when R is small, there is a correction for R as well.

$$R_y ' = \sqrt{R^2 + e_y^2} \quad (13)$$

ρ-components

R-axis pitch (e_{RP})

R-pitch $e_{RP}(R)$ is given by a 6th order polynomial fit to pitch measurement data acquired with two probes, the difference between which divided by their separation gives a slope as a function of R-axis position. The ρ-error is the product of this slope and the offset between the probe and the R-axis encoder readhead (d_y) in the y-direction (nominally 120 mm)

$$e_{\rho P}(R) = e_{RP}(R) * d_y \quad (14)$$

θ-axis spindle ρ-error ($S_{\theta\rho}$)

θ-axis spindle ρ-error is measured using a reference ball and a pair of cap gauges in the x- and y-directions. The ρ-error component is calculated from the θ-axis position. A 6th order polynomial fit to the error data gives the error $S_{\theta\rho}(\theta)$.

ρ-alignment of probe to θ-axis($e_{\rho\theta}$)

ρ-alignment is measured using a tilted flat at R=0. It is a constant expressed as $e_{\rho\theta.}$

Combined ρ-errors (e_ρ)

The combination of all ρ-errors is:

$$e_\rho (R) = e_{RP}(R) * d_y + S_{\theta\rho}(\theta) + e_{\rho\theta} \quad (15)$$

ρ-Error correction

ρ-errors only affect R-axis position:

$$R_\rho ' = R - e_\rho \quad (16)$$

τ-components

τ-alignment of probe to θ-axis($e_{\tau\theta}$)

τ-alignment is measured using a tilted flat at R=0. It is a constant expressed as $e_{\tau\theta.}$

R-axis τ-straightness ($S_{R\tau}$)

R-axis τ-straightness ($S_{R\tau}$) is given by a 6th order polynomial fit to straightness measurement data acquired with the probe at the measurement coordinate system origin and R=0.

Combined τ-errors (e_τ)

The combination of all τ-errors is:

$$e_\tau = e_{\tau\theta} + S_{R\tau}(R) \tag{17}$$

τ-Error correction

τ-errors affect R-axis position:

$$R_\tau ' = \left(R^2 + e_\tau^2 \right)^{1/2} \tag{18}$$

and θ-axis position:

$$\theta_\tau ' = \theta + \tan^{-1}\left(\frac{e_\tau^2}{R} \right) \tag{19}$$

Error Correction procedure.

The R-error correction can be performed sequentially. Since the errors are small, the operation is commutative and the order of the following operations is not significant and the corrections become:

$$R_x ' = \sqrt{R^2 + {e_x}^2 + 2Re_x sin\theta} \tag{5}$$

$$R_\tau ' = \left({R'}_x^2 + e_\tau^2 \right)^{1/2} \tag{18}$$

$$R_y ' = \sqrt{{R'}_\tau^2 + e_y^2} \tag{13}$$

$$R_\rho ' = {R'}_y + e_\rho \tag{16}$$

θ-correction, likewise becomes:

$$\theta_x ' = \sin^{-1}\left(\frac{{R_x}'^2 - R^2 + e_x^2}{2R_x' e_x} \right) \tag{6}$$

$$\theta_\tau ' = {\theta'}_x + \tan^{-1}\left(\frac{e_\tau^2}{R} \right) \tag{19}$$

And the ϕ–axis correction remains

$$\phi_y ' = \phi + \tan^{-1}\left(\frac{e_y}{R} \right) \tag{12}$$

The calculated errors for any combination of axis positions can then be subtracted from the measurement data. The calculations are executed in the post processing of measurement data, so the measurement data must also contain the error compensation data. Therefore, each of the errors described above is given in the header file of the measurement data. Single values are just single-value parameters while more complex data is given in a predefined form.

Error forms

All straightness, roll, pitch, and yaw errors are 6^{th} order polynomials of the form:

$$e(x) = q_0 + q_1 x + q_2 (x - b)^2 + q_3 (x - b)^3 + q_4 (x - b)^4 + q_5 (x - b)^5 + q_6 (x - b)^6 \quad (20)$$

Where the terms are given in the error template by

x_straightness_error = q_0 ,q_1, q_2 , q_3 , q_4 , q_5 , q_6 , b

The error is given in µm and the axis positions are in mm.

All spindle (ϕ–axis) errors are given as fourier series of the form:

$$e(\phi) = a_2 \sin(2\phi + p_2) + a_3 \sin(3\phi + p_3) + a_4 \sin(4\phi + p_4) + a_5 \sin(5\phi + p_5) + a_6 \sin(6\phi + p_6) \quad (21)$$

While the format of the parameters in the error file is:

Phi_spindle_error = a_2 , p_2, a_3 , p_3, a_4 , p_4, a_5, p_5, a_6, p_6

The error is given in µrad and the axis positions are in mm.

1.3 ERROR MEASUREMENT

1.3.1 MEASUREMENT OF AXIS ERRORS

Both linear and angular errors must be measured. The location of straightness measurements will determine the location of the neutral axes for determining offsets for angular errors. This is because there is never truly a neutral axis for rotational errors, therefore, any location where the straightness of an axis can be measured and removed from motion becomes a neutral axis. This is true for both straightness measurements determining the neutral axis for roll, pitch and yaw as well as radial runout measurements determining the neutral axes for rotary tilt measurements. For errors measured in the direction of travel, offsets are measured from the position sensing mechanism, in this case the optical probe.

For measuring roll, pitch and yaw as well as straightness errors of linear axes, twin capacitance gauges are used. For the measurements, an ADE Model 3910 capacitance probe system is used to measure displacement against a 300 mm Zerodur straightedge. The difference in displacement divided by the separation of the probes produces the angular error while the displacement of one of the probes provides straightness. Linear resolution of angle error measurements is equal to the probe separation, in this case 12.7 mm (0.5”). This resolution is adequate since air-bearing slide angular errors are typically low-spatial frequency errors. Angle measurement resolution depends on probe resolution divided by the probe separation. The best-possible noise-limited resolution attainable from the capacitance gauge is 10 nm, resulting in an angular resolution of 0.8 µrad (0.16 arcsec).

1.3.2 MEASUREMENT PROCEDURE

R- axis

Roll

Measurement of R-axis roll is unnecessary if straightness are measured at the probe height since vertical errors are limited to (1-cos) errors.

Pitch and y-straightness

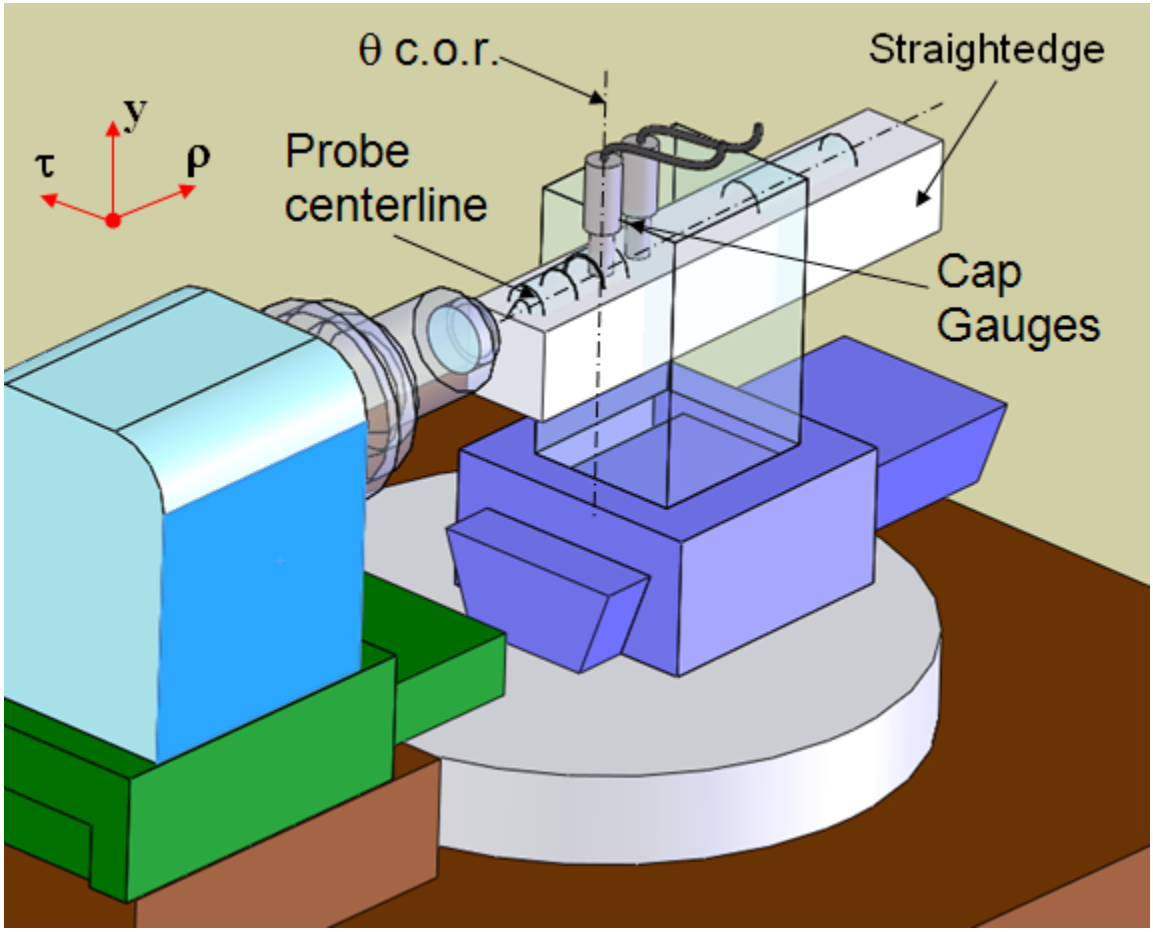

Figure 4. Pitch and y-straightness measurement performed using two capacitance gauges mounted to the ϕ-axis spindle (mounting not shown). Note that the straightedge coincides with the measurement axis of the probe and that the forward cap gauge (used for measuring straightness) coincides with the θ-axis center of rotation (c.o.r.).

As shown in Figure 4, pitch measurement of the R-axis is performed with two cap gauges mounted to the ϕ-axis spindle and the Zerodur straightedge mounted to the R-axis with the measurement axis coincident with the probe centerline both in the τ- and y-directions i.e. the

probe centerline is coincident with the centerline of the top face of the straightedge. The probe is removed for this operation and the figure shows of ghosted image of where the probe would be located. The cap gauges are mounted in a special holder keeping them a fixed distance of 12.7 mm apart. The difference in reading divided by the distance between the cap gauges represents the pitch of the axis. The output of the forward cap gauge provides straightness data. Also important to note are the distance from the cap gauges to the θ-axis centerline and the position of the straightedge relative to the R-axis carriage. By aligning the front cap gauge with the θ-axis centerline, this measurement position will coincide with the probe location at R=0 during operation.

Yaw and τ-straightness

Yaw and τ-straightness are measured in a similar manner to pitch and y-straightness with the exception that now the measurement face in the ρ/y-plane of the straightedge must now be aligned with the probe axis.

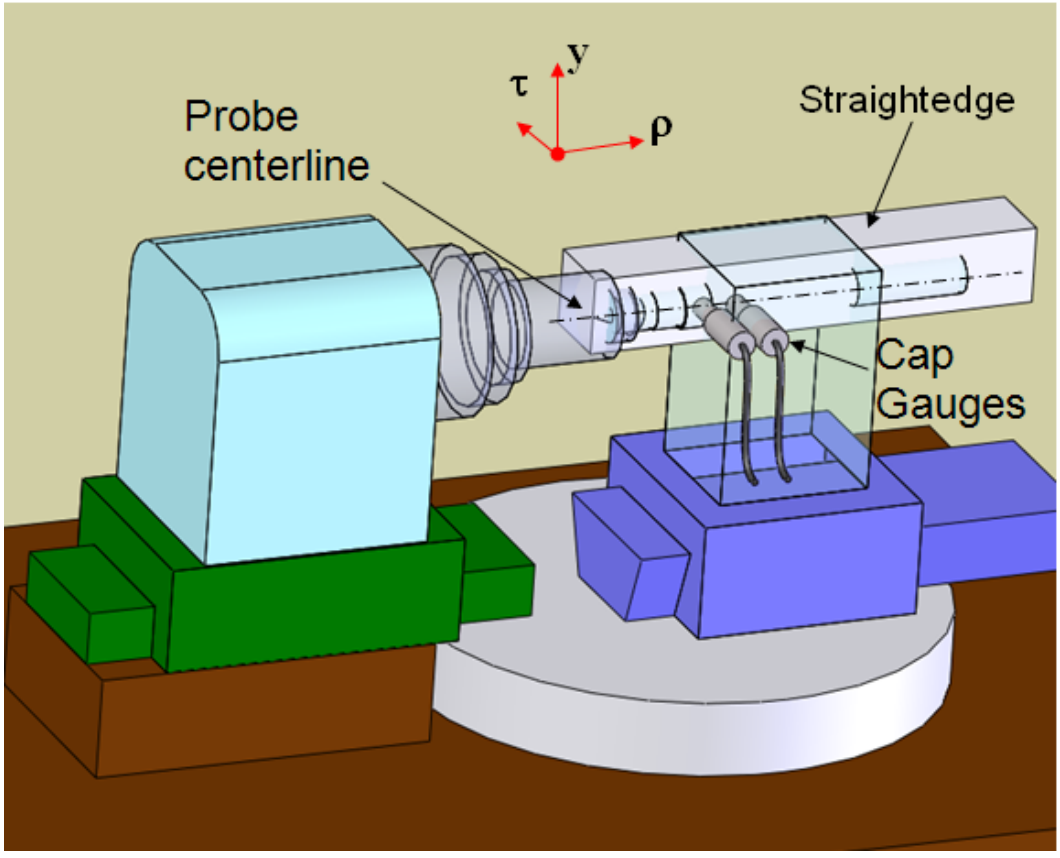

Figure 5. Yaw and τ-straightness measurement performed using two capacitance gauges mounted to the ϕ-axis spindle (mounting not shown).

Z-axis

Roll

Again, measurement of Z-axis roll is unnecessary for the same reasons as for the R-axis as long as measurements are performed at the probe height

Pitch and y-straightness

Pitch and y-straightness of the Z-axis are performed with the same setup as used for measuring pitch and y-straightness for the R-axis. In this case, the R-axis is positioned at its origin while the Z-axis is translated for data collection of error as a function of axis position.

Yaw and x-straightness

Yaw and x-straightness of the Z-axis are performed with the same setup as used for measuring yaw and τ-straightness for the R-axis. Again, the R-axis is positioned at its origin while the Z-axis is translated for data collection of error as a function of axis position.

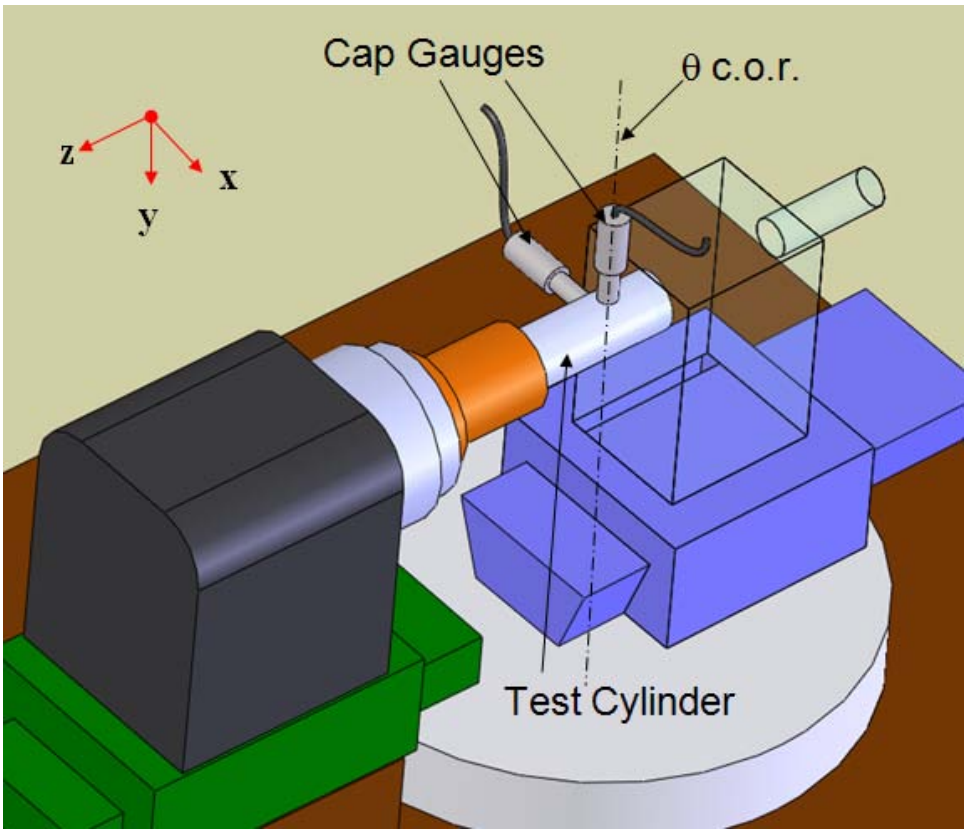

Figure 6. Measurement of ϕ-axis spindle radial error motion. Note that the vertical cap gauge is aligned with the θ-axis center of rotation.

ϕ-axis

Tilt and radial error measurements

The part spindle radial error motion measurements are performed with a diamond turned aluminum cylinder mounted on the spindle whose error motions in the x- and y-directions are measured with a pair of orthogonally mounted capacitance gauges as shown in Figure 6. The errors in the cylinder are considered to be negligible. Measurements are made at two different Z-positions with the cap gauge measuring the y-error mounted coaxial to the θ-axis center of rotation. The two sets of spindle area data are then subtracted and dividec by their z-separation distance to obtain tilt error motion. Measurements are also made at various spindle speeds to determine variability as a function of rpm.

Axial error measurements

For this measurement, a diamond turned flat was placed in on the ϕ-axis spindle. The displacement of this flat was measured in the z-direction using a capacitance gauge as a function of axis position at various rpm.

θ-axis

Radial error measurement

The part spindle radial error motion measurements are performed with a spheres mounted on the axis at probe height and measured with a pair of orthogonally mounted capacitance gauges, one masuring in the x and the other in the z-direction. The errors in the sphere are considered to be negligible.

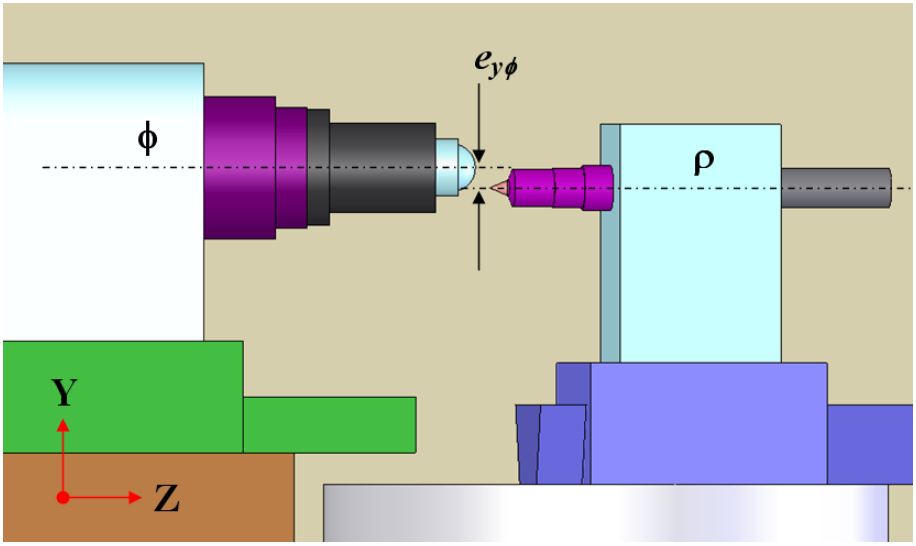

Figure 7. Y- Alignment of probe to ϕ-axis origin. This error is a vertical offset between the centerlines of the probe and the part spindle.

1.3.3 MEASUREMENT OF ALIGNMENT ERRORS

ρ- and τ-alignment of probe to θ-axis origin

ρ- and τ-alignment of the measurement probe has remained unchanged for the 3D version of Polaris, with the procedure well established on the 2D version [1, 2].

y- alignment of probe to ϕ-axis origin

This error produces a simple y-offset of the probe as shown in Figure 7. This measurement can be performed with the tilted flat shown in Figure 8. The tilted flat was made by attaching a diamond turned aluminum flat with epoxy adhesive and a spacer onto a brass substrate mold plug. This was measured on the PEC's Brown & Sharpe CMM for both tilt angle and orientation. The tilt angle wasmeasured to be 7.451º (0.130 rad), with the axis through the high and low spots rotated with respect to the fiducial flats on the side of the part by 13.899 º (0.2426).

Figure 8. Tilted flat used for measuring y- alignment of probe to ϕ-axis origin

ϕ/θ-alignment and ϕ/Z-parallelism in the x- direction

Both ϕ/θ-alignment and ϕ/Z-parallelism (ϕ_x tilt) in the x- direction are measured in one procedure. Four values of R are measured with the optical probe with the machine in following mode as shown in Figure 9. Points 1, and 2 are taken with ϕ=0° and θ=-90° separated by a distance of ΔZ and points. Points 3, and 4 are taken with ϕ=180° and θ=+90°. The errors can then be calculated by

$$\phi_x \text{ tilt} = (3\text{-}2\text{-}4+1)/2\Delta Z \quad (22)$$

$$\phi/\theta\text{-err} = (3\text{-}2+4\text{-}1)/2 \quad (23)$$

Once measured, the errors are corrected using the axis adjusters that locate the spindle.

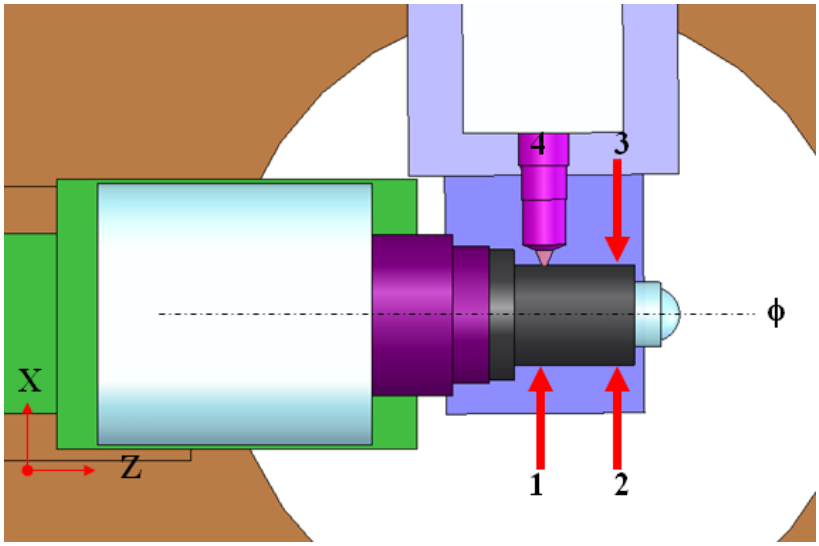

Figure 9. x-alignment of ϕ-axis to the θ-axis origin and Z-axis. Four measurements are taken at points on a cylinder and processed to calculate errors.

ϕ/Z-parallelism in the y-direction

ϕ/Z-parallelism in the y-direction, as illustrated in Figure 10 is essentially a vertical tilt of the ϕ-axis spindle with respect to the z-axis.

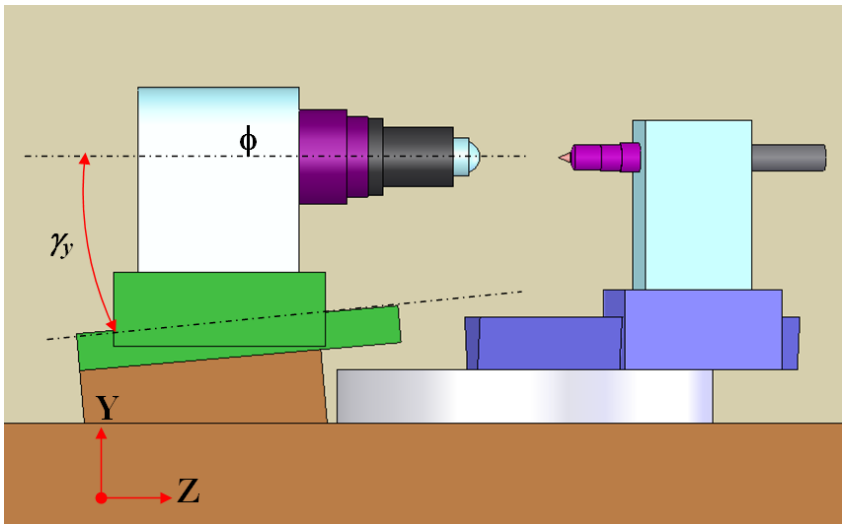

Figure 10. y-alignment of ϕ-axis to the Z-axis.

To measure this error, a reference cylinder is installed in the part chuck and measured above and underneath the axis at ϕ=0° and ϕ=180°, respectively, using a cap gauge or electronic indicator as a function of Z-axis position. The slope of the difference between the two measurements reveals the vertical tilt of the ϕ-axis, which is adjusted using the vertical tilt adjuster at the rear of the spindle.

R/Z parallelism in y and x

Measurement of R/Z parallelism is performed using the setup for measuring straightness. When both axes are moved in unison, the residual slope in the measurement is the relative angle between the two axes. Adjustment of y-parallelism is performed using the axis adjuster at the rear of the base of the Z-axis. Adjustment of x-parallelism is achieved by offsetting the the θ-axis origin.

1.3.4 MEASUREMENT RESULTS

Collected data for axis measurements was tabulated and processed using JMP® 8 Software. Selected data sets are shown for the most significant errors. Other errors were treated in a similar manner.

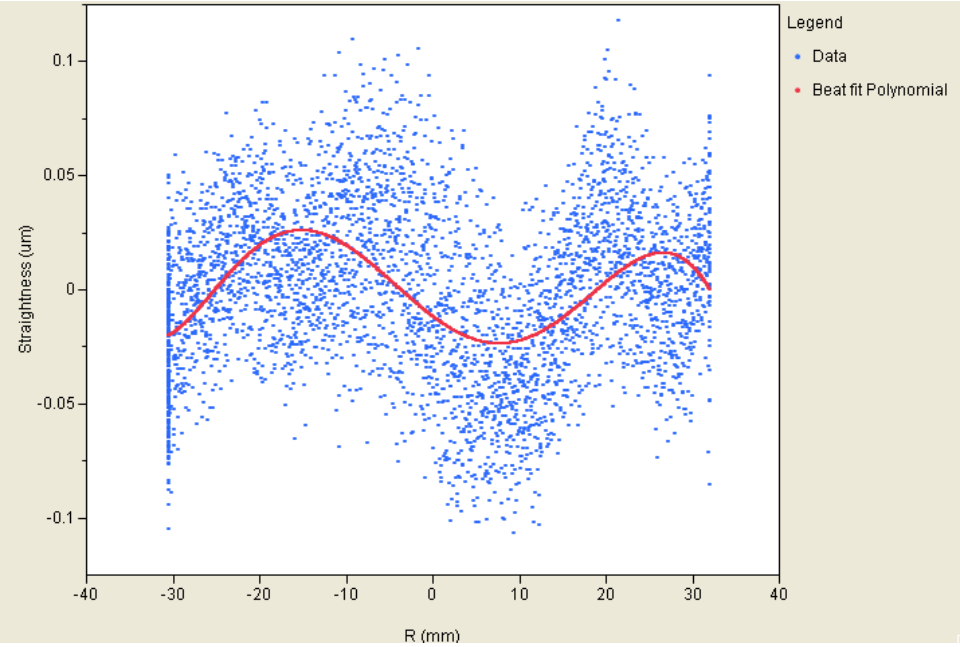

Figure 11. R-axis y-straightness measurement results.

R-axis Y-straightness

Collected data for the R-axis is first converted from capacitance gauge voltage readings to displacement in μm using the sensitivity of the the cap gauges (2.5 μm/V). The measurement

data from each gage was leveled by fitting and subtracting a linear least squares fit. For straightness data, the A gauge reading is fit to a 6th order polynomial using nonlinear regression and plotted, as shown in Figure 11 along with the fit polynomial. The resultant fit function is:

$$\text{R-straightness (um)} = -0.011975 - 0.0030323*R\,(mm) + 9.7845e^{-5}*(R\,(mm)+0.9158)^2 + 8.6043e^{-6}*(R\,(mm)+0.9158)\text{^}3 - 1.5947e^{-7}*(R\,(mm)+0.9158)^4 - 5.1228e^{-9}*(R\,(mm)+0.9158)^5 + 6.356e^{-11}*(R\,(mm)+0.9158)^6$$

The coefficients for Eq. 20:

r_straight_vertical = -0.011975 , - 0.0030323, $9.7845e^{-5}$, $8.6043e^{-6}$, $-1.5947e^{-7}$, $-5.1228e^{-9}$, $6.356e^{-11}$, -0.9158

R-Axis Pitch

R-axis pitch results were calculated by dividing the difference of the cap gauge data by the cap gauge separation distance of 12.7 mm. The result was fit to a 6th order polynomial and the result is shown in Figure 12.

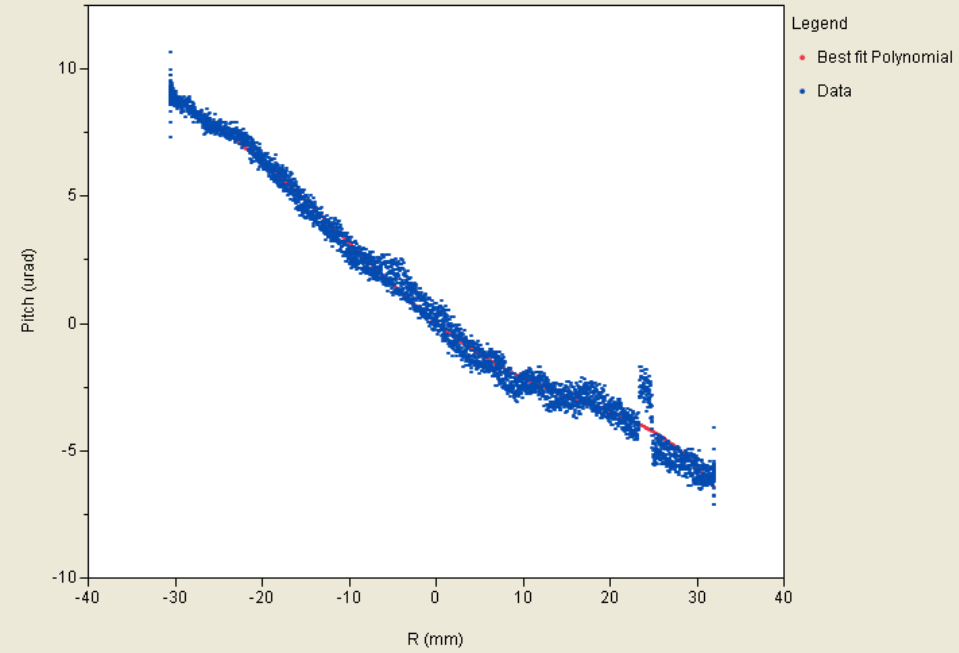

Figure 12. R-axis Pitch measurement results.

The resultant fit function for R-axis pitch is:

$$m\,(urad) = -0.000017 - 0.2840208*R\,(mm) + 0.0049338*(R\,(mm)+0.9158)^2 + 0.0001169*(R(mm)+0.9158)^3 - 4.1031e^{-6}*(R\,(mm)+0.9158)^4 - 7.5183e^{-8}*(R(mm)+0.9158)^5 + 6.483e^{-10}*(R\,(mm)+0.9158)^6$$

ϕ-AXIS RADIAL ERROR MOTION

Data for ϕ-axis radial error motion was collected at several spindle speeds. Data for 12 rpm is considered to be quasi-static. The data was processed first by calculating displacement from cap gauge voltage data. Runout was removed by fitting and removing any primary sinusoidal component from the data. A 6^{th} order fourier series was then fit to the data using nonlinear regression. The resulting data are shown in Figure 13 for both x- and y-radial error motion.

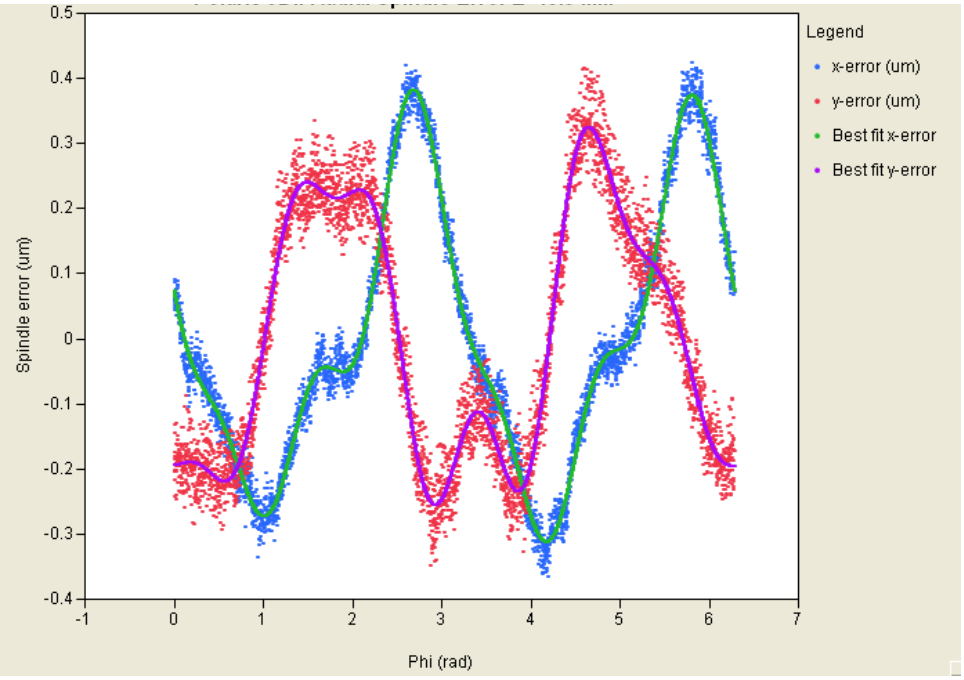

Figure 13. Measurement results for ϕ-axis radial runout in the x-and y-directions.

The resultant best fit Fourier series in the x-direction with φ in radians:

x-error (µm) = -0.26709 *(Sin2φ – 6.8253) -0.01800 * Sin(3φ-4.84096) -0.05491* Sin(4φ- 0.23570) + 0.00512 * Sin(5φ – 1.62753) -0.06540 * Sin(6φ - 1.4005)

and in the y-direction:

y-error (µm) = -0.24858 * Sine(2φ - -1.1926) - 0.00705 * Sine(3φ- 1.2556) + 0.04250 * Sine(4φ -1.30602) -0.04342 * Sine(5φ- 0.18016) + 0.06345 * Sine(6φ- 0.06640)

Variation with spindle speed

ϕ-axis radial error motion is dependent on the spindle speed. To establish the magnitude of error variation with spindle speed, radial error motion data was collected at 12, 30, 60, 120 and 240 rpm. The largest error motion is in the x-direction as shown in Figure 14. Variation of y-error was similar. While the variation is significant, particularly at the higher spindle speeds,

implementation of a speed-dependent correction algorithm is considered of secondary importance because most measurements will be made below 120 rpm.

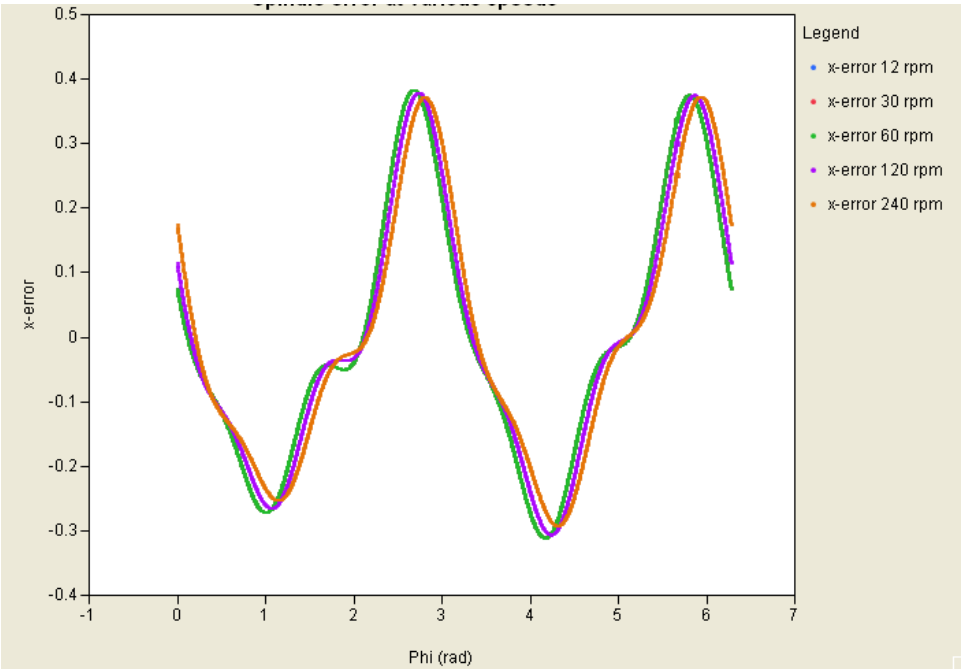

Figure 14. Speed dependence of ϕ-axis radial error motion in the x- direction.

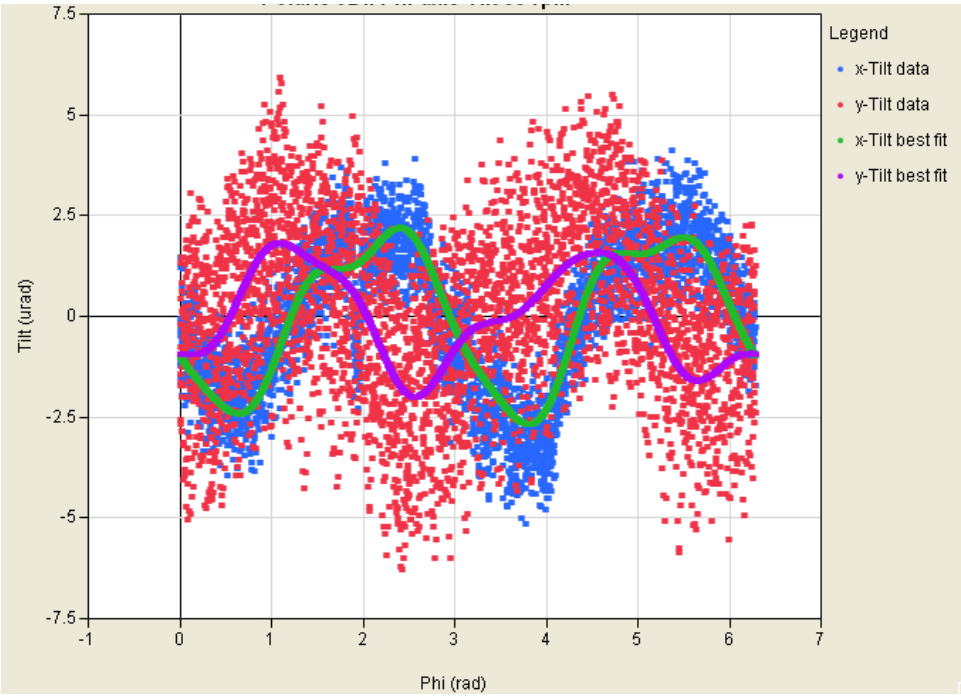

Figure 15. Tilt error motion of ϕ-axis at 30 rpm.

ϕ-AXIS TILT ERROR MOTION

ϕ-axis tilt error motion was obtained by dividing the difference of two sets of radial error motion data by the probe separation distance which was 34 mm. The resulting data are shown in Figure 15 for tilt error motion and the best-fit Fourier series in both the xz- and yz-planes.

θ-AXIS RADIAL ERROR MOTION

θ-axis radial error motion was obtained from capacitance gauge data for both x-and z-radial error motion of a reference sphere mounted on the R-axis carriage. The component in the R-axis direction is calculated and a best fit polynomial shown in Figure 14.

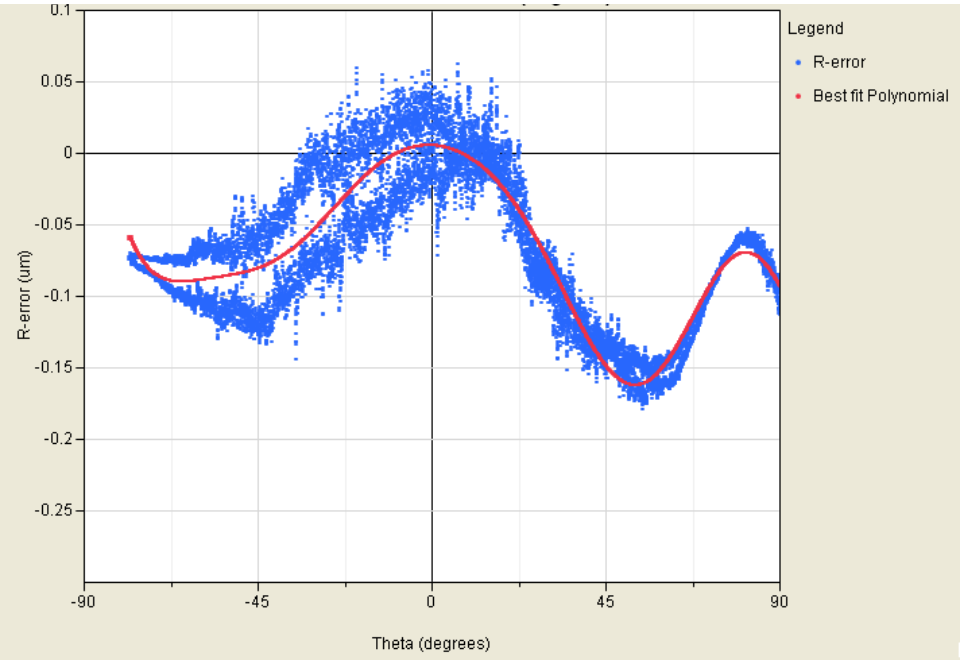

Figure 16. θ-axis radial error motion in the R-direction.

Y- alignment of probe to ϕ-axis origin

Data collection was performed on probe displacement as a function of ϕ-axis rotation. Figure 15 shows a data set where the tilted flat's 0 phi corresponds to slope aligned with positive y-axis. Since the tilted flat slope tilt is 7.4º, the y-error (at 0 rad) is -0.1 µm/tan (7.4º) and the x-error (at 1.57 rad) is -0.2 µm/tan (7.4º) giving errors of:

y-error=-0.77 µm

x-error=-1.5 µm

though only the y-error is adjusted, the x-error being equivalent to probe τ-error, which is more accurately obtained with the proper probe alignment technique.

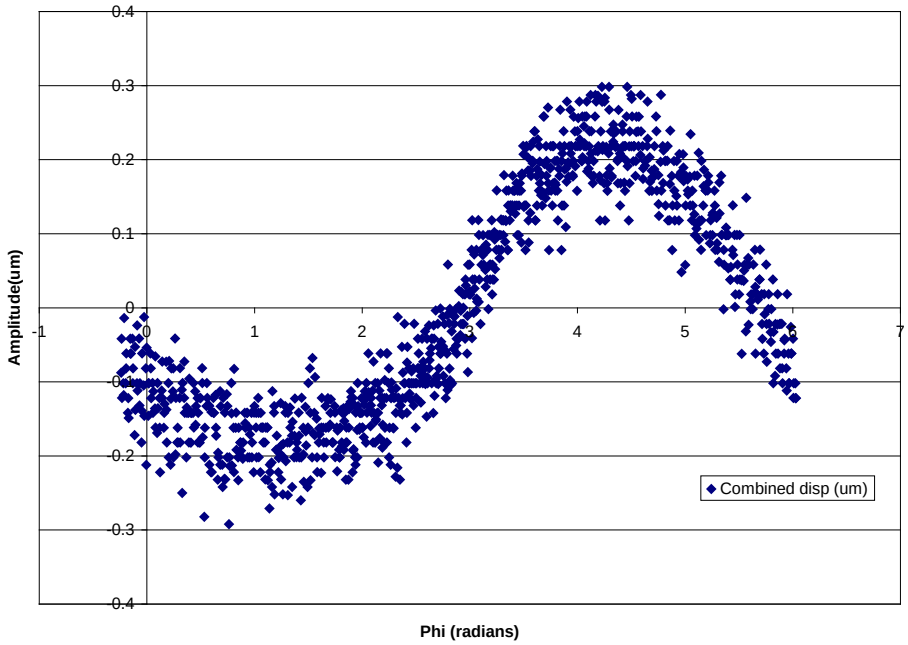

Figure 17. Probe to ϕ-axis alignment error data

1.4 CONCLUSIONS

Error compensation of the axis and alignment errors on Polaris3D is a work in progress. While the algorithms have been developed, measurement techniques designed and tested and a large amount of data collected, the correction has not yet been tested or implemented at the time of writing. The methods are, however, close to their final form and when completed will increase the overall accuracy of the machine by approximately one order of magnitude to the final goal of 100 nm.

REFERENCES

1. Sohn A. and K.P. Garrard, "Tip Waviness Compensation in a Polar Profilometer, " *Proceedings from the ASPE 2003 Annual Meeting*, Vol. 30, pp 355-358.
2. Sohn A., K.P. Garrard, and T.A. Dow, "Ultraform 2D," *2003 Precision Engineering Center Annual Report*, Vol. 21, pp45-60.

2 POLARIS 3D OPERATION AND CONTROL

Kenneth Garrard
Senior Research Associate
Precision Engineering Center

An instrument for the metrology of high-aspect surfaces has been constructed and delivered to a sponsor. This new profilometer has a spherical measurement volume 100 mm in diameter inside of which highly non-rotationally symmetric optical and mechanical surfaces with large surface sags can be measured with an accuracy of 100 nm. Fast aspheres, torics, biconics and freeform surfaces can be measured with deviations from a sphere of several millimeters.

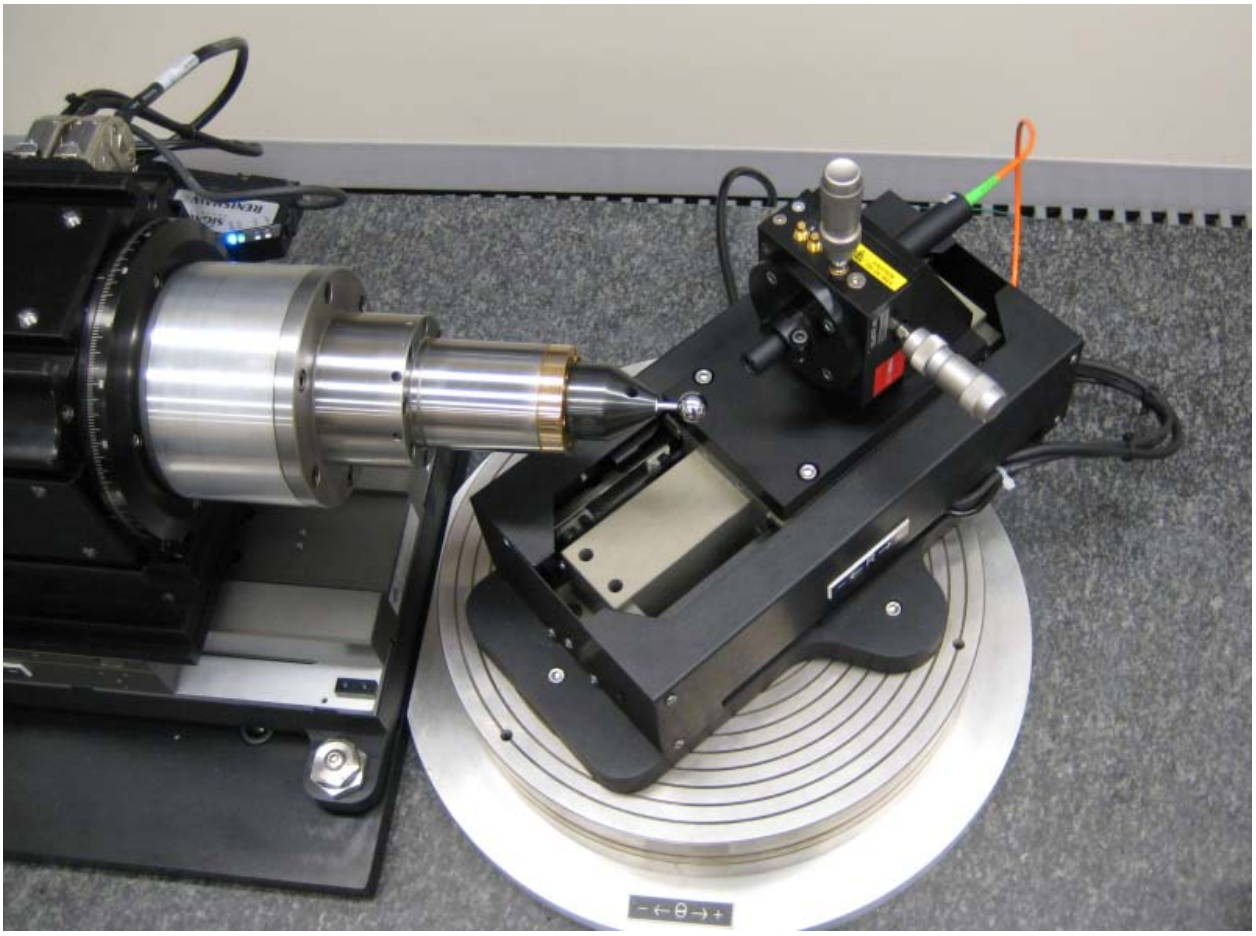

2.1 INTRODUCTION

The polar profilometer Polaris has been successfully retrofit with an optical probe and a part spindle to create a spherical coordinate measuring machine (SCMM) [1, 2]. This new machine, Polaris3D, has unique capabilities for quantifying complex surface features.

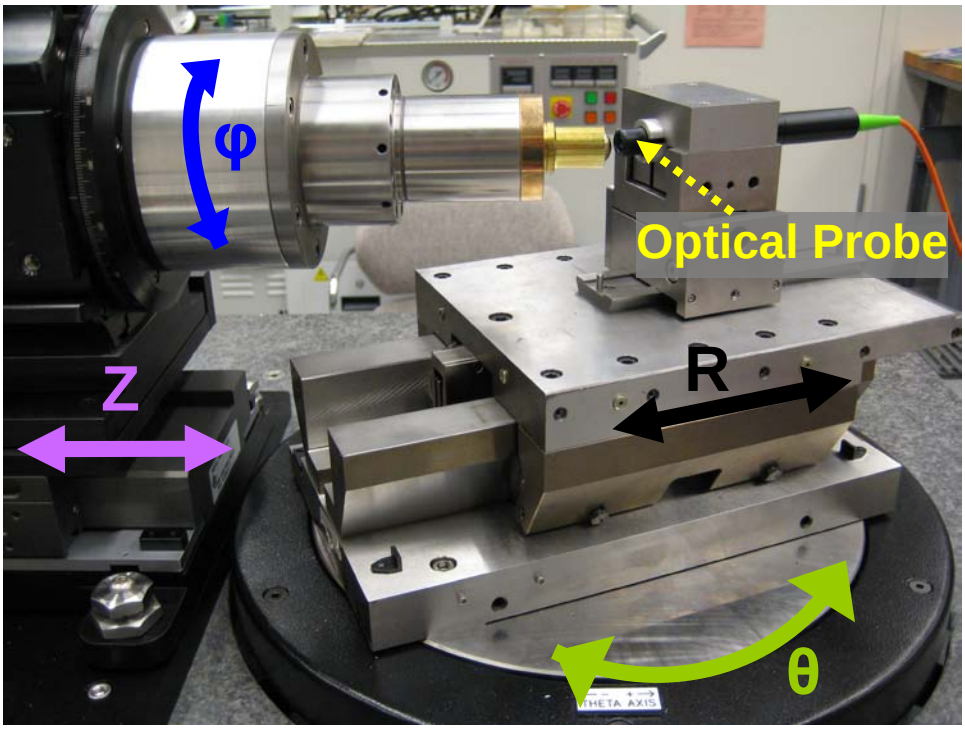

Figure 1. Polaris 3D

As shown in Figure 1, mounting a linear axis (R) and an optical probe on top of a rotary table (θ) and rotating a surface on an orthogonal spindle (φ) a creates hemispheric measuring volume. An additional linear axis (Z) allows a variety of convex and concave surfaces to be measured while keeping the probe nearly normal to the surface as it sweeps out a spiral path from the pole to the equator. The optical probe provides damage free measurement data.

2.2 OPERATION

The Polaris 3D instrument includes four types of software.

1) Feedback servo control of the moving axes of the machine
2) PLCs for machine setup, calibration, measurement and haptic operations
3) A general purpose expert user interface (*TDProfiler*)
4) A Matlab™ measurement data analysis GUI (*Polar3d*)

This report describes the PLCs, expert user interface and the Matlab data analysis GUI. Servo control aspects of the Polaris 3D machine were described previously [1]. Data flow through the Polaris 3D system is illustrated in Figure 2 with the software components show in yellow. The controller is a Delta Tau UMAC with an imbedded PC/104. This system controls the axes motions, acquires data and provides a platform for an expert operator interface for machine calibration and setup as well as a method for measuring a part. The PC/104 and the UMAC processor communicate via a shared bus. The PC/104 acquires measurement data in real-time and saves it to a networked partition on its hard drive. The analysis PC hosts a Matlab™ application that retrieves raw data files from the controller and assembles the data into a spiral cloud of points in spherical, Cartesian and cylindrical coordinates. It also compares the measurement to a sphere and displays the results graphically. All communication between the controller and the analysis PC is via the ethernet LAN.

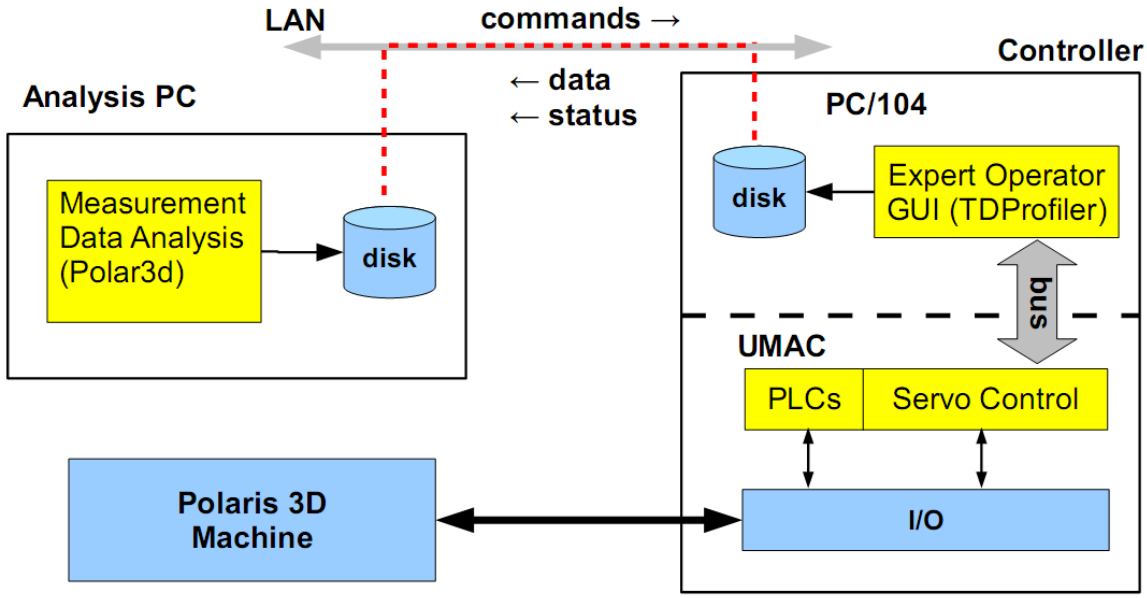

Figure 2. Polaris 3D data flow schematic.

The optical probe used on Polaris 3D is a STIL CHR 150N. The UMAC uses both the R axis encoder feedback and the probe signal to maintain a constant flying height of approximately 5 mm when measuring a part. Thus the R axis follows or tracks the surface as the θ and φ axes rotate the probe and the part. Provided the angle of incidence of the probe with the surface is less than about 14° tracking can be maintained. Presently the rotary axes move at constant velocity during a measurement and data is collected at a constant sampling interval. This produces a data set that spirals from the equator to the pole and is more densely packed at the pole, one circumference of latitude being a shorter distance than at the equator.

X.2.1 PLCs

PLCs have been written to safely move the axes to their home positions, engage tracking control, perform part setup and probe calibration functions and to measure a part and send data to the PC/104 user interface program. The UMAC is responsible for motion control of all axes (R, θ, Z and φ) and data acquisition during part setup, calibration and measurement. Software PLCs are used to home the axes and to detect faults and respond appropriately (e.g., stop motion if an axis is moved beyond its range). The UMAC is not programmed as a general purpose computer to control the machine axes. Rather the servo code (PID plus acceleration and velocity feedforward) and motion program interpreter are embedded in firmware and the user/OEM specifies operating modes, a mapping of the machine geometry to a coordinate system, controller gains and the I/O configuration. The firmware performs trajectory generation along a specified path through Cartesian space and servo control for the motors as a high priority real time task. Background processing (i.e., while waiting for the next real time interrupt) includes responding to commands from a host computer, reporting motor positions, machine fault detection and other housekeeping tasks. These later functions are implemented as software PLCs (programmable logic controllers). Table 1 lists the Polaris 3D PLCs and their function.

Table 1. Polaris 3D Controller PLCs.

estop	monitor hardware for emergency stop conditions initializes controller, phases motors, recovery from fatal errors
cyclestop	abort all axis motion, resets PLCs with handwheel functions enabled
axpos	report axis positions and error conditions
probetrack	the probe tracking servo filter and data acquisition function
jog	controls handwheel jog functions, absolute and incremental motions
jogzero	moves the selected axis to its zero position
trigger	move the R or Z axis until a probe signal is received enables probe tracking with the R axis servo control
unload	move the axes to the predefined part load/unload position
spin	starts and stops the part spindle at constant velocity
measure	measures a part surface, measures part runout
homeall	homes all the axes in a predetermined sequence to avoid collisions
homeR	moves the R axis to its home position
homeTheta	moves the rotary table to its home position
homeZ	moves the Z axis to its home position
homePhi	moves the part spindle to its home position
probe	performs probe alignment motion sequence and error calculation
switcher	invokes PLC functions based on user command input
watcher	motion sequence timeout watchdog – only used for PLC debugging

The UMAC firmware has the capability to execute motion programs describing the path through space of groups of axes in the same coordinate system, similar to traditional NC machine tool controller G-codes. Polaris 3D does not use this feature of the UMAC, rather, the axes are commanded to move individually and the PLCs coordinate the motion. The **estop**, **cyclestop, axpos** and **probetrack** PLCs run continuously. The remainder are started and stopped as needed. The **measure** PLC implements an algorithm to measure a single annular region of a part and to optionally measure its runout on the part spindle. This includes ancillary motions to find the part with the probe, position the part with respect to the machine coordinate system and to return to the load/unload position when the measurement is complete. Measurement data is acquired by the **probetrack** PLC and sent to the expert user program (TDProfiler) via a circular queue of shared memory on the UMAC bus. An overflow region of private memory accessible only to the UMAC processor is used in case the queue fills. This can happen due to the asynchronous nature of the host PC/104 and non-support for hard real time systems by the Windows OS. Upon completion of the measurement any data saved in the overflow memory is transferred to the PC/104. The result is a raw data file that must be processed to recover the original data stream and convert the axes positions into a part surface map. Provided that the PC/104 is essentially idle except for TDProfiler, data can be streamed to the PC/104 hard drive indefinitely (i.e., until the disk fills) at the default collection rate of 752 Hz.

2.2.2 EXPERT USER INTERFACE

A general purpose controller interface developed by a consultant[1] has been configured as an expert operator interface for Polaris 3D. It provides a direct connection between on-screen GUI controls and the UMAC PLCs. All interaction with the machine is either through its manual controls or the TDProfiler application. Many of the capabilities of TDProfiler are not used for Polaris 3D.

TDProfiler communicates directly with the PLCs via shared variables and does not maintain machine state information. That is, each display item, button and toggle control reads or changes one such shared variable without regard to the present or prior state of any other variable. The exception is the data acquisition feature. In this case, a circular queue shared by two processes is implemented by TDProfiler (the reader) and the **probetrack** PLC (the writer). The acquired data file is saved on the embedded PC/104 hard drive. The operator is responsible for initiating the sequence of operations required to acquire meaningful data.

The main screen shown in Figure 3 contains the axis position information and optical probe signal values. Additional buttons engage probe tracking, initiate data acquisition, start a measurement cycle and control the part spindle. Numeric values displayed in green can be

[1] Tisfoon Ulterior Systems, Cary NC.

modified by the user. On the main screen these five values (part spindle speed, rotary table velocity, rotary table starting and ending angles and the ZR offset) are set by the operator to define a measurement. The Measure button triggers the **measurement** plc to move the axes into position to measure a single annular zone on a part. When motion stops the raw measurement data file can be read from the hard drive. Additional information show on the lower left of the main screen allows the operator to track the progress of data acquisition. A measurement (or any other motion sequence) can be stopped immediately by clicking on the Stop sign button.

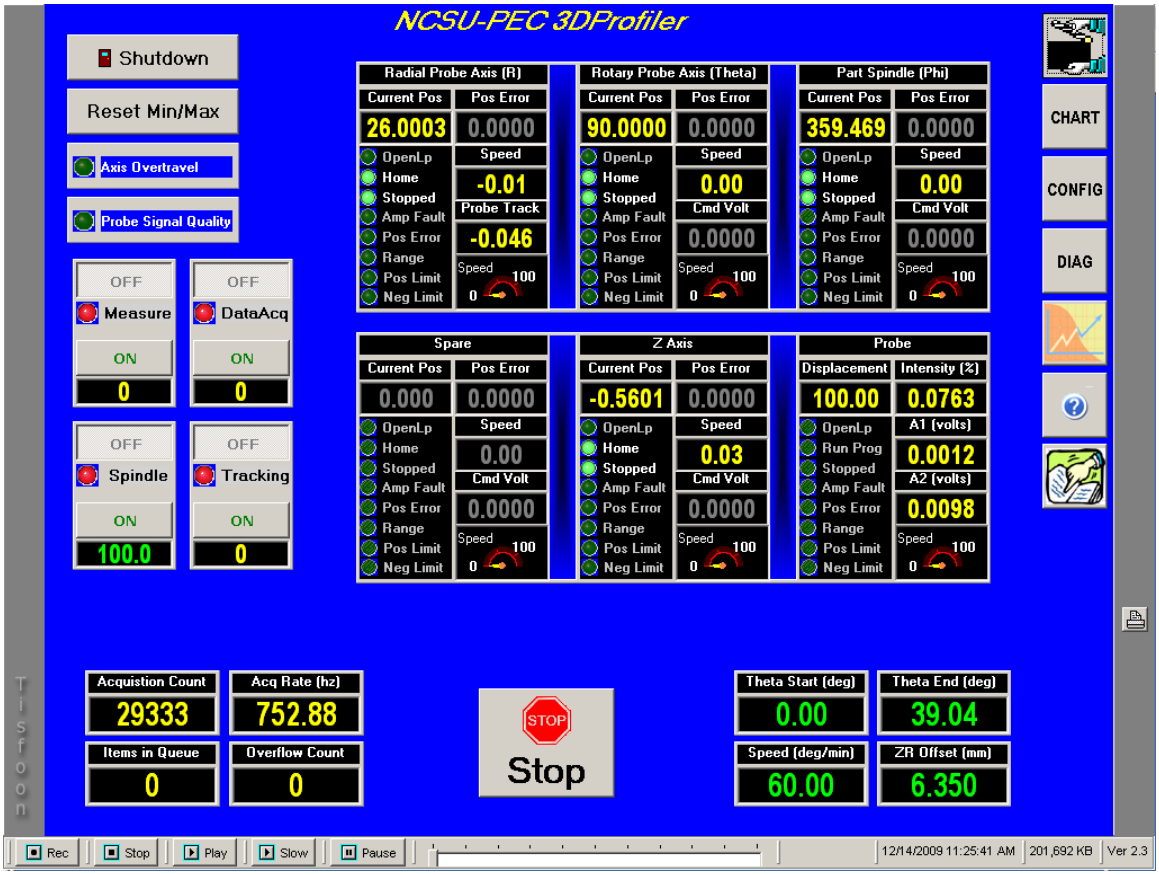

Figure 3. TDProfiler main screen.

The CONFIG button loads the screen shown in Figure 4. This screen contains the toggle controls needed to home the axes, jog an axis to its zero position, find the part with the probe (and engage the tracking control), jog the axes to the part load/unload location and initiate the probe setup procedure. It also has data entry locations for **measurement** PLC options and the residual errors calculated by the probe setup procedure. Additional toggle controls set the current position of an axis to zero and abort operation with an emergency stop (complete axis shutdown) or a cycle stop (stop-and-hold position).

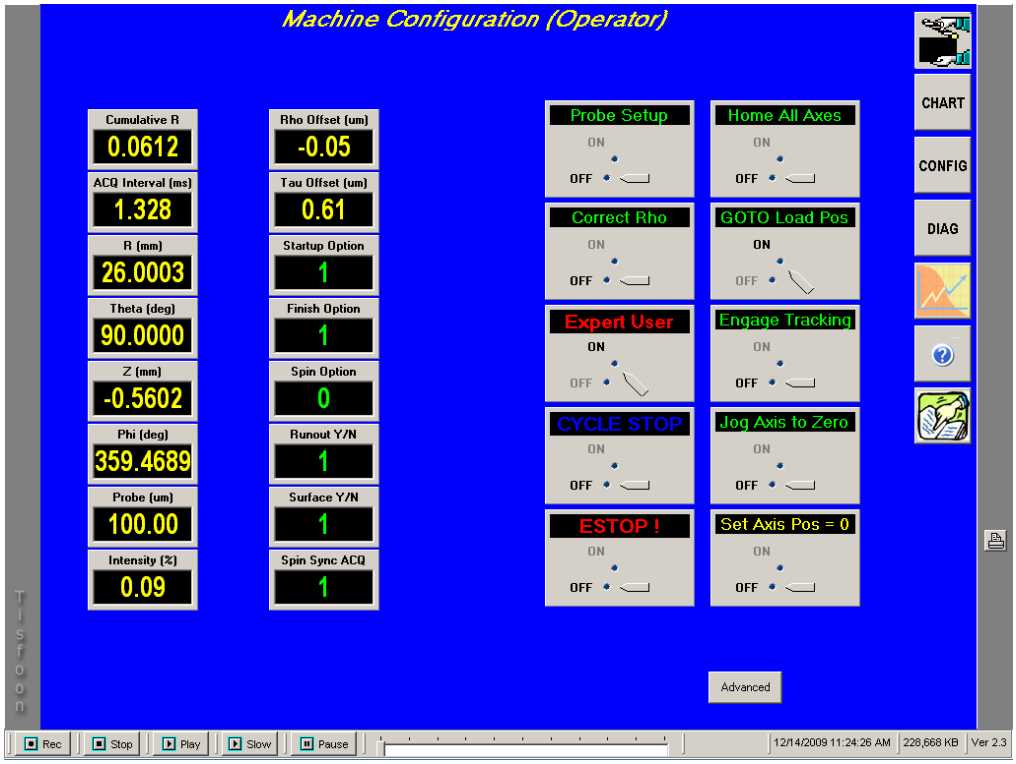

Figure 4. TDProfile configuration screen.

Figure 5. TDProfiler advanced configuration screen.

The screen shown in Figure 5 is displayed by clicking on the "advanced" button on the configuration screen. It contains numeric parameters for data acquisition, probe tracking and alignment and more measurement parameters. Information displayed includes load/unload motion velocities and positions and probe signal parameters.

The TDProfiler diagnostics screen is accessed by clicking on the "diag" button. This screen allows the probe-triggered motion velocities and limits to be changed. It also displays information related to the probe setup operation and status variables for the **measurement**, **unload** and **homeall** PLCs as well as overall machine and axis status codes.

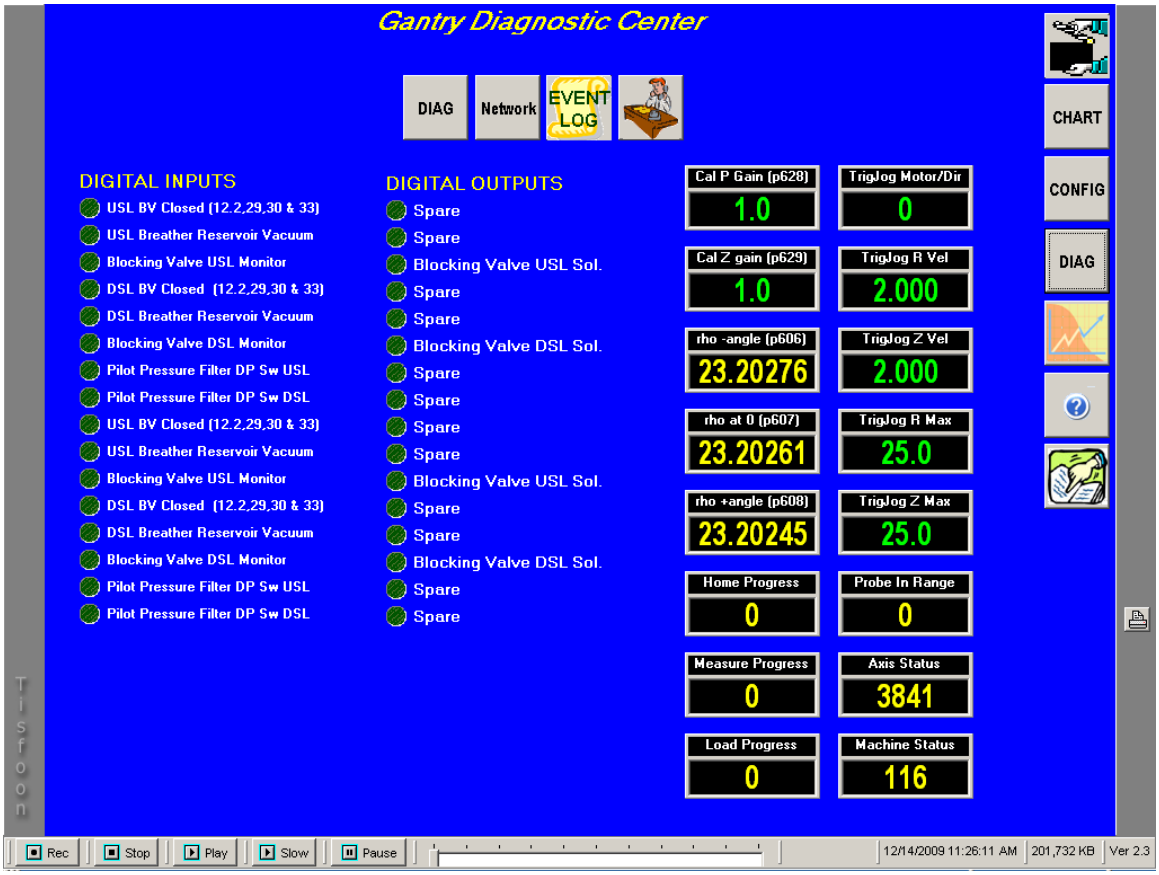

Figure 6. TDProfiler diagnostics screen.

2.3 DATA ANALYSIS

Upon completion of a measurement the operator can read the data file with the **Polar3d** application. The three tab panels for this Matlab application are shown in Figures 7 and 15. **Polar3d** can be run on any PC and retrieve data files directly from the UMAC controller.

Figure 7. Polar3d design and filter tabbed panels.

Figure 7 shows the panel controls for reading and processing design data (left) and specifying filter coefficients, options and machine offsets (right). Design files read by **Polar3d** specify a surface in cylindrical coordinates as one half of the cross section of a rotationally symmetric surface plus a sagittal deviation matrix on a web-like grid. These files are read and processed by **Polar3d** to calculate the optimal placement of the part in machine coordinates for measuring the specified annular region, determine if the probe will collide with the part during measurement and calculate the rotational speeds needed to collect data at the desired spacing on the surface. Presently, **Polar3d** does not subtract or compare the design data set with the measured data.

2.3.1 REGION OF INTEREST AND COLLISION AVOIDANCE

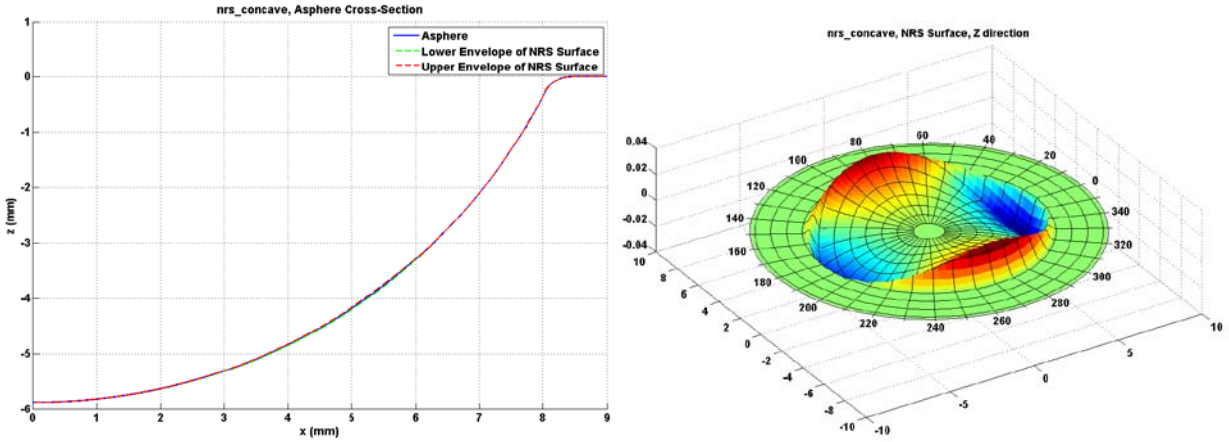

Figure 8. Design file: concave asphere cross-section (left), NRS sagittal deviation (right).

Figure 8 shows the aspheric base surface for a non-rotationally symmetric concave part. The upper and lower envelope of the deviation from symmetric is shown as the red and green dotted lines. On the right in the figure the non symmetric deviations from the asphere are shown as a shaded surface.

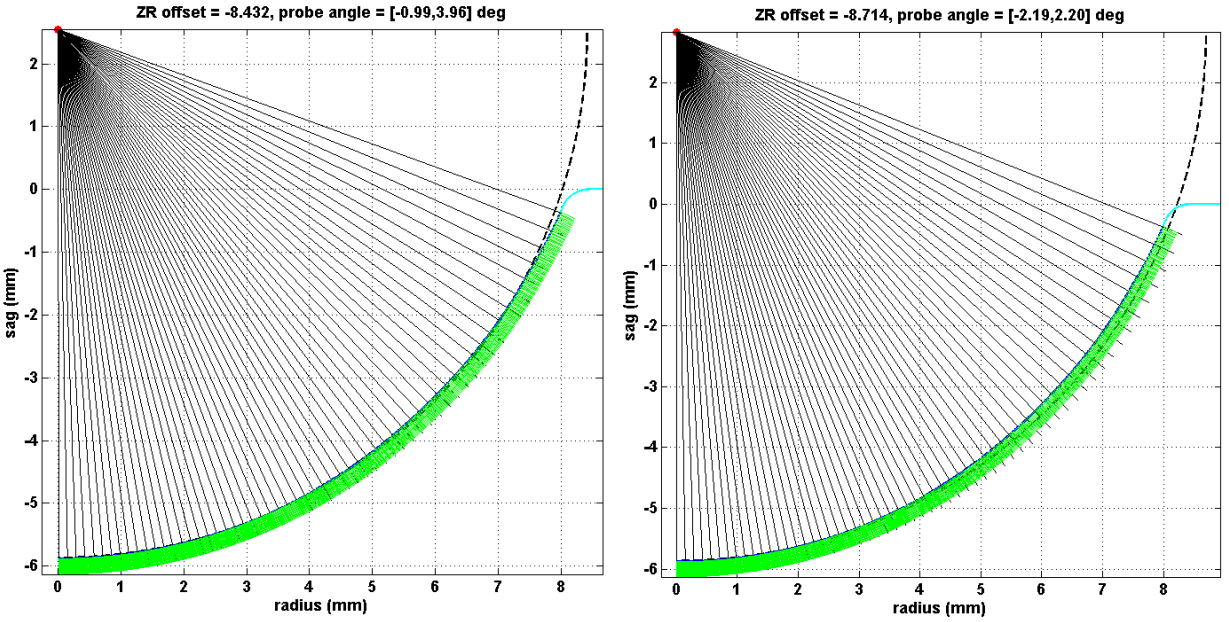

Figure 9. Optimization of offset location for measuring the surface in Figure 8 from the pole to a cylinder radius of 8mm.

The Z axis location of the part set before measurement starts. Ideally the part is located with respect to the probe such that the probe light has normal incidence with the surface as the rotary

table rotates through the range of measurement. The part design is specified in cylindrical coordinates so the starting and ending angles of the rotary table for a given starting and ending cylindrical radius depend on the this location as well. For a non-spherical surface the probe cannot maintain normal incidence unless both the part and the probe are moved during measurement. However there is a location (called the ZR offset) that optimizes the incidence angles for a given range of measurement. The maximum incident angle is about 14°. Figure 9 (left) illustrates the initial placement of a part by choosing the radius of the best fit sphere as the ZR Offset. This offset is equal to the distance between the apex of the part (at Theta = 0°) and the center of rotation of the rotary table. It is an offset instead of the position of the Z axis because the length of the part and its mounting fixture is unknown. On the right in the Figure the incidence angles have been equalized by increasing the offset 300 µm.

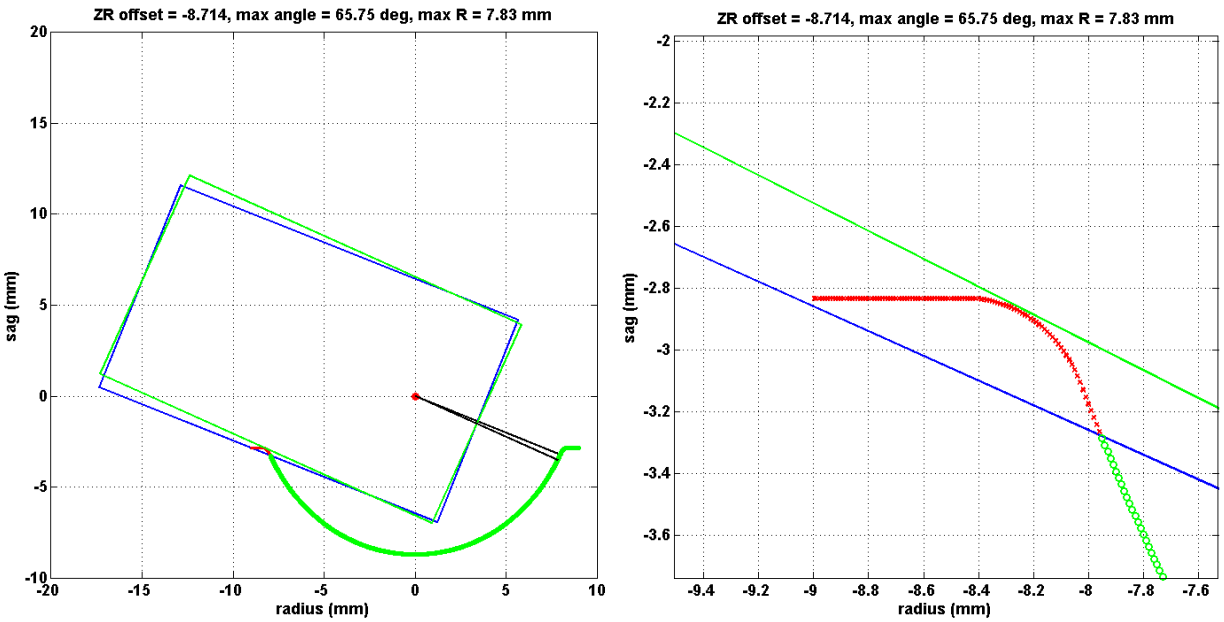

Figure 10. Part-probe interference. (a) collision of probe with edge of concave surface (red region) (b) detail showing maximum part rotation angle (green line).

For convex parts there will rarely be interference between the probe and the part during a measurement due to the 5 mm working distance of the CHR 150N. However the barrel of the probe is more than 11 mm in diameter so for a small concave surface the edge of the probe might hit the side of the part at a large rotation angle. Such is the case for the measurement setup shown in Figure 9. After calculating the ZR offset, **Polar3d** determines whether or not the probe will hit the part during measurement. This is done by moving the nominal probe shape (a rectangle slightly larger than the actual probe) through the proposed angular range of measurement and finding any points on the surface profile that are inside of that rectangle. This calculation is performed by a simple application of the Jordan Curve Theorem [3] at an arbitrary number of steps between the starting and ending rotation angles. The Jordan Curve Theorem

implies that for any closed curve and a two points the points are on opposite sides of the curve if and only if a line drawn between them intersects the curve an odd number of times. By considering the probe as a closed polygon and each point (x, z) on the design surface profile along with a point at (x, ∞) it be easily determined if any point on the surface is "inside" the probe for a given ZR offset and rotary table measurement angle. The results are shown in Figure 10 for the part setup of Figure 9. On the left plot, the probe is shown as the blue rectangle and the part as the green concave surface profile. The red dot is the center of rotation of the probe. The small red region is the location of the collision of the probe with the edge of the part. This region is shown in detail on the right side of the figure. The red surface points are inside of the probe. The green rectangle represents the maximum rotary position of the probe for this geometry (65.75°) and the maximum measureable cylinder radius is 7.83 mm instead of the desired 8 mm.

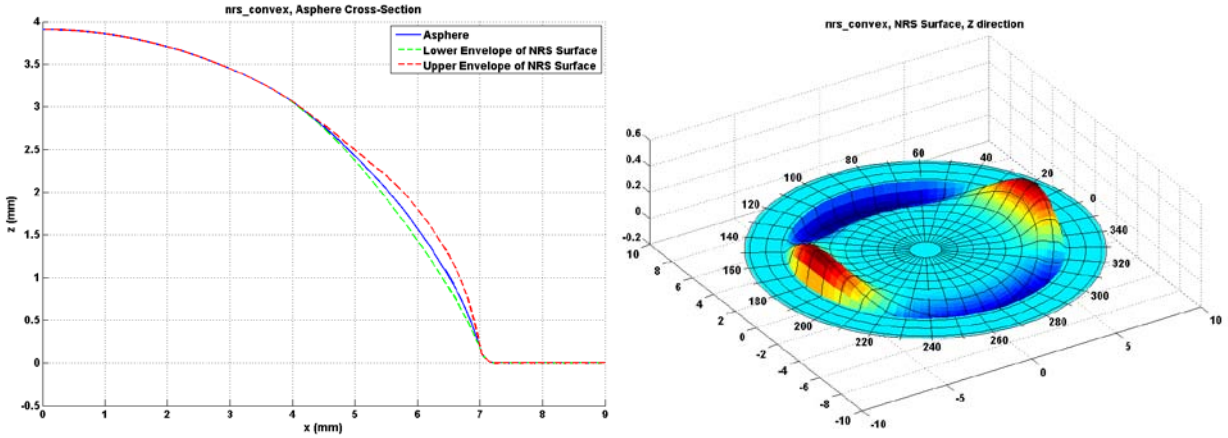

Figure 11. Surfaces in a design file: convex asphere cross-section (left), non-rotationally symmetric sagittal deviation (right).

Figure 11 shows a convex design surface with several hundred micrometers of non-rotationally symmetric deviation from a base asphere. If the desired radial measurement range is between 5 and 7.1 mm, the initial ZR offset (the radius of the best fit sphere) will not allow the entire surface to be measured. The probe incident angle would be 19° at a radius of 7.1 mm. This is shown as the red vectors in the left plot of Figure 12. On the right an optimized part location is found with a ZR offset of 9.188 mm and the probe incidence angle range is ±13.37°.

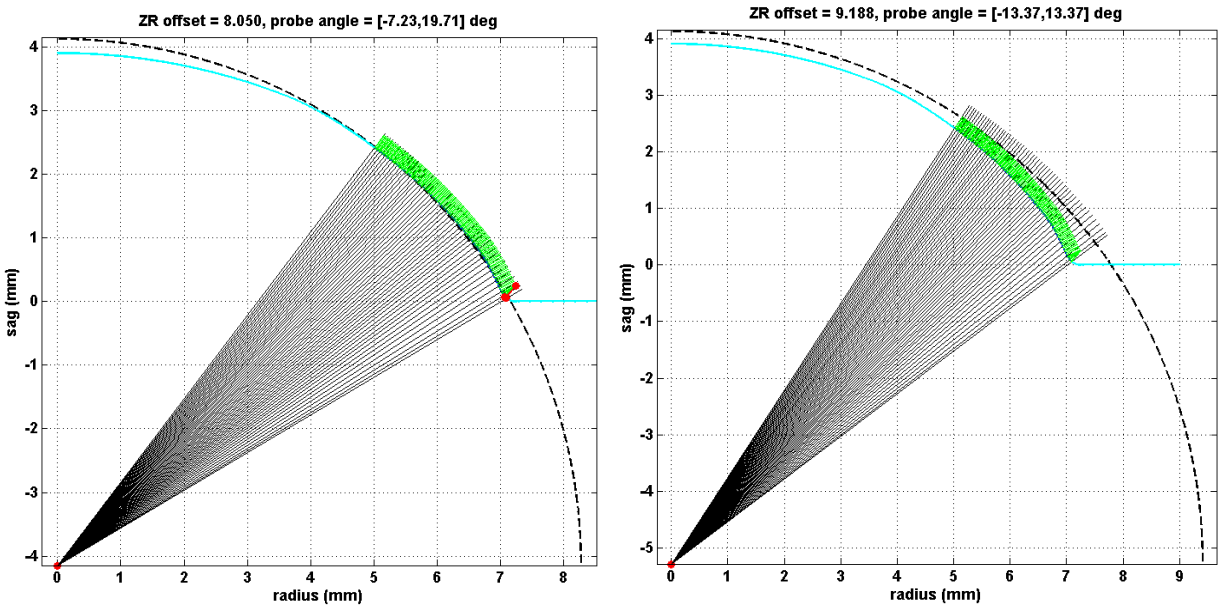

Figure 12. Optimization of offset location for measuring part in Figure 11.

2.3.2 DATA DENSITY

The data density (i.e., azimuth and elevation spacing) is set by the part spindle and rotary table velocities. And the time required to measure a part is given by the range of rotary table angle need for the selected part annulus divided by the speed of that axis. If the rotary speeds are constant then this is equal to the number of part revolutions divided by the part spindle speed. And the spacing between data points will be at equal angular intervals in both directions since the data acquisition rate is a constant. The result is a spiral pattern from the equator to the pole of a surface. If the spindle and rotary table speeds are increased as the pole is approached then the density can be made more uniform in arc length across the part. The speeds do not have to go to infinity at the pole since 1) the probe spot size is 7 μm and 2) the sample rate is finite. An example is shown in Figure 13 for the part and region of interest in Figures 11 and 12. For a spacing of 4 points per mm of arc in the elevation direction and 192 points per mm of circumference only 13 part revolutions are required with the spindle speed varying from 7 to 10 rpms and the rotary table speed varying from 10.4 to 15.2 degrees/min. The parameters are shown in the right side of the Figure as entered into **Polar3d** and the change in velocity is plotted on the left. The measurement time for this example is 1:38 minutes. If a fixed velocity is selected, then a worst case speed is selected for the azimuthal direction at the largest circumference (i.e., the largest rotary table angle) and the measurement time is increased to almost minutes.

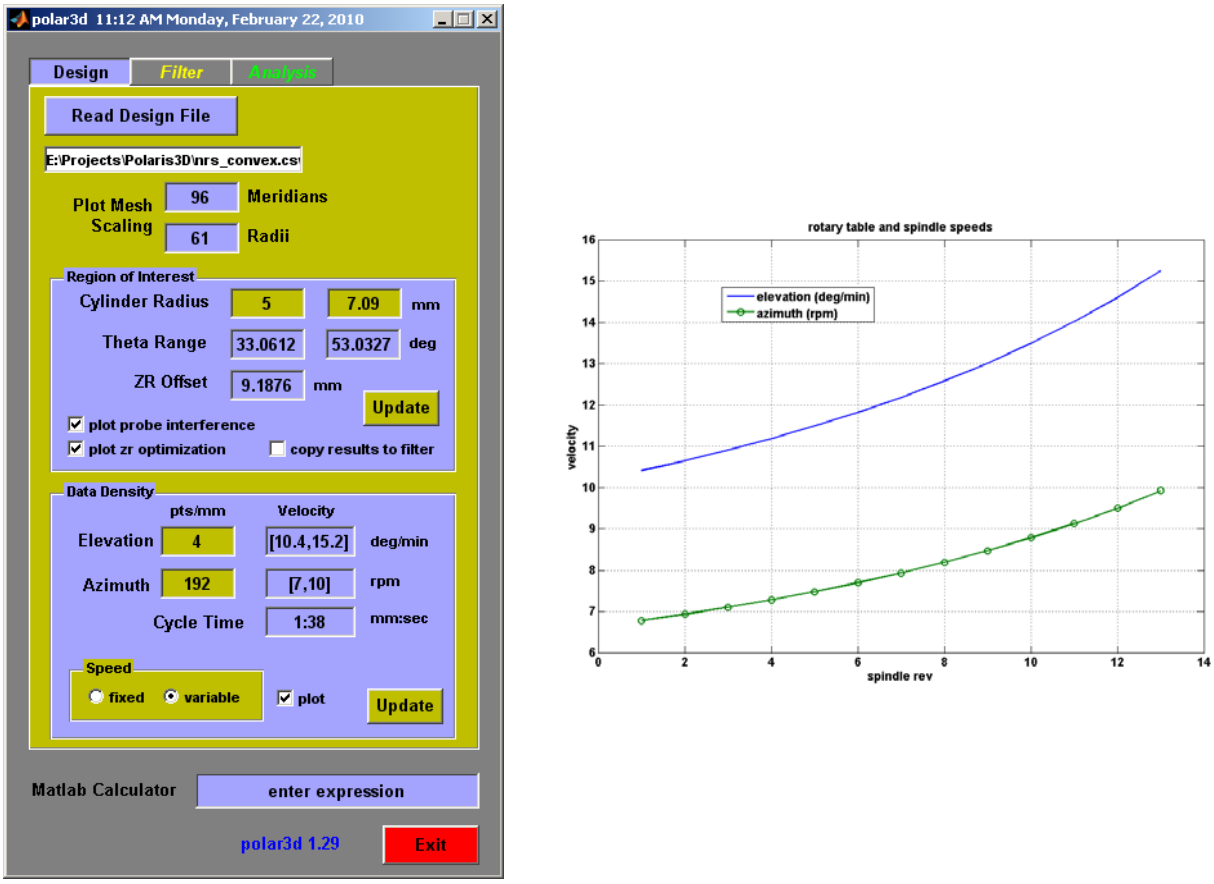

Figure 13. Data density calculation.
Measurement time: variable speed = 1:38 min, fixed speed = 1.55 min.

2.3.3 PROBE FILTERING

Data from the CHR 150N probe is noisy, especially if the probe signal is disturbed by dust or scratches on the part. There is also a know delay in the probe response of about 3 milliseconds, regardless of the sample rate selected. It has also been found that a small percentage of data points are outliers. These spikes in the data stream are not repeatable and would represent surface features with an improbable aspect ratio if the data were accepted. The filter panel shown in Figure 7 is used to specify parameters for several probe filtering operations. First data points with low intensity levels and points with any axis in overtravel are rejected; next an outlier filter based on distance from the mean value is used to find spikes. The distance parameter is specified in units of standard deviation. Finally a maximally flat Butterworth filter is used to smooth the data. The filter is implemented as a zero-phase filter to avoid an unwanted time shift in the probe signal with respect to the other axis data. Typical results of this filtering are shown in Figure 14. The blue line (with +'s) is the raw probe signal, the green line (with o's) is the data after the threshold and outlier filters are applied and the solid red line is the final smoothed data.

This latter line is also time shifted 3 milliseconds to account for the delay in the probe electronics.

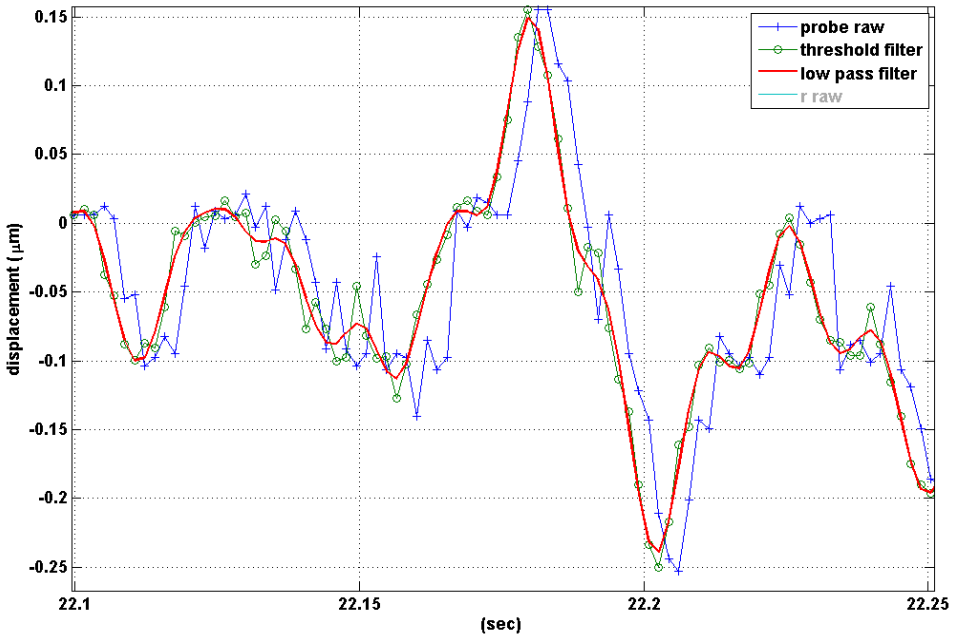

Figure 14. Effect of probe smoothing filter and time shift.

2.3.4 SPHERICAL ANALYSIS

The third tab panel of **Polar3d** is for the input and analysis of a measured data set. This panel is shown in Figure 15. **Polar3d** converts the raw axis position data into spatial coordinates (spherical, cylindrical and Cartesian) and produces plots of the surface and the deviation of the surface from a sphere (least squares or user specified radius and center). The parameters from the filter panel are applied when the data is read or re-loaded. There is a selection for reading directly from the Polaris machine via the shared network drive or reading a previously saved data set. At the time of writing only two types of analysis can be performed: spherical fit to surface data and runout analysis of data from the OD of a part. Runout analysis is simply fitting a circle to data from a fixed number of part revolutions collected with the rotary table parked at 90°. The location of the best fit circle and its distance to the origin give the magnitude and direction of the runout, which can be removed from the surface data before further analysis. For cylinders, the best fit circle gives the cylinder diameter.

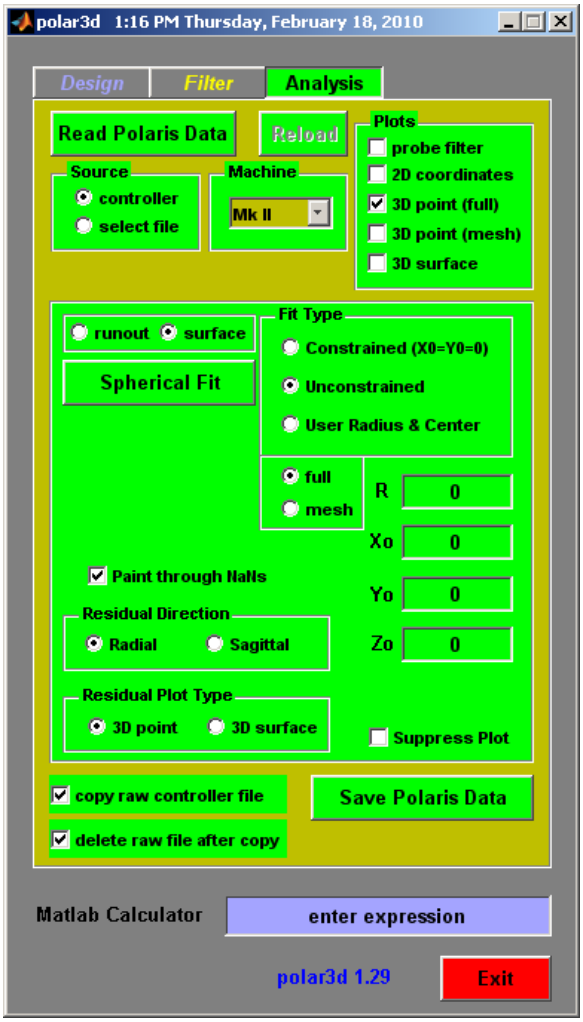

Figure 15. Polar3d analysis tabbed panel.

Specifically **Polar3d** performs the following operations when reading a measurement data file.

1) Read a raw data file (from controller PC/104 or user selected)
2) Reconstruct the data stream into axes positions and probe displacement
    a) sort by pseudo-clock value
    b) perform cumulative sum for each axis data stream
    c) apply scaling factors and offsets
3) Trim the data based on desired theta measurement range
4) Filter the data
    a) reject data points where the axes were in overtravel
    b) reject data points with low probe intensity
    c) reject outlier probe data points based on a standard deviation threshold filter
    d) expand rejected points to encompass a region of interest (ROI)

e) interpolate through the gaps in the probe data
f) apply a zero-phase, butterworth filter to reduce noise in the probe signal

5) Offset axes position data
6) Combine probe, R and Z data into a radius value (distance to machine origin)
7) Form spherical coordinate representation of the measurement (azimuth, elevation, radius)
8) Convert spherical data to Cartesian coordinates (x, y, z)
9) Convert Cartesian data to cylindrical coordinates (theta, r, z)
10) Interpolate the data to a cylindrical mesh (uniform spacing in angle and radius, i.e., a spider web) with a user specified radial range and spacing (full annulus)

The data is now available in three coordinate systems for analysis and comparison to a design. However, only the data produced in step (10) is on a regular cylindrical grid. A spherical fit can be performed with several options.

1) Selection of the data source: Cartesian spiral or Cylindrical mesh
2) Fit type: least squares sphere, least squares sphere with origin along cylinder axis, user specified parameters (radius and center)
3) Residual direction: radial or sagittal
4) Plot type: surface plot or point cloud

As discussed above, **Polar3d** reads a part design file to setup the measurement of a region of interest. The part design files define a rotationally symmetric asphere as a radial cross-section and a matrix of sagittal deviations from this asphere on a cylindrical mesh, whereas the measurement data recorded at equal time intervals from constant velocity rotary axes will lie on an Archimedean spiral. Subtraction of the measured surface from the design data has not been implemented. One approach that has been tried manually with promising results is to interpolate the cylindrical grid design data to the measurement spiral. Interpolating the noise-free design data instead of the measurement data should yield better fidelity to the true surface. Subtracting one data set from the other only makes sense if they are both on the same grid and have the same origin so an optimization process that aligns the two data sets to produce a minimal difference is needed.

2.4 MEASUREMENT RESULTS

A 25.4mm diameter Bal-Tec sphere was measured 15 times to assess repeatability and accuracy of Polaris 3D. The mounting of the sphere on the spindle had significant runout: approximately 80 µm. For a sphere (or any rotationally symmetric surface) the runout can be easily removed from the resulting data. The radius of the best fit sphere to this data is 12.7002 mm. The standard deviation in radius for the repeated measurements is about 100 nm.

Figure 16 shows a measurement of a concave spherical surface with a radius of 8.188 mm over an angle range of 47°. Figure 17 shows the residual after fitting a sphere to this data. The fit radius is about 1 µm too large and the peak-to-valley residual is 742 nm.

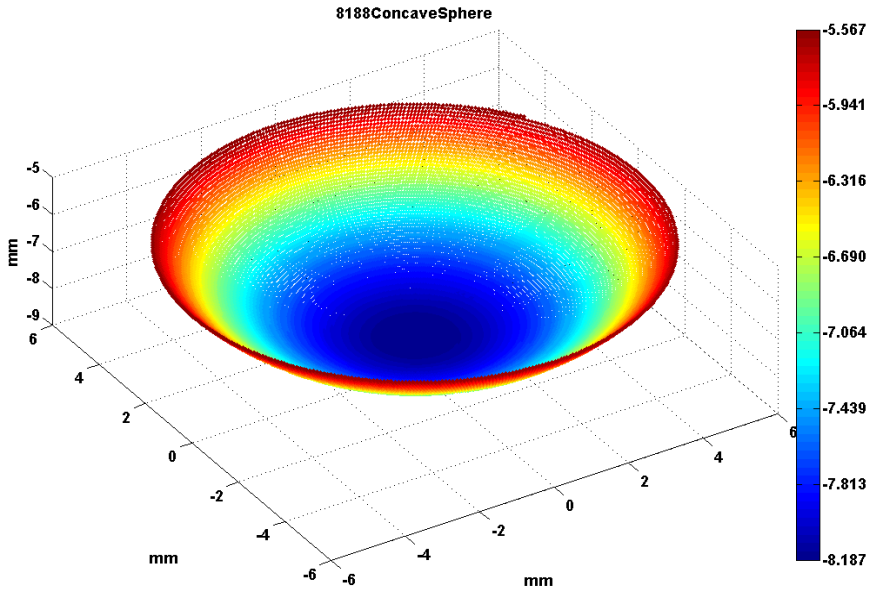

Figure 16. Concave spherical surface.

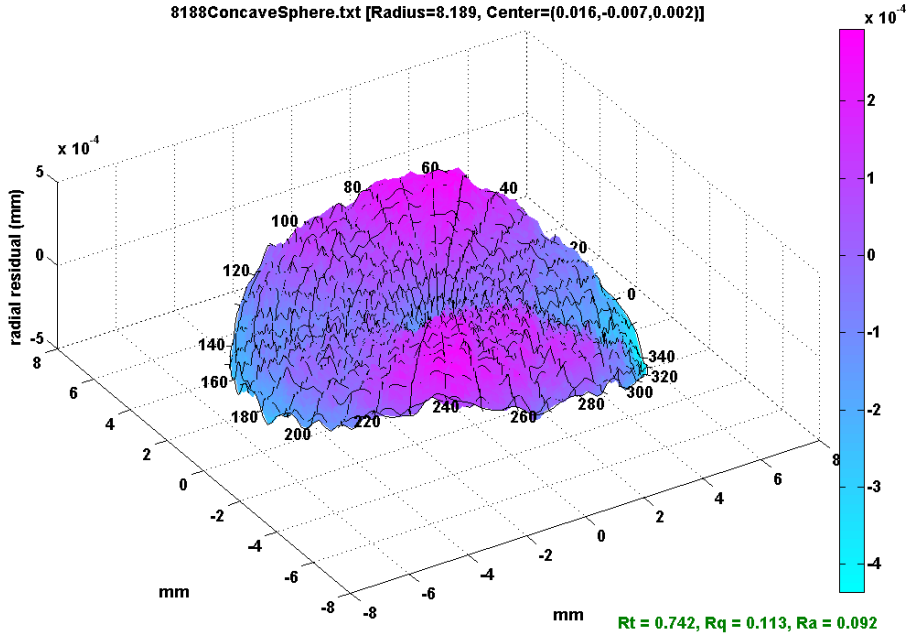

Figure 17. Radial direction residuals for surface in Figure 16.

Figure 17 shows an annulus of a non-rotationally symmetric convex surface. Little can be seen from the raw data plot other than that the sag is about 1.5 mm. After subtraction of a best fit sphere the sagittal dependence on azimuth angle is revealed in Figure 18.

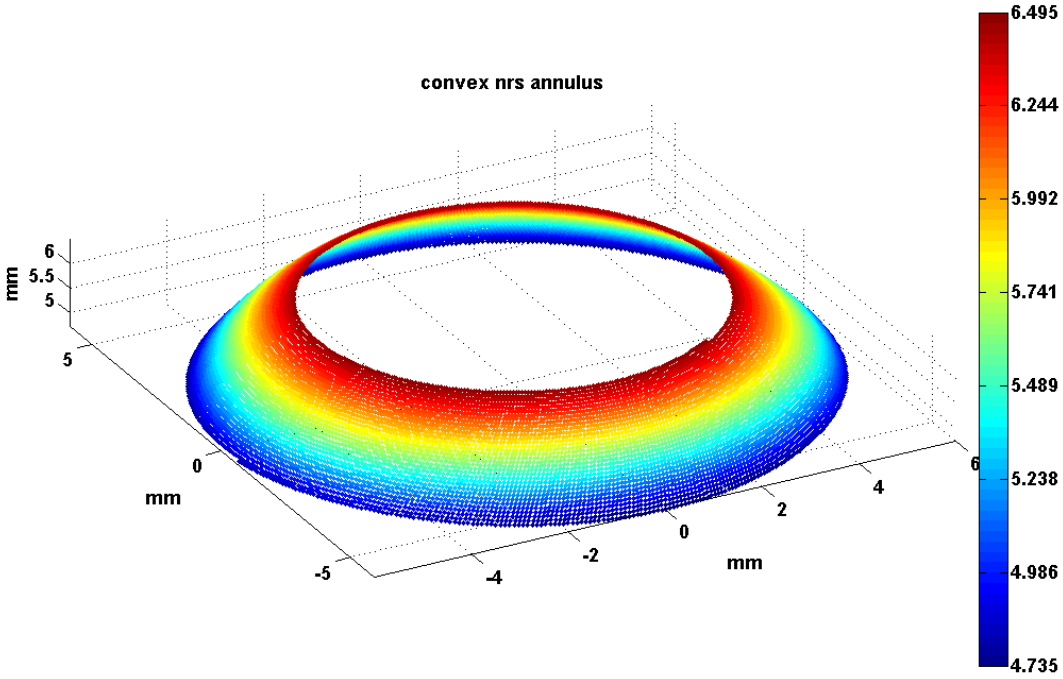

Figure 18. Convex non-rotationally surface – annular measurement.

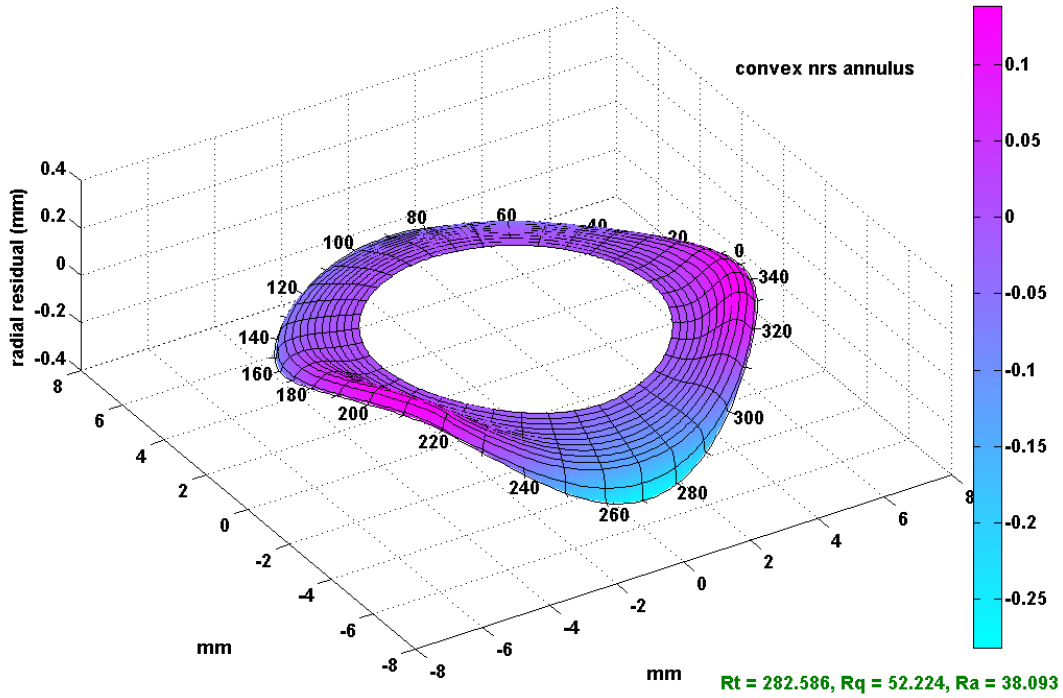

Figure 19. Radial residual after remove a least squares sphere.

2.5 CONCLUSIONS

The Polaris3D spherical coordinate measuring machine is operational. Repeatability of measurements is outstanding and accuracy is nearly as good as the manufacturer specifications for the optical probe provided the axes are properly aligned. Future work will focus on implementation of residual alignment error compensation and comparison of design surface data with measurement data.

REFERENCES

1. Sohn, A., K.P. Garrard and T.A. Dow, The Polar Profilometer *Polaris*. Proceedings of the American Society for Precision Engineering Sixteenth Annual Meeting, **v. 25**, pp. 28-31 (2001).

2. Garrard, K. and A. Pirzadeh. Polaris 3D Operation and Control. Precision Engineering Center Annual Report, 26, 149-166, North Carolina State University (2008).

3. http://en.wikipedia.org/wiki/Jordan_curve_theorem, 2010.

3 DESIGN OF A FAST LONG RANGE ACTUATOR – FLORA II

Erik Zdanowicz
Graduate Student[1]
Jeffrey Eischen
Associate Professor
Thomas Dow
Professor
Department of Mechanical and Aerospace Engineering

Non-Rotationally Symmetric (NRS) optical surfaces are useful to optical designers because they provide additional degrees of freedom that can be used to improve optical performance and reduce system size. However, these benefits bring complications with regard to fabrication, assembly and metrology. This paper discusses the design process for a long range actuator that can be used to fabricate such surfaces with large sag (4 mm) at frequencies up to 20 Hz. The first generation Fast Long Range Actuator (FLORA I) was created to operate at ± *2 mm and 20 Hz while creating a high-quality optical surface. FLORA I suffered from large physical size, moving mass and unwanted vibrations. A new system, FLORA II, has been designed to address these problems. This design uses a porous graphite air bearing, hollow SiC piston and a voice coil motor to improve the performance compared to FLORA I. The structure and air bearings were modeled Finite Element Analysis (FEA) software. FLORA II is smaller and lighter than its predecessor while achieving a high bearing stiffness coupled with smooth motion.*

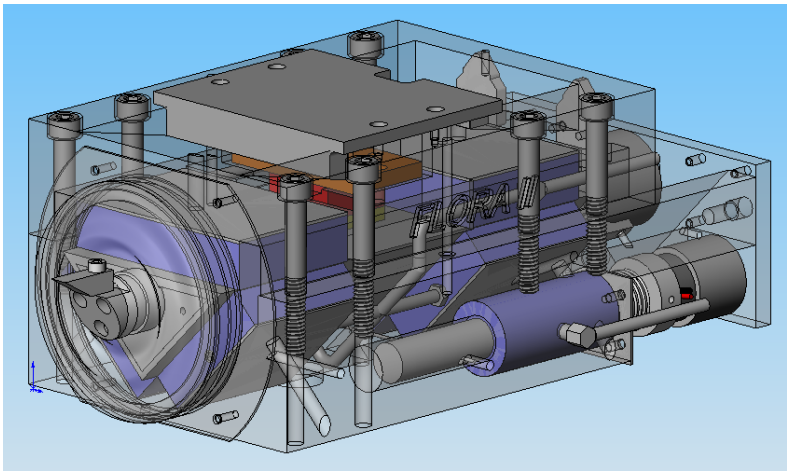

[1] Currently an engineer at Harris Corp in Melborne, FL

3.1 INTRODUCTION

The objective of this research project was to develop a new tool for machining Non-Rotationally Symmetric (NRS) surfaces. NRS optical surfaces have traditionally been machined using slow spindle speeds for large features or limited range with piezoelectric actuators. A Fast Long Range Actuator (FLORA I) was constructed in 2005 with a goal of machining NRS surfaces with a sag of ± 2 mm at 20 Hz. For the surface to have the same quality as conventional diamond turning machines the surface must have a form error of less than 150 nm peak to valley and a surface finish of 5 nm RMS.

The FLORA I system consists of a triangular aluminum honeycomb piston supported by orifice type air bearings and driven by a 3-phase linear motor. While machining with FLORA I has had success, the system package is large when compared with the size and path of the diamond tool. FLORA I had an observed spurious 200 nm vertical vibration which had an adverse impact when machining precision surfaces.

Therefore, the goal of the research presented here is a new actuator (FLORA II) designed to address the limitations of its predecessor. The FLORA II package is smaller and lighter than FLORA I while improving air bearing stiffness and system dynamics. This was accomplished through extensive use of computer simulation (structural mechanics and dynamics) supplemented with experimental testing and validation. The design described in this report will allow the FLORA II to produce high quality NRS optical surfaces from a small, lightweight system. Complete details of this new tool can be found in the MS thesis of Zdanowicz [1].

3.2 MECHANICAL DESIGN

There were many factors that affected the design of FLORA II including the air bearings, piston geometry and material, housing, piston position encoder, counterbalance system, and controller design. Each of the factors listed not only affect the performance of the new design, but also interact with each other. For example, an important issue is the design is to model the structure and air bearing to predict the effect of the structure on the bearing performance. If the piston had excessive mass or the bearing possessed inadequate stiffness, the resulting low natural frequencies could decrease performance. The thickness of the air film was another critical aspect of the new design with a goal of 5 µm. This air film is created through the expansion of the housing as well as the compression of piston. The influence of every component in the design on each other made this a challenging project. The details of the piston, air bearing, and housing were described in the 2008 PEC Annual Report. Since that time the effort has focused on voice coil motor integration, counterbalance system design, assembly of the system, controller tuning, and machining performance characterization. Figure 1 shows an overall photograph (top) and a

transparent image (bottom) of the final design of the Flora II system. The tool holder is on the left, encoder access is at the top, the main voice coil motor is at the right above the two counterbalance motors. The transparent view of the design shows further detail such as the silicon carbide piston, custom New Way air bearings, counterbalance system, and air supply plumbing. Table 1 presents a comparison of the key specifications of the Flora I and Flora II designs. It can be seen there has been a substantial reduction in package mass and physical size.

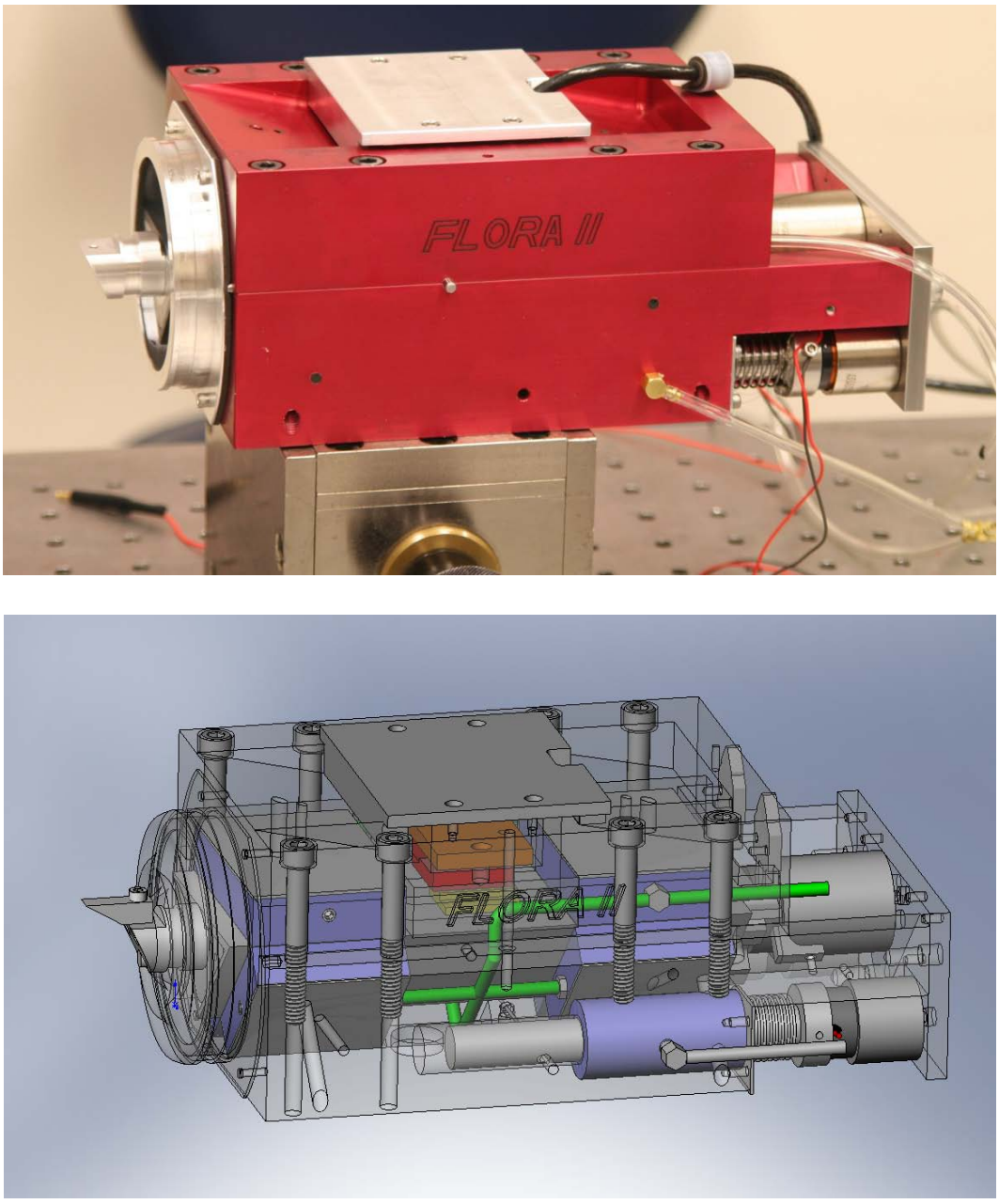

Figure 1. Flora II final configuration, photograph at top and transparent design view at bottom.

Table 1 Comparison of Flora I and II Specifications

Total Mass, Kg	36	7
Piston mass, Kg	0.65	0.36
End-load stiffness, N/μm	52.5	8.2
First natural frequency, Hz	1000	2700
Housing height, mm	130	90
Housing width, mm	205	110
Housing length, mm	305	208

3.2.1 COUNTERBALANCE DESIGN

To create a system that performs the precise cutting desired from FLORA II, a counter balance was introduced to generate a force equivalent to the force generated by the actuation of the piston. The counterbalance force is opposite to the piston force to cancel the dynamic loads. To reduce the size of the housing, a new approach was taken to utilize unused volume on the FLORA II housing, resulting in a side-mount configuration. After careful examination there were two spaces found where a large volume of material was present, but not contributing to the function of the system, see Figure 2. The location is still in a relatively small space so the first task was to find a type of air bearing which could fit. New Way Air Bearings provided 13 mm ID diameter (OD=24mm, length=50mm) air bushing. The use of the air bushing constrained the counter balance to a circular shaft. Two counter balances were employed to eliminate any off-axis moment about the vertical axis. The inherent vertical moment was determined to be negligible when compared with the amount of space saved with this design.

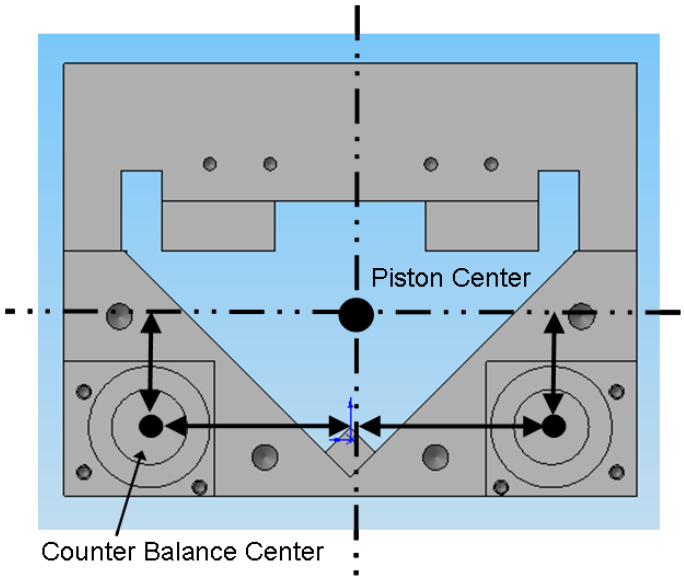

Figure 2. Horizontal and vertical offsets of counter balance shafts from FLORA II piston.

The total moving mass of the FLORA II piston was 360 gm, thus the moving mass of each stainless steel counterbalance shaft was 180 gm. As a comparison, the moving mass of FLORA I was 650 gm.

Position holding was an important aspect in terms of control of the counter balance motion. The counter balance masses must be centered in the correct position at the beginning of any machining process so that their motion is in unison with the piston moving mass. If the motion is not matched than the counter balances could actually cause more harm than good to the surface quality. The main moving mass is driven under closed-loop control meaning the position is controlled using feedback from a position sensor, in this case the encoder/glass scale. It would be expensive to mount a sensor on each of the counter balances. Also, closed-loop control would add more coding to an already complex control algorithm. Therefore, it was determined that the counter balance masses would be driven by voice coil motors in an open-loop scenario.

The simplest method for controlling the position of the counter balance masses was through use of a spring. The spring introduces additional dynamics into the counter balance system. The dynamic force generated by the acceleration of the main piston is

$$F = ma = -m\omega^2 A\sin(\omega t) \tag{1}$$

where m is mass, ω is the frequency of actuation, and A is the amplitude. Based on the mass and a sinusoidal motion of ± 2 mm at 20 Hz yields a maximum force of 10 N. This is the force that must be cancelled by the counter balances. A MATLAB simulation was written to predict the dynamic force generated by the counterbalance spring mass system. A counterbalance spring stiffness value equal to 122 N/m was chosen because it is not very stiff yet will still center the counter balance mass. The total resultant force (piston+ counterbalances) is shown in Figure 3.

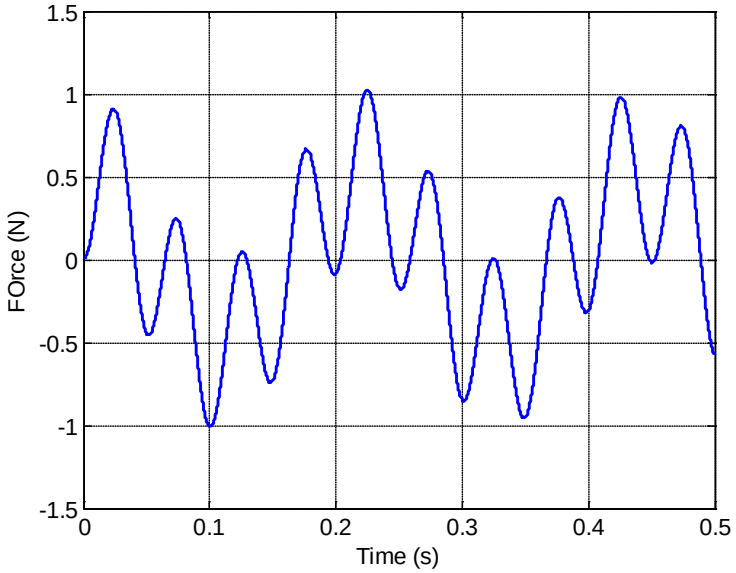

Figure 3. Resultant force after counter balances influence piston moving mass.

The sinusoidal force variations shows the excitation frequency (20 Hz) as well as the natural frequency of the counterbalance mass/spring (~3 Hz). The unbalanced force is approximately 1 N. This is 10% of the force generated by the FLORA II moving piston itself. Based on experience with FLORA 1, this force should not have a significant influence on machined surface properties.

Two types of spring arrangements were designed and implemented for use on the FLORA II counterbalances. The first arrangement was developed as a coil spring around the counter balance shaft. One end of the spring was glued to a shorter section of the counterbalance shaft with a larger diameter. The other end was glued to a plate which was bolted to the housing as seen in Figure 4. This figure shows how the spring will center the counter balance shaft as well as keep the motor coil from drifting out of its operating range.

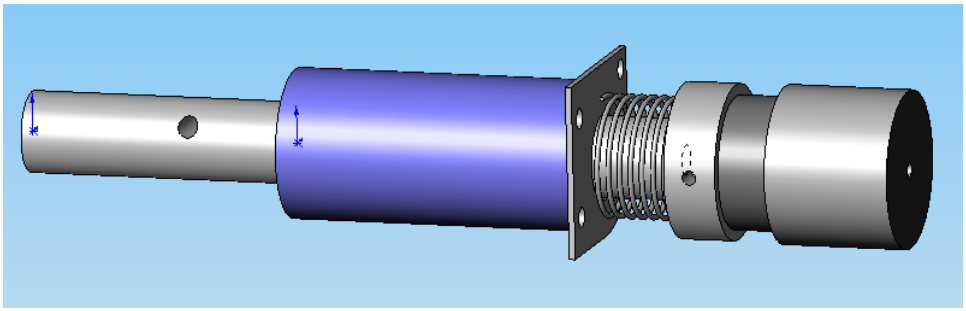

Figure 4. FLORA II counter balance assembly (two identical assemblies used).

The 13 mm counterbalance shafts supported by the air bushing are 108.5 mm long and the large diameter shafts (25 mm) that bolt to the motor coil are 8.5 mm long. An image of the counter balance using a coil spring in the FLORA II housing can be seen in Figure 5.

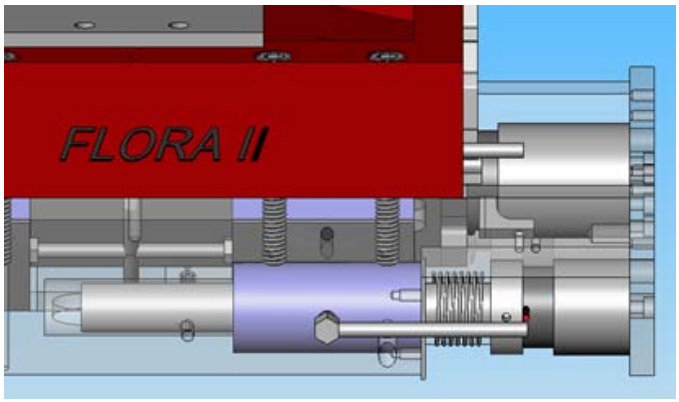

Figure 5. View of counter balance assembly in FLORA II housing.

Figure 5 shows the location of the counter balance assembly in the FLORA II housing. The lower corner of the housing bottom has been machined to allow space for the voice coil motor and counter balance shaft. There is also a single steel plate at the rear of the housing to support all three voice coil motors.

The second spring arrangement for position holding was a flexure type spring. This consisted of a small diameter aluminum rod which was fixed at the center of the housing. The two free ends run through the two small diameter counter balance shafts shown in Figure 6.

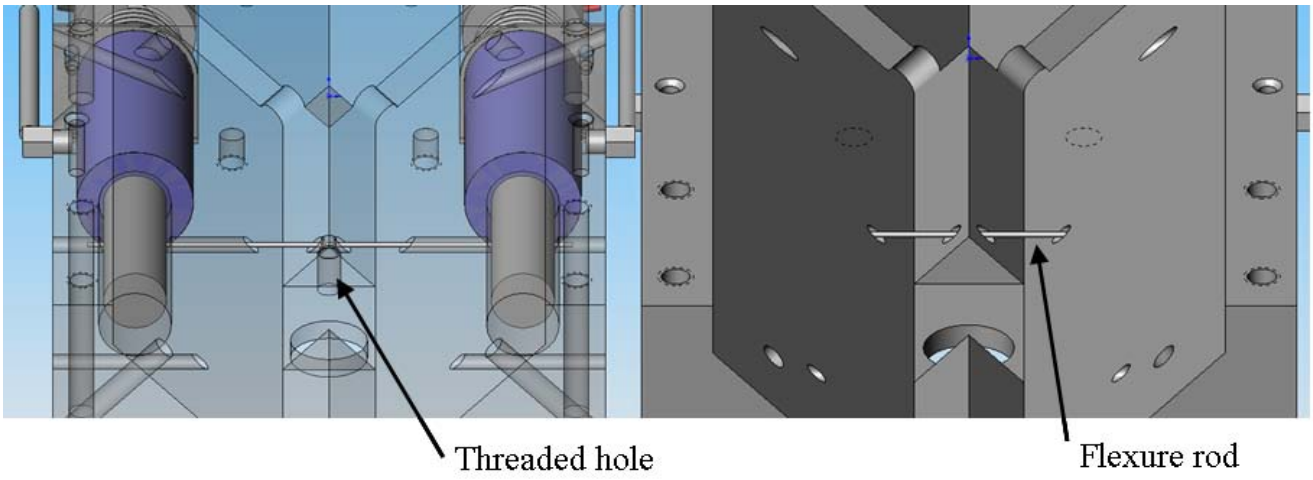

Figure 6. Transparent and solid view of flexure spring in FLORA II housing.

Figure 6 shows how the flexure spring fits into the FLORA II housing. The rod can be inserted through one side of the housing and through both shafts. The shafts both have holes which are aligned with the rod hole in the housing. The rod also passes through a hole in the center of the housing as seen in the solid image in Figure 6. Once the rod is aligned correctly, a set screw can be tightened from the bottom of the housing to clamp the rod in place as seen in the transparent image in Figure 6. While only one of the spring arrangements are used at a time, the ability to use both options where machined into the FLORA II housing in the event that one method proved advantageous.

To determine the effectiveness of the counter balances a series of experiments were run. FLORA II was run with just the piston, with the counter balances and piston 180^{o} out of phase and in phase. This will show the worst case scenario, a baseline of the piston and the best case scenario. The experimental setup can be seen in Figure 7. An accelerometer was attached to the front of the housing to determine the acceleration (force) the housing underwent during the tests. Accelerometers were also placed on the piston and counter balance to measure the force they were generating.

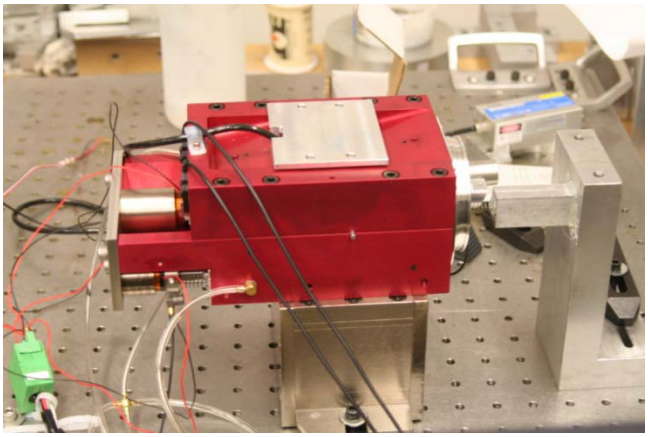

Figure 7. Experimental setup of counter balance tests with accelerometer.

Figure 8 shows the acceleration measured on the piston, the counterbalance masses and the housing (small values). When the piston is run in phase with the counter balances the amplitude of acceleration on the housing is roughly twice that when the counter balances are effectively 180^{o} out of phase. The piston oscillating by itself has an amplitude in-between the two shown in Figure 8. The system is extremely stiff and the mass of the piston is small (0.3 Kg) so even without counterbalance, the loading on the diamond turning machine will be small.

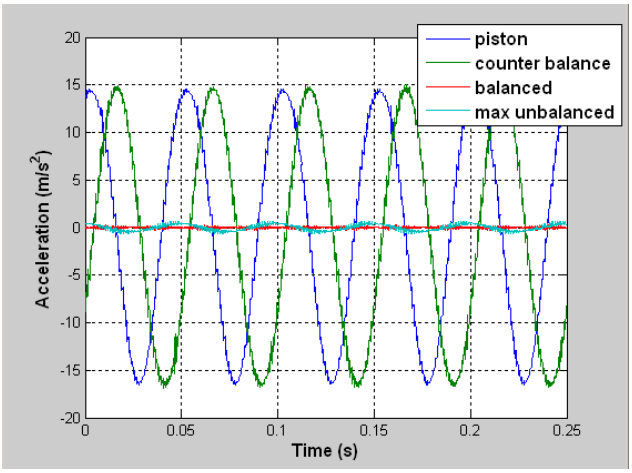

Figure 8. Plot of acceleration measured on piston, counter balances and housing.

3.2.2 MOTORS, AMPLIFIERS AND POSITION FEEDBACK

The moving piston mass is equal to 360 gm and operates at up to ±2 mm and 20 Hz requiring a peak force of 10 N. The goal was to select a motor that could handle the force and stroke while

remaining as small as possible. The VCM which fit the profile for the FLORA II moving mass application was the BEI Kimco LA12-17-000A. The single-phase characteristics of the VCMs were advantageous when compared to the three phase brush linear motor implemented in FLORA I. The peak force required for each counter balance mass was 5 N. The VCM which fit the profile was the BEI Kimco LA10-12-027A. To address concern of overheating, temperature measurements revealed an increase of only 1.9^{o}C after 15 minutes of continuous operation at 2 mm and 20 Hz.

Two Trust Automation TA 115 linear amplifiers were chosen to power the piston and counterbalance VCMs because of their low noise characteristics.

Position feedback was provided by a Sony BH25-005REHBT01 Reflective LASERSCALE encoder read head and glass scale. The Sony LASERSCALE position sensing package consists of a glass scale and an encoder read head which reads the relative position of the scale. To begin, the encoder read head is capable of emitting a laser beam and is also fitted with a photo detector. The glass scale is composed of gratings placed above a reflective λ/4 phase plate where λ is the wave length of the laser emitted from the encoder read head. A general diagram of the operation between the read head and glass scale is shown in Figure 9.

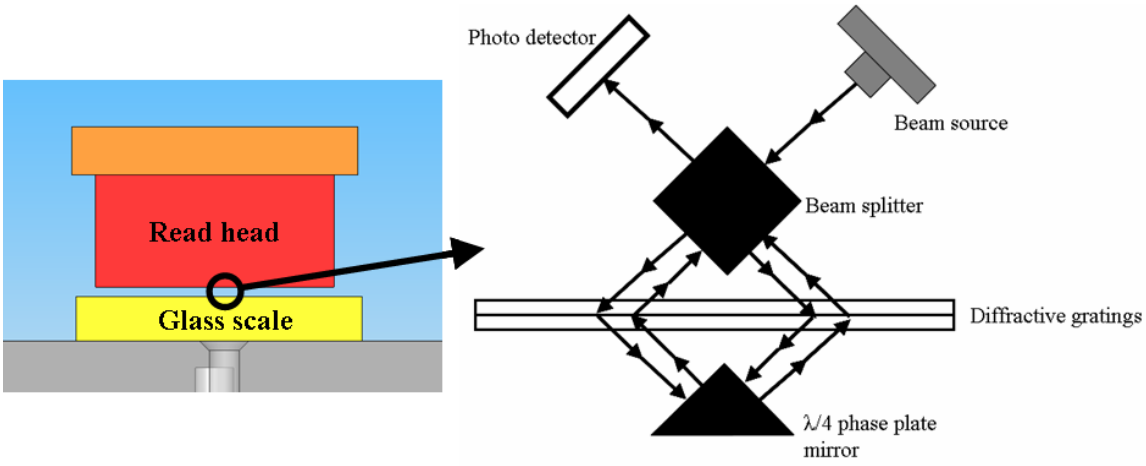

Figure 9. Position sensing function between encoder read head and glass scale.

3.3 CONTROLLER DESIGN

The control system implemented for the FLORA I was also used for the FLORA II with some changes. The controller gains had to be modified since the drive system and piston are different between FLORA I and II. To identify the new controller gains, the FLORA II system was characterized using open loop tests. Once the dynamic behavior was characterized, a control

filter was tailored for FLORA II. Closed loop tests were run to observe the controllers performance. The experimental setup for the controller tests is shown in Figure 10.

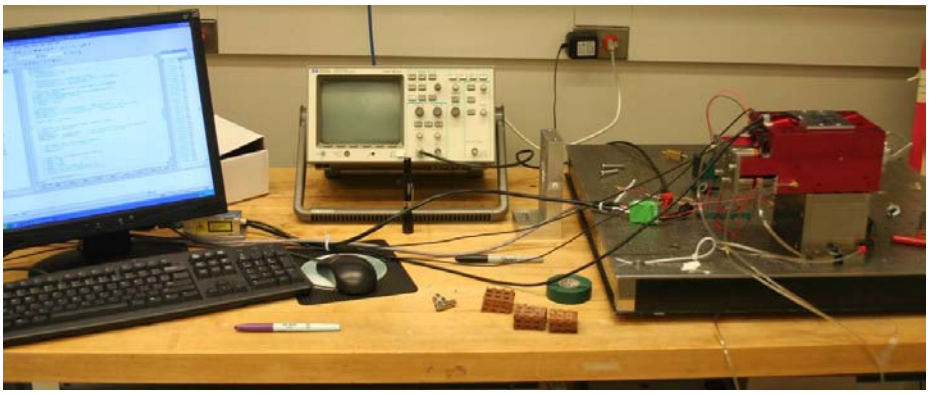

Figure 10. Experimental setup for FLORA II controller design and testing.

3.3.1 OPEN LOOP SYSTEM IDENTIFICATION

The first task for the controller design was to identify the open loop dynamics of FLORA II. This would provide a model to design the controller. One way to capture the dynamics of the system was to perform a series of experiments with the servo excited at different single frequency sine waves. Linear dynamic systems respond to a sinusoidal excitation with motion at that same frequency but with an increased or diminished magnitude and a different phase. For the FLORA II, it was determined that a range of 0 to 4 kHz would be sufficient so a sinusoidal command was run every 10 Hz from 0 to 4 kHz.

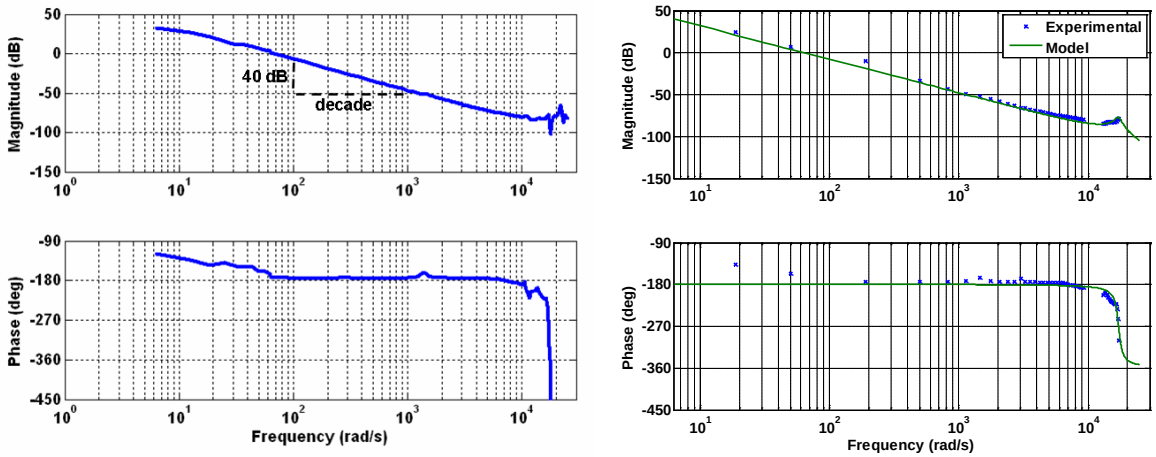

Figure 11. Open loop transfer function of FLORA II from sine sweep. Left is the original data and right is the model used for the controller design.

The data for amplitude ratio and phase were collected, analyzed and are plotted as a function of frequency (rad/sec) in the left hand side of Figure 11. This transfer function relates the output in mm to an input in volts to the motor. A model was fit to the experimental transfer function shown on the right in Figure 11 by combining expressions that describe the behavior of the different components in the system. Because the input command is voltage (which produces current or force in the motor and acceleration in the piston) and the output is position, there will be a theoretical reduction in amplitude of 40 dB for each decade of increased frequency and 180° phase shift between input (force) and output (displacement). The gain G_A of the system (magnitude at a specific frequency) is a function of the amplifier gain and the mass of the piston. In addition to the linear change with frequency, there is a peak at about 2800 Hz (17.5 rad/sec) and a 180 phase shift indicating a resonance in the system. Combining of these effects with values of $\zeta = 0.05$, $\omega_n = 17{,}216$ rad/s and $G_A = 4158$ mm/V, the following equation approximates the experimental transfer function. This matches the measured data as shown in Figure 11.

$$\frac{G_A\omega_n^{\,2}}{s^4 + 2\zeta\omega_n s^3 + \omega_n^{\,2}s^2} = \frac{1.23e^{12}}{s^4 + 1722s^3 + 2.96e^8 s^2} \tag{1}$$

3.3.2 CLOSED LOOP CONTROLLER DESIGN

The control system implemented for FLORA II is a PID controller with acceleration feed forward. A block diagram for this filter is shown in Figure 12. The gains, K_P, K_I, and K_D for the controller were determined using frequency design procedure based on the desired bandwidth.

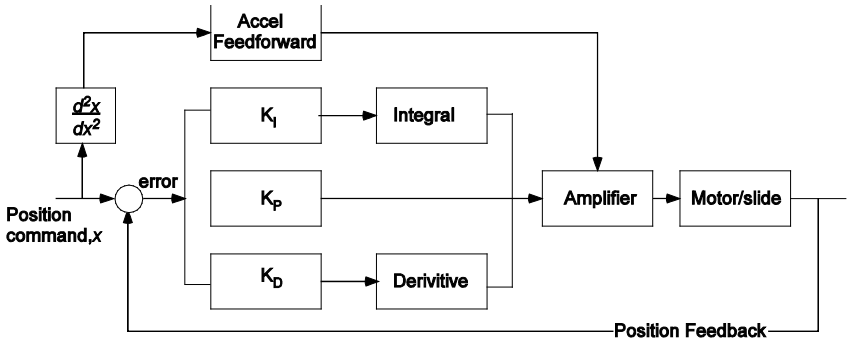

Figure 12. Block diagram for FLORA II control system.

The magnitude of the integral and derivative gains are associated in the frequency response of those two filters and the desired bandwidth, ω_b, of the system. The integral term increases the low frequency gain for steady-state accuracy while the derivative term is used to improve stability and increase response. By changing the frequency where the integral and derivative filters influence the system, the response can be manipulated. The standard design is to make the integral gain end at 10% of the desired bandwidth and the derivative to start at 50%. Based on these relationships, the gains can be calculated as:

$$\frac{\omega_b}{10} \simeq \frac{K_I}{K_P} \quad \text{and} \quad \frac{\omega_b}{2} \simeq \frac{K_P}{K_D}. \tag{2}$$

The shapes of three filters with different gains (described in Table 2) are shown on the right side of Figure 13. The medium and high have similar frequency characteristics but the low gain shows the effect of reduced integral gain at low frequency. Changing the gain K_P shifts the entire response curve up and down.

Table 2. Controller gains used for FLORA II tuning

Controller	**K_P**	**K_I**	**K_D**
High	200		
Medium	135	16200	0.225
Low	60	1	0.179

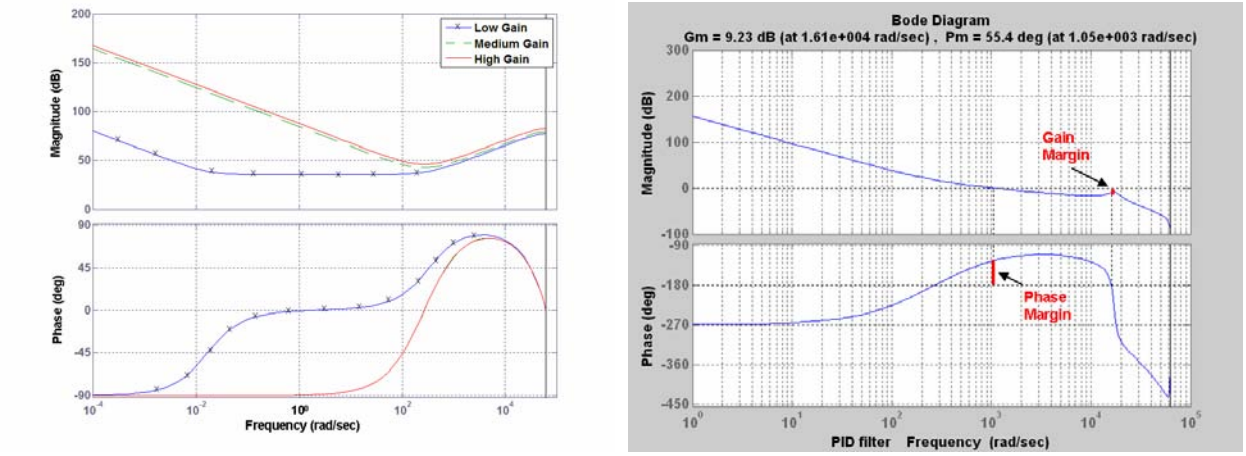

Figure 13 Frequency response of different PID controllers (left) and the medium gain case applied to the open loop FLORA II motion (right).

The right side of Figure 13 shows the open loop response from Figure 11 but modified by the medium gain controller. Two measures of the utility of the controller are the gain margin and the phase margin. The Phase Margin is the phase angle of the response from 180° when the system passes through 0 dB magnitude. In this case it is about 55° which is considered good for stability. The Gain Margin is the additional gain that could be added before the system goes unstable. The 9 dB for this example is excellent. Therefore, the FLORA II system with the medium gain filter should perform well.

The FLORA II controller also uses acceleration feed forward to anticipate changes in command by applying a voltage command directly to the motor current that is proportional to the desired acceleration. The feed forward term also has a gain, K_A, which is the reciprocal of the system gain, G_A.

3.4 CLOSED LOOP EXPERIMENTS

Once the candidate controller gains were determined, closed loop experiments were performed. The first experiment involved sending a step command to the piston and a swept sine wave showed the effective bandwidth of the controller.

3.4.1 STEP RESPONSE

The step command has amplitude of 12 µm step that corresponds to the largest command needed for a 2 mm amplitude, 20 Hz sine wave. The response can be characterized in terms of rise time, overshoot and settling time. The actual response using the three gain sets is shown in Figure 14. A simulation of the system was created to compare to the actual system but it does not have limits on current and force as the actual case. The model was given a unit less step input but the same PID gains. A comparison of the results in Figure 14 indicates that the actual system responds slower because of its force limits but the different gains produce similar action.

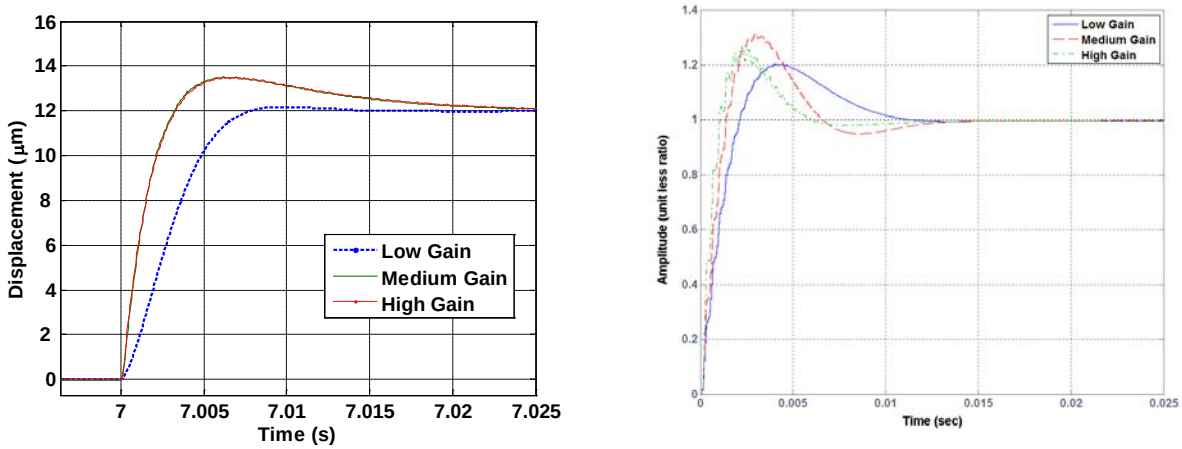

Figure 14. Actual 12 µm step response (left) and simulated step response (right) of the FLORA II system using low, medium and high gains.

3.4.2 CLOSED LOOP SINE WAVE TRACKING

The step test shows the response to a step command but optical fabrication will typically be lower frequency sine wave commands. The following experiments show the response to a 20 Hz, 0.5 mm amplitude sine wave command. Figure 15 shows the difference between the command and the response for the low and medium gains. The following error for each of these commands is large (4 µm for the low gain and 1.6 µm for the medium gain) but that value is a result of both amplitude and a phase angle.

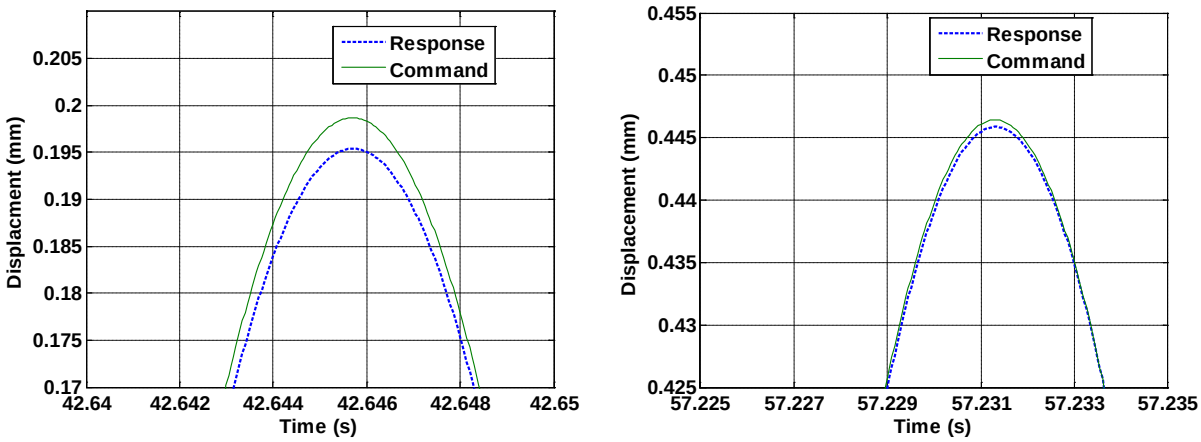

Figure 15. 20 Hz, 0.5 mm amplitude sinusoidal command and response using the low gains (left) and medium gains (right) for the FLORA II system

Figure 16 shows the error transfer function from the model for these two controllers. From the magnitude plot the amplitude ratio for the low and medium gain at 125 rad/s (20 Hz) are -69 dB and -78 dB. For the 500 µm amplitude command, these errors will correspond to 350 nm for the low gain and 130 nm for the medium gain. While the experimental errors are significantly higher than the theoretical values, the ratios (350 nm/1.6 µm = 0.22 and 130 nm/600 nm=0.22) are nearly the same indicating some systematic problem.

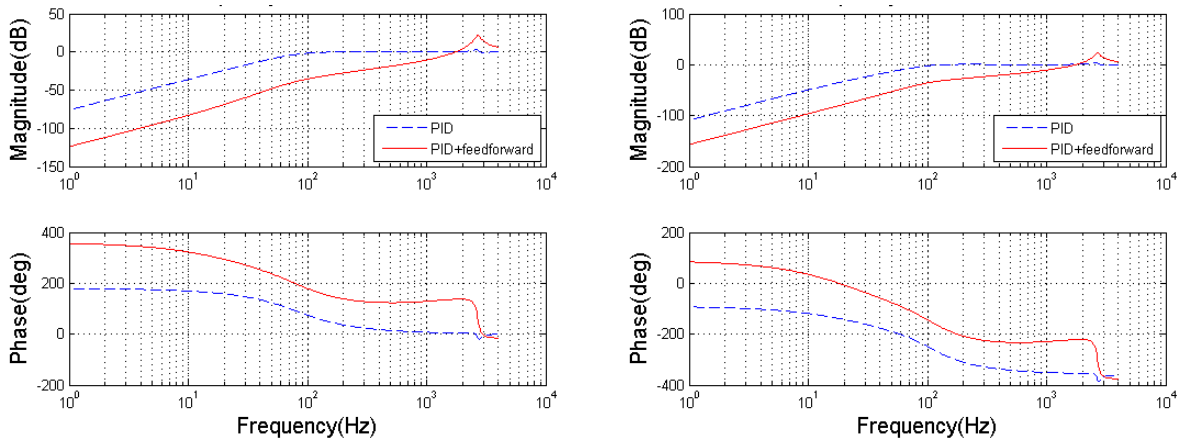

Figure 16. Error transfer function for the FLORA II for low gain (left) and medium gain (right)

3.4.3 POSITION HOLDING EXPERIMENT

The ability of the controller to hold a specified position is an important attribute when the FLORA II is used to machine a rotationally symmetric part. The position holding using the medium gains is shown in Figure 17. Figure 17 shows the PV error when holding position to be

approximately 6 nm with the largest spikes at 60 and 180 Hz. This is a vast improvement over the FLORA I system which had a PV position holding error of 50 nm.

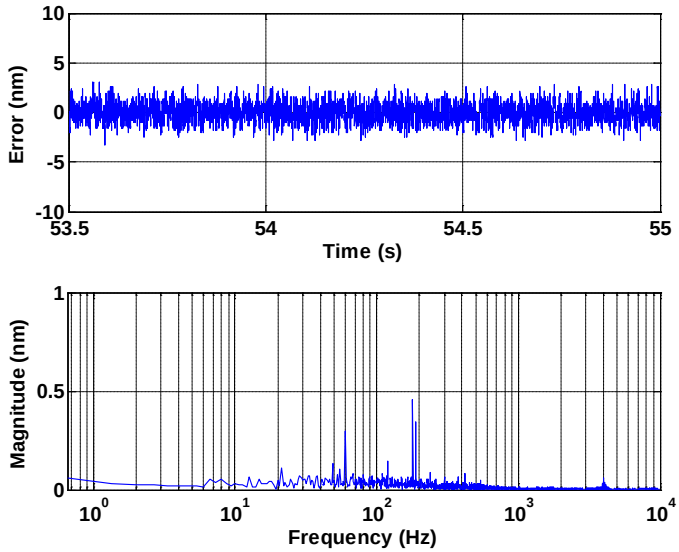

Figure 17. Position holding data for time domain (top) and frequency spectrum (bottom) for FLORA II using controller gains K_P = 135, K_I = 16,200, and K_D = 0.225.

3.5 MACHINING EXPERIMENTS

There were two types of cutting experiments performed by the FLORA II system. The first experiment was to cut a flat surface to demonstrate the ability to hold position and produce an optical surface finish. The second test involved cutting a tilted flat that tests the ability of the servo to follow a commanded tool path and maintain surface quality.

3.5.1 BRASS FLAT

A brass flat with a 12.9 mm diameter was machined with the FLORA II holding position. The theoretical RMS roughness was set to 1 nm by selecting a tool with *R* of 2.3 mm, a spindle speed of 500 rpm and a feed-rate of 4 mm/min. The surface finish measured with a Zygo NewView had a PV of 36 nm and RMS of 2 nm. This is an extremely good finish for a long range servo. Position data was collected during this experiment and the result was somewhat larger than holding position without cutting in Figure 17 with a PV of 8 nm and a broad spectrum of components with the largest peak magnitude of 0.8 nm at 500 Hz. A brass sphere was also machined to center the tool for the next experiment and the PV figure error was 158 nm.

3.5.2 ACRYLIC TILTED FLAT

The tilted flat is an excellent measure of the performance of a long range actuator because it requires a range of amplitudes from 0 to 2 mm (maximum total motion per rev is 4 mm) but creates a flat surface that is easy to measure in a laser interferometer. An image of the FLORA II mounted on the DTM with the tilted flat is shown in Figure 18. Beginning with a milled flat surface at the approximately the proper tilt, the surface was finished in 5 tool passes. The first cut was at 20 µm depth of cut (DOC) while the remaining three were at 40 µm. A feed rate of 20 mm/min was used during rough cutting while 4 mm/min was used on the single finish pass. The DOC of the finish pass was 5 µm.

Figure 18. FLORA II mounted on DTM with acrylic tilted flat.

The resulting flat surface was measured in the Zygo GPI. This measurement is the best flat surface without regard for the phase of the commanded sine wave. Figure 19 shows a measurement where the maximum peak-to-valley (PV) form error was 1.829 µm. Superimposed on this figure is the error at about half the outside radius with a PV of 0.74 µm. It can be seen that there are two high spots and two low spots on the surface of the tilted flat after the slope has been removed from the surface.

From the Zygo New View SWLI recall that the surface finish decreased at the outer edge of the part from radius high to radius low while the surface finish improved at the outer edge along the neutral line.

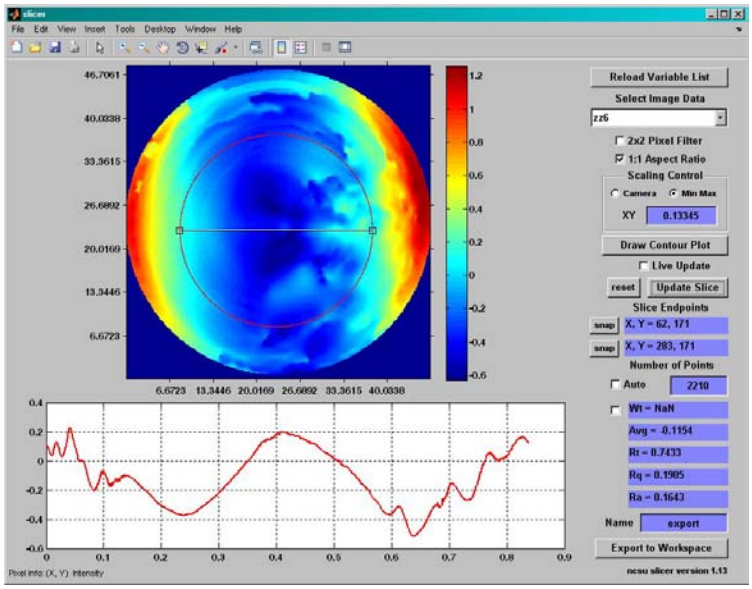

Figure 19. Zygo GPI laser interferometer measurement of tilted flat surface with plane removed. A single revolution measurement of surface at half of the radius shows the two highs and lows per revolution and a PV=0.74 µm.

Figure 20 shows where surface roughness measurements were made on the tilted flat. Profilometer measurements were made along 4 lines at 45° increments. The right hand image is the measurement of the surface starting from the low spot to the high spot with tilt removed. Note that half of the surface has better figure error than the other half. The part is rotating counterclockwise with the tool moving from center to left side. The half with the poor surface finish was the portion of the surface where the tool was moving into the part. The best surface finish was observed where the tool was moving away from the part. This implies that the tool is behaving differently when moving out than when moving in. There is no expected explanation for this behavior and must have to do with a mechanical influence.

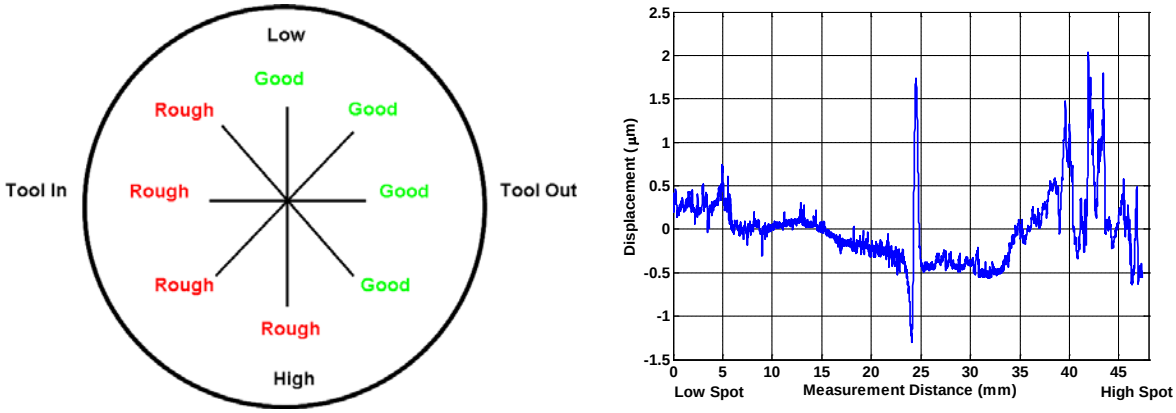

Figure 20. Talysurf Profilometer surface roughness measurements across surface of tilted flat.

The surface finish was also measured on the white light interferometer. Images of two measurements along the low to high line in Figure 20 are shown in Figure 21. Normally the grooves observed from the machined surface are from the radius of the tool and are spaced at the feed rate (6.7 µm/rev). Upon examination of these grooves it was seen that they were approximately twice this value. The surface finish in both cases is well beyond the predicted value. The likely cause is noise on the command signal that is producing variation in the command from one revolution to the next and masking the feed rate with larger amplitude tool motion.

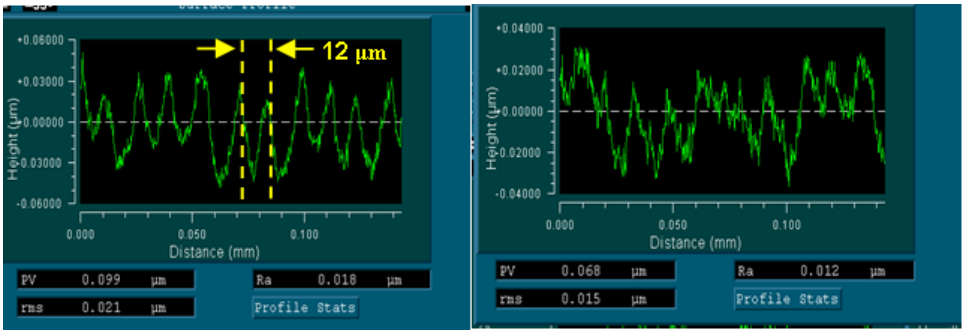

Figure 21. Surface profile at mid-radius on the low side (left) and the high side (right).

3.7 CONCLUSIONS

The Fast Long Range Actuator, FLORA II, was designed and fabricated to machine non-rotationally symmetric surfaces at high speed with an optical quality surface finish. The following conclusions are based on the performance of the actuator to date.

- A switch from orifice type air bearings to porous carbon air bearings was rewarded by more uniform pressure distribution, higher stiffness, reduced air flow and quieter operation. Equivalent stiffness values were derived so the air bearings could be modeled using ANSYS FEA software. The model was tested by comparing simulations to experimental results obtained with an air bushing. The porous carbon air bearings produced less vibration and that the equivalent stiffness model was a good approximation in FEA software.
- The SiC piston material produced a light stiff piston. The shape and material of the piston that is supported by the air bearings was chosen based on a series of simulations. Different cross sections were evaluated through end-load, modal and compressive pressure simulations in ANSYS. The cross sections were also assessed based on assembly requirements. A Silicon Carbide triangular cross section performed best overall and was chosen.
- Higher performance and smaller size was achieved. The housing for FLORA II was designed to be significantly smaller (63% less front area) and lighter (75%) than FLORA

I. Pressurized air is delivered to the air bearings by a system of small tubes and fittings. The structure of the housing was designed to create a uniform air gap of 5 μm in the bearings. Counter balances were added below the main motor to save space and cancel vibrations induced by the main piston.

- Controller performance was improved. The same controller used for FLORA I was also used for FLORA II with modifications based on the piston mass and the new motor. Open loop experiments defined the system dynamics and a closed loop controller was developed.
- Machining performance was improved. Machining experiments to create a brass flat and sphere showed the capability of FLORA II to hold position. A PMMA tilted flat was machined at 10 Hz with total sag of 4 mm.
- Problem areas remain. Unexpected behavior was observed in the tilted flat where the motion of the tool was influence by its direction. Misalignment of the motor windings and magnet are being investigated along with other possible causes. The tilted flat was machined at 10 Hz because there appeared to be electrical noise when operated at 20 Hz on the DTM. Why it should be a function of frequency is not clear and additional tests both on the DTM and on the bench are planned. The command signal collected during the experiments showed high frequency noise that could also affect the surface roughness.

3.8 REFERENCES

[1] Zdanowicz, E., *Design of a Fast Long Range Actuator*, MS Thesis, Department of Mechanical and Aerospace Engineering, North Carolina State Univ., Raleigh, NC, 2009.

4 DIAMOND TOOL WEAR IMPROVEMENTS WITH ELIPTICAL VIBRATION ASSISTED MACHINING

Brandon Lane
Graduate Student
Thomas Dow
Professor, Department of Mechanical and Aerospace Engineering
Ronald Scattergood
Professor, Department of Materials Science and Engineering

Studies have shown the benefits of applying micrometer scale vibration motion of a diamond tool during diamond turning (DT). Reported benefits include a decrease in machining forces and wear of the diamond tool. The particular causes for decrease in force and wear while utilizing elliptical vibration assisted machining (EVAM) are not well understood, nor is there great understanding in the wear mechanics of a conventional diamond turning operation for many materials. Conventional and EVAM cutting experiments using 6061 Aluminum and 1215 Steel were conducted and wear of the diamond tool was measured. Wear models are drawn from conventional cutting experimental results and used to compare different types of tool wear. These observations and models are then further compared with results from EVAM experiments and finite element simulation results. Conclusions are drawn regarding the mechanisms behind the reported improvements to diamond machining using EVAM.

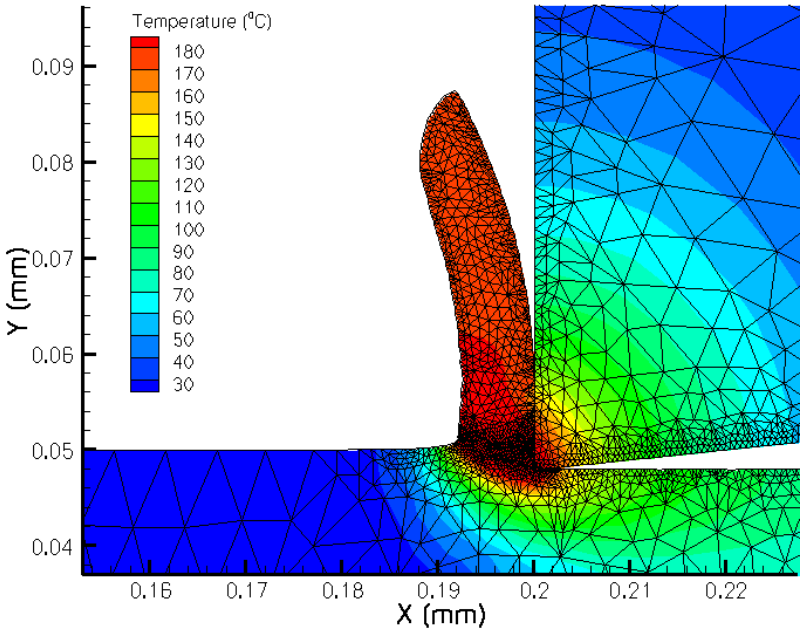

4.1 INTRODUCTION

Diamond turning (DT) has revolutionized the fabrication of optics and precision devices since its inception in the early 1970s. Some materials, however, have proven to be difficult if not impossible to machine with a single crystal diamond by standard turning methods. This difficulty is due to either the brittle nature of the material or excessive wear on the diamond tool. Vibration assisted machining (VAM) was introduced into the DT process to alleviate these issues by allowing the diamond tool to separate from the workpiece and return to contact in cycles occurring 1000s of times per second. VAM has been proven through many studies to decrease tool forces and tool wear while sustaining optical quality surface finish on precision turned parts [1]. Of particular interest is a variation of VAM called elliptical vibration assisted machining (EVAM). An EVAM device created at the Precision Engineering Center (PEC) at North Carolina State University called the Ultramill enables the tool vibration frequency to be altered from 1-4 KHz along with the size and shape of the elliptical tool path. This enables the EVAM process to be studied while varying the cutting parameters. A comprehensive study is underway to determine the principles behind the improvements encountered with EVAM, and quantitatively explain processes such as material flow, heat generation, tool wear, and tool forces.

The cutting process is complicated in nature combining interactions such as high stresses accompanying plastic material flow, strain-rate temperature effects, friction forces and heating, and chemical interactions. This process is simplified as much as possible by proceeding with orthogonal cutting conditions during experimentation. This allows cutting interactions to occur at approximately the same rate along the length of the tool edge. Figure 1 shows a schematic of orthogonal cutting geometry for standard cutting and EVAM. By creating a workpiece that is smaller than the width of the diamond edge, the process is simplified more by having a specific location on the tool where the cutting process will occur. This also creates a section of diamond that can be worn by the workpiece material while maintaining and unworn region for direct comparison.

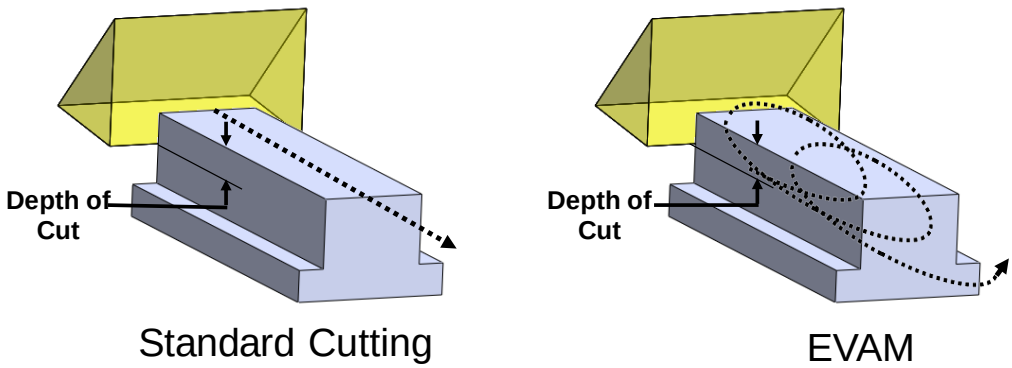

Figure 1: Tool paths for Standard orthogonal cutting *(left)* and orthogonal EVAM *(right)*

In previous studies at the PEC [2,3], a method for measuring tool wear was developed that is capable of resolutions of less than 10nm. Utilizing electron beam induced deposition (EBID) encountered during use of a scanning electron microscope (SEM), a stripe is created perpendicular to the tool edge. This stripe creates a traceable contrast on the SEM image that follows the edge of the diamond tool and can be used to accurately measure the worn profile of the diamond tool. To date, no reports on the use of the contamination stripe method to measure tools worn after VAM or EVAM cutting have been found. Apart from EBID, tool wear can be measured using a scanning white light interferometer (SWLI). Tilting the tool an appropriate angle allows flat regions of tool wear to be observed and measured in the SWLI. The EBID and SWLI methods have been used extensively in this paper to describe the diamond tool wear.

Before experiments are conducted using EVAM, baseline studies on standard DT processes must be conducted as a means for comparison. Aluminum and steel alloys are common engineering materials that pose challenges to standard DT due to tool wear, but are more machineable when VAM is utilized. 6061 aluminum is a standard aluminum alloy that contains hard alloying microstructures that cause tool wear after extended cutting. The method of wear is presumed to be abrasive in nature due to these included microstructures. Steel alloys have proven to be even more of a challenge than 6061 aluminum. Wear rates of diamond on steel are exceedingly high, and have been found to be on the order of one carbon atom lost from the tool for every five atoms of clean metal passing over the diamond [4]. Wear due to steel and other ferrous alloys occur from chemical interactions between the diamond and cutting material. These reactions are exacerbated by high cutting temperatures. 1215 steel was chosen for this experiment due to its similar hardness properties to 6061 aluminum, and the promised effect of high wear rates.

Finite Element Modeling (FEM) methods have been applied to model conventional machining as well as diamond turning. FE models address both the material flow as well as the temperature field that influences that flow. The theoretical predictions described here were done using ThirdWave AdvantEdge to create cutting simulations that mimic experimental conditions and provide force data to compare with measurements as well as temperature needed to test wear hypothesis.

Comparisons of diamond tool wear are presented for orthogonal machining of alloy aluminum (6061-T6) and a low-carbon, easy to machine steel[1] (1215). Cutting force measurements coupled with EBID and SWLI wear measurements allow for an in depth view of the cutting process. These standard cutting experiments are coupled with results from FEA simulations to form wear models for diamond tools cutting 6061 aluminum (abrasive wear) and St1215 (chemical wear). These baseline studies are then compared to EVAM experiments on aluminum, and FEA simulations on steel. Results from aluminum EVAM experiments show that improved

[1] This typically means that the tool does not tend to generate a built up edge.

surface finish is not necessarily due to a reduction in tool wear. While EVAM experiments on 1215 steel have yet to be accomplished, FEA simulations show that the extended tool life described by other researchers is likely due to the exceedingly high conductivity of the diamond tool.

4.2 EXPERIMENTAL SETUP

4.2.1 WORKPIECE MATERIAL

Aluminum 6061-T6 and 1215 steel were chosen for comparison because of their similar mechanical but dissimilar chemical properties. 6061 aluminum contains hard alloying inclusions that contribute to abrasive wear, while the iron constituent of 1215 steel produces chemical wear.

Table 1: Properties of workpiece materials

	6061 aluminum	**1215 steel**
Density	2.7 g/cc	7.87 g/cc
Vickers Hardness	1185 MPa	1850 MPa
Young's Modulus	70 GPa	200 GPa

Different workpieces and workpiece holders were fabricated for standard cutting and EVAM experiments. Cutting experiments on 6061 aluminum may require many kilometers cut distance to produce measurable wear and therefore replaceable aluminum disks were fabricated for standard cutting (non-EVAM) experiments. The fabricated holder for the disks consists of a thick aluminum base and cover plate that fastens the workpiece disks with four cap screws. The thick base and cover plate prevents deformation caused by the vacuum chuck, and limit plate waviness and runout in the spindle axis direction. Figure 2 shows the aluminum and steel workpieces for standard cutting experiments. Axial runout of the disks was measured prior to machining using a Federal gauge, and resulted in magnitudes of less than 15µm. A sheet metal form of 1215 steel could not be purchased; therefore it was decided to fabricate turned surfaces and holder out of one piece. Fins were machined on a 4in diameter rod of 1215 steel that could be diamond turned in the same manner as the aluminum. Axial runout of the steel fins was found to be less than 10µm.

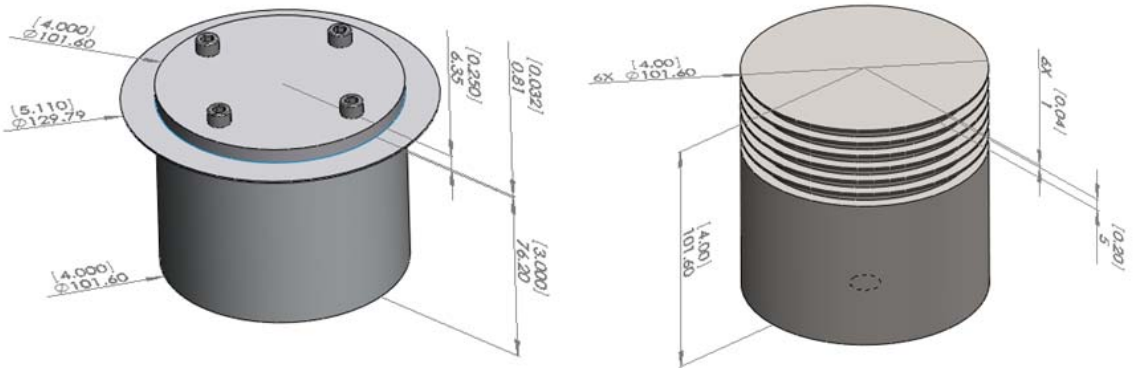

Figure 2: (*left*) Holder for replaceable 6061 disks. (*right*) fins created directly in 1215 steel

Sliding of the diamond tool over the workpiece produces wear and the change in geometry influences the cutting and thrust forces. Therefore a force measurement system was incorporated into the tool post during standard cutting using a Kistler 9271A three-axis load cell. The load cell allows cutting forces to be resolved into three components while maintaining the high required preload.

EVAM workpieces were constructed from 6061 aluminum and 1215 steel. Due to limited motion of the EVAM tool, the circular workpieces used in standard cutting experiments could not be employed. In addition, force measurements require a transducer to be placed under the workpiece, which cannot be done with a turning workpiece. Figure 3 shows a straight-fin workpiece used in EVAM wear experiments. The same load cell used in standard cutting experiments was used in EVAM experiments but in this case it holds the workpiece, not the tool.

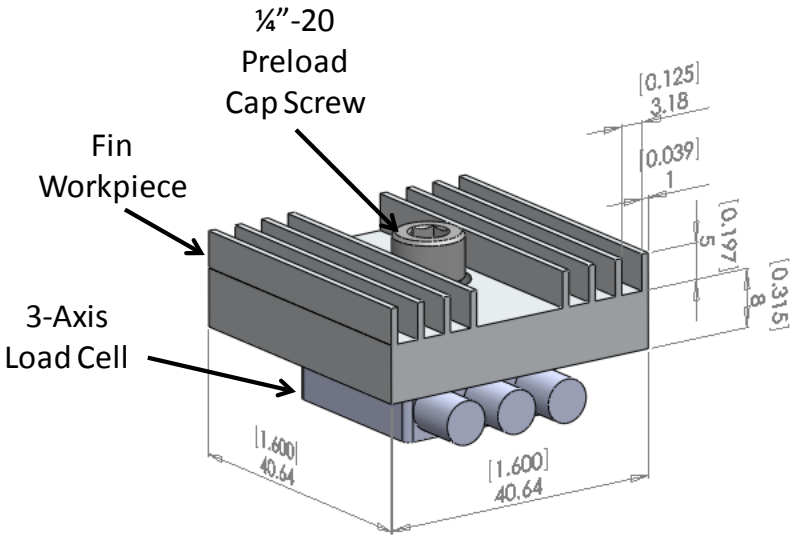

Figure 3: Fin workpiece and load cell used in EVAM experiments

4.2.3 CUTTING PARAMETERS

STANDARD CUTTING PARAMETERS

A depth of cut of 2µm was chosen for standard cutting experiments on 6061 aluminum and 1µm was chosen for 1215 steel. Table 2 gives cutting conditions for the standard cutting experiments. Standard cutting was conducted on an ASG 2500 diamond turning machine. All cutting was conducted with an oil stream of Mobilmet Omicron and compressed air directed at the cutting region. Cutting distances were chosen to compare to previous research diamond machining 6061 aluminum [5]. Excessive wear was expected for 1215 steel, therefore cut distances were limited to tens of meters.

Table 2: Cutting parameters for two materials used in standard cutting experiments.

	6061 aluminum Disk	**St1215**
Cutting Distance, d_s	10 km (4 x 2.5 km)	40 m (4 x 10m)
Cutting Velocity	3.40 - 2.66 m/s†	1.06-4.24 m/s††
Depth of Cut	2 μm	1 μm
Material Width, w	0.813 mm	1.20 mm
† Cutting velocity is reduced as disk diameter is reduced †† Separate experiment sets were conducted at 1, 2, and 4 m/s		

The tool used to turn the 6061 aluminum and 1215 steel was a flat edge synthetic diamond tool with 2.045mm wide cutting edge, 0° rake, and 6° clearance angle. Four cuts were made for the 6061 aluminum at 2.5km intervals. The tool was relapped by the manufacturer (Chardon Tool) between aluminum and steel experiments. 1215 steel was initially machined at a cut speed of 2.12 m/s for 4 intervals of 5m cut distance. Further experiments varied the cut speed at either1.06 m/s or 4.24 m/s for various cut distance intervals up to a final distance of 60m. Between successive cuts, the tool was cleaned, and tool wear was measured.

EVAM CUTTING PARAMETERS

EVAM machining was conducted using the piezoelectrically driven Ultramill mounted to a 3-axis Nanoform 600 diamond turning machine. This device enables elliptical tool vibrations with variable ellipse shapes and frequencies (1-4 kHz). Two piezoelectric stacks oscillate out of phase which drives the ceramic tool holder tip in an elliptical path. The shape of the motion is shown in Figure 4. The tool moves in an elliptical shape with period T while being fed across the workpiece surface with velocity, v.

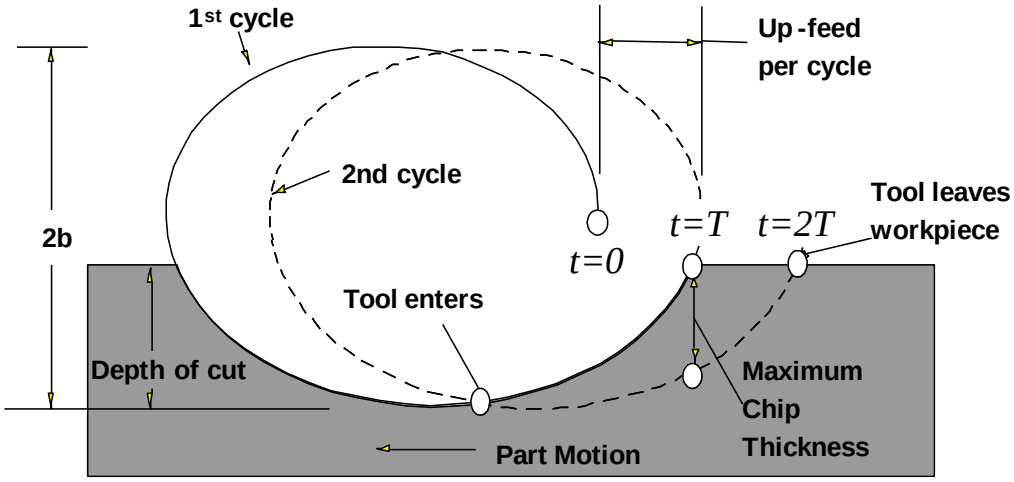

Figure 4: Side view schematic of the EVAM cutting process

With EVAM, the tool is in contact with the workpiece for a longer distance than the upfeed during one cycle. Since wear depends on sliding distance, this factor is calculated to compare EVAM with standard DT.The same depth of cut (2 µm) was chosen for EVAM of 6061 aluminum as with conventional machining with the same distance for upfeed. Table 3 gives the EVAM parameters. The minor axis and depth of cut are the same to observe if resultant chips are continuous of discrete. With the chosen depth of cut, workpiece velocity and ellipse minor axis, the maximum chip thickness is effectively half the depth of cut. EVAM experiments on 1215 steel have not been completed.

Table 3. Parameters for EVAM of 6061 Al

Material Width	1.0 mm
Depth of Cut	2 µm
Workpiece Velocity	2 mm/s
Operating Frequency	1 kHz
Ellipse Shape	a = 11µm b = 2 µm
Upfeed	2 µm
Sliding Distance / Upfeed	6.465 µm/µm

5.2.4 DIAMOND TOOL WEAR MEASUREMENT

Diamond tool wear is measured between successive cuts using two different techniques. Section 5 of this PEC Annual Report describes a technique called Electron Beam Induced Deposition (EBID). A worn diamond tool edge is difficult to discern in the 2D image created from a scanning electron microscope (SEM). A hydrocarbon contamination stripe can be created within the SEM chamber that lays on the diamond surface perpendicular to the cutting edge. This stripe creates a contrasting line that allows the worn tool profile to be discerned. Tilting the tool a known amount and changing the aspect ratio of the SEM image allows the profile of the worn edge to be recovered. Figure 5 shows a tilted diamond tool as it appears in the SEM viewing monitor plane. Once the EBID stripe is placed on the edge, the tool is viewed at this angle for the EBID image to be taken. The aspect ratio of the digital image is then changed according to the tool tilt angle. Figure 6 shows examples an EBID stripe on a stretched SEM image.

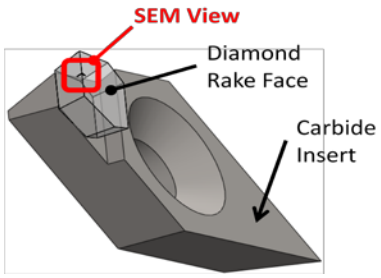

Figure 5: Schematic showing viewing angle of EBID images

A Matlab program called Digitize09 was created to select individual pixels on the image, shown as dots in Figure 6. Subroutines in Digitize09 were created to measure edge radius, wear land length, and cross-sectional worn area. Since only orthogonal cutting with straight edge tools are used, the wear pattern is relatively invariant along the cutting edge. This allows the worn volume to be determined by multiplying the worn cross-sectional area by the workpiece material width.

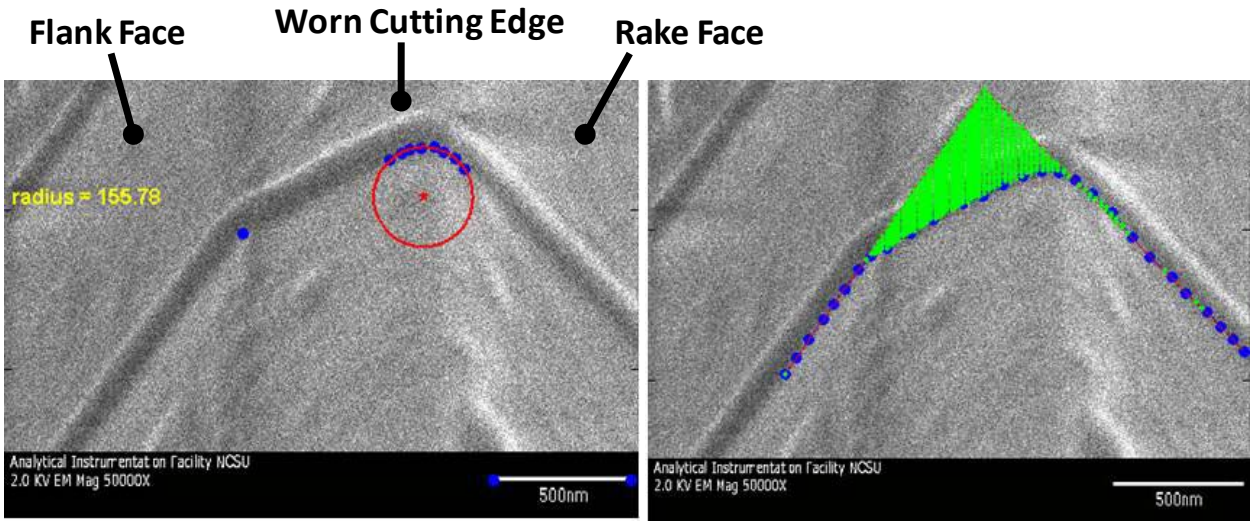

Figure 6: Tool edge measurements taken via Digitize09 of tool worn after cutting 10m of St1215. *(left)* Tool edge radius measured from circle-fitting algorithm along with wear land, and measurebar. *(right)* Worn area and tool edge angle are measured.

While the EBID technique allows measurement resolution of tens of nanometers, the process is time consuming because of the SEM. Another technique that offers relatively rapid measurement uses a white light interferometer (SWLI) to measure the flat portion of a worn tool edge (the wear land). Figure 7 shows the process of tilting a diamond tool on the SWLI stage to measure the wear land. The horizontal resolution of SWLI wear land measurements is 100nm, but allows dozens of measurements to be made rapidly along the tool edge.

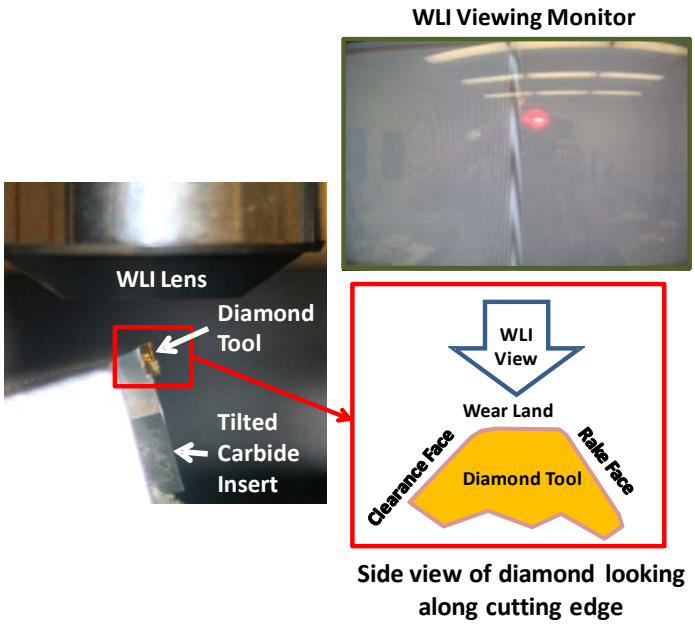

SWLI wear land measurements are compared with more accurate EBID measurements of the same worn tool. Empirical transfer functions are created that relate SWLI wear land measurements to EBID wear land measurements to EBID worn areas. Worn areas are then multiplied by the width of the workpiece to give worn volume.

Figure 7: Schematic of SWLI wear land measuring process.

4.3 EXPERIMENTAL RESULTS

4.3.1 TOOL FORCES

Increased machining distance yielded increasing tool forces for the 6061 aluminum, as illustrated in Figure 8. The increase in tool force is due to the geometry change due to tool wear and reveals the relationship between forces and wear. Tool forces cutting steel were significantly higher despite cutting at half the depth of cut. Tool forces scale with uncut chip thickness (which is equal to the depth of cut in standard cutting) and material hardness [5], but the 60% higher hardness of steel (Table 1) does not account for the higher tool forces. Steel forces also increased little with further cut distance. This is indicative of rapid initial wearing with a reduced wear rate during continued cutting.

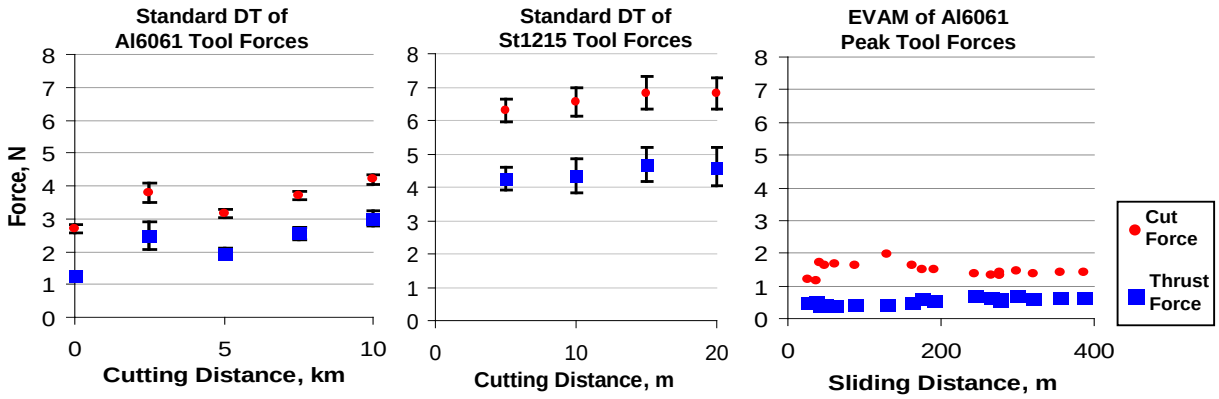

Figure 8: Measured tool forces from standard and EVAM cutting experiments. Error bars indicate one standard deviation.

Peak EVAM tool forces cutting aluminum were smaller than the standard aluminum tool forces. The EVAM cutting process creates a maximum uncut chip thickness smaller than the depth of cut (Figure 4). As the tool forces scale with the uncut chip thickness, the reduced EVAM chip creates smaller tool forces. This indicates that the tool may wear less as a result of reduced tool forces, though further wear measurements show this is not the case for EVAM of aluminum.

4.3.2 TOOL WEAR

Figure 9 shows examples of EBID images obtained after standard cutting of 6061 aluminum and 1215 steel, and EVAM of 6061 aluminum. Tool cross sections directly traced from the EBID stripe show the general pattern of wear for the respective experiment. The standard cut 6061 aluminum tool had an increasing edge radius and a wear land that was parallel to the uncut surface. The standard cut 1215 steel had an increasing wear land that formed at an angle with the uncut surface. The angle of this wear land remained the same with further machining.

EVAM of 6061 aluminum produced an increasing edge radius but no wear land. Micro-chipping was also observed on the EVAM tool rake face. The micro-chipping became more severe, while the flank region of the tool remained smooth.

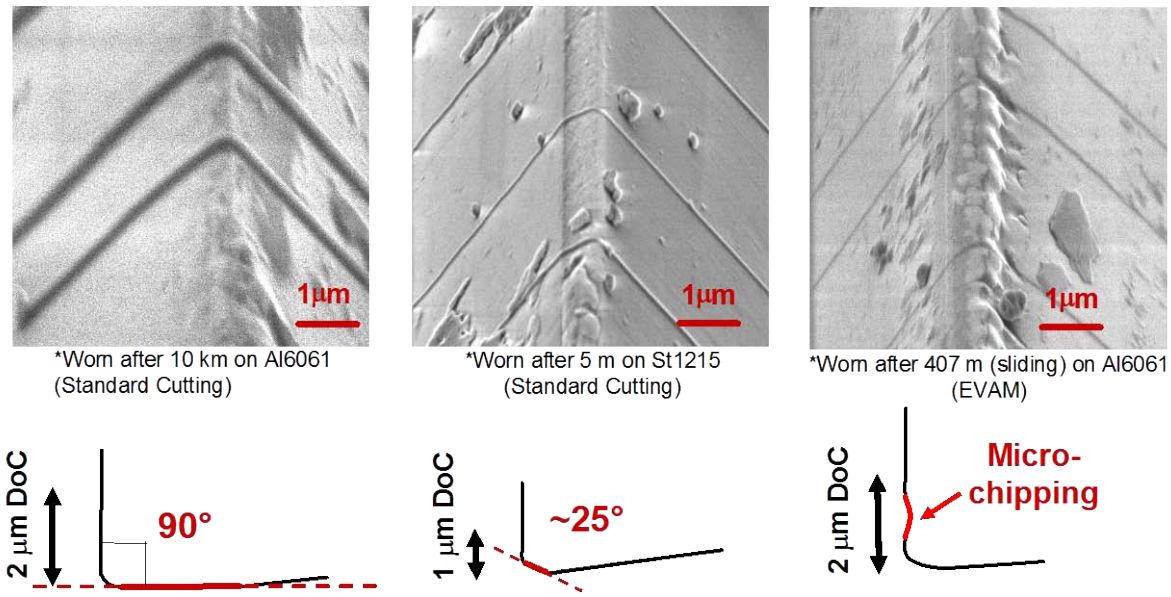

Figure 9: EBID images of the tool edge for conventional diamond turning of Aluminum 6061 (left), conventional machining of 1215 steel (center) and EVAM of Aluminum 6061 (right). The bottom images are cross sections of the tool from the EBID images.

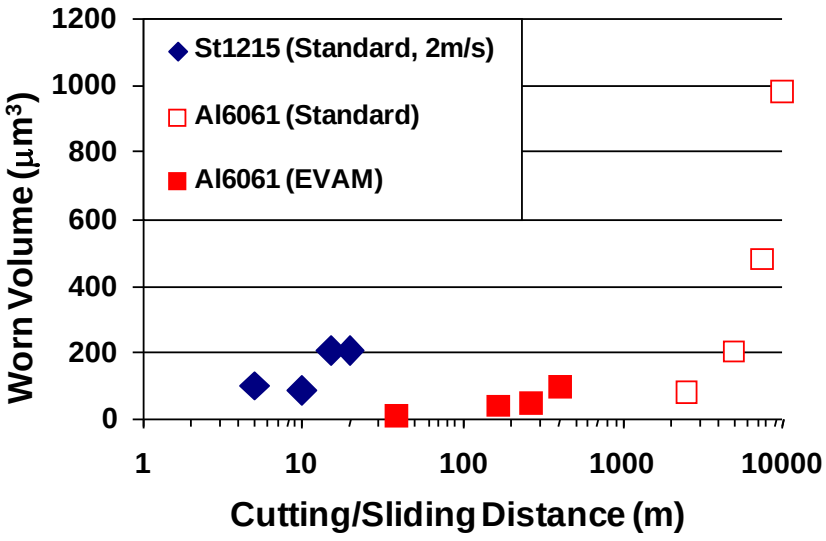

Figure 10. Worn volume of diamond tool as a function of cutting distance (standard cutting) or sliding distance (EVAM)

Figure 10 shows the measured wear volume as a function of the sliding distance for two

conventional and one EVAM experiments. The volume removed from the tool for conventional machining of steel was the largest, and increased sharply after initial cutting. This sharp increase in tool wear explains the high tool forces measured while cutting steel. Similar wear for conventional machining of 1215 steel was observed at 500x less cutting distance than that of 6061 aluminum. This higher wear rate is undoubtedly due to a chemical wear mechanism. The sliding distance for EVAM is significantly larger than the cutting distance (650%) and is still much smaller than the cutting distance for the conventional machining experiments. Future experiments will provide data for EVAM machining on steel and other materials.

Further standard cutting tests on 1215 steel at varying cut speeds showed a marked difference in volumetric wear rates (diamond removed per time). Diamond tools used to cut steel cut at 4.24 m/s and 1.06 m/s cut speed were measured using EBID and the SWLI technique. The wear lands measured from the SWLI were related to worn volume determined from EBID and compared with the time the tool was in contact with the workpiece. Figure 11 shows volumetric wear vs. cut time. Initial wear occurred within the first second of cut time. The higher cut speed resulted in a higher wear rate.

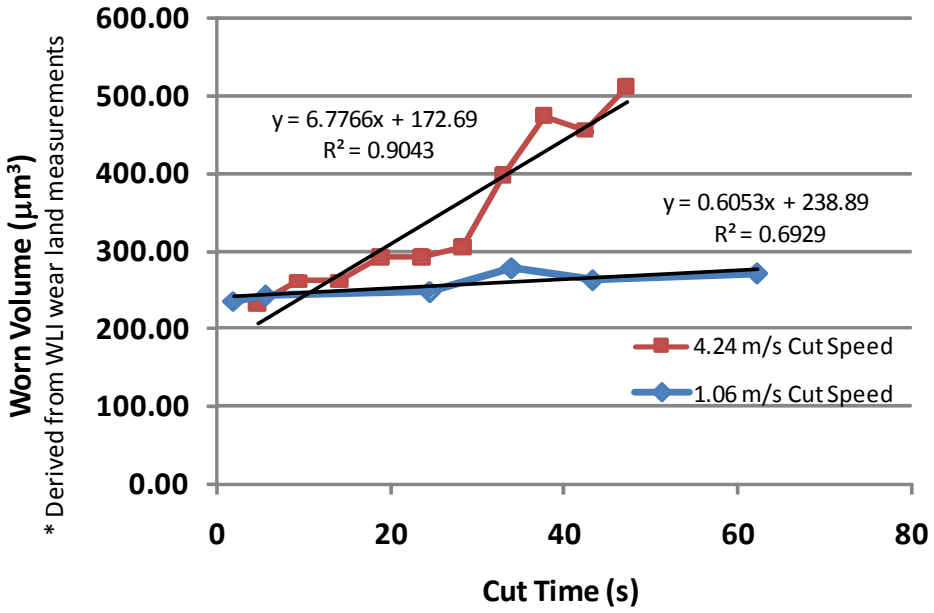

Figure 11: Worn volume calculated from SWLI wear land measurements as a function of time indicate different wear rates at different cut speeds.

It is well understood that increasing cut speed will result in increased tool temperature [6]. The measured increase in tool wear with cut speed and the increased tool temperature with cut speed presents a bridge between calculated tool temperatures and the wear rate.

4.3.3 SURFACE FINISH

While the worn edge radius of the EVAM tool was greater than that for conventional machining, the surface finish was markedly better for aluminum workpieces. Figure 12 shows images of machined surfaces taken in a white light interferometer. The surfaces generated by conventional machining showed scratches stemming from hard particles dragged across the surface by the tool. This was not observed on the EVAM surface. The 1215 steel surface exhibited similar scratching to the 6061 aluminum.

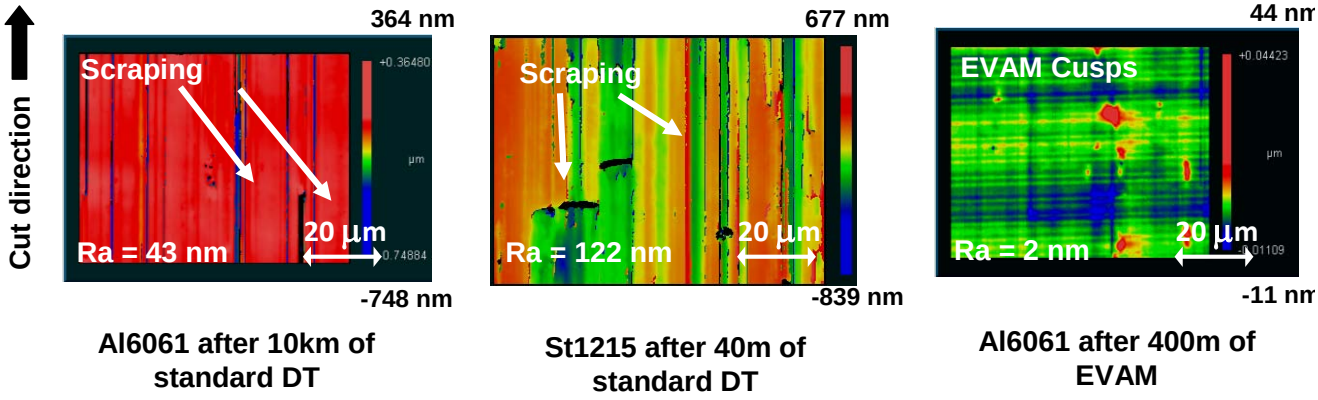

Figure 12: White light interferometer images of machined surfaces. The Ra roughness is shown in the lower left on each image. Scratching was reduced on the EVAM specimen.

Surface finishes for the three experiments changed little (< 10%) for each cut distance. Though inevitable wear occurred, the orthogonal geometry of the experiments excludes the formation of spanzipfels seen in facing operations. The orthogonal cut geometry highlights the surface finish affects due to particle dragging. The reduction of dragging on the EVAM surface explains previously reported improvements in surface finish on abrasive materials [1] despite the amount of tool wear present. The EVAM tool may either lift out the hard particles with the chip, or push them into the workpiece under the tool. Regardless of the mechanism, the EVAM tool resulted in improved surface finish by reducing hard particle dragging.

4.4 TOOL WEAR MODELING

4.4.1 STANDARD CUTTING ABRASIVE MODEL

The data for tool forces and wear from the 6061 aluminum experiments may be evaluated using the Archard abrasive wear equation. For this model, the worn volume of an abraded material is proportional to the normal contact force and sliding distance. The normal contact force on a cutting tool is complicated, though an average normal forces can be derived from a simplified tool force model [5]. Figure 13 shows how average normal and friction forces act on the faces of

a worn tool. These forces can be resolved into the two measureable tool forces; cut force (F_C) and thrust force (F_T).

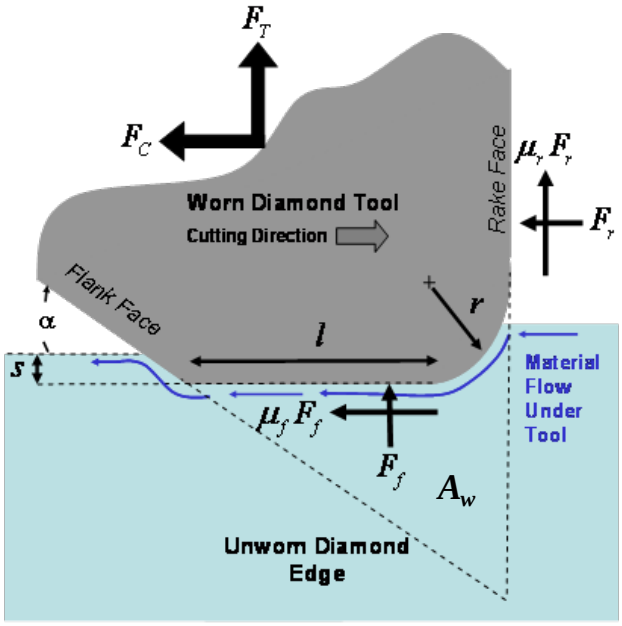

Figure 13: Side-view schematic of worn diamond tool, average forces acting on the tool, and resultant tool forces.

Based on measurements of aluminum worn tools, the majority of wear on the tool occurs from the formation and recession of the wear land. The normal force acting on the wear land is the average flank force, F_f. This force is used in relating tool wear to Archards equation. The volume of tool wear, determined by the worn cross section area Aw and workpiece width w, is thus proportional to the average flank force and sliding distance:

$$V = A_w \cdot w = k \cdot F_f \cdot d_s \tag{1}$$

A force balance on the tool in Figure 13 is used to determine the average flank force as a function of friction and measured tool forces:

$$F_f = \frac{F_T - \mu_r F_C}{1 - \mu_r \mu_f} \tag{2}$$

Rake and flank friction coefficients are not available, though they can be approximated from various literature sources [7]. Values of 0.4 for μ_r and 0.2 for μ_f are used. The use of the average flank force here improves upon a previous model [8] which utilized an empirical formula for flank stress developed by Arcona [5], which he presumed led to inaccuracies in his

tool force model. The model for average flank force described here doesn't require material properties of the workpiece to be known and only varies with friction parameters.

ABRASIVE WEAR MODEL RESULTS

Measured tool forces and measured tool wear were combine via equations (1) and (2). Figure 14 shows the results of the volumetric wear vs. average flank force and sliding (cutting) distance. A best fit line was applied to determine the Archard wear coefficient, *k*.

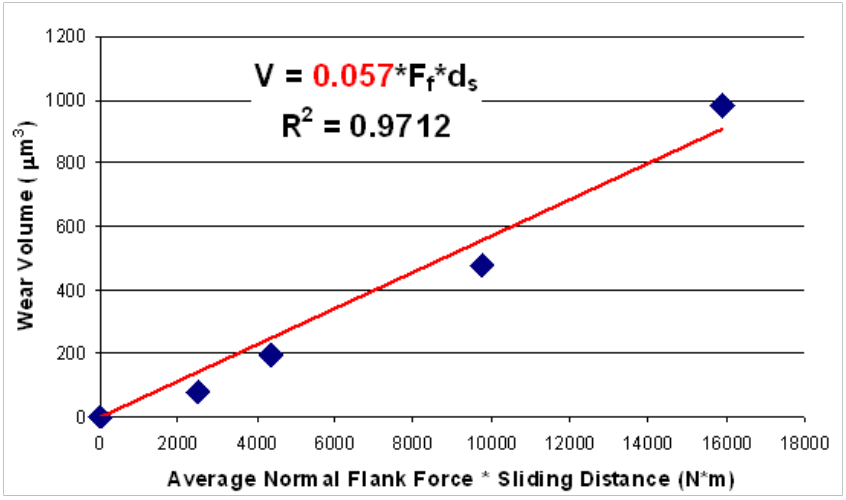

Figure 14: Archard wear constant determined for diamond machining of 6061 aluminum.

Using this process, a wear coefficient of 0.057 μm^3/N-m was found for the diamond machining of 6061 aluminum. The high linearity of the results confirms the wear of diamond tools while cutting 6061 aluminum is an abrasive process.

4.4.2 CHEMICAL WEAR MODEL

THE ARRHENIUS EQUATION

The chemical wear of diamond tools is hypothesized to occur due to either diffusion of diamond into the workpiece and chip, or graphitization of the tool surface catalyzed by the ferrous workpiece. Both processes are described by the Arrhenius equation, which describes volumetric (V) loss rate as a function of process temperature (T).

$$\frac{dV}{dt} = A\exp\left(\frac{-E_a}{RT}\right) \tag{3}$$

In the Arrhenius function, the two experimentally determined constants E_a and A are the activation energy and the pre-exponential constant, respectively. While much research has reported diffusive or graphitizing diamond tool wear, few have related measured wear to the Arrhenius equation. This is due to the difficult tasks of measuring micrometer-scale tool wear and acquiring tool temperatures during cutting. Many methods for measuring or modeling tool temperatures have been developed [6], though few possess the ability to predict temperatures in precision machining. Temperature measurement techniques are limited by the scale of the precision machining process, and modeling vary greatly in their methods and results. Finite element modeling of the cutting process provides data that is difficult to measure experimentally, including tool temperatures.

FE MODELING FOR TOOL TEMPERATURES

Third Wave AdvantEdge is a commercial finite element code developed to optimize machining processes. The orthogonal geometry used in experiments can be modeled in AdvantEdge as a 2D simulation. Figure 15 shows the simulation geometry and mesh. Adiabatic and isothermal boundary conditions are set automatically by AdvantEdge. Custom tool shapes were created to match those measured by EBID (Figure 9) and correlate to specific cutting distance.

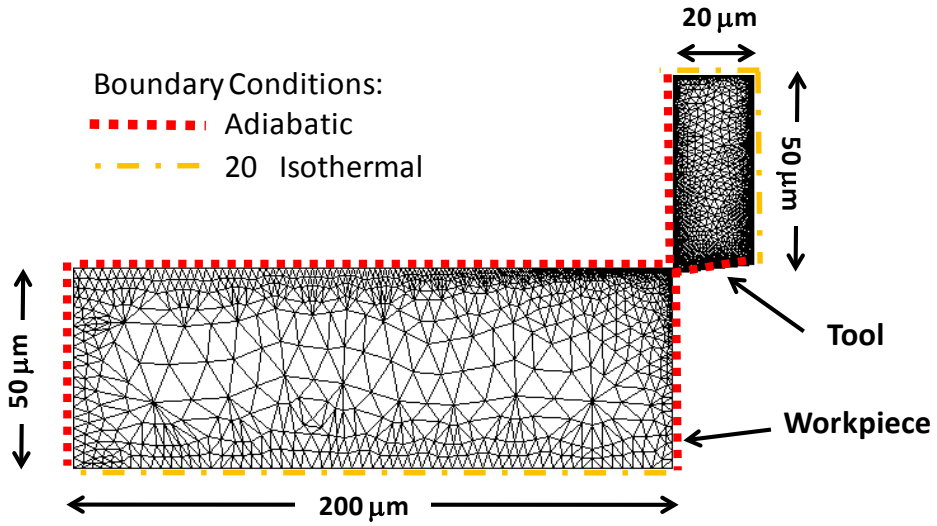

Figure 15: Geometry, boundary conditions, and mesh of AdvantEdge FE cutting simulations.

1215 steel was not available in the AdvantEdge library. 1118 steel has similar material and thermal properties as 1215, and was chosen as the workpiece material. Four simulations with custom tool shapes were created that mimic the cutting conditions of the 1215 steel experiments. Sixteen other simulations were created with 4 cut speeds ranging from 1.06-4.24 m/s, and 4 depths of cut ranging from 0.5-2 µm.

FE AND CHEMICAL WEAR MODEL RESULTS

Thermal contour plots from the simulations showed a dramatic increase in tool temperature within the chip and tool with increased cut speed. Figure 16 shows two examples of temperature contour results from ThirdWave. Temperatures within the chip increased with cut speed at a higher rate than tool temperatures. Peak tool temperatures occurred at the vicinity of the tool tip.

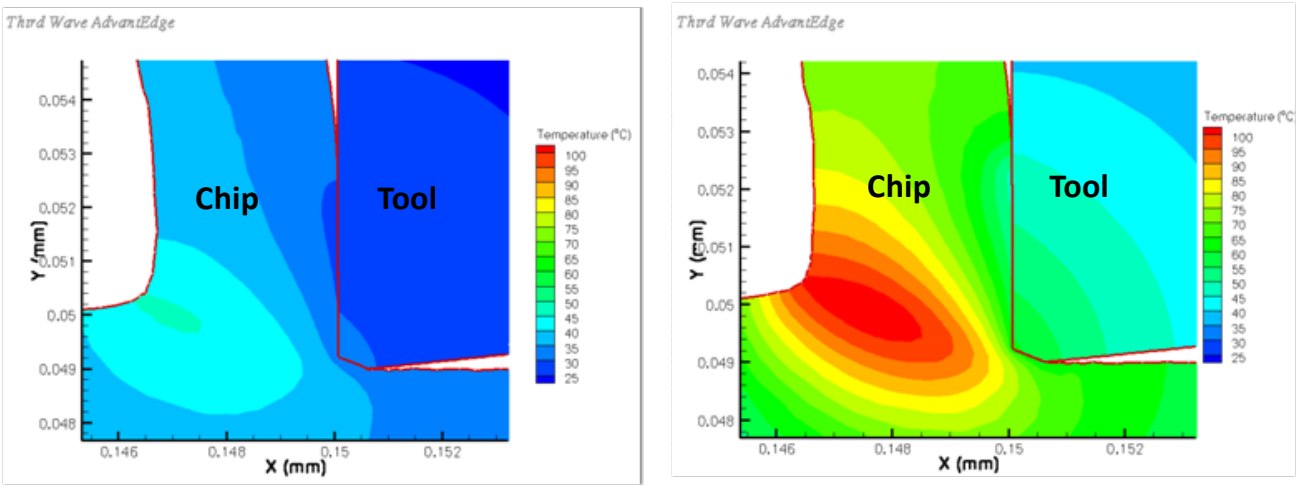

Figure 16: Steady state temperature contour plot of 1.06 m/s *(left)* and 4.24 m/s *(right)* simulations cutting 1118 steel (2 µm depth of cut).

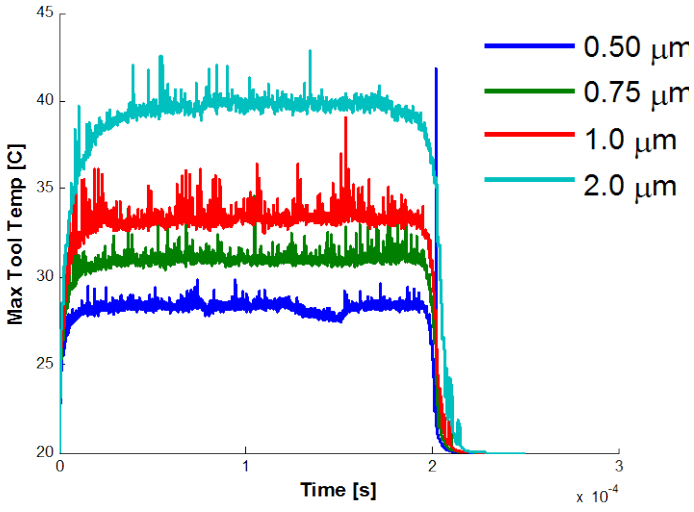

Figure 17: Example of max tool temperatures for 4 depths of cut (1.06 m/s cut speed) determined from FEA simulations.

Tool temperatures did not vary from simulations using custom tool shapes that mimic worn tools, and simulations using new tools. Peak tool temperatures were plotted vs. cut time for the 16 simulations, 4 of which are shown in Figure 17. Maximum tool temperatures increased with depth of cut as well as cut speed. The average steady state tool temperature for each simulation was calculated by taking the mean of 50% of the data centered about the middle of the cutting period. These steady state temperatures were plotted vs. depth of cut for the 4 diefferent cut speeds, shown in Figure 18. A best fit surface was also determined describing the temperature as a function of

depth of cut and cut speed. Steady state maximum tool temperatures increased linearly with speed, and logarithmically with depth of cut.

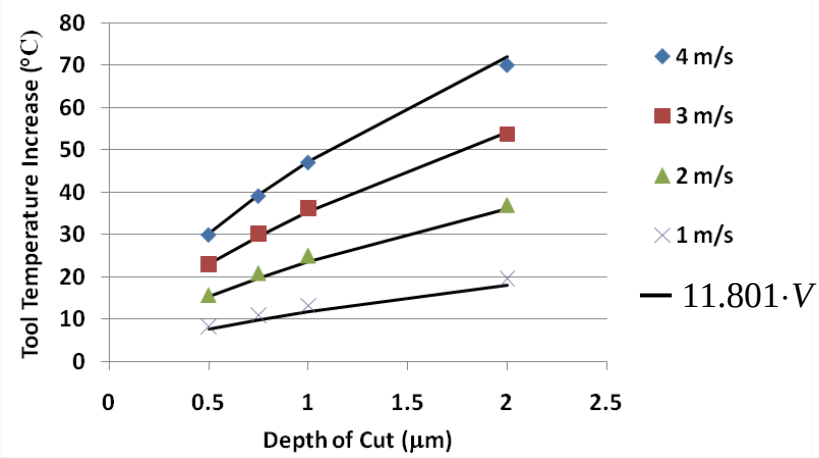

Figure 18: Increase in max steady state tool temperature (T-20°C) for varying cut speed and depth of cut (St1118). A best fit surface is also found for the sample space.

In order to determine the characteristic constants A and E in the Arrhenius equation, tool temperatures were taken for the 1.06 m/s and 4.24 m/s experiments at 1 µm depth of cut shown in Figure 11. Volumetric wear rates from Figure 11 and max steady state tool temperatures from the FE simulations are plotted in an Arrenius plot in Figure 19. Using a value of 8.3144 J/K-mol for the universal gas constant, the pre-exponential constant A is determined to be $2.894*10^{11}$ μm^3/sec, and the activation energy E_a as 67.973 kJ/mol.

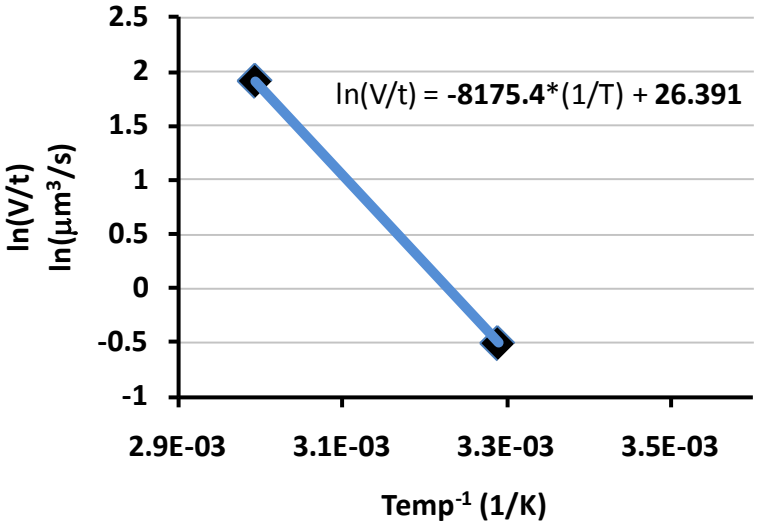

Figure 19: Arrhenius plot utilizing wear data from Figure 11 and temperature data from Figure 18.

The activation energy of 67.973 kJ/mol is relatively low compared to other research concerning the graphitization of heated diamond in vacuum [9], meaning equivalent wear occurs at much lower temperatures in the presence of 1215 steel. This is likely an affect of several phenomena; the clean surface contact between the diamond and workpiece, the combined effects of graphitization and diffusion, and a likely catalyzing action of the ferrous alloy.

TRANSIENT TOOL TEMPERATURES

A principle hypothesis how EVAM reduces tool wear is that the interrupted cutting process reduces average tool temperatures. This is a result of the decreased uncut chip thickness inherent with EVAM. A decrease in tool temperature with uncut chip thickness is evident from FEA simulation results presented in Figure 18. Other reasons for hypothesized decreased in EVAM tool temperature is the ability of the tool to cool while it is not in contact with the workpiece, and the limited contact time in which the tool can heat up. To study the temperature affects of EVAM, the dynamic tool temperatures need to be known. While transient conduction problems are usually very complicated, they may be simplified if the process-specific Biot number is relatively small (<0.1). The Biot number describes the ability of a conducting solid in a convective environment to retain uniform temperature distribution. Biot number is related to the heat convection coefficient, h, and characteristic length, L_c, over the thermal conductivity, k:

$$Bi = \frac{h \cdot L_c}{k} \tag{4}$$

Processes with a low Biot number are well approximated by Newton's Law of Heating, or the lumped capacitance (LC) method. These simplified, analytical processes describe heat transfer scenarios where the temperature (assumed to be uniformly distributed throughout the solid) increases or decays exponentially. Diamond exhibits very high conductivity (~2000 W/m-K) compared to other highly conductive materials such as copper (~400 W/m-K). Due to the micrometer scale of the process, the characteristic length would also be small. This indicates that diamond heat transfer processes have low Biot numbers, and may be accurately simplified by Newton/LC methods, and exponential temperature functions of time.

In Newton/LC method, non-dimensional temperature is used, where T is the time dependant temperature, T_f is the steady state temperature, and T_i is the initial or ambient temperature:

$$\Theta = \frac{T - T_i}{T_f - T_i} \tag{5}$$

The non-dimensional temperature changes exponentially with time in both Newton/LC heating or cooling processes:

$$\Theta_h = 1 - \exp\left(\frac{-t}{\tau_h}\right) \qquad \Theta_c = \exp\left(\frac{-t + \Delta t}{\tau_c}\right) \tag{6}$$

Tool temperature results from AdvantEdge simulations (Figure 17) are used to determine the transient heating and cooling. This is done by fitting exponential curves to temperature data during the heating and cooling process, shown in Figure 20. Heating curves (Θ_h) are taken from the start of data till steady state temperature is reached and cooling curves are taken from the end of data till 33% steady state temperature.

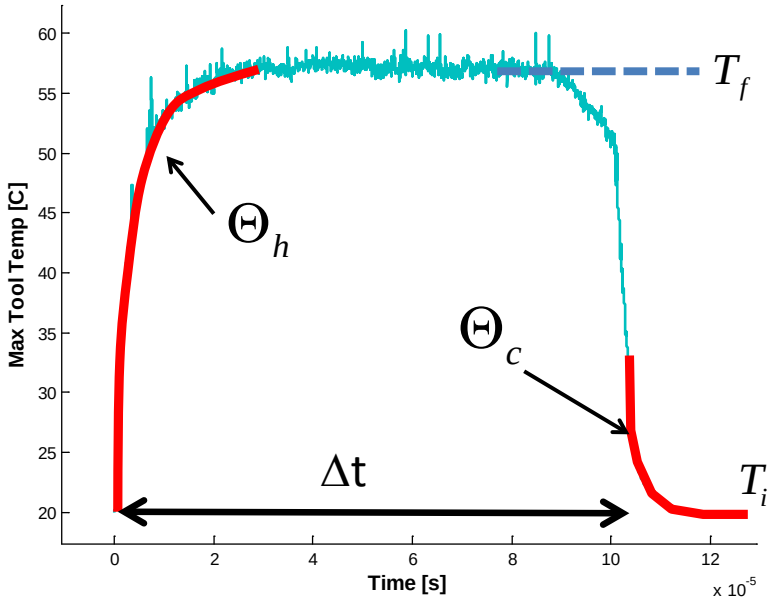

Figure 20: Example of non-dimensional temperature curves taken from AdvantEdge simulation data to be fit by an exponential function.

Best fit exponential curves were applied using Matlab's curve-fitting tool incorporating the Gauss-Newton fitting algorithm. Time constants τ_c and τ_h were determined from the best fit curves. Figure 21 shows heating and cooling time constant results for the 16 simulations. Cooling curves varied less with cut speed and depth of cut than did heating curves. Cooling time constants ranged from 2.3 µsec to 3.0 µsec while the heating time constants ranged from 0.9 µsec to 3.8 µsec. This is as expected, since the tool cools outside the workpiece in the same manner for every simulation. The heating is affected by both cut speed and depth of cut as the tool enters the workpiece, thus changes with the different cutting conditions.

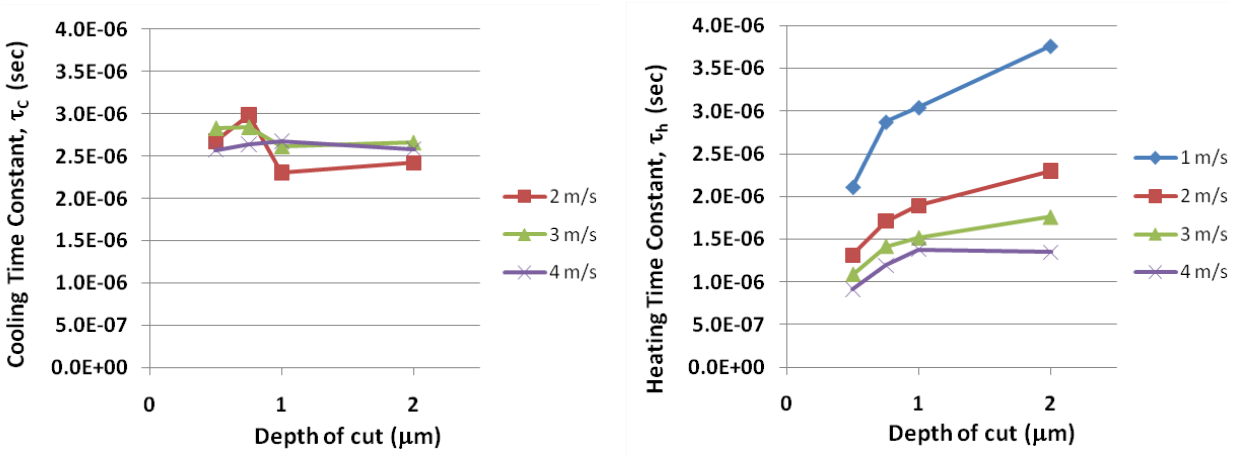

Figure 21: Cooling time constant *(left)* and heating time constant *(right)* for varying depth of cut and cut speed. Exponential fit curve could not be generated for the 1 m/s cooling time constant.

Cooling curves were better approximated by an exponential function than heating curves. The average correlation coefficient for the cooling curves was 0.97 while average correlation for heating curves was 0.91. The high correlation of the cooling curve with an exponential function is indicative of the low Biot number for the process. The mean cooling coefficient was found to be 2.65 µsec (σ = 0.20 µsec).

The cooling time constant is significant with regards to EVAM. In one EVAM cycle, the tool is out of contact with the workpiece and is cooling for approximately ¾ of the cycle. Assuming the tool cools with a time constant of 2.6 µsec, an EVAM tool operating at 28.3 kHz will cool to within 0.005% from ambient temperature after each cycle. It would take an EVAM tool to operate at 61.5 kHz to cool to within 1% of ambient temperature. All reported ultrasonic EVAM actuators operate below 40 kHz, and most operate around 20 kHz [1]. The low time constant for the dynamic cooling of a diamond tool results in very fast recovery to ambient conditions, and explains the reported decrease in thermally inspired tool wear when utilizing EVAM.

4.5 CONCLUSIONS

Abrasive Wear

1.) The EBID process was used to measure the wear of a diamond tool turning 6061 aluminum. A simplified tool force model based on measured forces was used to show that the wear of diamond machining 6061 aluminum follows Archard's law for abrasive wear. An Archard wear constant of 0.057 μm^3/N-m was determined.

2.) EBID measurements showed a higher degree of volumetric wear for the EVAM tool compared to the standard cutting tool. Despite the degree of wear, the EVAM tool produced a superior surface finish.

3.) Standard cutting resulted in hard inclusions within the aluminum alloy to be dragged across the workpiece surface while the EVAM tool limited this dragging. This is proposed as the reason for EVAM's superior surface finish. The particular cutting geometry of these experiments is different, however, than facing operations, which add additional relationships between surface finish and tool wear.

Chemical Wear

1.) Finite element models using ThirdWave AdvantEdge mimicked cutting conditions of experiments cutting 1215 steel. Peak tool temperature results showed a linear relationship with speed, and logarithmic relationship with depth of cut.
2.) EBID and SWLI wear measurements from 1215 steel cutting experiments were combined with simulation tool temperatures in the Arrhenius equation for chemical processes. A pre-exponential constant A is determined to be $2.894*10^{11}$ μm^3/sec, and the activation energy E_a as 67.973 kJ/mol. This activation energy is low compared to other diamond wearing experiments, and likely due to clean surface contacts, combined effects of graphitization and diffusion, and/or catalyzing effects of the ferrous alloy workpiece.
3.) FE simulations studied the transient temperature changes of diamond tools. The decrease in temperature of a tool leaving a workpiece was found to decrease in a repeatable exponential manner, as a result of the process's low Biot number. The exponential time constant for a cooling diamond tool was found to be 2.65 μsec (σ = 0.20 μsec). This short time constant explains how EVAM tools can cool to near ambient temperatures with each cut cycle, thus reducing thermally inspired tool wear.

4.6 ACKNOWLEDGEMENTS

Primary funding for this work was by National Science Foundation Grant CMMI-0800560 monitored by G. Hazelrigg. Chuck Mooney of the Analytical Instrumentation Facility at North Carolina State University provided training for the contamination stripe growth method, the AIF granted use of the SEM, and Meirong Shi provided stripe growth and SEM image analysis. Ken Garrard of the PEC provided conceptualization of Digitize09 and incorporation pixel selection and circle-fitting algorithms. Chardon Tools supplied the diamond tools used in the machining experiments.

4.7 REFERENCES

1. Brehl D.E., Dow T.A., Review of vibration-assisted machining, Precis. Engr. 32 (2008) 153-172.
2. Drescher, J., Scanning electron microscopic technique for imaging a diamond tool edge, Precision Engineering 15 (1993) 112-114.

3. Shi, M., Scattergood, R., Dow, T.A., Diamond tool wear measurement by EBID, Precision Engineering. (2010) (Pending Publishing)

4. Thornton, A.G., Wilks, J., Clean surface reactions between diamond and steel, Nature 274 (1978) 792-793

5. Arcona, C., Tool force, chip formation, and surface finish in diamond turning, PhD. Dissertation, North Carolina State University, 1996

6. Abukhshim, N.A., Mativenga, P.T., Sheikh, M.A., Heat generation and temperature prediction in metal cutting: A review and implications for high speed machining, Int. J. of Mach. Tools and Manuf. 46 (2005) 782-800

7. Lane, B., Shi, M., Dow, T.A., Scattergood, R., Diamond tool wear when machining 6061 aluminum and 1215 steel, Wear (2010) (Pending Publishing)

8. Lane, B., Dow, T.A., Scattergood, R., Wear analysis of diamond tool on 6061 aluminum and 1215 steel. Precision Engineering Center Annual Report (2009)

9. Davies, G., Evans, T., Graphitization of diamond at zero pressure and at high pressure, Proc. R. Soc. London. Ser. A 328 (1972) 413-438

5 DIAMOND TOOL WEAR IN ORTHOGONAL CUTTING OF 6061 AL, 1215 STEEL AND 416 STAINLESS STEEL

Meirong Shi
Graduate Student
Ronald Scattergood
Professor, Department of Materials Science and Engineering
Thomas Dow
Professor, Department of Mechanical and Aerospace Engineering

A study of thermo-chemical wear of diamond tools while machining ferrous material has been performed and the results are described. 1215 steel and 416 stainless steel were selected as the target materials. To separate the abrasive wear effect, 6061 Al with comparable hardness is selected as the baseline material. Orthogonal cutting experiments with similar machining conditions were performed on these workpieces. Tool wear was measured using electron-beam-induced deposition (EBID) and white light interferometer. Wear rate was calculated based on the tool wear measurement. Microstructures of the workpiece material show that 6061 Al has more and larger hard inclusions than 1215 steel and 416 stainless steel. Wear pattern of diamond tool cutting 416 stainless steel is similar to that for 6061 Al while the tool for cutting 1215 steel has a different worn profile. The wear rate of a diamond tool cutting 416 stainless steel is about three orders higher than that for 6061 Al and 18 times higher than that for 1215 steel under similar cutting conditions. For orthogonal cutting of 416 stainless steel, tool forces and cutting chip images indicate that steady state cutting can only last for short cutting distances. After a few tens of meters, the cutting process becomes unstable and the diamond tool plows and rubs on the workpiece surface. This is attributed to an adhesive layer formed on the rake face.

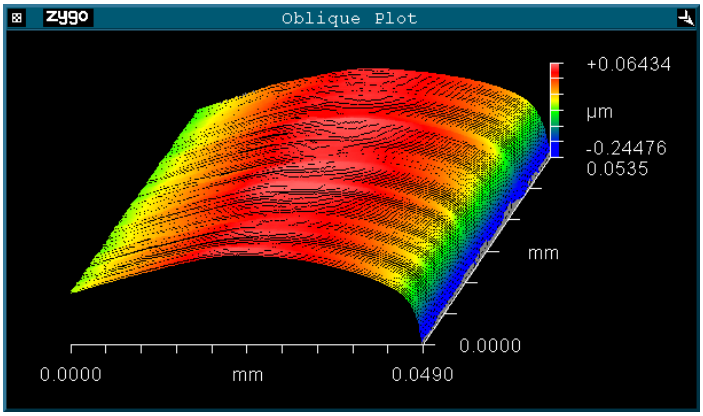

5.1 INTRODUCTION

It is well known that ferrous materials are difficult to fabricate efficiently using conventional diamond machining technology. The diamond tool wears at an extremely high rate when turning the ferrous materials, especially those with low carbon content. This high wear rate was believed to be caused by a thermo-chemical mechanism rather than a mechanical wear process. The wear rate of diamond tools machining mild steel has been estimated to be 10,000 times greater than that of turning brass with comparable hardness [1]. Experimental results have shown that diamond tool wear can be reduced by applying elliptical vibration assisted machining (EVAM) or intermittent cutting. Moriwaki and Shamoto reported that high quality surfaces can be obtained for cutting distances of 1600 m on free machining austenitic stainless steel SUS 303Se [2]. Song et al. [3] carried out a series of intermittent cutting experiments on stainless steel SUS304 to control the tool–workpiece contact time and reduce the diamond tool wear.

Studies including grinding, static erosion, diffusion test and cutting experiment have been performed to investigate the wear mechanism of diamond on ferrous materials. Komanduri and Shaw slid a single diamond particle against a low carbon steel plate and studied the worn surface of the diamond using scanning electron microscopy (SEM) [4, 5]. They concluded that carbon atoms are removed from the worn surface after diamond is converted to graphite. Ikawa and Tanaka also suggested that diamond wear is due to thermal induced graphitization which is greatly accelerated by the presence of the iron [6, 7]. Wilks et al. conducted a series cutting experiment on mild steel at different cutting speeds and air pressures [8, 9]. Results show that graphitization is the main mechanism to dissolute the carbon atoms from diamond lattice. Because of the enhanced chemical activity of the fresh surface generated during cutting, graphitization can proceed even when there is only a small temperature rise due to low the cutting speed. Oxygen may also play an important role in the solid reaction process. Paul and Evans proposed that the chemical wear is related to the unpaired d electrons in the workpiece [10]. The chemical wear happens through a lower energy path by forming the metal-carbon complex or metal-carbon-oxygen complex. Recent molecular dynamics simulation demonstrates that diamond should be converted into graphite before the carbon atoms are diffused into the iron [11, 12].

However, the inherent thermo-chemical mechanisms for tool wear are still not clear, because many factors, such as temperature, pressure and the state of the tool-workpiece interface are difficult to quantify during the wear process. What is needed is an accurate measurement of the gradual diamond tool wear to quantify this process. Unfortunately, the previously studies used interferometry or weight loss to measure diamond tool wear and the resolution was low.

This report describes the results of orthogonal diamond cutting ferrous material to study the thermo-chemical wear process. To separate the effect of mechanical and thermo-chemical wear, nonferrous material with comparable hardness is selected as the baseline material. Conventional orthogonal cutting experiments were conducted and tool forces were collected. To quantitatively characterize the gradual wear of the diamond tool, edge radius, wear land and wear profile after gradual cutting were measured through electron-beam-induced deposition (EBID) and white light interferometer. Wear rate was calculated based on the wear measurement. All these data can be a basis for planned EVAM experiments on ferrous material at the PEC.

5.2 DETAILS OF THE PROJECT

5.2.1 WORKPIECE MATERIAL SELECTION

1215 steel is a low carbon steel with good machinability. The composition is mainly pure iron (98.42-98.95%) and the carbon content is less than 0.09 %. Small amounts of alloying elements or impurities, such as manganese and aluminum, are used to enhance the mechanical properties. 0.26-0.35% sulfur was added as free machining additive to improve the machinability. The Vickers hardness of 1215 steel is 1850 MPa. 6061 Al, with the hardness of 1185 MPa, was selected as the baseline to compare the mechanical wear effect.

Stainless steels usually have poor machinability when compared to regular carbon steel because they are tougher, gummier and tend to work harden rapidly [13]. It is believed that machinability is influenced by both the hardness and the microstructure of the material. In the preliminary orthogonal diamond cutting experiment on 430 stainless steel, severe built up edge was observed on the rake face and wear land of the diamond tool after 5 m of cutting, as shown in Figure 1.

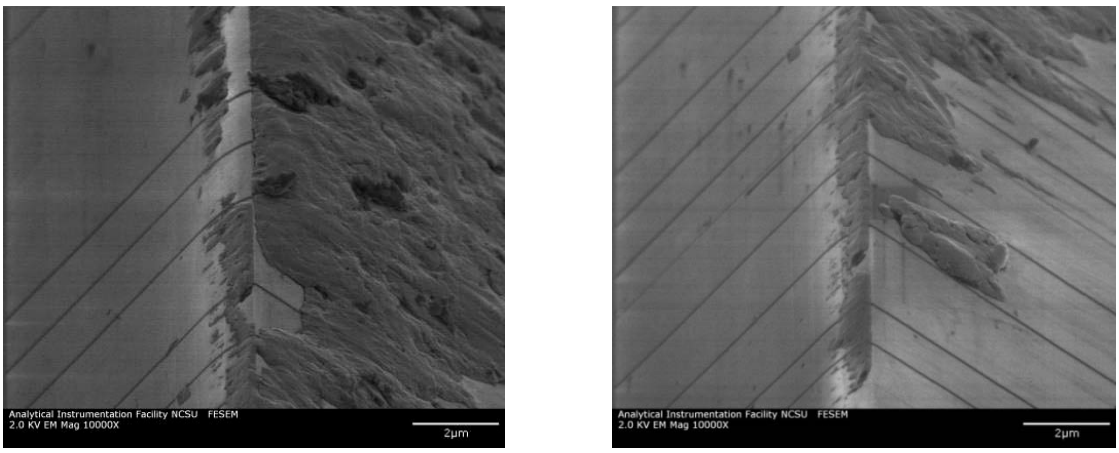

Figure 1. SEM images showing the severe built-up edge after cutting 5 m 430 stainless steel at 2.13 m/s.

To improve the machinability, a variety of chemicals, such as sulfur, selenium, phosphorous and calcium et al., can be added to stainless steel. These additives may work by lubricating the tool-chip interface, decreasing the shear strength of the material or increasing the brittleness of the chip [14]. Sulfur has been the primary element used to provide free-machining characteristics in stainless steels. It improves the machinability of steel by forming discrete sulfide inclusions with low shear strength in the cutting zone that allows the stainless steel to deform more easily. It has been observed that increases in sulfur content continuously increase the ease of cutting and the amount of sulfur that can be added to a stainless steel is limited by the allowable degradation of other properties [15]. 416 stainless steel is a martensitic alloy with a sulfur content of >=0.15%. Table 1 summarized the chemical compositions of some common stainless steel and 1215 steel. Figure 2 shows the comparison of the machinability for various stainless steels and shows that 416 stainless steel has the best machinability due to its higher sulfur content. In this study, 416 stainless steel was selected as another workpiece material. The Vickers hardness of 416 stainless steel is 1223 MPa.

Table 1. Chemical composition (%) of some common stainless steels and 1215 steel [16].

	st1215	sst416	sst430	sst304	sst303
Fe	98.42-98.95	84.0	>=79.31	66.345 - 74.0	67.05 - 74.85
Cr	--	13.0	16-18	18.0-20.0	17.0 - 19.0
C	<=0.09	<=0.15	<=0.12	<=0.08	<= 0.15
Mn	0.75-1.05	<=1.25	<=1.0	<=2.0	<= 2.0
Ni	--	--	<=0.5	8.0 - 10.5	8.0 - 10.0
Mo	--	<=0.6	--	--	<= 0.60
P	0.04-0.09	<=0.06	<=0.04	<= 0.045	<= 0.20
Si	--	<=1.0	<=1.0	<= 1.0	<= 1.0
S	0.26-0.35	>=0.15	<=0.03	<= 0.03	>= 0.15

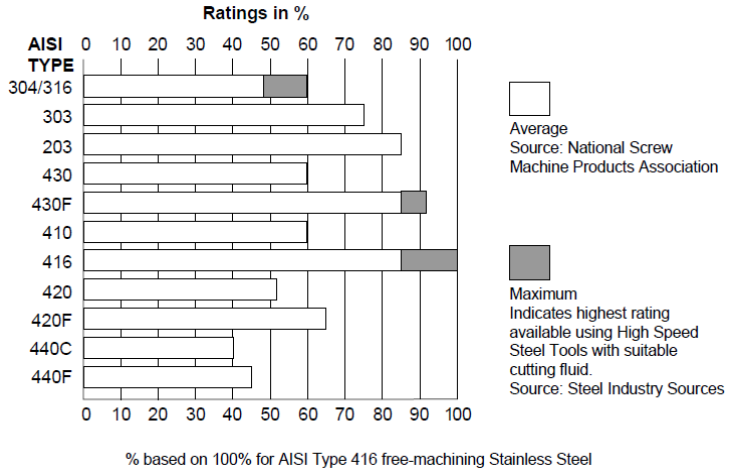

Figure 2. Comparison of the machinability for various common stainless steels [17].

5.2.2 MICROSTRUCTURES OF 6061 AL, 1215 STEEL AND 416 STAINLESS STEEL

The microconstituents present in the workpiece material have important effects on machining characteristics. It is generally thought that insoluble abrasive constituents will exert a detrimental effect on tool life and surface quality. Metallurgical samples of the 6061 Al, 1215 steel and 416 stainless steel were prepared to evaluate the microstructure of each. Cross section samples were cut from the bulk material, prepared with 120, 240, 320, 400, 600 grit silicon carbide paper and then polished with 1.0, 0.3, 0.05 μm alumina solution until a flat and smooth surface was obtained. Selective etchants were used to etch the sample surface to reveal the microstructures and inclusions. 10% NaOH solution, 2% Nital and diluted aqua regia (2.5 parts hydrochloric acid, 1 part nitric acid and 3 parts of water) were used as etchant for 6061 Al, 1215 steel and 416 stainless steel, respectively. The etched surface is examined under the SEM and an optical microscope. The optical images are then processed using Image J software to get the particle distribution.

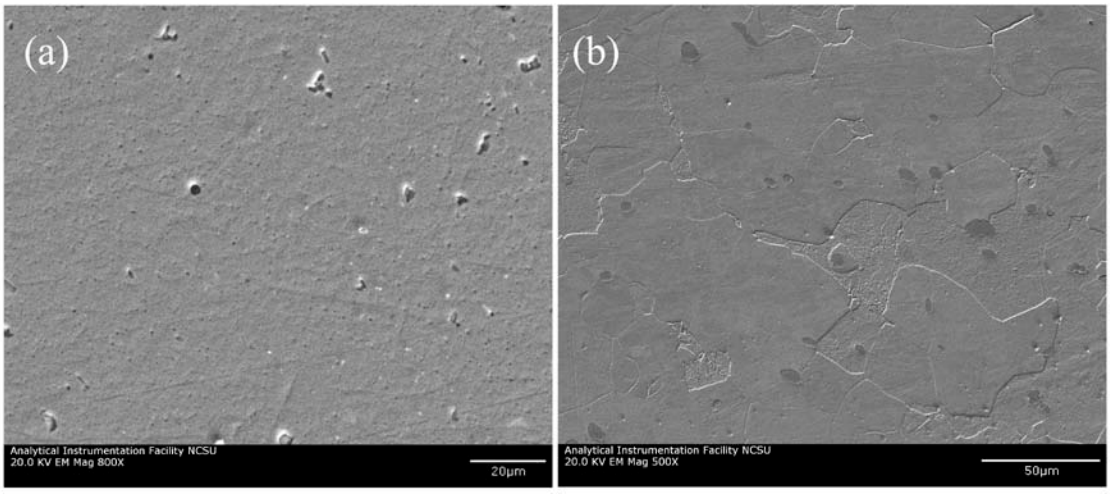

Figure 3. (a) SEM images showing microstructure of 6061 Al (a) and 1215 steel (b).

Figure 3(a) and 3(b) are the SEM images of the etched 6061 Al and 1215 steel surface. Figure 3(a) shows the typical microstructure morphology for wrought aluminum alloys after heat treatment. The dispersed secondary phase particles such as Al-Fe-Si and Mg_2Si have a round shape and size on the order of micrometers. These hard particles are thought to induce the abrasive wear on the diamond tool edge, especially the flank face. Figure 3(b) is an SEM image of 1215 steel surface. Different phases including ferrite, pearlite and inclusions can be identified. The matrix is ferrite and the iron carbide (cementite) has nucleated and grown on the ferrite grain boundaries. Cementite is hard and brittle phase which is detrimental to formability. The carbides can range from massive carbides to small and round particles. Microstructure also

shows some pearlite islands in the ferritic matrix. The lamellar morphology of pearlite is composed with alternating plates of cementite and ferrite.

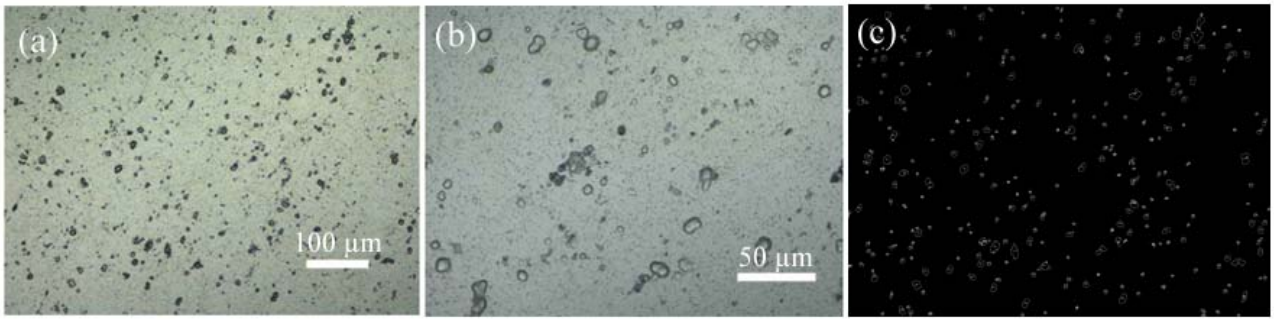

Figure 4. Optical images of the 6061 Al surface showing hard particle distribution. (a) 200x, (b) 500x, (c) hard particles in (a) are outlined in Image J with a circle to calculate the distribution.

Figures 4(a) and 4(b) are the optical images showing microstructures of 6061 Al, while 4(c) shows the micrometer size particles in 4(a) counted and outlined using Image J software. The area fraction of the inclusions is 3% and the average size (area of particle) is about 44 μm^2.

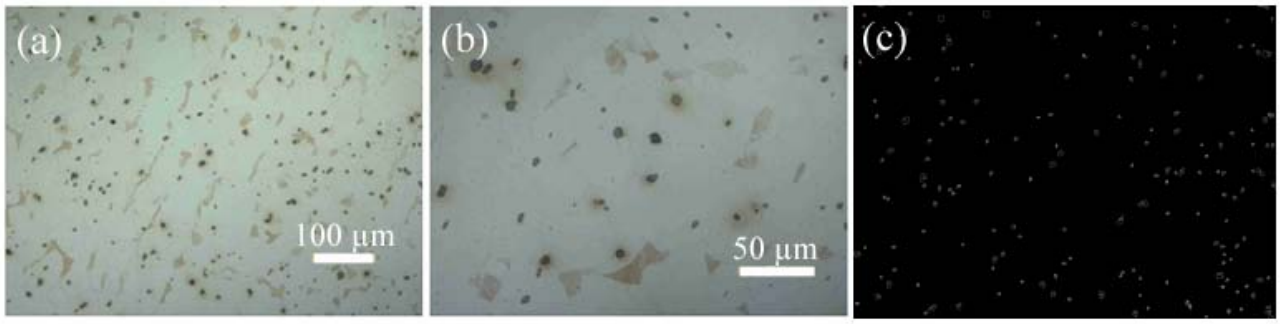

Figure 5. Optical images of the 1215 steel surface showing hard particle distribution. (a) 200x, (b) 500x, (c) hard particles in (a) are outlined in Image J with a circle to calculate the distribution.

Figures 5 shows optical images and particle distribution of 1215 steel. The area fraction of the inclusions is 1.2% and the average size is about 21 μm^2. Figure 6(a)-(c) are the optical images of 416 stainless steel surface showing the inclusions. The inclusions are generally in round shape and much smaller. The area fraction of the inclusions is 2.1% and the average size is about 5 μm^2. It has reported that larger and rounder sulfide inclusions can provide a greater benefit for machining than the smaller and elongated inclusions. The large number of round sulfide inclusion found in 416 stainless steel indicates the improved machinability. Hard sulfide and carbide inclusions can also cause the abrasive wear, resulting in the abrasive grooves on the cutting tool. From the comparison of the inclusion distribution at same magnification for three

workpiece material, it can be seen that 6061 Al has more and larger particles than that in 1215 steel and 416 stainless steel.

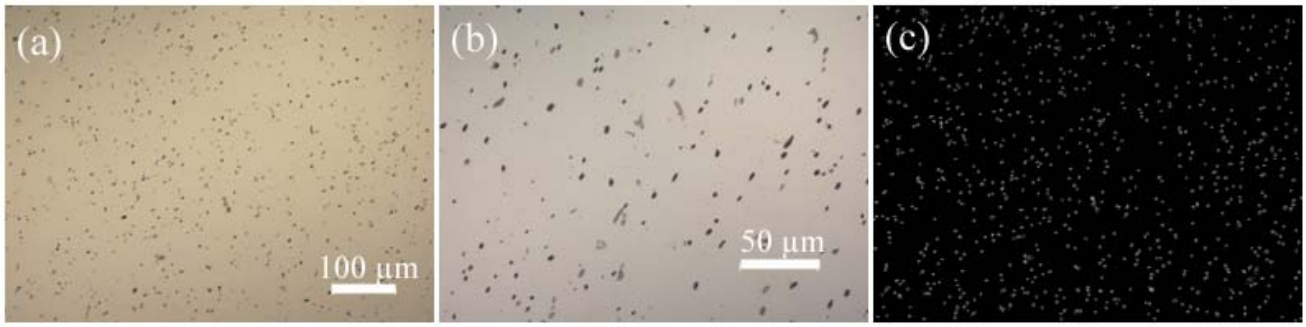

Figure 6. Optical images of the 416 stainless steel surface showing hard particle distribution. (a) 200x, (b) 500x, (c) hard particles in (a) are outlined in Image J with a circle to calculate the distribution.

Figure 7(a) and (b) are SEM images of chips from cutting 6061 Al and 1215 steel. In both images, similar micrometer wide grooves at the side contacting the tool can be seen. The grooves are thought to be generated by the abrasive particles built up on the cutting edge. These hard particles can also cause the abrasive wear on diamond tool. From the comparison of microstructures and hardness of the three materials, it can be expected that 6061Al will have comparable abrasive wear as 1215 steel and 416 stainless steel.

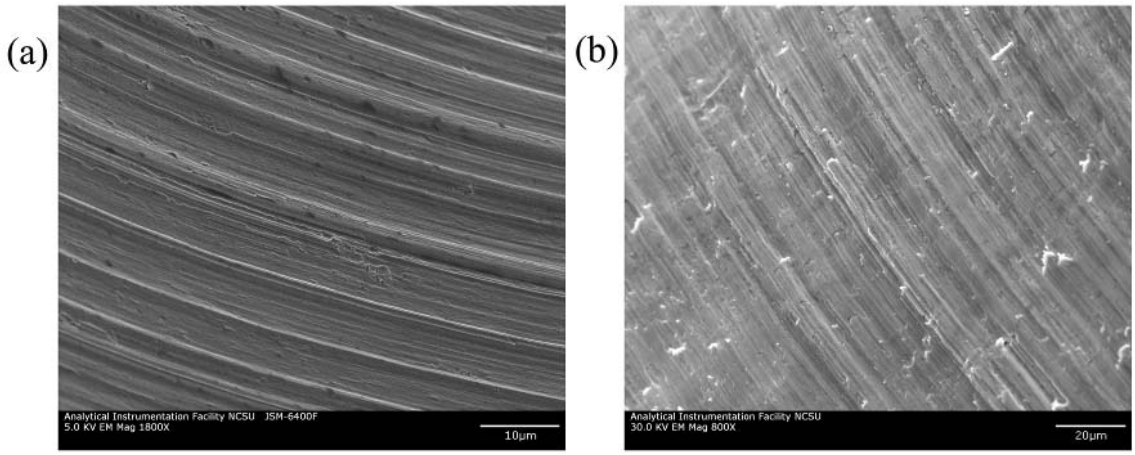

Figure 7. SEM image of cutting chips from cutting (a) 100 m 6061 Al using a new tool and (b) 20 m 1215 steel using a worn tool.

5.2.3 ORTHOGONAL CUTTING ON 6061 AL, 1215 STEEL AND 416 STAINLESS STEEL

Orthogonal machining of 6061 Al, 1215 steel and 416 stainless steel were performed on the ASG2500 diamond turning machine. Conditions for the three cutting experiments were similar. The average cutting speed was 2.8 m/s for 6061 Al and 2.13 m/s for 1215 steel. Two cutting speeds of 1.06 m/s and 2.13 m/s were used for 416 stainless steel. The depth of cut was 2 μm for 6061 Al and 1 μm for both 1215 steel and 416 stainless steel, respectively. Four 6061 Al disks with the total of 10 km cutting distance were machined to study the gradual abrasive wear. For 1215 steel, a total cutting distance was only 20 m in 5 m increments. For the two cutting experiments on 416 stainless steel, total cutting distance was 90 m and 85 m. The width of the disk for 6061 Al, 1215 steel and 416 stainless steel were 0.81 mm, 1.2 mm and 1 mm, respectively. The same single crystal diamond tools (flat nose with 6° clearance angle supplied by Chardon Tool) were used in the cutting experiments but were relapped between experiments. The diamond tool was measured using the EBID method after each test. The edge radius of the new sharpened diamond tool for cutting 6061 Al, 1215 steel, 2.13 m/s 416 stainless steel and 1.06 m/s 416 stainless steel, determined from EBID measurement, are 25, 23, 20 and 16 nm, respectively. All cutting experiments were done with Mobilmet cutting fluid and compressed air to remove chips. The diamond tool wear were measured using the EBID method and the white light interferometer. Cutting chips were observed in the SEM and an optical microscope.

Wear Result from EBID

Table 2. Worn data determined by EBID for cutting 6061 Al and 1215 steel.

Cutting distance	Edge radius (nm)	Wear land (μm)	Worn area(μm^2)	Disk width (mm)	Worn volume (μm^3)
St_5m	74	0.61	0.09	1.20	108
St_10m	94	0.53	0.09*		108
St_15m	105	0.87	0.16		192
St_20m	130	0.88	0.19		228
Al_2.5 km	142	1.20	0.19	0.81	153.9
Al_5 km	168	1.96	0.34		275.4
Al_7.5 km	297	2.99	0.48		388.8
Al_10 km	299	4.45	0.63		510.3
*worn profile of steel for 10 m cutting distance looks the same as 5 m.					

Wear results for cutting 6061 Al, 1215 steel and 416 stainless steel measured by EBID are shown in Figures 8-11 with a summary the 6061 Al and 1215 steel results determined from the EBID measurement in Table 2.. Wear profiles are drawn directly from the EBID lines after stretching the SEM images to display the tool cross section. The worn area of the cross section, edge radius

and wear land are obtained by processing the digital SEM image in Matlab. The unworn tool edge geometry formed by two straight lines along the rake face and flank faces was obtained as the base line. Then the base line was transferred to the worn tool image. The deviation from the base line is used to describe the flank wear land and to fit a circle to evaluate the edge radius. An example of the EBID images and analysis in Matlab are shown in Figure 8(a)-(e). The worn volume is estimated as the product of worn area and disk width.

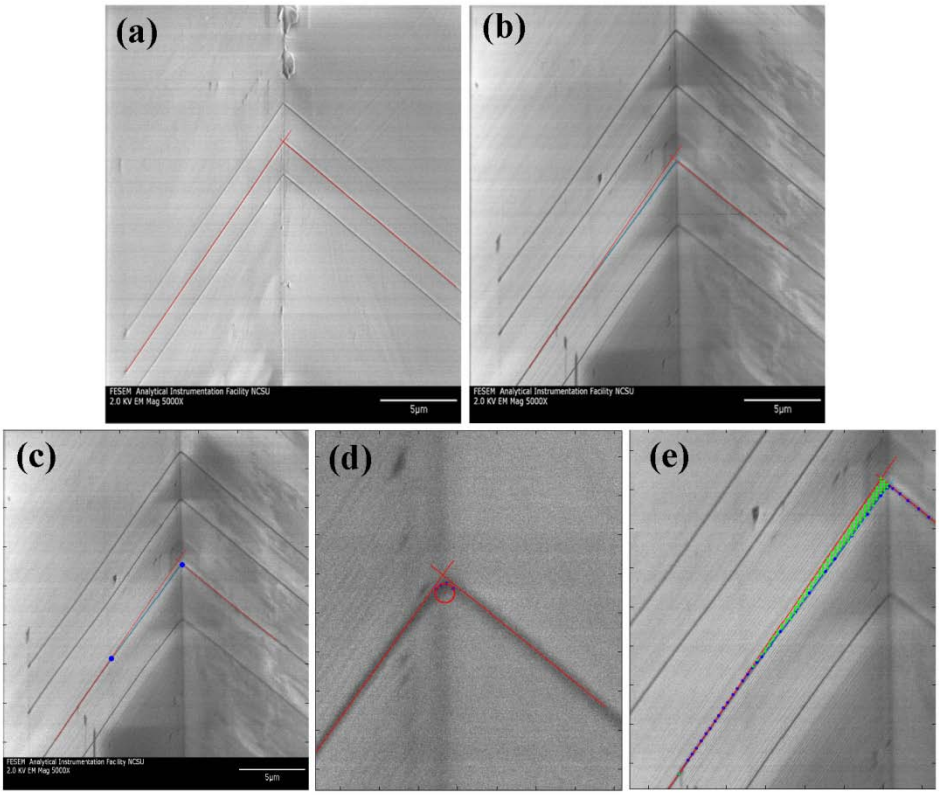

Figure 8. EBID images of tool wear after 4 m cutting of 416 stainless steel at the cutting speed of 1.06 m/s. EBID lines measured at the unworn tool edge area (a) and at the center of the worn diamond tool edge (b); Matlab analysis results of the wear land (c), edge radius (d) and worn area (e).

From the EBID images of tool wear, it can be seen that wear patterns are different for 6061 Al, 1215 steel and 416 stainless steel. Figure 9 shows the worn profile of diamond tool cutting 6061 Al. The cutting edge gets rounder and the wear land gradually increased with cutting distance. The angle between wear land and flank face is about 2°. The worn profile for 1215 steel is much different as shown in Figure 10. A wear land, 25° away from the flank face , is formed after 5 m of cutting. Gradual retracted wear lands are parallel to each other. The worn pattern for 416 stainless steel (Figure 11) is similar to that for 6061 Al except a much longer wear land, which forms a 2° angle with the flank face.

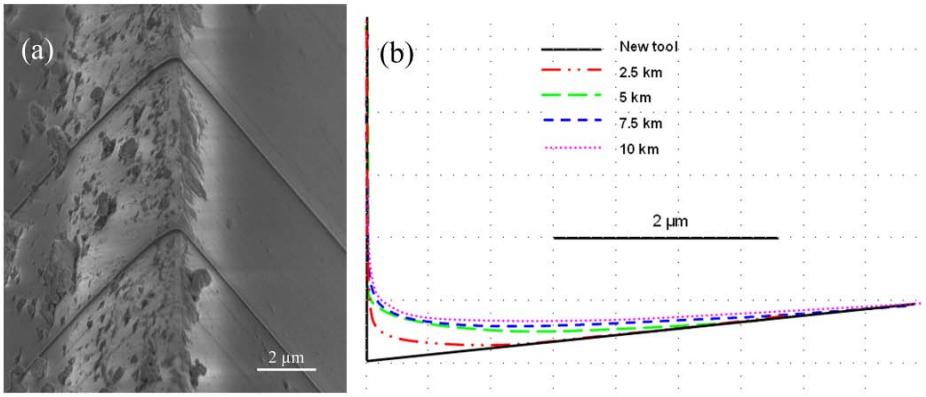

Figure 9. Wear result for cutting 6061 Al. (a) EBID lines on a worn diamond tool after cutting 7.5 km 6061 Al; (b) wear profiles of diamond cutting edge for cutting 6061 Al.

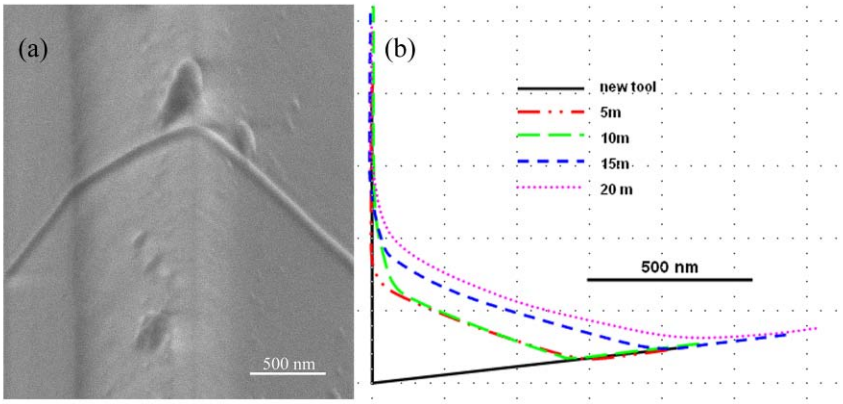

Figure 10. Wear result for cutting 1215 steel. (a) EBID lines on a worn diamond tool after cutting 15 m 1215 steel; (b) wear profiles of diamond cutting 1215 steel.

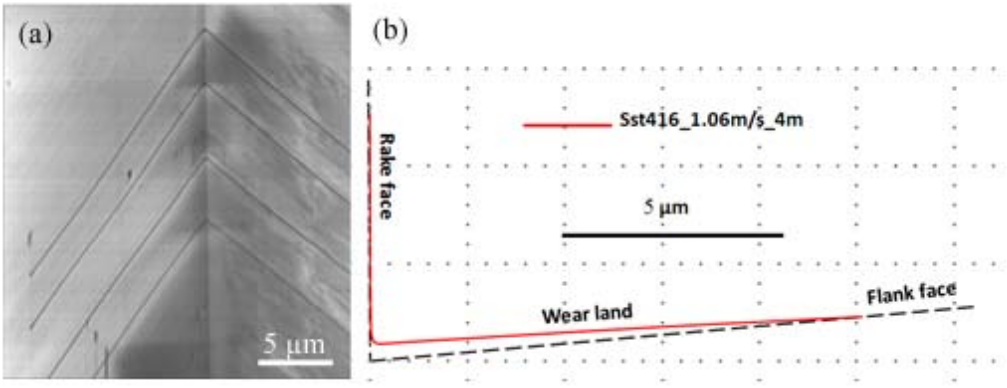

Figure 11. Wear result for cutting 416 stainless steel. (a) EBID lines on a worn diamond tool after cutting 4 m 416 stainless steel; (b) wear profiles of diamond cutting 416 stainless steel.

Detailed SEM images of flank face (Figure 12) for diamond tool cutting 416 stainless steel show grooves on the wear land of the flank face and grooving increases with cutting distance. Compared with diamond tool machining 6061 Al, the diamond tool used to machine 1215 steel and 416 stainless steel are worn significantly after only several meters.

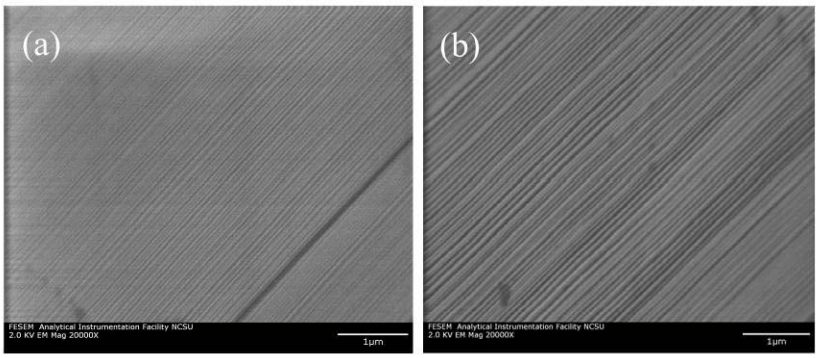

Figure 12. SEM images showing grooves on the flank face of diamond tool after 4 m at 1.06 m/s (a) and 85 m at 2.13 m/s (b) cutting 416 stainless steel.

Wear Results using Scanning White Light Interferometery

EBID is an effective way to measure the tool wear profile especially at high magnification. However, it requires that the diamond tool surface be clean enough to control the deposition rate and to resolve EBID lines. Moreover, the operation process and the following analysis are time-consuming. To measure the tool wear more efficiently, scanning white light interferometry was used for the wear land length measurement for 416 stainless steel cutting after the wear pattern of the diamond tool was determined by EBID. For the interferometer measurement, wear area can be tracked easily through the change of interference fringes. Figure 13 is an example of wear land length measurement using white light interferometer.

While the length of the wear land can be measured in the SWLI, the technique of following the tool edges in the EBID images (Figures 9-11) to determine the wear area cannot be used because the angular range is too small. To allow useful information to be generated from the SWLI measurements, a calibration technique has been developed to match the EBID and SWLI measurements. This technique assumes that there is a fixed relationship between the wear land length and the worn volume. Based on data from EBID measurements for tools used to machine 6061 Al and 416 stainless steel (see Table 3), a calibration curve (Figure 14) has been constructed. This figure (and equation for the linear fit) can be used to estimate the worn area based on the wear land length. Worn volume is then determined as a product of worn area and workpiece width, which is 1 mm for the 416 stainless steel disk.

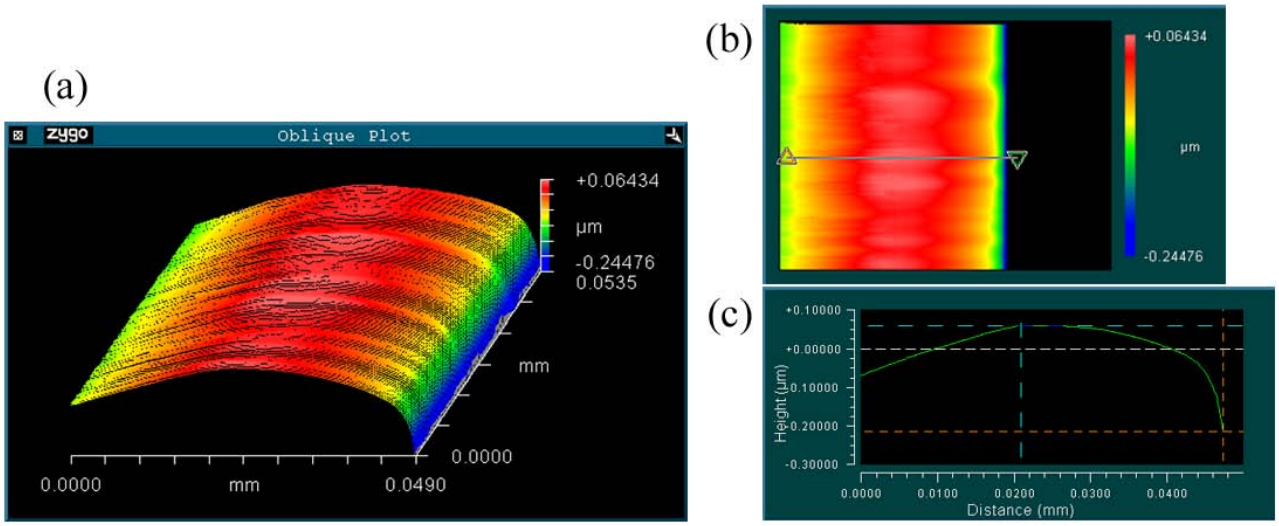

Figure 13. Wear land of the diamond tool after cutting 45 m 416 stainlesss steel at 2.13 m/s measured using white light interferometer. (a) oblique plot; (b) surface profile; (c) wear land length measurement.

Table 3. Relationship between wear land length and worn area determined from EBID results.

	Cutting distance	**wear land (µm)**	**worn area ($µm^2$)**
sst416_2.13 m/s	5 m	2.05	0.12
	10 m	7.68	1.11
	15 m	9.69	3.31
sst416_1.06 m/s	4 m_position1	11.01	2.92
	4 m_position2	14.51	4.00
Al6061_2.8 m/s	2.5 km	1.71	0.11
	5 km	2.35	0.33
	7.5 km	3.79	0.54
	10 km	4.19	1.04

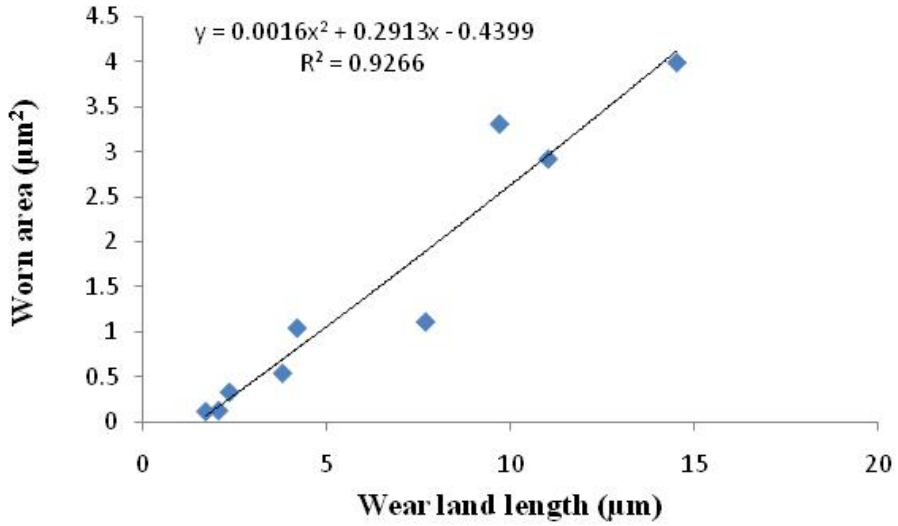

Figure 14. Fitting curve for wear land length and worn area measured from EBID.

Figure 15 and 16 are the summary of the tool wear results for cutting 416 stainless steel at 1.06 m/s and 2.13 m/s, respectively. It can be seen that wear land length and the worn area increased gradually with the cutting distance. However, the wear length increased quickly at the beginning. After 5 cuts, the wear land length increased more gradually.

Cutting distance (m)	Actual distance (m)	Wear land (µm)	Worn area (µm²)
2	0	0	0.00
4	2	10.87	2.92
8	6	12.25	3.37
12	10	14.93	4.27
16	14	17.22	5.05
20	18	18.62	5.54
30	28	19.68	5.91
40	38	20.93	6.36
50	48	22.54	6.94
70	68	26.48	8.40
90	88	29.56	9.57

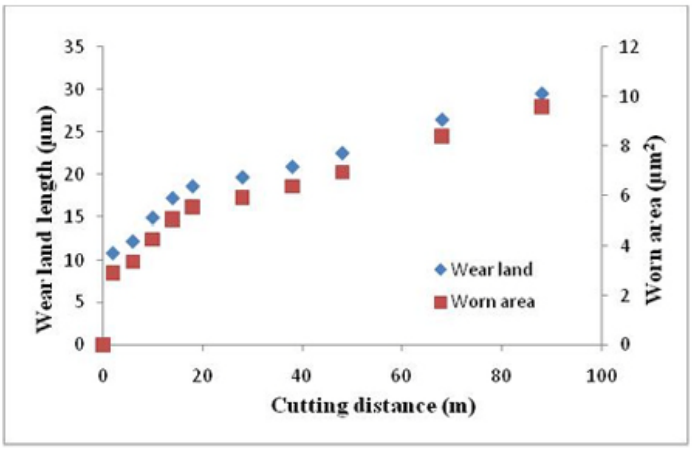

Figure 15. Summary of tool wear results cutting 416 stainless steel at 1.06 m/s.

Cut distance (m)	Actual distance (m)	Wear land (μm)	Worn area (μm²)
10	5	7.68	1.97
15	10	9.69	2.55
25	20	15.56	4.51
35	30	20.53	6.25
45	40	23.37	7.28
55	50	26.63	8.5
65	60	28.61	9.26
85	80	29.47	9.59

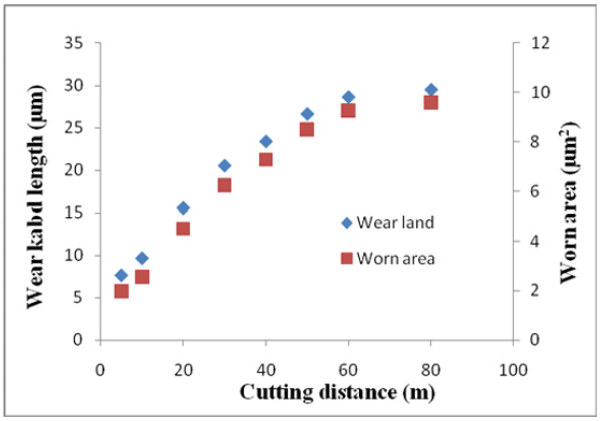

Figure 16. Summary of tool wear results of cutting 416 stainless steel at 2.13 m/s.

Wear Rate Comparison

After the worn area and worn volume was determined, the wear rate was calculated as volume lost divided by contact time. For both 1.06 m/s and 2.13 /s cutting on 416 stainless steel, only the first five data points are used to calculate the wear rate. Figure 17 is the wear rate comparison for three different workpieces. The wear rate for 416 stainless steel is 18 times higher than that of 1215 steel and 2558 times higher than that of 6061 Al. The wear rate for 2.13 m/s and 1.06 m/s for cutting 416 stainless steel are at the same order, except the 2.13 m/s cutting has a slightly higher wear rate - 1.8 times higher than at 1.06 m/s. Compared with 6061 Al, the cutting distance for 1215 steel and 416 stainless steel are very short, so the worn volume caused by the abrasive wear can be ignored. The high wear rate can be thought due to the thermal-chemical effect.

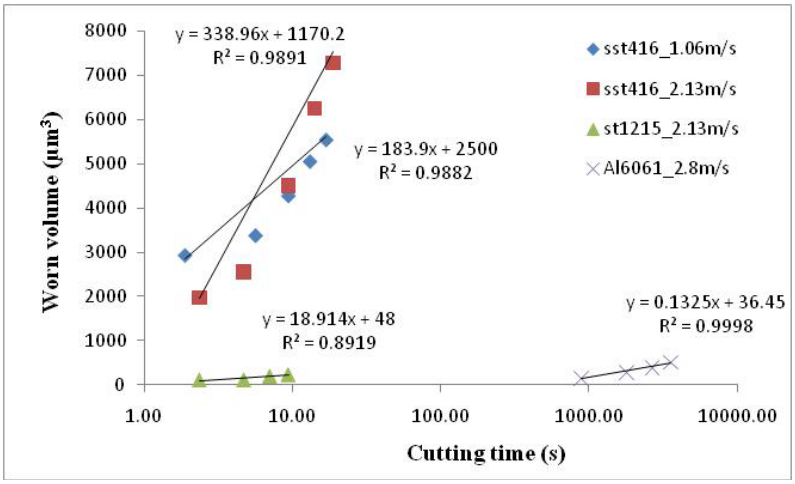

Figure 17. Wear rate comparison for cutting different workpiece materials.

Tool Forces for Cutting 416 Stainless Steel

Forces results show that tool forces changed significantly during machining the 416 stainless steel. The thrust force and cutting force were stable only for a relatively short cutting distances. Figure18 and 19 are selected tool forces plots for 2.13 m/s and 1.06 m/s cutting. For the first 0-5 m cutting at the speed of 2.13 m/s, there is a gradual increase in both thrust force and cutting force (Figure 18(a)). This is due to the increased cutting width which is a result of the misalignment of the workpiece and the diamond tool[1]. The thrust force and cutting force reached the steady state during the following cutting until to 35 m (Figure 18(b) and 18(c)). After 35 m, the cutting process became unstable. Figure 18(d) shows that the thrust force and cutting force changed periodically. The thrust force decreased while at the same time the cutting force increased. It appears that the tool does not cut but only rubs the workpiece intermittently. From SEM observations, chip build-up was found on the rake face. This build-up time is short as shown in the measurements. The built-up edge increases the force because the steel is transferred to the tool and becomes the cutting edge but is not sharp. This built-up edge finally breaks off and the diamond tool begins to cut the workpiece again. The thrust force becomes very large (big contact area and little cutting) until the tool does cutting again and thick chips are generated. For cutting at 1.06 m/s, the forces changed in a similar way as 2.13 m/s, except that the steady state cutting process was reduced to a shorter cutting distance (Figure 19(a)-(d)).

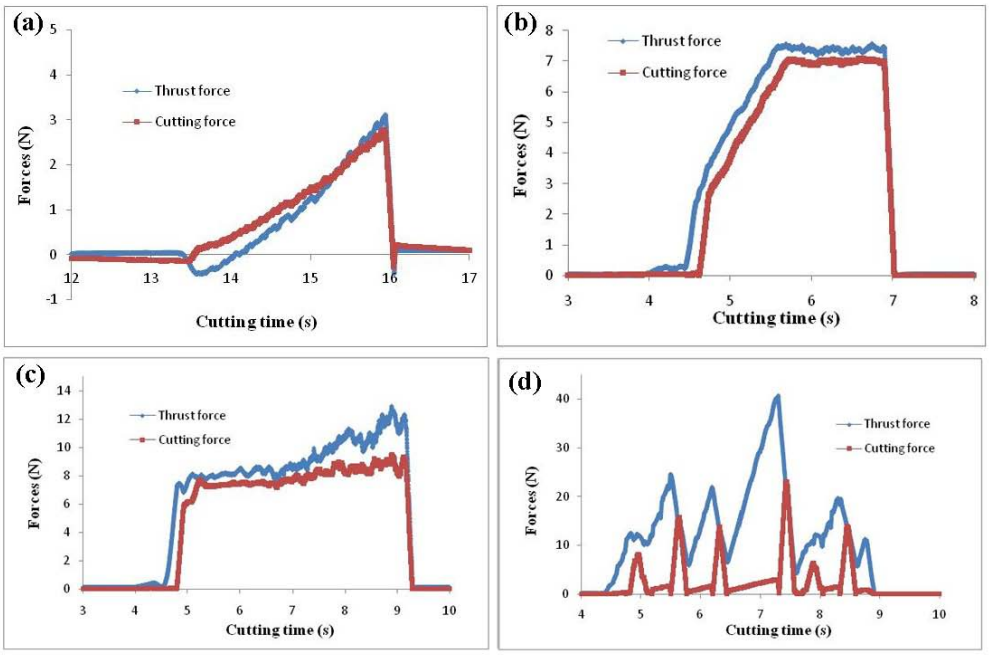

Figure 18. Tool forces at 2.13 m/s cutting 416 stainless steel for 0-5 m (a), 10-15 m (b), 15-25 m (c), 35-45 m (d) cutting distance.

[1] The flat tool is not exactly parallel to the workpiece face at the start of the experiments. As the depth increases, the tool cuts across the workpiece width and the change in width accounts for the initial increase in force.

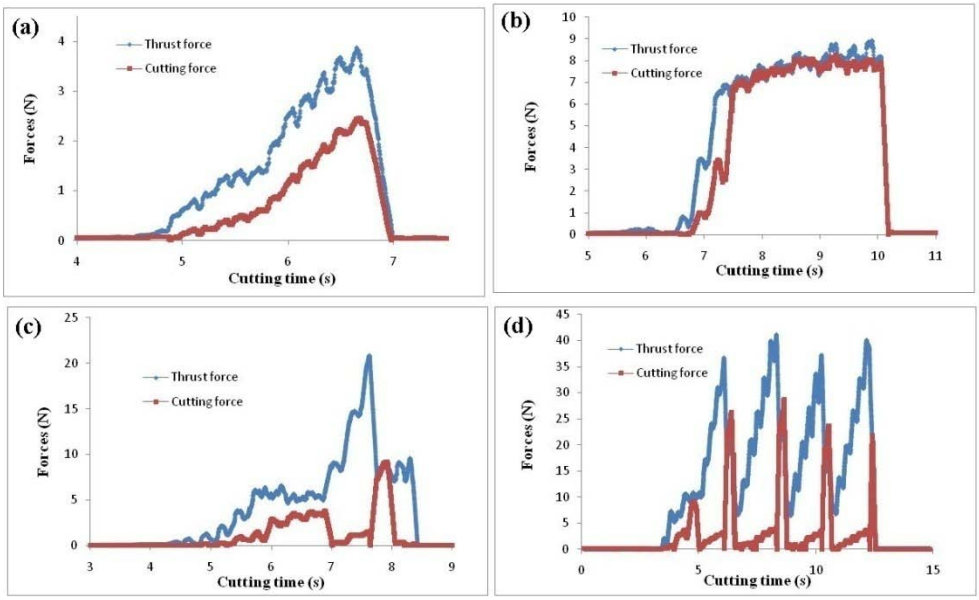

Figure 19. Tool forces at 1.06 m/s cutting 416 stainless steel for 0-2 m (a), 4-8 m (b), 16-20 m (c), 20-30 m (d) cutting distance.

Cutting Chips collected for 416 Stainless Steel

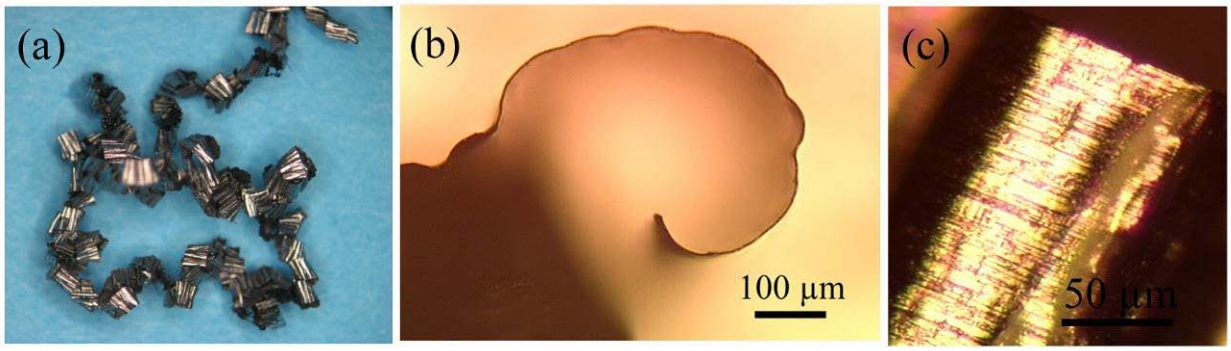

Figure 20. Cutting chips from 15-25 m cutting 416 stainless steel at 2.13 m/s. (a) lower magnification image showing long continuous chips; (b) higher magnification image (80x) showing chip thickness; (c) image at 250x showing features on the chip surface of shiny side.

Thickness and surface feature of the cutting chips changed a lot during the cutting process of 416 stainless steel. Figure 20 shows some optical images of cutting chips from 15-25 m cutting at 2.13 m/s, while Figure 21 are the images of 35-45m cutting at the same cutting speed. Long and continuous chips are generated during 15-25 m cutting. The thickness of the chip is about 3 µm. Small grooves are observed on the shiny side which contact the rake face of the cutting tool. For

35-45 m cutting, the chips are getting thicker. Figure 21(a) shows chips with different thickness. The thickness of the thickest chip is about 13 μm. It also can be seen that the grooves on the surface are getting deeper and wider. More flaws are found, indicating the increased roughness of machined surface. The depth of cut was 1 μm in all cases.

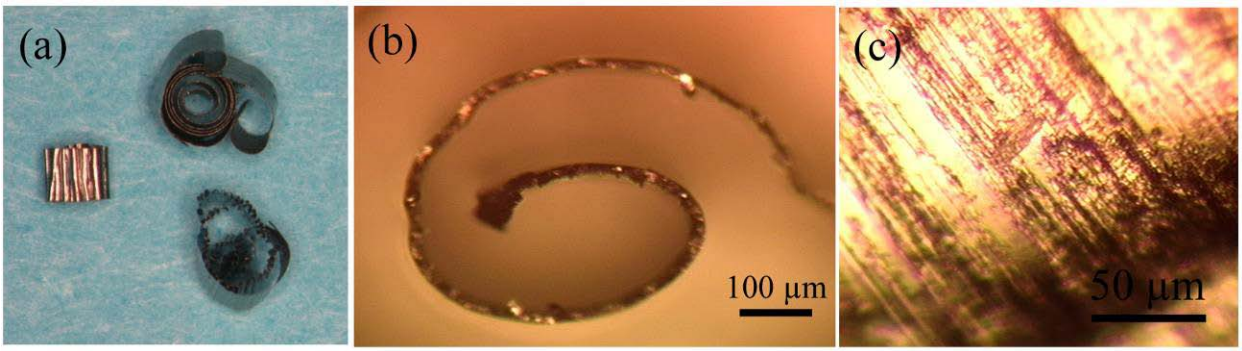

Figure 21. Cutting chips from 35-45 m cutting 416 stainless steel at 2.13 m/s. (a) lower magnification image showing three kinds of chips with different thickness; (b) higher magnification image (80x) showing the thickness of the thickest chip; (c) image at 250x showing features on the chip surface of shiny side.

5.3 CONCLUSIONS

A study of thermo-chemical wear of diamond tools while machining ferrous material is described. 1215 steel and 416 stainless steel were selected as the target materials to address chemical wear phenomenon. To separate the abrasive wear effect, 6061 Al with comparable hardness is selected as the baseline material. Microstructures of the two workpiece materials show that 6061 Al has more and larger hard particles than 1215 steel and 416 stainless steel. Since hard particles are the main reason for the abrasive wear, 6061 Al is expected to cause comparable or more abrasive wear on diamond tool than 1215 steel and 416 stainless steel. From the quantitative measurement obtained using EBID, gradual wear profiles can be drawn from the EBID images directly. The tool wear pattern for cutting 416 stainless steel is similar to that for 6061 Al, while 1215 steel has a different worn profile. The wear rate of a diamond tool cutting 416 stainless steel is about three orders higher than that for cutting 6061 Al and 18 times higher than that for 1215 steel under similar cutting conditions. For cutting experiments on 416 stainless steel, tool forces and cutting chip images indicate that steady state cutting can only last for short cutting distances. After a few tens of meters, the cutting process becomes unstable and the diamond tool plows and rubs on the workpiece surface. This is attributed to an adhesive layer formed on the rake face. In the future work, slower speed cutting on 416 stainless steel and 1215 steel will be done to further study the wear process.

REFERENCES

1. Thornton AG, Wilks J. *Clean surface reactions between diamond and steel*. Nature, 274: 792-793 (1978).
2. Moriwaki T, Shamoto E. *Ultraprecision diamond turning of stainless steel by applying ultrasonic vibration*. Annals of the CIRP, 40: 559-562 (1991).
3. Song YC, Nezu K, Park C, Moriwaki T. *Tool wear control in single-crystal diamond cutting of steel by using the ultra-intermittent cutting method*. International Journal of Machine Tools & Manufacture 49: 339-343 (2009).
4. Komanduri R, Shaw MC. *Wear of synthetic diamond when grinding ferrous metals*. Nature, 255: 211-213 (1975).
5. Komanduri R, Shaw MC. *On the diffusion wear of diamond in grinding pure iron*. Phil. Mag. 34: 195-204 (1976).
6. Ikawa N, Tanaka T. *Thermal aspects of wear of diamond grain in grinding*. Ann. CIRP. 19:153-157 (1971).
7. Shimada S, Tanaka H, Higuchi M, Yamaguchi T, Honda S, Obata K. *Thermo-chemical wear mechanism of diamond tool in machining of ferrous metals*. Ann. CIRP. 53:57-60 (2004).
8. Thornton AG, Wilks J. *Tool wear and solid state reactions during machining*. Wear, 53:165-187 (1979).
9. Thornton AG, Wilks J. *Factors affecting chemical wear during machining*. Wear, 93:63-80 (1984).
10. Paul E, Evans CJ, Mangamelli A, McGlauflin ML, Polvani RS. *Chemical aspects of tool wear in single point diamond turning*. Prec. Eng. 18: 4-19 (1996).
11. Narulkar R, Bukkapatnam S, Raff LM, Komanduri R. *Molecular dynamics simulations of diffusion of carbon into iron*. Phil. Mag. 88: 1259-1275 (2008).
12. Narulkar R, Bukkapatnam S, Raff LM, Komanduri R. *Graphitization as a precursor to wear of diamond in machining pure iron: A molecular dynamics investigation*. Computational Materials Science, 45: 358-366 (2009).
13. Machining of Stainless Steels. ASM handbook, Volume 16, ASM International (1992).
14. Kovach CW, Sulfide inclusions and the machinability of steel, sulfide inclusions in steel, American Society for Metals, 459-479 (1975).
15. Akasawa T, Sakurai H, Nakamura M, Tanaka T, Takano K. *Effects of free-cutting additives on the machinability of austenitic stainless steels*. Journal of Materials Processing Technology 143-144: 66-71 (2003).
16. http://www.matweb.com.
17. Stainless steel for machining. http://www.ssina.com/publications/machine.html.

6 INTEGRATED PRESCAN OPTICS FOR LASER PRINTERS

Alex Sohn
Research Assistant
Kenneth P. Garrard
Senior Research Associate
Precision Engineering Center

The design of a reflective optical system for a laser prescan unit has been completed. The optical system can be machined from a single piece eliminating the need to assemble and align the two mirrors. However the optical surfaces in their final orientation are not rotationally symmetric about any axis. A plan for machining a prototype of this optical system using a fast tool servo has been developed. The tool path has been developed for fabricating it on the ASG 2500 Diamond Turning Machine augmented with a long-range piezoelectric long-range fast tool servo (Variform) driven by a dSPACE controller.

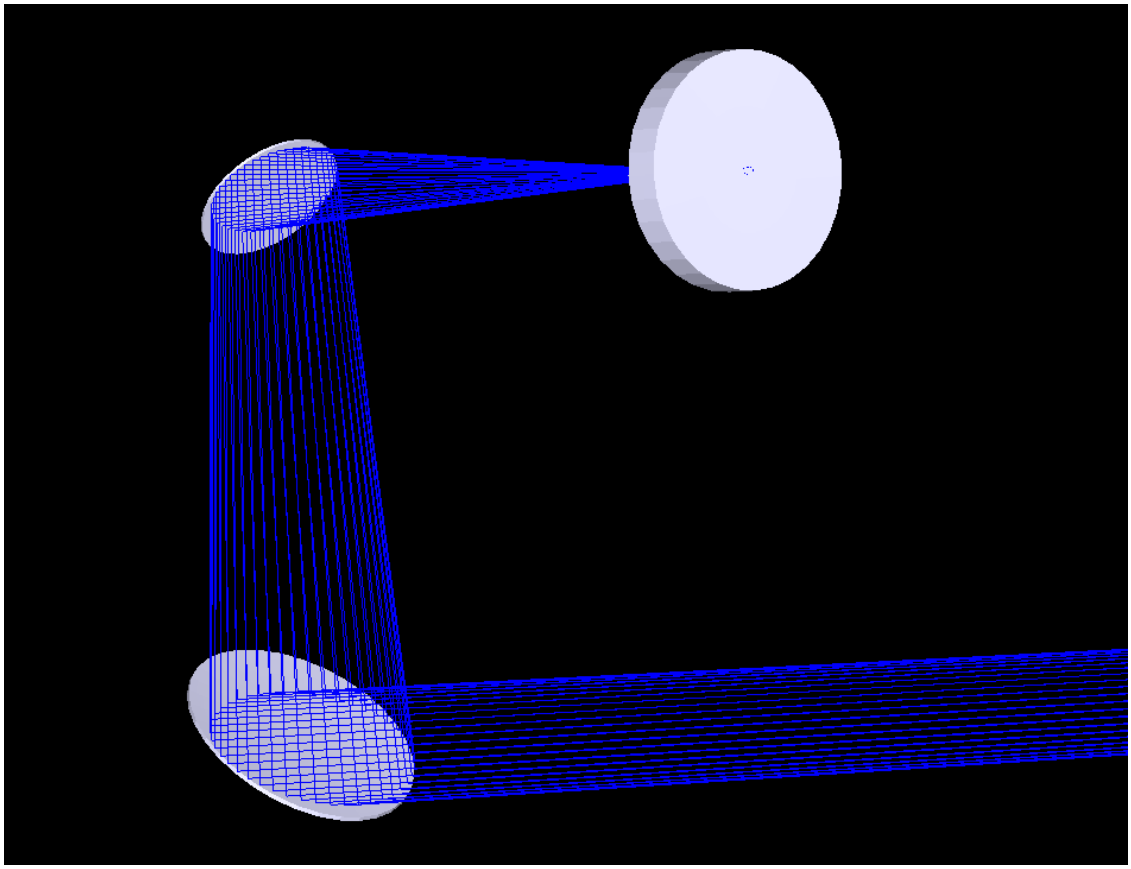

6.1 INTRODUCTION

In the manufacture of laser print engines, one of the costliest and most challenging subsystems are the prescan optics. This group of components illustrated in Figure 1 conditions the laser beam from the exit aperture of a small diode laser and allows it to be directed to the surface of the paper and focused to a spot size as small as 10 μm. Typically, the prescan optics consists of the laser diode, a collimating lens to bring the laser beam as close as possible to collimated and a cylindrical lens to remove the astigmatism from the nearly collimated beam. The optics and their alignment add a significant cost to the final product, so the goal is to simplify the design and use materials that are less expensive to procure and manufacture

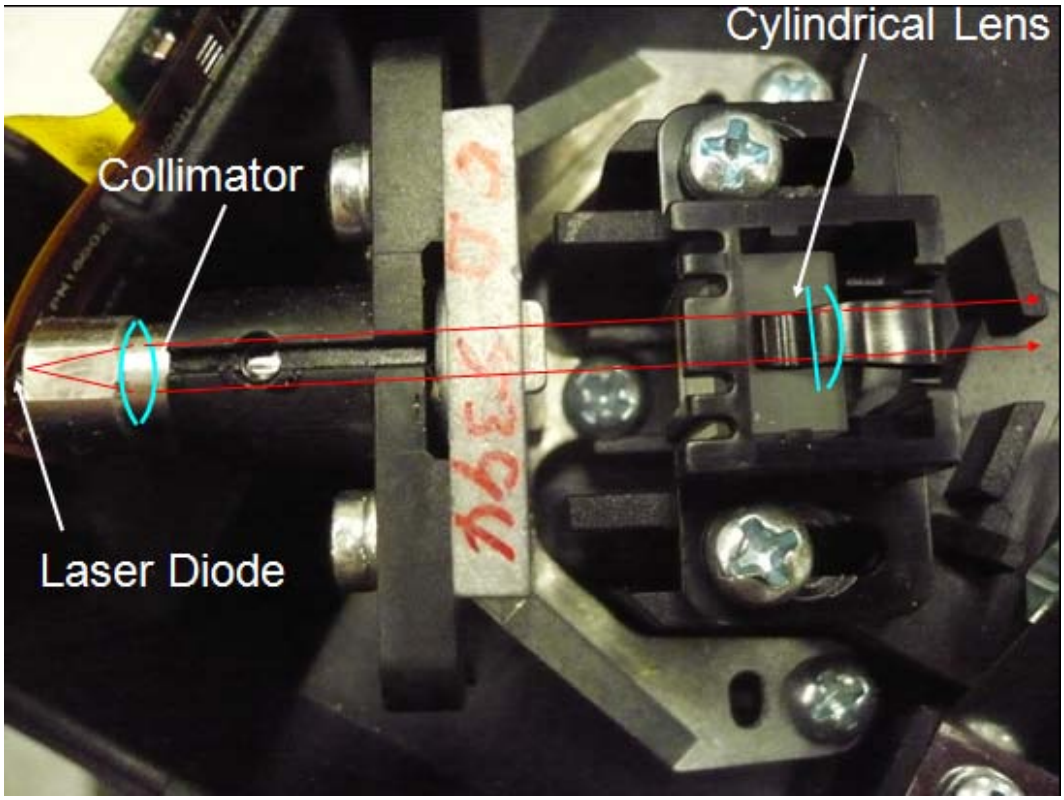

Figure 1. Commercial laser prescan system layout.

6.2 OPTICAL SYSTEM DESIGN

Figure 2 shows the conventional system of Figure 1 in a schematic form. The collimating lens and the cylindrical lens are commonly made of optical glass and must be ground and polished. Cheaper polymer lenses cannot be used due mainly to the change in refractive index in the material with temperature. The printer must operate in an environment with a wide temperature range.

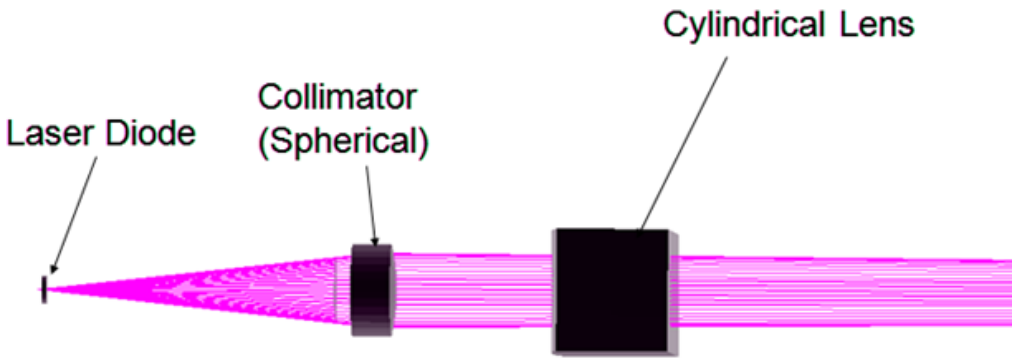

Figure 2. Conventional prescan lens design.

If the lenses shown in Figure 2 are replaced with reflective optics, the refractive index of the material becomes irrelevant. Thus, molding polymer reflectors becomes a distinct possibility. One possible layout for such a design using reflective optics is shown in Figure 3.

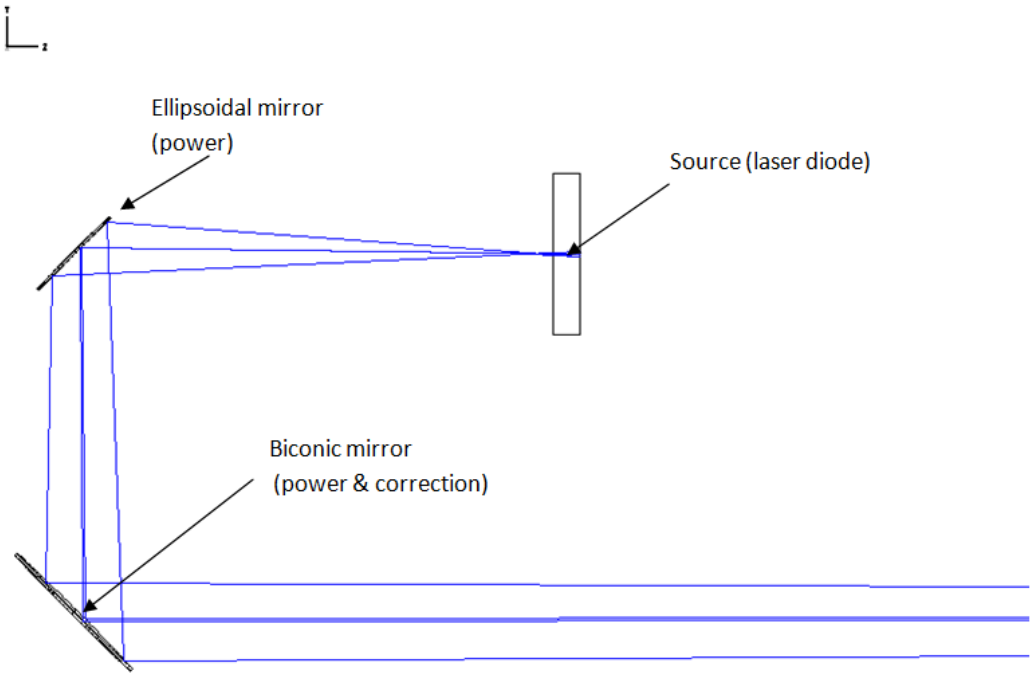

Figure 3. Two mirror reflective design.

The primary mirror is an ellipsoid that removes most of the divergence from the beam while the secondary mirror removes whatever divergence remains as well as the aberrations due both to

laser diode astigmatism and the off-axis placement of the primary mirror. Thus, the secondary mirror is biconic.

As a prototype, both mirrors will be machined into the end of a small cylinder using a fast tool servo (FTS). As shown in Figure 4, the mirrors have a substantially larger radius than the radius of rotation and appear almost as two flat surfaces in a spherical parent surface. The cross section in Figure 4 shows the spacing of the mirrors and the laser source.

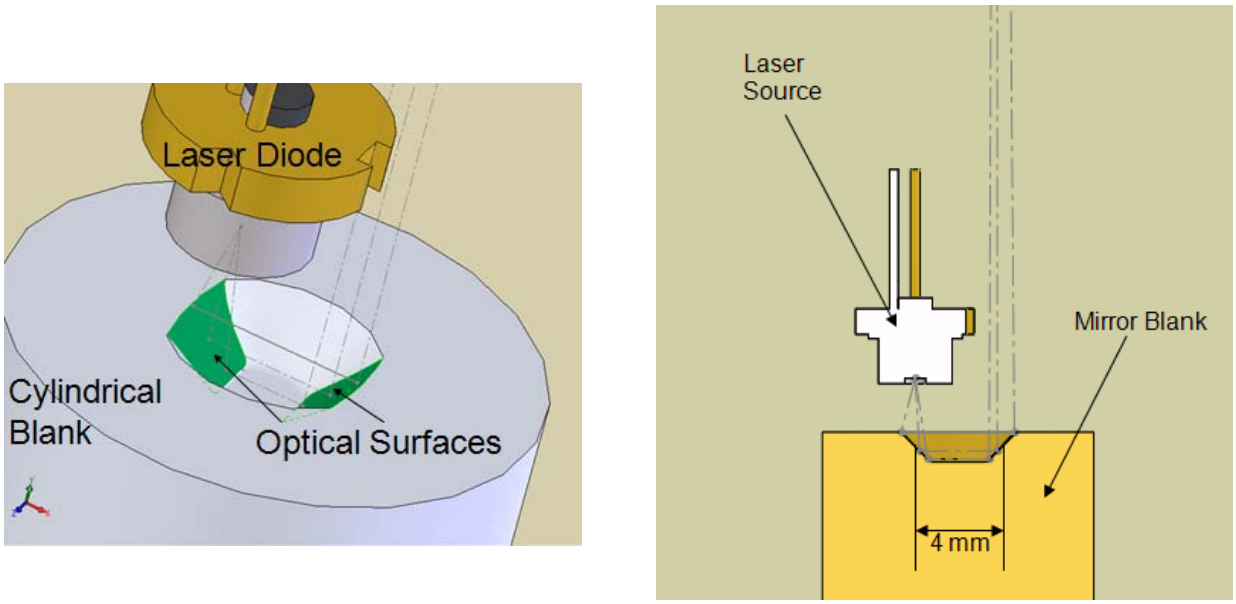

Figure 4. Solid model of mirror surfaces and beam path and a cross section of the system..

6.3 PROTOTYPE FABRICATION

Both optical surfaces can be machined in a single setup on a metal substrate, guaranteeing the alignment of the two mirrors. As shown in Figure 6, the volume of material to be removed is quite small and the prototype can be fabricated without rough machining a spherical pocket or slot prior to performing the final machining operation. Machining time will be on the order of a few minutes. The diamond tool must be selected to reach into the pocket and machine the non-rotationally surface without touching the clearance

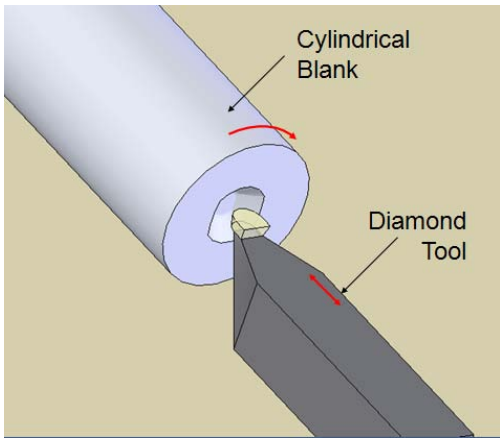

Figure 5. Machining Layout

face of the tool

6.3.1 GEOMETRIC ANALYSIS

Each mirror can be defined as a general biconic in Cartesian coordinates with Equation (1),

$$Z(x,y) = \frac{c_{XZ}\cdot(y-y_0)^2 + c_{YZ}\cdot(y-y_0)^2}{1+\sqrt{1-(1+k_{XZ})\cdot(x-x_0)^2\cdot c_{XZ}^2-(1+k_{YZ})\cdot(y-y_0)^2\cdot c_{YZ}^2}} \quad (1)$$

where the origin is (x_0,y_0,0), c_{XZ} is the curvature in the XZ plane, c_{YZ} is the curvature in the YZ plane and k_{XZ} and k_{YZ} are the conic constants in the two orthogonal planes [1]. The prototype design parameters are given in Table 1 and the apertures and their orientation with respect to each other are defined in Table 2.

Table 1. Surface parameters for prescan optics.

	Plane	Curvature	Conic constant
M1	XZ	1/30	1
	YZ	1/30	1
M2	XZ	1/13.905686	-2.396222
	YZ	1/34.682089	-60.00092

Table 2. Aperture definition of prescan optics.

	Aperture			Translation			Tilt		
	radius	**x decenter**	**y decenter**	**x**	**y**	**z**	**x**	**y**	**z**
M1	0.572995	0	0	0	2	0	pi/4	0	0
M2	0.916568	0	0	0	-2	0	-pi/4	0	0

Both surfaces are on-axis (i.e., no decenter) and M1 is an oblate ellipsoid of revolution while M2 is a non-rotationally symmetric surface of two very different hyperboloids. These two mirrors are shown in Figure 7. They have been translated to the correct separation but not tilted. Figure 8 shows M1 and M2 after tilting the mirrors along with a wireframe plot of an annular segment of the best fit sphere whose center is constrained to lie on the z axis (i.e., the axis of rotation during machining). The chief ray at the center of each aperture is shown as a red dotted line and the center of the best fit sphere is shown as a black dot.

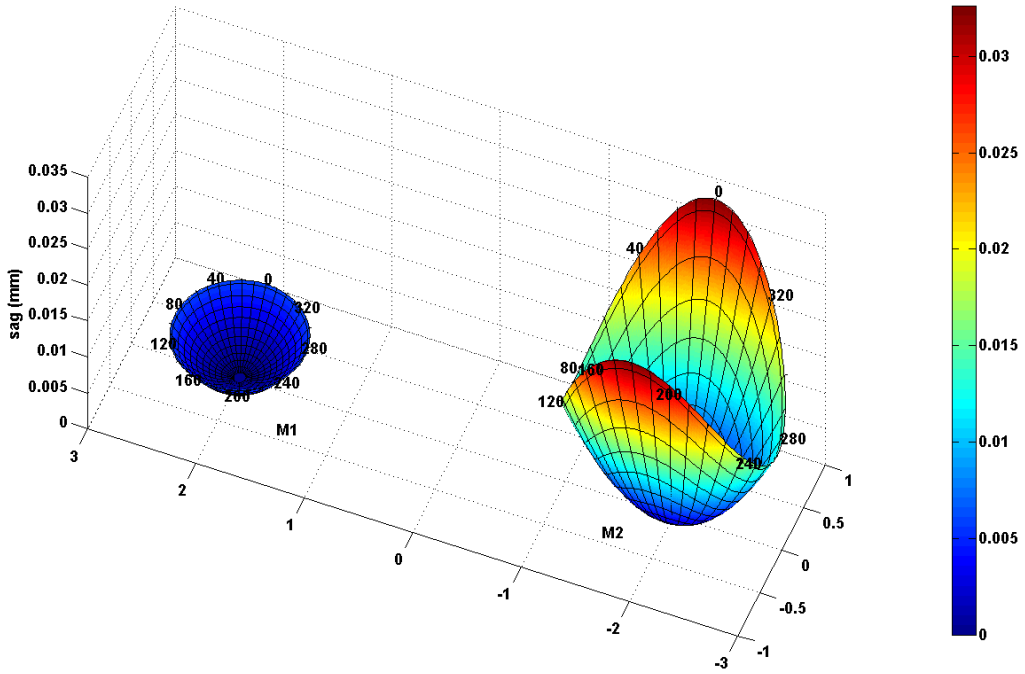

Figure 7. M1 and M2 surfaces.

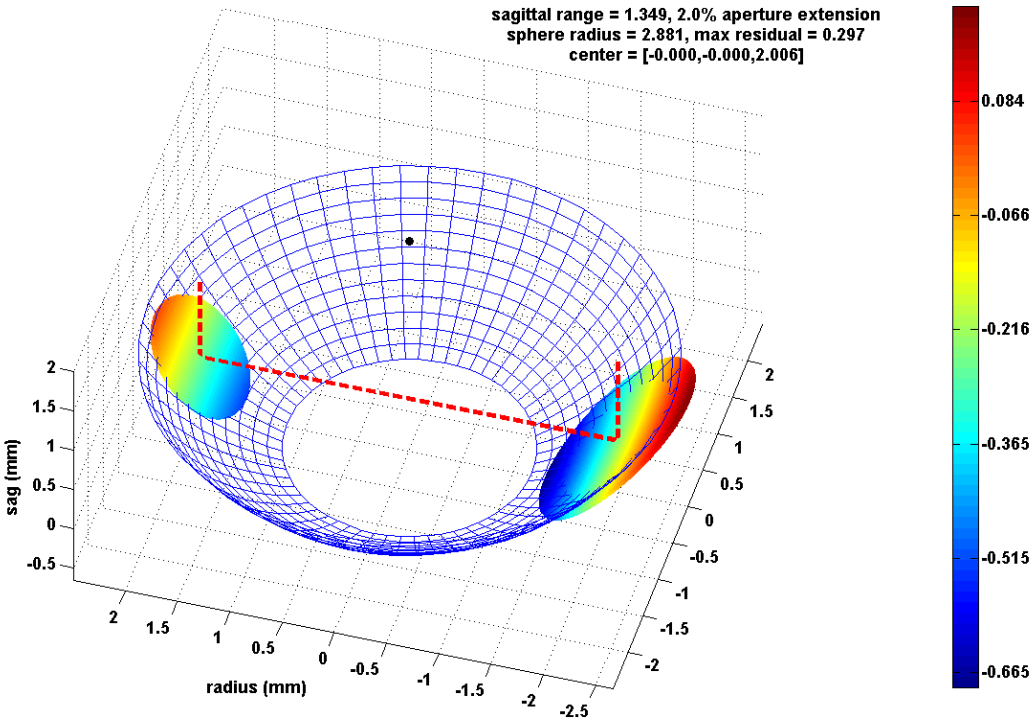

Figure 8. Laser prescan optical system

6.3.2 TOOLPATH GENERATION

The ASG 2500 diamond turning machine can be programmed to produce the spherical surface shown in Figure 8 while the Variform FTS moves the tool in the sagittal direction as a function of the spindle rotation angle and the cross-feed axis position. The FTS motion plus the underlying sphere form the desired mirror surfaces. The mirror curvatures are much smaller than that of the best-fit sphere (i.e., they are "flatter" than the sphere), thus the shape of the FTS motion within the mirror apertures will be convex. The range of servo motion required is 297 μm which is well within the 400 μm range of the Variform FTS.

Surface finish and form fidelity are likely to be improved if the range of FTS excursion is minimized. This can be done by machining an aspheric surface with the DTM. Compensation must also be made for the radius of the tool. This compensation is done along meridians from the axis of rotation to the edge of the workpiece. An asphere is then subtracted from the result to form a 2D lookup table of FTS positions as a function of radial angular position. A part program for the ASG 2500 has been created to machine the aspheric shape. A Matlab script has been developed to generate a lookup table for the dSPACE Variform controller as well as the aspheric motion program for any two surface biconic optical system. The steps in this algorithm are as follows.

1. Generate a circular aperture grid for each mirror, M1 and M2.
2. Calculate z positions for each (x, y) point within the apertures.
3. Translate and rotate the mirror surface data sets to their positions in the optical system.
4. Create a cylindrical coordinate grid for the optical system. The center of this coordinate system is along the axis of rotation of the DTM spindle.
5. Find the data points on the cylindrical grid that are within the elliptical apertures of the tilted M1 and M1 surfaces.
6. Interpolate mirror surface data to the cylindrical coordinate aperture grid.
7. Extend the aperture masks to equal radii and uniform angles.
8. Perform tool radius compensation along each meridian in each aperture.
9. Interpolate compensated points onto a common radial grid.
10. Find the mid-range sagittal value at each radius.
11. Fit a radial polynomial to the mid-range data.
12. Form a table of residuals. This is the FTS excursion.
13. Create a motion program following the cross-section of the aspheric surface.

The aperture masks for M1 and M2 in the cylindrical coordinates of the optical system are ellipses. But the FTS control system requires a matrix of data to describe the motion of the tool. Each row contains height data at a radius and each column at an angle. The rows and columns

need not be equally spaced, but the matrix must be plaid; that is, all rows (radii) have a data point for each column (angle). Thus Step (7) extends the elliptical apertures to angular segments, shown as blue shadows on the floor the plot in Figure 9. The red pole represents the spindle axis for turning the optical system and the two shaded patches are the M1 and M2 mirror surfaces. The origin of the cylindrical coordinate system is (θ=0, r=0); however this is not necessarily the optimal location for the axis of rotation. The (x, y) center of a least squares sphere fit to the system data for the prescan optics has an origin 17 µm from (0,0). In this case, the FTS excursion is reduced by only a few micrometers by including this additional translation of the mirrors. To reduce the complexity of the system analysis and machining setup the origin was fixed at (0,0).

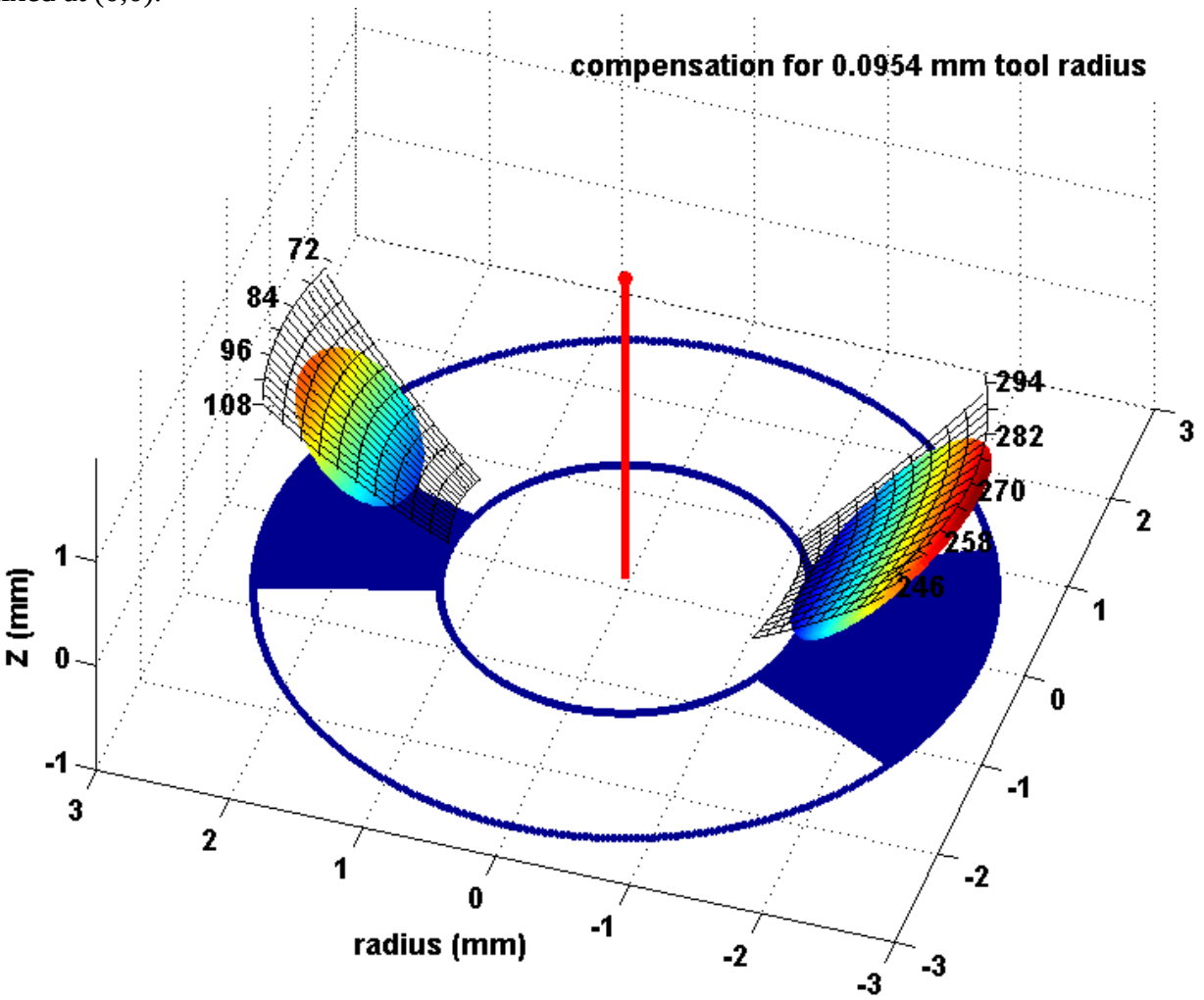

Figure 9. Optical system with tool radius compensation.

Figure 9 also shows the effect of tool radius compensation along each meridian on the cylindrical aperture grid. The wire frame overlay gives at the position of the tool center when machining each mirror. The tool radius is 95.4 µm.

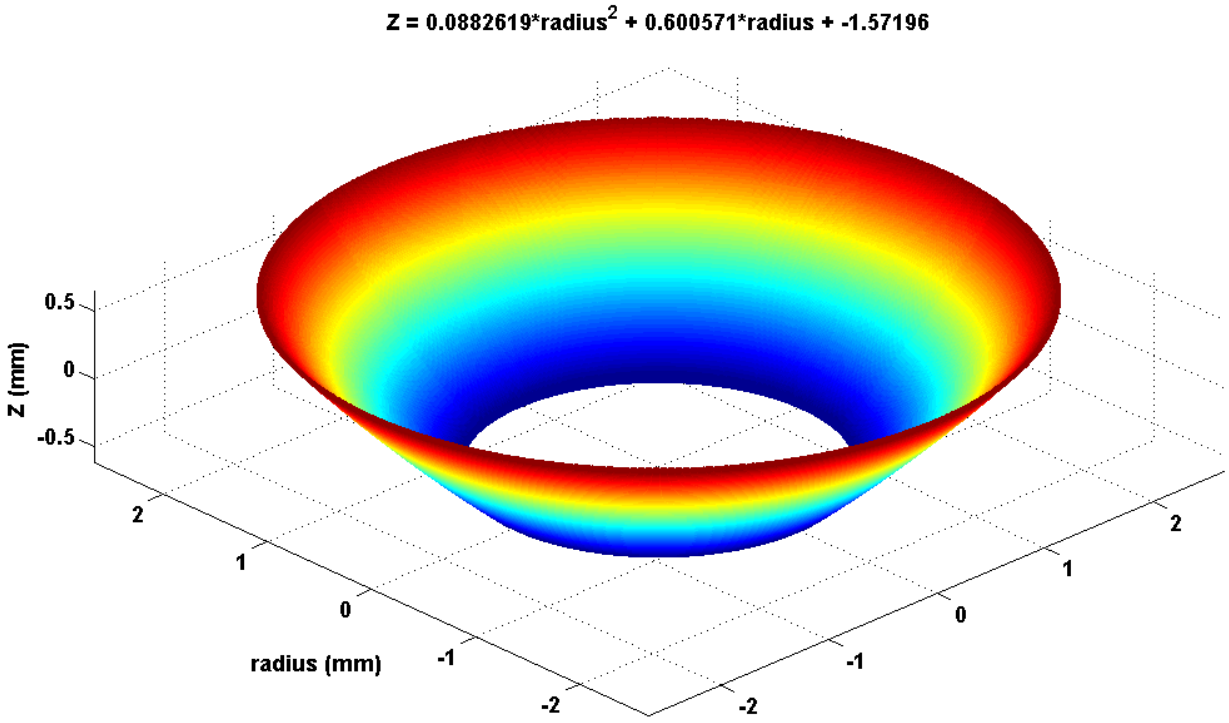

Figure 10. Best fit rotationally symmetric aspheric surface.

The majority of the z direction motion in the optical system is rotationally symmetric. The optimal rotationally symmetric asphere is defined as the surface that minimizes the FTS excursion when the part is machined. This asphere is easily formulated as a point-to-point surface by taken the average of the largest and smallest sag value at each radius over both apertures. The resulting surface is very nearly conical, but some advantage is gained by approximating it with a second order polynomial instead of a cone. This quadratic surface is shown in Figure 10.

Subtracting the best fit asphere shown in Figure 10 from the radius compensated tool positions shown in Figure 9 gives table of FTS positions for machining the optical system. These positions are on a fine cylindrical grid with a maximum spacing of 5 µm between grid points. Figure 11 shows the complete FTS tool path within the radial aperture of the mirrors. The tool positions are extended 10° to either side of each aperture so that the FTS doesn't abruptly change direction at the edge of the desired clear aperture. The space between the mirrors in the azimuthal direction is a linearly interpolated surface that will be added to the asphere swept out by the DTM axes.

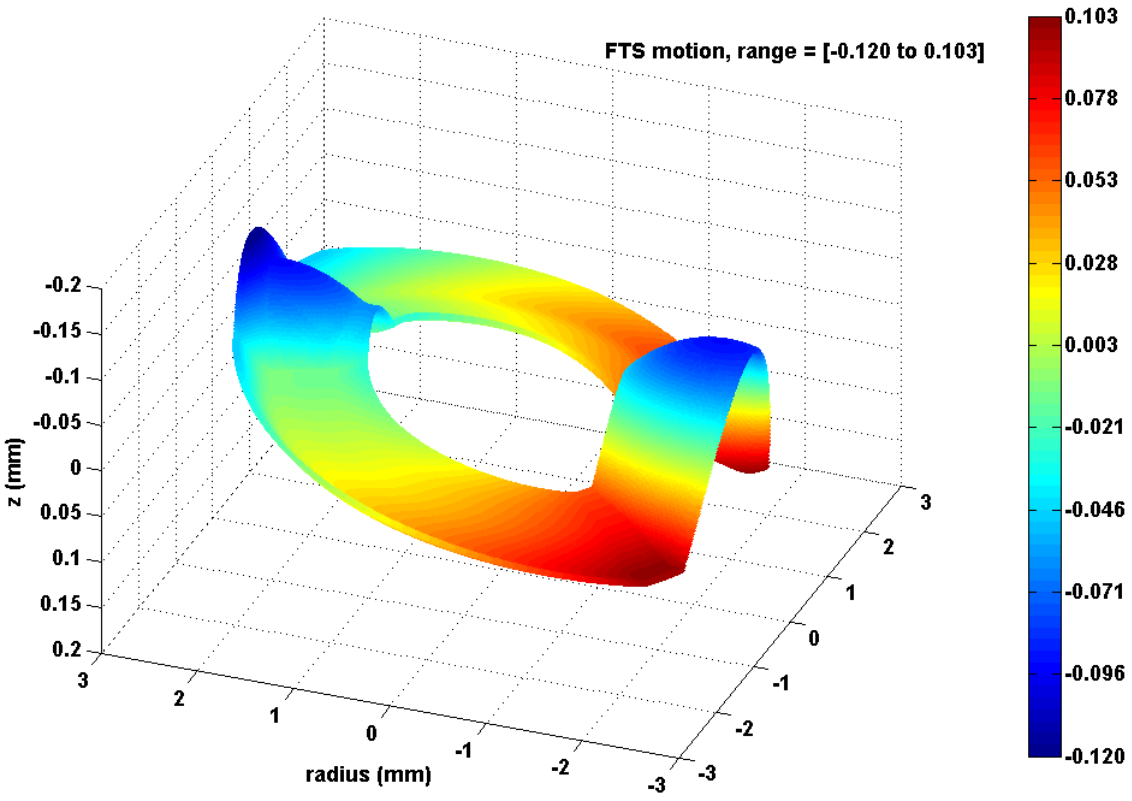

Figure 11. Variform FTS motion for monolithic prescan optics machining.

Figure 12 shows the DTM tool path for machining the prescan optics from a cylindrical blank similar to that in Figure 6. The rotationally symmetric asphere is in the area between the vertical red lines and the starting and ending point is shown as a red dot. Waypoints along the path are indicated by blue squares. Revolving this path creates the aspheric shape of Figure 10.

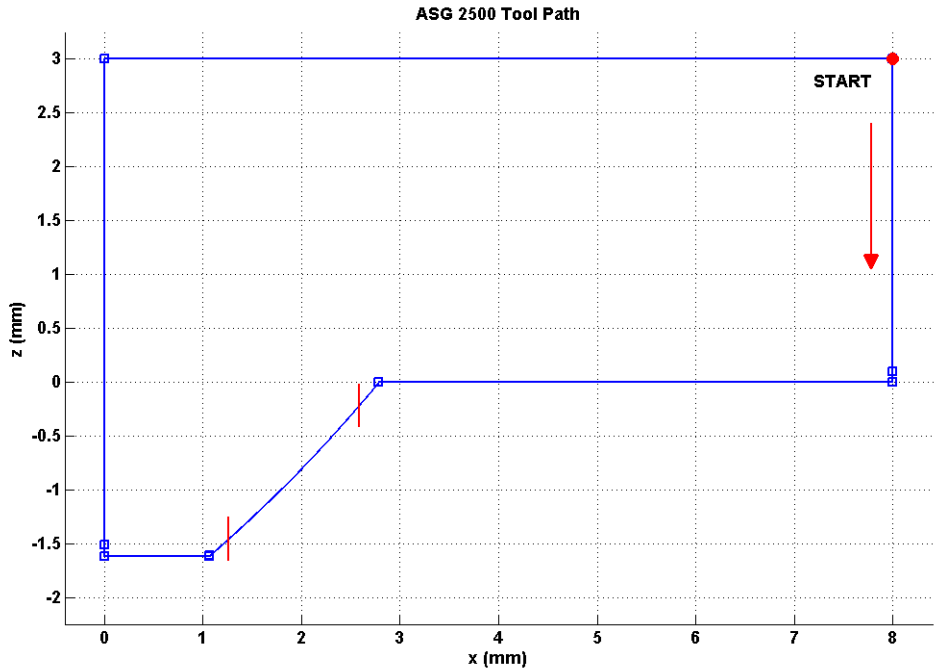

Figure 12. ASG 2500 DTM motion program for machining prescan optics.

The FTS tool motion and the best fit asphere can be added to create the surface shown in Figure 13. This annular surface describes the location of the tool center when machining the prescan optical system.

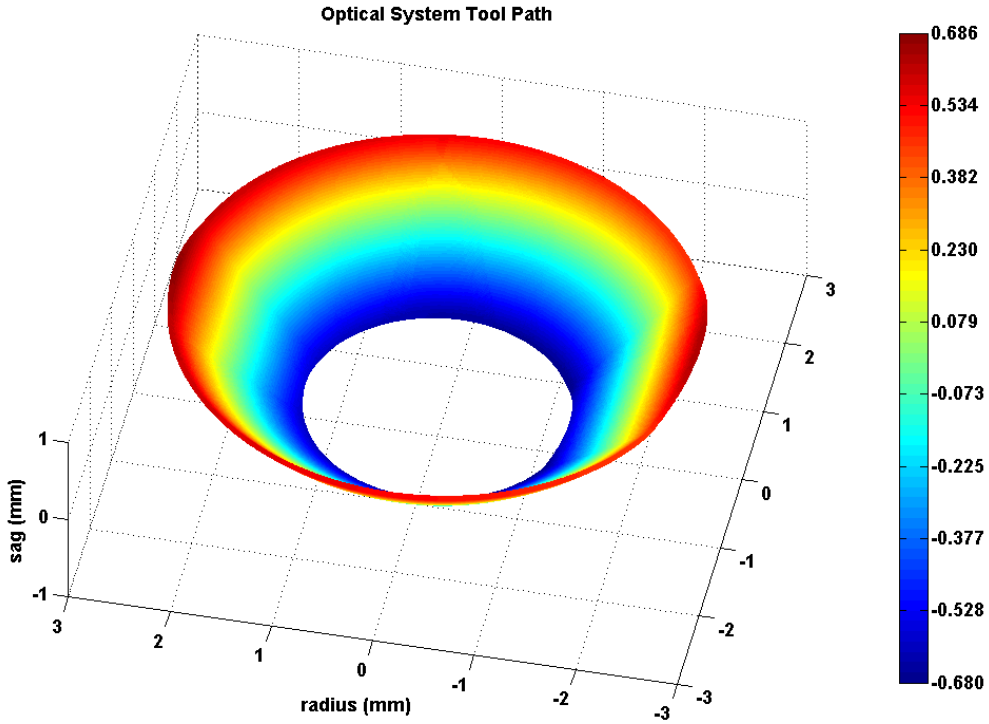

Figure 13. Combined DTM and Variform optical system tool path.

6.4 CONCLUSIONS

A design for a reflective prescan laser optical system has been completed. Tool path generation for an arbitrary biconic two mirror system has been coded in Matlab. The data tables needed to machine the mirrors with the Variform FTS control system are generated by this Matlab script. In addition a motion program is output describing the best-fit rotationally symmetric asphere that is machined simultaneously by the ASG 2500 Diamond Turning machine.

REFERENCES

1. Malacara, D. Optical Shop Testing, 2nd Ed., J. Wiley & Sons, New York. p. 743, (1992).

7 FABRICATION AND TESTING OF AN AIR AMPLIFIER AS A FOCUSING DEVICE FOR ELECTROSPRAY IONIZATION MASS SPECTROMETRY

Guillaume Robichaud
Graduate Student
Thomas Dow
Dean F. Duncan Distinguished Professor
Department of Mechanical and Aerospace Engineering
Alex Sohn
Precision Engineering Center Staff

Mass spectrometry is an analytical method used to measure the mass to charge ratio of complex molecules and proteins. It is extensively used in cancer research, drug testing and explosive detection. The first step of mass spectrometry is to ionize the molecule to analyze and isolate it in gas phase. A technique of obtaining gas phase ion that has revolutionized mass spectrometry is called electrospray ionization, where gas phase ions are extracted from a solution flowing in a thin capillary using a powerful electrical field. However, it is estimated that less than 1% of ions generated by an electrospray ionization source will be sampled by the mass spectrometer. This is mainly due to the low transfer efficiency of ions between electrospray source and the instrument inlet. Through the joint effort of precision engineering and computational fluid dynamics, an aerodynamic ion focusing device has been designed and fabricated using a single point diamond turning machine.

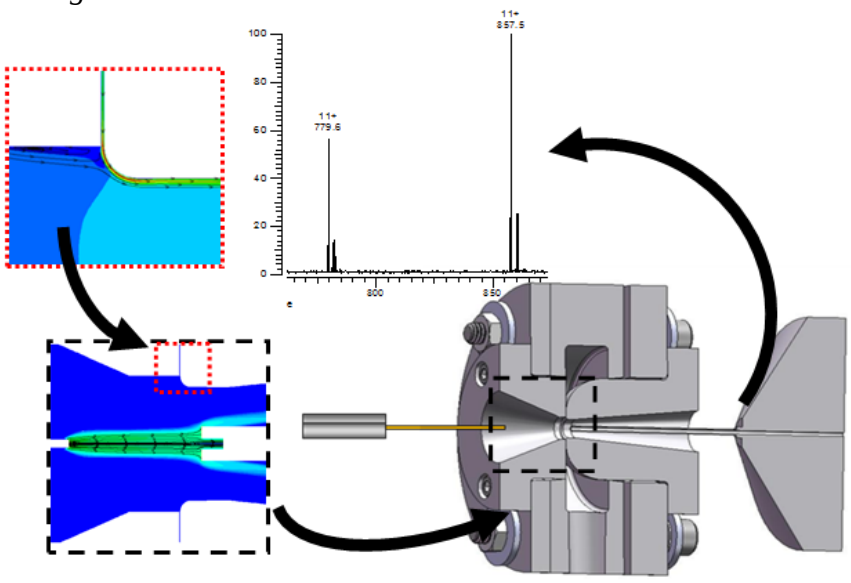

7.1 INTRODUCTION

Mass spectrometry is the analytical technique most widely used in biochemistry to characterize and identify molecules and proteins (analyte). Modern mass spectrometers use electric or magnetic fields to differentiate chemical components according to the relation between their mass and charge [1]. The proteins of interest are most often ions in solution and the first step to measurement by the mass spectrometer is to transfer those ions to the gas phase. The preferred method for the analysis of large biomolecules is the electrospray ionization technique (ESI) [1]. ESI-MS is a method developed by Yamashita and Fenn at Yale in 1984 [2] that allows large ions to be transferred directly to gas phase, keeping intact the analyte while minimizing the energy added to the system. ESI-MS consists of a small capillary tube through which flow an analyte diluted in a solvent. The intake needle of the mass spectrometer is positioned a few millimeters from the capillary exit and an electrical potential between the capillary and the mass spectrometer needle is applied, as shown on Figure 1. The resulting electrical field will cause a thin jet of highly charged solution to be ejected from the ESI tip, from which gas phase ions will eventually arise as solvent evaporates. Creation of singular ions during electrospray depends upon a complex interaction between the size of the analyte molecule, the flow rate, the nature of the solvent, the intensity of the electrical field, the concentration of the analyte in the solvent and the temperature.

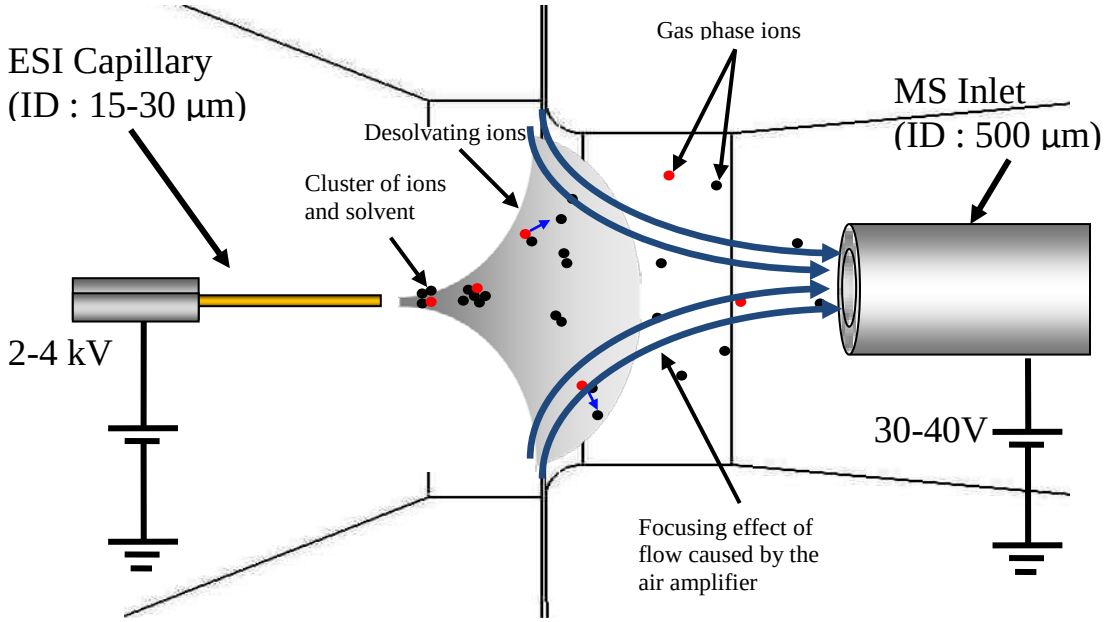

Figure 1. Electrospray Ionisation with Air Amplifier

[1] The dimensionless mass-to-charge ratio (m/z) is used to characterize the mass spectrum, where m is the unified atomic mass (in Dalton) and z is the number of elementary charges.

However, the efficiency of the ESI-MS does not only depend on the ability to create gas-ions from liquid analyte but mainly depends on the efficiency of the transmission of these ions to the mass spectrometer. It is estimated that for every 10^3-10^4 ions generated by electrospray ionization, only one will be sampled by the mass spectrometer. Most of the loss is encountered during the transfer between the ESI capillary and the MS inlet, as ions of same polarity will be scattered by repulsive Coulombic force before they can reach the inlet of the mass spectrometer. Efficiency of ESI-MS is critical because the size of the sample to be analyzed in applications such as medical research or forensics can be limited. Improving the efficiency or the sensitivity of the ESI-MS would lower the detection limit or the minimum sample size required. This project addresses the design of an air nozzle that fits around the ESI and adds inertia to the ions to help direct them toward the MS. It involved faculty and staff in mechanical engineering studying fluid flow and design/fabrication as well as faculty and staff in chemistry to study the efficiency in MS experiments.

7.2 DESIGN, FABRICATION AND TESTING

7.2.1 FLOW MODEL

The NC State Computational Fluid Dynamics Lab worked together with the PEC to develop the shape of the surface that provided the proper flow characteristics and could be diamond machined. The first calculations of the gas dynamics of the flow within the air amplifier devices was performed using an in-house computational fluid dynamics code called REACTMB. The air amplifier uses the Coanda effect[2] to create a low pressure zone that enables air entrainment into the air nozzle. This focuses the ions generated by electrospray ionization into the mass spectrometer and increases its sensitivity. The model can be viewed in Figure 2.

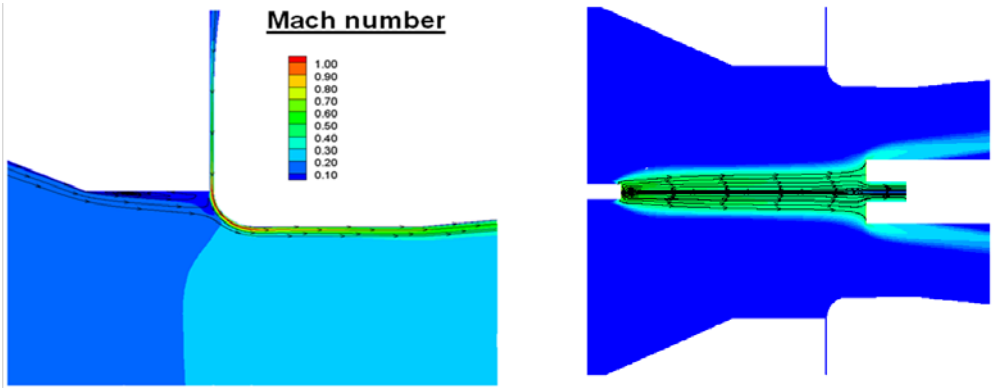

Figure 2. Aerodynamic model of the air amplifier (Left : Coanda profile. Right : droplet stream lines.

[2] Tendency of a fluid to stay attached to an adjacent curved surface

7.2.2 MECHANICAL DESIGN AND FABRICATION

Because the Coanda based air amplifier was sensitive to the gap width and parallelism and that optimal gap would have to be optimized experimentally, the device gap is controlled using 3 D1CM20 PZT actuators from Kinetic Ceramics. Preload of the device is done ensured by a stack of Belleville washer. A section view of the first design is presented on Figure 3.

The top and bottom inserts are interchangeable items so that other profiles can be tested without having to fabricate an entire new device. 6061 aluminum was selected for its machinability and resistance to chemical corrosion. Rough machining of the first iteration of the air amplifier was performed in by an external machine shop. Final machining that was performed at the PEC using a single point diamond turning machine or DTM (ASG 2500 from Pneumo Rank). The resolution of the tool position is on the order of 0.01μm and as as result the dimension of the parts can be fabricated to a resolution of μm. Surface finish control and measurement is critical as computer simulations assume that surfaces are perfect. These critical surfaces can be seen on Figure 4.

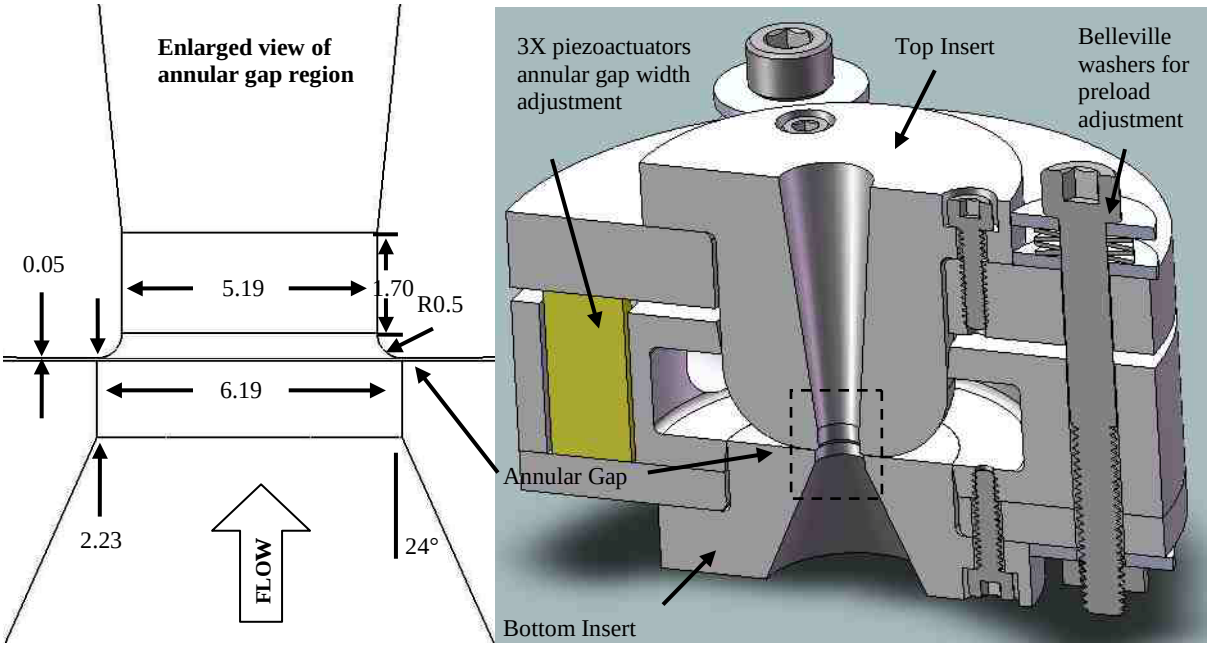

Figure 3. Section view of first iteration of air amplifier design

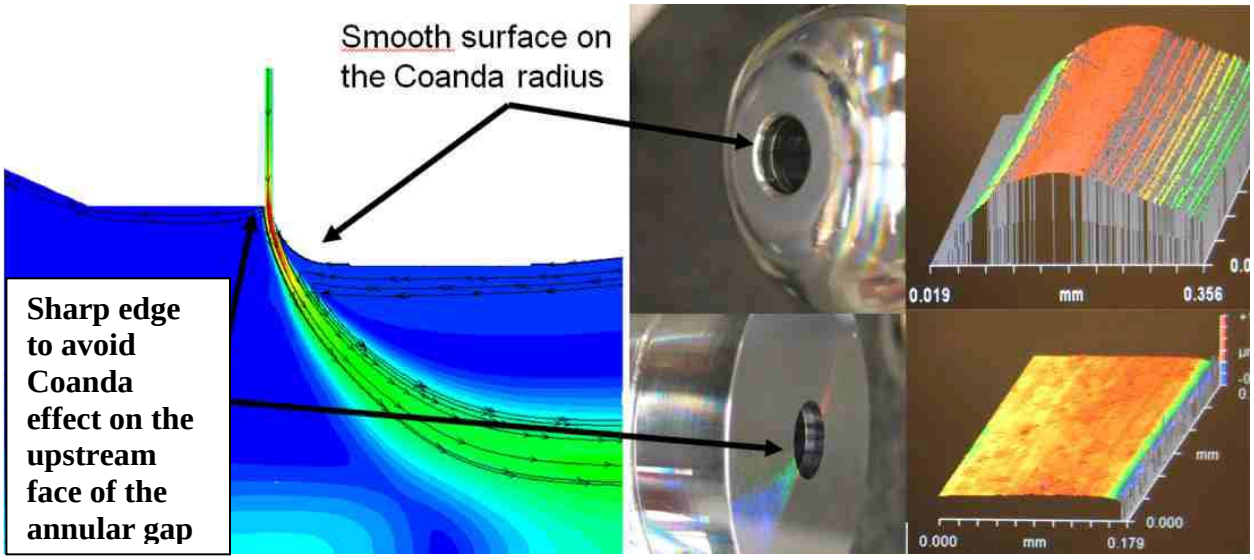

Figure 4. Diamond turning of critical surfaces and verification using New View (white light interferometer)

Dimensional measurements were performed using a Gage 2000 Coordinate Measurement Machine (CMM) from Brown and Sharpe. As represented on Figure 5, the CMM was used to measure parallelism and the difference in elevation between the bottom insert face and the surface where the top insert is bolted. The CMM was used to measure the final elevation of the top flange to ensure that the initial gap was set to 50µm. According to final measurements, a parallelism of less than 3 µm was achieved between the 2 inserts.

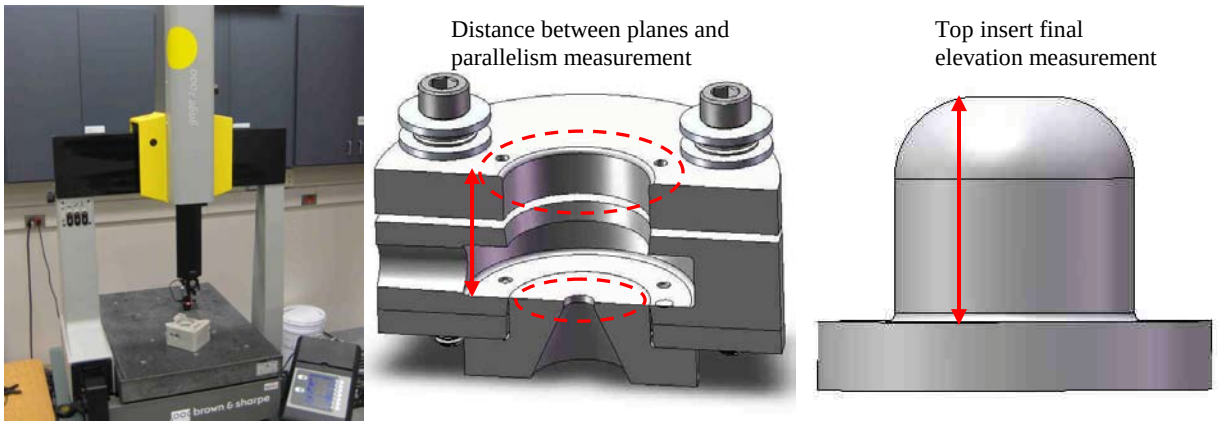

Figure 5. CMM machine used to measure annular gap indirectly

Annular gap can be changed be using the three PZT actuators and CMM was used to predict a measurements and the plot the gap vs voltage curves shown in Figure 6.

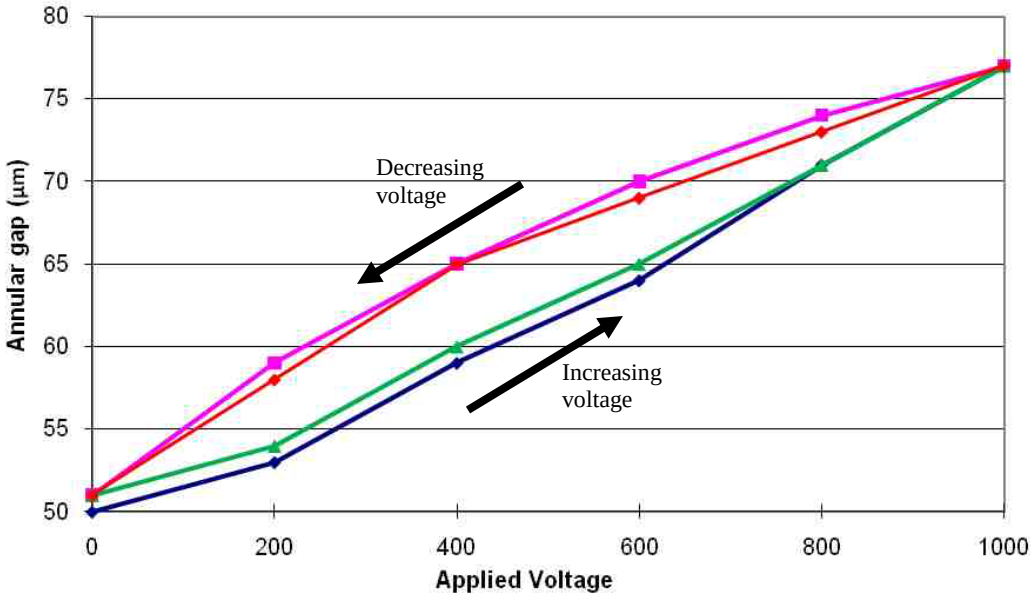

Figure 6. PZT actuators calibration for air amplifier

7.2.3 TESTING OF THE AIR AMPLIFIER

Pitot Tube measurements

When pressurized, the air amplifier successfully created a Venturi effect and static pressure has been measured along the flow axis for different pressure and annular gap position using a pitot tube. These results showed that for every gap and plenum condition, the maximum vacuum pressure: 1 mm downstream of the annular gap. Also, as shown in Figure 7, increasing the plenum pressure or increasing the annular gap both increased the maximum vacuum pressure while keeping the pressure profile nearly the same. Moreover, even though a higher vacuum peak can be obtained with a larger annular gap if pressure is kept constant, the maximum vacuum obtained for each annular gap is the same as seen on Table 1. This is caused by the fact that the Coanda effect is eventually lost when a maximum plenum pressure or annular gap threshold is reached. For example, at 30 psi the annular nitrogen jet exiting from the 50 µm annular gap reaches Mach 1 at the nozzle exit and expands slightly to supersonic flow speeds. It then curves around the Coanda surface, remaining attached to the surface. In contrast, the annular jet formed through the 70 µm annular gap detaches from the Coanda surface, inhibiting the Coanda effect.

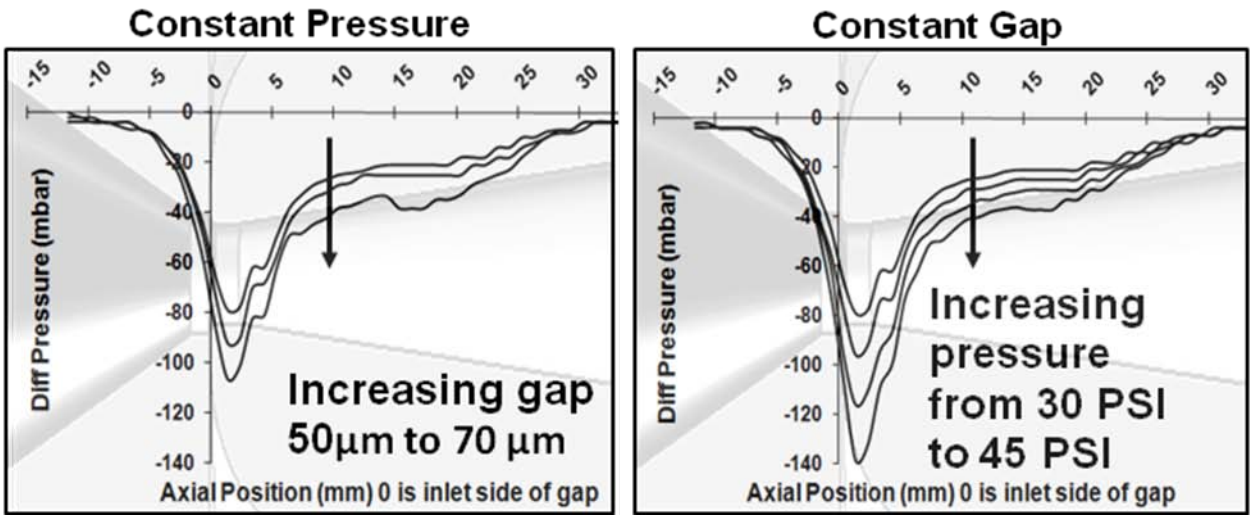

Figure 7. Effect of plenum pressure increase vs annular gap increase on pressure profile

Table 1. Maximum vacuum obtained along air amplifier axis

		Annular Gap		
		50 µm	60 µm	70 µm
Plenum Pressure	30 psi	-79 mbar	-92 mbar	-107 mbar
	35 psi	-96 mbar	-120 mbar	-144 mbar
	40 psi	-116 mbar	-140 mbar	No Coanda
	45 psi	-139 mbar	No Coanda	No Coanda

From these static pressure measurements, we could conclude that piezoelectric actuators would not be needed for the next iteration of the air amplifier as the effect of increasing the gap can be reproduced by increasing the plenum pressure. This reduces significantly the final cost of the device. Furthermore, results obtained have been used to confirm and reinforce the CFD models.

To optimize the design of the air amplifier, the performance of the device has to be tested and analyzed according to a specific figure of merit. Three different instruments have been used to test the performances of the air amplifier: 1) measuring electrospray currents using an electrometer, 2) measuring the output signal of a Fourier Transform Mass Spectrometer and 3) measuring the abundance on a triple quadrupole mass spectrometer.

1- Characterization of the air amplifier by current measurement

In order to give an indication of the performance of the air amplifier, the number of charges captured by a capillary and hitting the skimmer cone of a vacuum box has been measured using a Keithley 617 electrometer (see Figure 8). The purpose of a skimmer cone in a mass

spectrometer is to collect the ions in a specific zone when they come out of the capillary and expand in the vacuum box. This zone is called silent zone, where the ions are moving at equal speed in the same direction [3]. Further away is located a Mach disc and passed that zone, ions are scattered and much harder to capture. In our experiment, the skimmer cone is grounded and used to collect the ions exiting the capillary. The Keithley 617 is used to measure the current flowing between the cone and the ground. This current (in Ampere or charge per seconds) is a direct measurement of the number of charges hitting the skimmer cone every second.
Both the ESI emitter and the air amplifier were mounted on XYZ stages with micrometers so that their position can be controlled with precision (see Figure 9). A LVDT was also installed to record the position of the air amplifier. Both the LVDT and the electrometer were connected to a data acquisition system so that the number of charges hitting the skimmer could be plotted as a function of the position of the air amplifier while exploring different condition of operation.

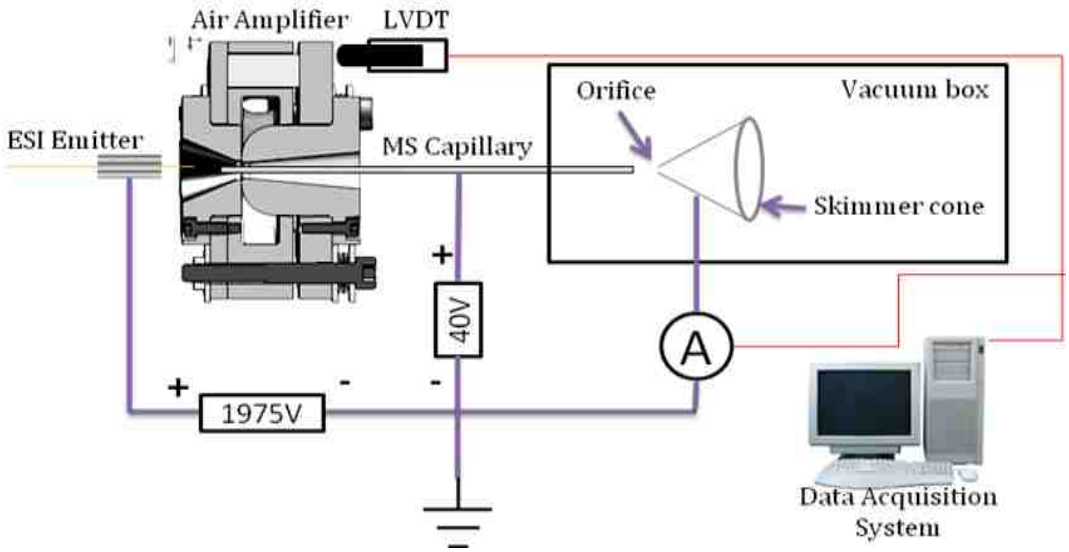

Figure 8. Schematic of setup for current measurement on MS skimmer cone

Pressure of the air amplifier was initially set at 30 psi and the annular gap was set at 50 µm. By electrospraying 2 different solutions[3] at a flow rate of 1 µL/min with electrospray gap of 3, 5, 7 and 9 mm it was found that the maximum current was obtained when the ESI tip was positioned 1 mm downstream of the annular gap of the air amplifier (see Figure 10). This zone corresponds to the peak of maximum vacuum pressure that was measured in the air amplifier during previous experiments [4]. Additional experiments were performed to show the effect of an increase of the plenum pressure (from 30 psi to 45 psi) or an increase of the annular gap of the air amplifier (from 50 µm to 70 µm) on the skimmer cone current. Even if such variation of pressure and gap had resulted in an increase of the vacuum pressure in the region of the annular gap of the air

[3] 1:1:1 tetramethyl:tetrabutyl:tetraheptyl amines and 50:50:0.1 ACN:H2O:FA

amplifier by up to 75 % according to pressure measurements, the increase on the skimmer cone current did not exceed 15 %. This indicates that the vacuum pressure intensity is not a valid figure of merit.

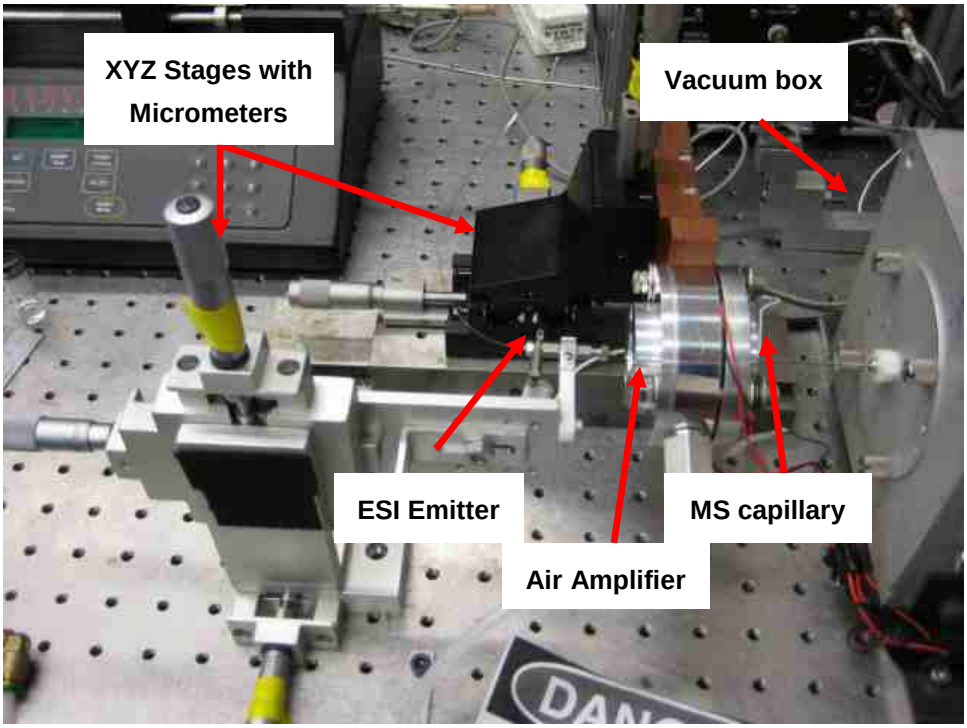

Figure 9. Setup for current measurement on MS skimmer cone

Because only the gas phase ions can be detected by the mass spectrometer, the skimmer cone current is not the best indicator of performance as it is not possible to discriminate the charges hitting the skimmer that are gas phase ions from whose that are ions in droplets of solvent that are poorly desolvated. Also, it is not possible to tell if an increase in the skimmer cone current is due to an increase in the performance of the charge transmission from the emitter tip to the mass spectrometer or simply to an overall increase of the electrospray current (number of charge emitted from the ESI tip). Monitoring the ratio of the skimmer cone current to the electrospray current would be a better figure of merit. Due to some limitation of the equipment used for this setup, it was not possible to perform these measurements simultaneously. It was decided to test the air amplifier with a mass spectrometer so that a direct measurement of effect of the air amplifier on the abundance on gas phase ions could be monitored.

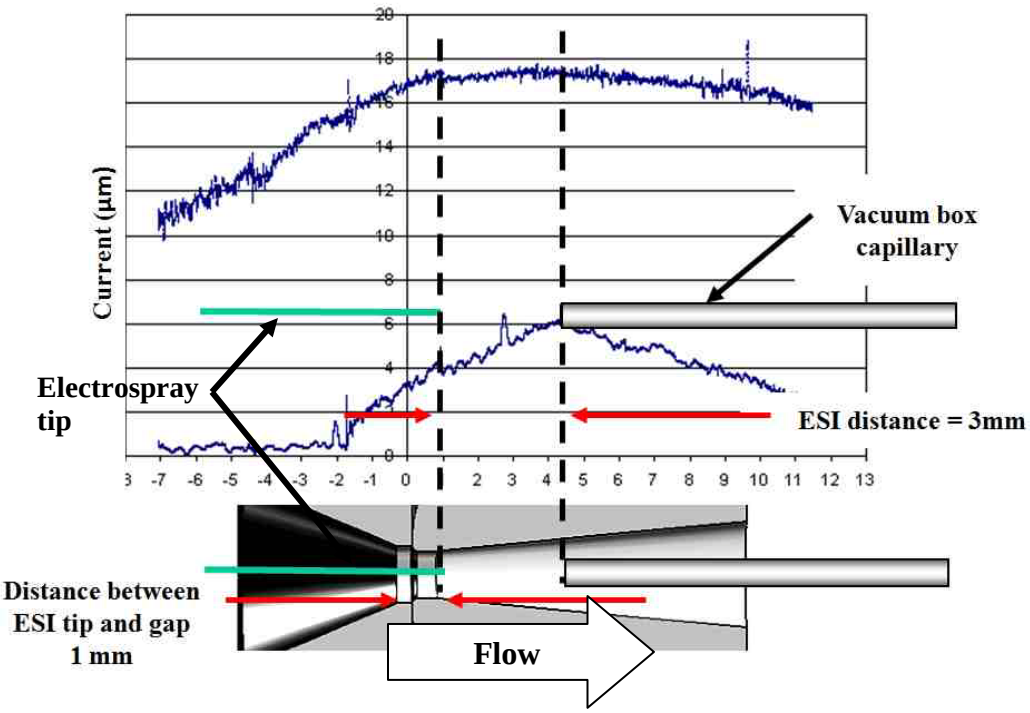

Figure 10. Skimmer cone current vs air amplifier position

2- Characterization of the air amplifier using a Fourier Transform Mass Spectrometer (FTMS)

A FTMS 9.4T located at the W.M. Keck FTICR Mass Spectrometer Laboratory was used to perform the experiments. The first attempt of characterization of the air amplifier with the FTMS was made by monitoring the abundance of specific ions in solution[4] while varying different parameters. A plot of the abundance of 857±1 m/z ion of a for a ESI gap of 9 mm is shown on Figure 11 : it revealed that the peak of abundance was found when the MS tip was located between 0 and 1 mm downstream of the air amplifier annular gap. This result the first set of experiment, where the maximum current was found when the ESI tip was located 1mm downstream from the annular gap. After setting the position of the air amplifier at its optimal position, the abundance of the ions with and without the air amplifier was compared for different ESI gap. It was found that the air amplifier was improving the signal for large ESI gap only. No improvement was measured at ESI gap of 3 mm and improvements up to 4.34 folds was measured for a ESI gap of 9mm (see Figure 12). One of the problems encountered during the preliminary experiments on the FT ICR was that the signal obtained was extremely sensitive to several internal settings proper to this type of instrument.

[4] 1 micromolar ubiquitin in 50:50:0.1% Acetonitrile:water:formic acid

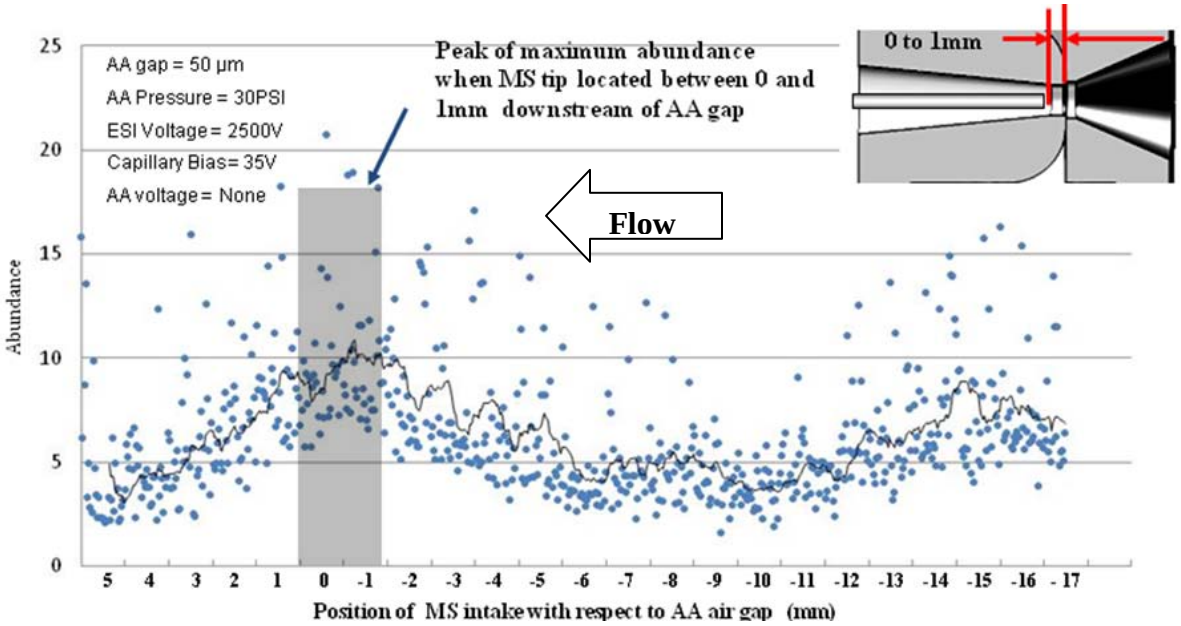

Figure 11. Abundance of 857±1 m/z ions as a function of AA axial position shows that there is a peak of abundance

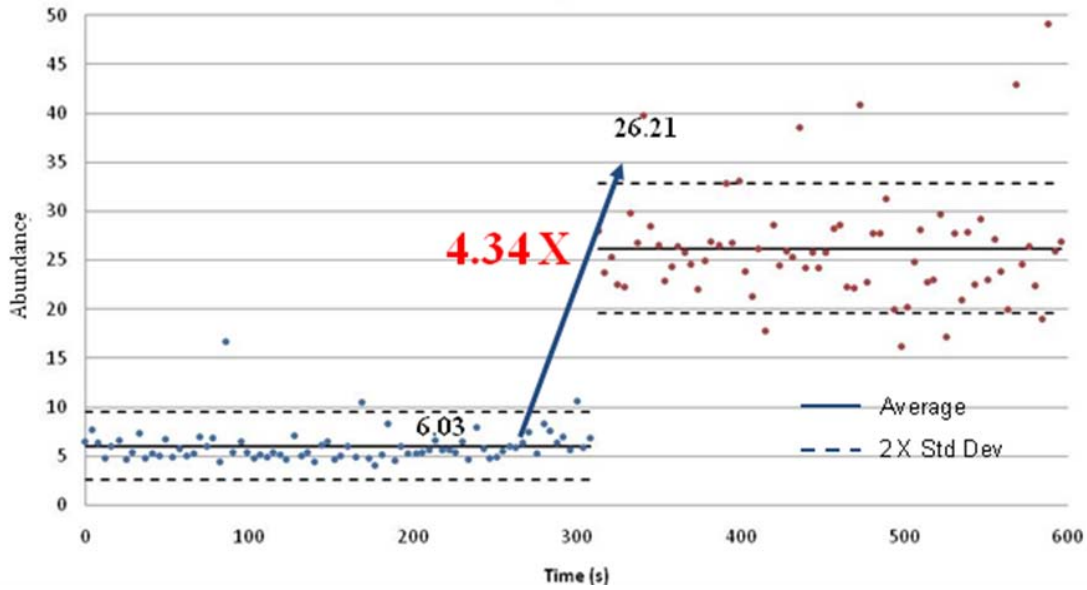

Figure 12 – Improvement of 4.34 folds of abundance measured for a ESI gap of 9mm (without and with AA)

3- QqQ Tests and Design of Experiment

Working under different principles, the triple quadrupole mass spectrometer (QqQ MS) does not have the mass resolving power (resolution) of the FT ICR. However it offers a more stable platform to test the air amplifier. It is also an instrument widely used in the industry.

During the preliminary tests performed with the air amplifier on previous instruments, several different variables or parameters were identified as potentially having an effect on the performance of the air amplifier. Clearly identifying the parameters that do have an effect on the output by randomly tuning each of the parameters individually will give no guarantee that all the experimental space has been covered. For this reason, a more methodical approach was implemented through a design of experiment strategy to screen these variables and determine the primary effects on the performance of the air amplifier.

A full factorial design is an intuitive way to systematically explore the entire experimental through a space, however it was not realistic in this case as it would have required to perform over 1000 experiments (2^n) . If one accepts to reduce the resolution of the analysis by allowing the confounding of the main effects with some interactions, the number of experiments can be reduced significantly. This is achieved using Fractional Factorial Design or FFD [5]. This approach was use throughout the rest of the experiments

Table 2. Variables affecting signal

Variable	Level +	Level -	Motivation
Position of vacuum peak	1 mm from ESI inlet	1 mm from MS inlet	Previous experiments showed that these 2 parameters could have a positive impact
ESI Gap	9 mm	6 mm	As no improvement was found at 3 mm with the amplifier during previous experiment, larger space was explored
ESI Voltage	3200 V	2800 V	Range that showed good performance in previous experiments
N2 Temperature	100°C	25°C	High temperature N_2 can improve desolvation
Air amplifier pressure	45 PSI	30 PSI	Amplifier pressure range
Composition	100% H_20	25% H_20/75% ACN	Test the hypothesis that the air amplifier can improve desolvation of aqueous solvents.
Air amplifier radial alignment	Centered	0.75 mm offset	Previous experiments performed earlier showed that some
ESI Tip size	100 µm	75 µm	As previous experiments showed no overall signal improvement with air amplifier. This is to test the hypothesis that better results can be obtained with larger tips
Flow	2 µL/min	1 µL/min	

Using the FFD approach mentioned above, results obtained from the variables and settings presented in Table 2 were compared. These experiments were performed with a 1 µM Melittin solution and abundance of 570.21 m/z and 712.31 m/z was monitored. The following was deduced from these experiments:

1- Confirmation that better signal is obtained when the low vacuum zone is focused on the mass spectrometer inlet (radially and axially).
2- Value of ESI voltage does not have a significant impact on the results. Once electrospray is established, increasing or lowering the voltage does not have a significant effect on the performance of the air amplifier. Voltage has to be adjusted so that ESI is established for each experiment.
3- Tip size, flow size and solvent composition do have an important contribution on the performance of the air amplifier. Better results were obtained were obtained with a 75 µm ESI tip, 2 µL/min flow and higher organic solvent composition.

Other series of experiments were then performed with a reduced number of variable to find an experimental space where using the air amplifier would offer an overall increase in signal when compared the best signal that can be obtained without the device. To do so, all four different combinations of solvent composition (50% H_2O/ 50% ACN and 100% H_2O) and ESI capillary tip ID (75 µm and 30 µm) were compared at different ESI flow.

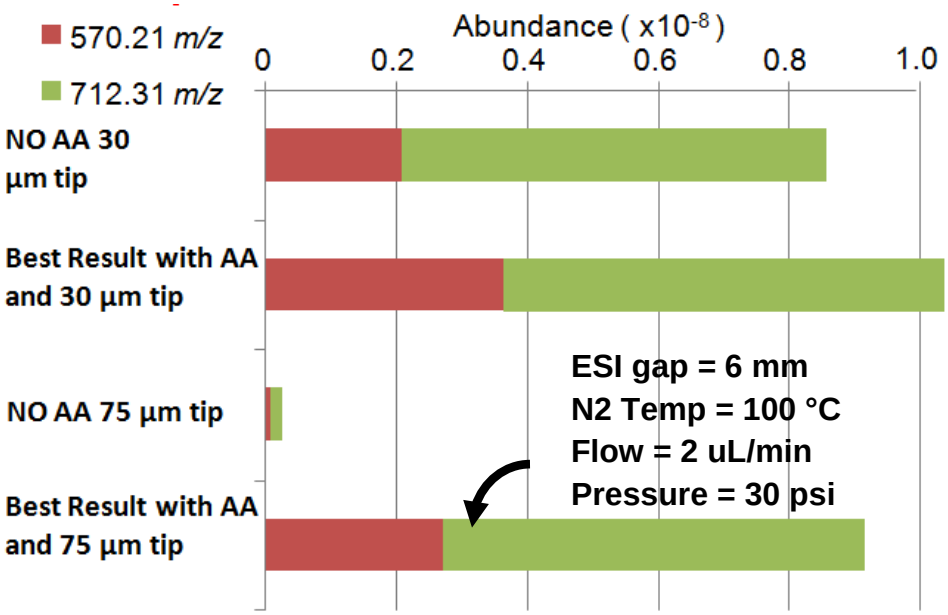

Figure 13. Best improvement with air amplifier

Results shows that no significant signal improvement was achieved by using the air amplifier for 50% H_2O/ 50% ACN when compared to the best result that can be obtained without using the air amplifier. However, for 100% H_2O solvent composition, it has been possible to obtain a signal with a 75 µm tip and the air amplifier that was superior or equal to the signal obtained with a 30 µm tip and no air amplifier. Note that without the air amplifier, it was not possible to obtain a stable signal under these conditions for a 75 µm tip as pointed out on Figure 13. This result is important as it shows that ESI MS can be performed at higher flow regime using larger ESI tips

when using the air amplifier. The advantage of using a large ESI capillary resides in the fact that it will not get clogged as often compared to a smaller 30 µm tip. Over a large volume of experiments, this can mean a significant increase in productivity for a pharmaceutical company or a research laboratory.

7.2.4 NEXT ITERATION OF THE AIR AMPLIFIER

Another iteration of the air amplifier has been designed. One of the main objectives was to make the device more compact in order to reduce as much as possible the length of the mass spectrometer inlet tube as shown on Figure 14. A longer tube reduces significantly the maximum signal that can be detected as ions tend to condense on the inner surface of the cold capillary and never reach the instrument. A more compact air amplifier is now possible since it has been demonstrated that the piezoelectric actuators could be taken out of the assembly. As for the first iteration, the CFD model was used to test different aerodynamic profile and test different configurations. As no indication that a change in the Coanda profile would result in significant signal improvement, it was decided to keep the dimensions and angle of the Coanda the same. Only the length of the inlet and outlet cones would change. CFD model was also used to verify the effect of these changes in geometry on the signal and also how close the air amplifier could be positioned with respect to the MS inlet before starting to obstruct the flow. With the new design, it will now be possible to reduce the MS tube length from 134 mm to 35 mm.

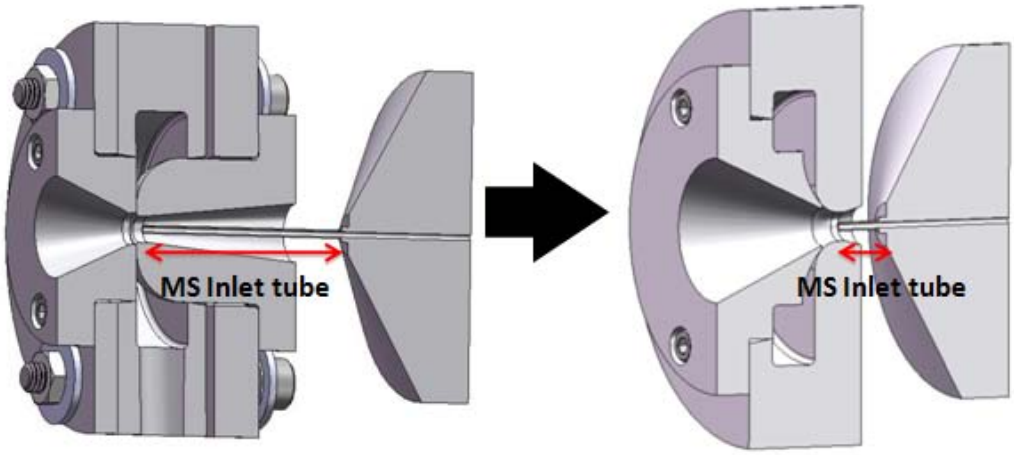

Figure 14. Reduction of MS inlet tube length

Once the final aerodynamic profile agreed upon, a FEA of the structure was performed in order to verify that the plenum pressure would not cause significant increase of the annular gap. New profile and FEA results are presented on Figure 15.

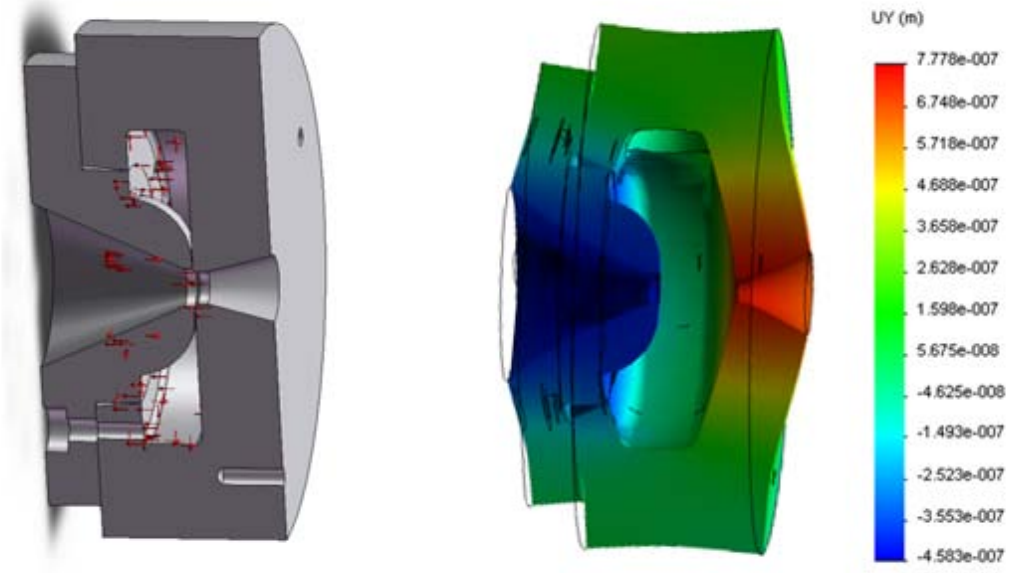

Figure 15. Next air amplifier shape and FEA results

7.3 CONCLUSION AND FUTURE WORK

Tests performed on the air amplifiers showed that the design and fabrication of a high precision air amplifier with adjustable annular gap has been successfully achieved.

Experiments showed that the air amplifier can have a positive influence on both of the abundance and the number of charged entering the mass spectrometer. Also, the number of parameter affecting these results has been significantly reduced and an area of the experimental space where the air amplifier has an overall positive effect has been identified. Based on these results and with help of the CFD model a new iteration, more compact has been designed and is currently been fabricated.

The W.M. Keck FT-ICR-MS Laboratory at NC State will have a linear ion trap Orbitrap (LTQ Orbitrap) mass spectrometer dedicated only to the new air amplifier experiments. This instrument, also widely used in the industry not only has a high resolving power but it also offers the capability to count ions as they enter into the mass spectrometer through its automatic gain control system. Based on the results of the experiments performed on the new iteration of the air amplification a 3rd generation will be designed and multiple copies will be fabricated. Those will then be sent to different mass spectrometry laboratories across the country to be field tested.

REFERENCES

1. Nadja, C. and Christie, E., "Practical Implications of Some Recent Studies in Electrospray Ionization Fundamentals", Mass Spectrometry Reviews, Vol 20, pg 362-387, 2001.
2. Yamashita, M. and Fenn, B, "Electrospray Ion Source. Another Variation on the Free Jet Theme", The Journal of Physical Chemistry, Vol 88, No 20, pg 4451-4459, 1984.
3. A. P. Bruins, "Mass Spectrometry with Ion Sources Operating at Atmospheric Pressure", Mass Spectrometry Review, Vol 10, pg 53-77, 1991.
4. 57th American Society for Mass Spectrometry Conference 2009, Philadelphia, PA. "Development of an Air Amplifier Assisted Protein-Cleavage Isotope Dilution Mass Spectrometry Method for Prostate Specific Antigen in the Nano-Flow Regime", R. B. Dixon, D. K. Williams Jr., D. Cassidy, J. R. Edwards, G. Robichaud, A. Sohn, T. A. Dow, D. C. Muddiman.
5. Louvar, J., Simplify Experimental Design.,Chemical Engineering Progress Magazine, p.g 35-40, Jan 2010

8 DIAMOND TOOL CENTERING FOR CYLINDRICAL TURNING

Alex Sohn
Staff
Precision Engineering Center

Centering diamond tools for turning to within 1 µm has become common practice as the demands for lower figure errors and higher sag optics have increased. The less common case of cylindrical turning, however, rarely sees such demands. However when a cylindrical radius is important, there are few methods available that can achieve tool centering to such a high degree of accuracy. This section describes a method of centering a tool and a test of its effectiveness showing its utility and accuracy.

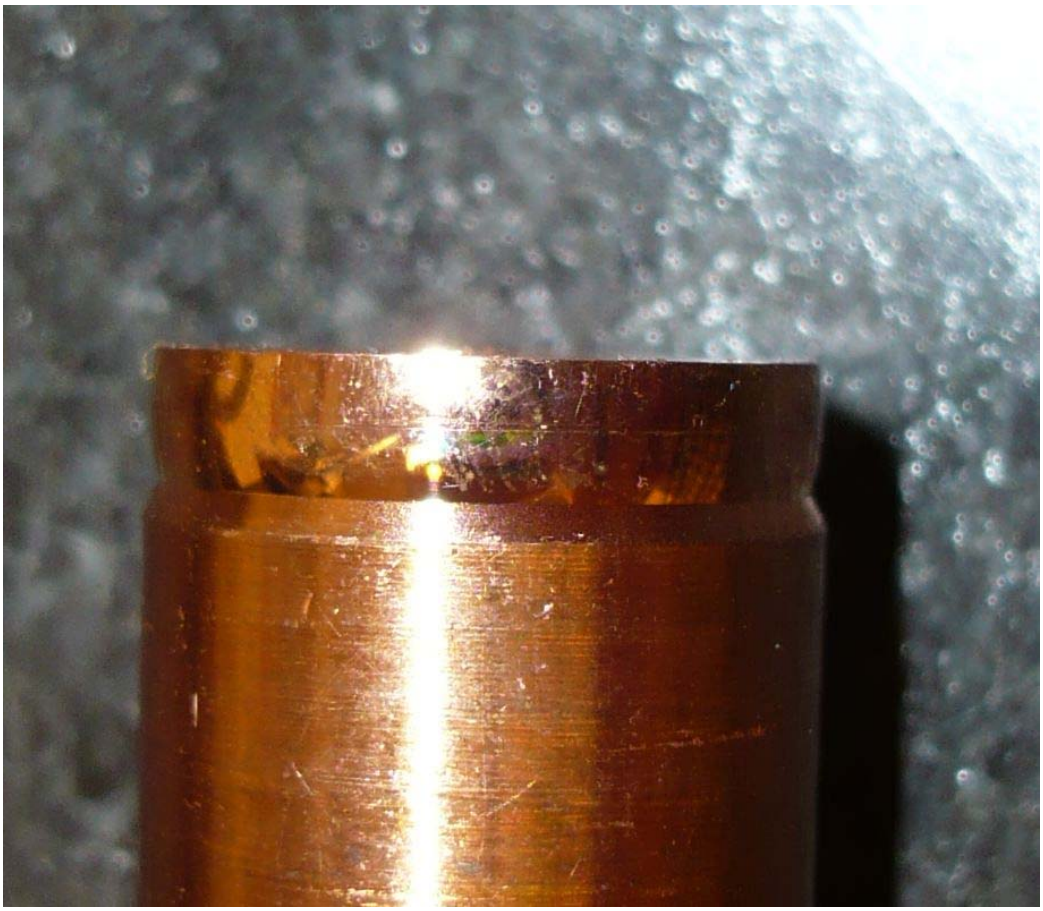

8.1 INTRODUCTION

Centering a diamond tool centering using the Ogive error [1] method has been extensively used for turning operations. This method of tool centering is, however, limited to cases where a spherical test part can be machined to include the center of rotation of the part spindle on the part. In the case of cylindrical turning, this is often not possible or would lead to significant error because a completely different portion of the tool is used for centering than for machining.

High-accuracy tool centering (centering accuracies of the order of 1 µm) for cylindrical diamond turning is often necessary for turning cylindrical lenses or mechanical components that require very close-tolerances. One demanding example of a close-fit tolerance is for the mass spectrometer air amplifier system being developed at North Carolina State University and discussed in Section 7 of this report. Several components must fit together with cylindrical clearances of 2 µm or less. This means that both the inner and outer diameter tolerances for mating parts are 1 µm.

8.2 THEORY

The centering method for cylindrical turning involves turning a sphere onto the outer diameter of a cylinder as shown in Figure 1. The tool interpolates a radius in the X/Z plane of the diamond turning machine (DTM) while the rotation of the part around the spindle axis forms an orthogonal radius.

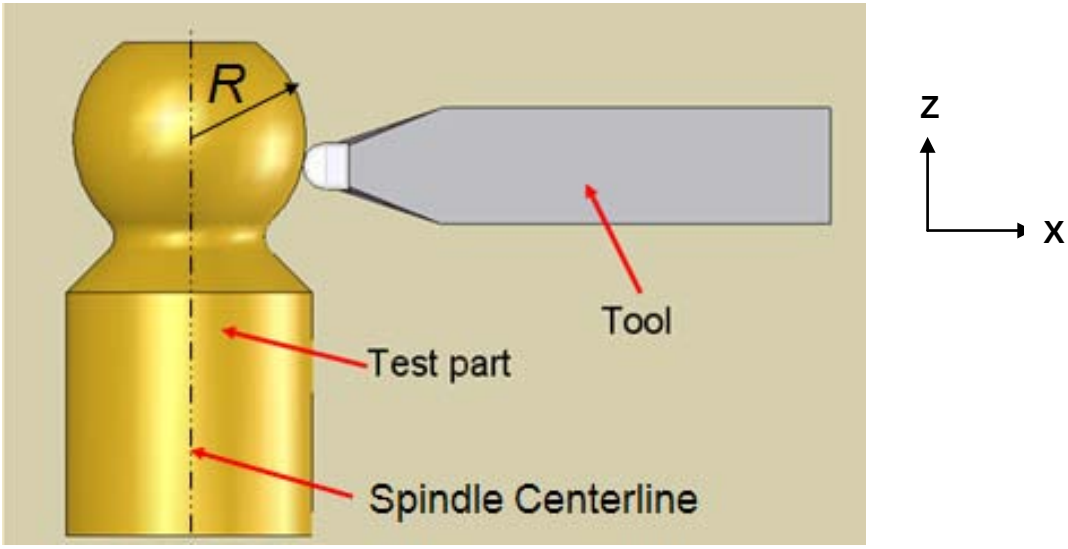

Figure 1. The nominally spherical test part for centering a tool nominally normal to the spindle rotational axis.

For an ideal part, these two radii would be equal to radius R in Figure 1. If these two radii are different, however, the result is a toroid with a radius of curvature equal to the toolpath radius minus the tool radius (otherwise known as the interpolated radius) defined as R_i, and a radius of revolution defined as R_t as shown in Figure 2. The centers of these two radii are separated by a distance of Δx, the tool centering error.

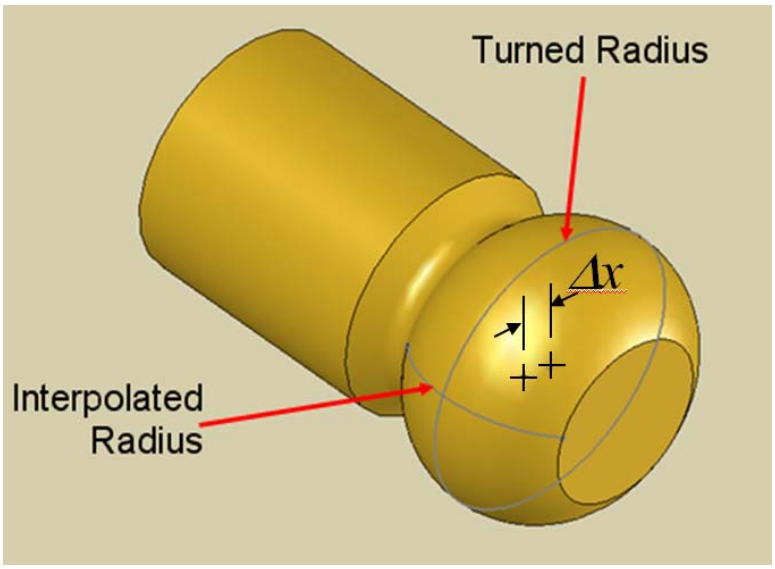

Figure 2. The turning of a non-ideal part during the centering operation results in the machining of a toroid with the centers its two constituent radii displaced by a distance of Δx.

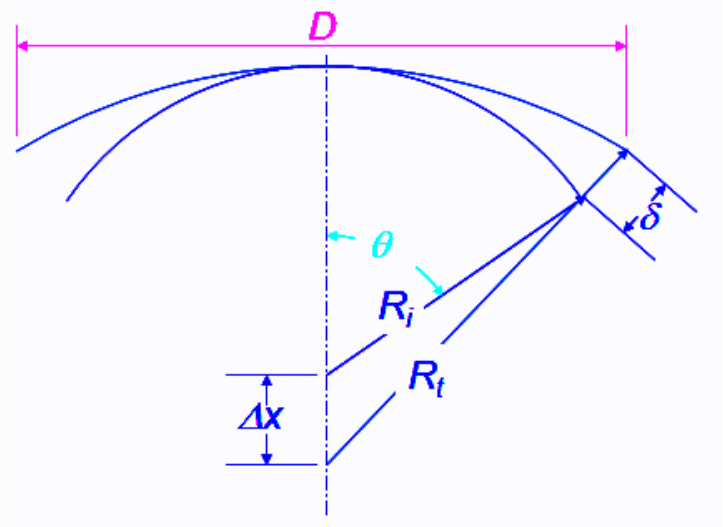

FIGURE 3. A two-dimensional schematic of the parameters involved in determining the tool centering error Δx.

To determine the centering error Δx, the difference, δ, between these two radii can be measured over a defined aperture D as shown in Figure 3. It turns out that this maximum deviation between the two radii as measured in a laser interferometer is equivalent to the magnitude of the astigmatic Zernike terms (4^{th} and 5^{th} order). Using the this astigmatic magnitude term is an advantage over simply measuring peak-to-valley error because it is resistant to local variations and other errors in the part.

To derive the tool centering error from the known parameters of R_i, D, and the measured quantity δ, the starting point is defining a triangle as shown in Figure 3 formed by the sides Ri, R_t and Δx. Using the law of cosines and the angle θ,

$$R_i^2 + 2R_i\Delta x\sin(\theta) + \Delta x^2 = \left(R_t - \delta\right)^2 . \tag{1}$$

The aperture angle, θ, can be expressed as:

$$\cos(\theta) \simeq \frac{D}{R_i} , \tag{2}$$

when the difference between R_i and R_t is small. Also,

$$R_t = R_i + \Delta x \tag{3}$$

The unknowns R_t and δ in Equation 1 can be eliminated by substitution and resulting expression for Δx is:

$$\Delta x = \frac{-2\partial R_i + \partial^2}{\left(-2R_i + GR_i + G\partial\right)} \tag{4}$$

where

$$G = \sqrt{-\frac{D^2 - 4R_i^2}{R_i^2}} . \tag{5}$$

The algebraic solution was determined and checked using Maple™ 12.0.

8.3 MEASUREMENT

The aperture D to be measured is shown in Figure 4. The measurement is made over this known aperture to determine the astigmatic magnitude or radial sag difference. The sag difference, δ, can then be directly related to the tool centering error by Eq. 4. Sign is determined from the interferogram. If the surface profile shows the rotation radius R_t, that is normal to the part axis of rotation, to be high at the edges, the tool zero is short of center. If the interpolated radius

direction R_t, that is parallel to the part axis of rotation, is shown to be high at the edges, the tool zero is past the spindle centerline.

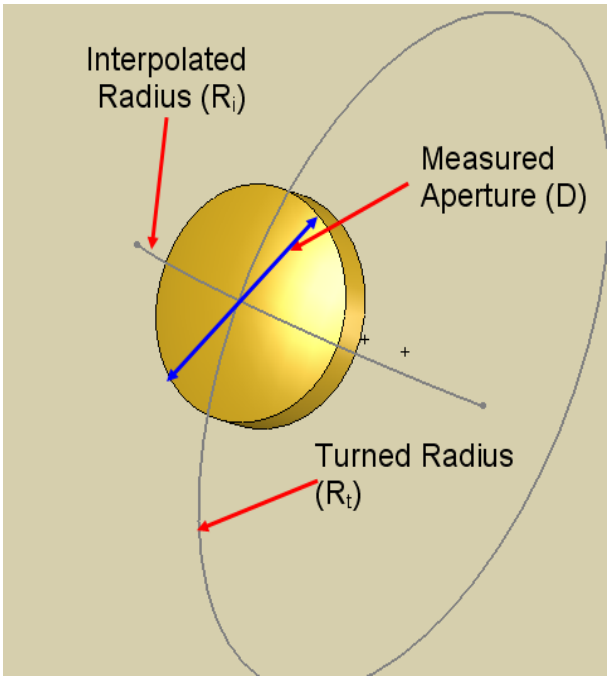

Figure 4. Illustration of the aperture D to be measured in the interferometer.

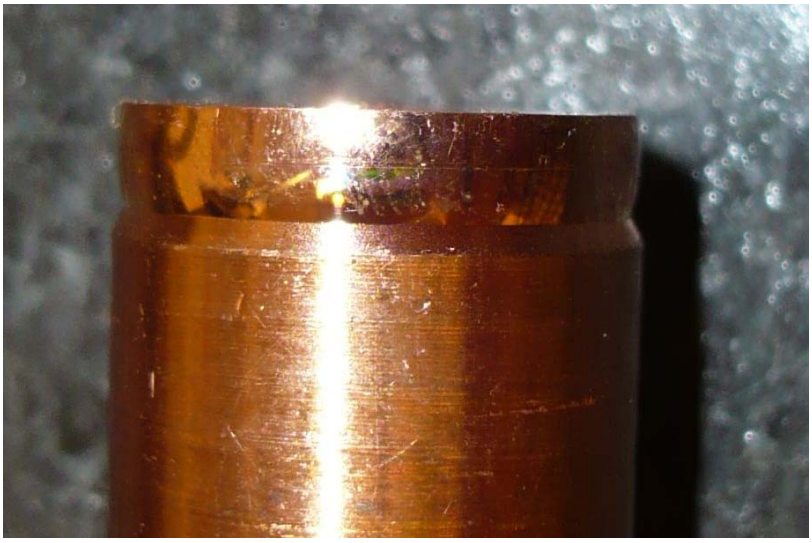

Figure 5. Copper test part of 12.7 mm nominal diameter. The toroidal region is approximately 2 mm wide at the top of the part.

8.4 PROCEDURE

To test the tool centering method, a test part was machined on the PEC's ASG 2500 Diamond Turning Machine. For rough centering, the diameter of a cylindrical copper test blank was first measured with a standard micrometer to be 12.778 mm. The part was then centered on the part spindle and the 0.1 mm radius tool used to touch off on the surface of the part. This position was then set to X=6.289 mm (D/2 – tool radius). The part shown in Figure 4 was then machined with an interpolated radius of 6.289 mm and the result measured in a laser interferometer.

The following part program was used to machine the test part:

```
units metric
move      8.00      0.360944  250
move      8.00      -3.49405  250
line      6.57589   -3.49405  10
circle    6.16275   -2.49987  10   0.961 cw
circle    6.08022   0.36094   10   6.289 ccw
move      8.00      0.360944
```

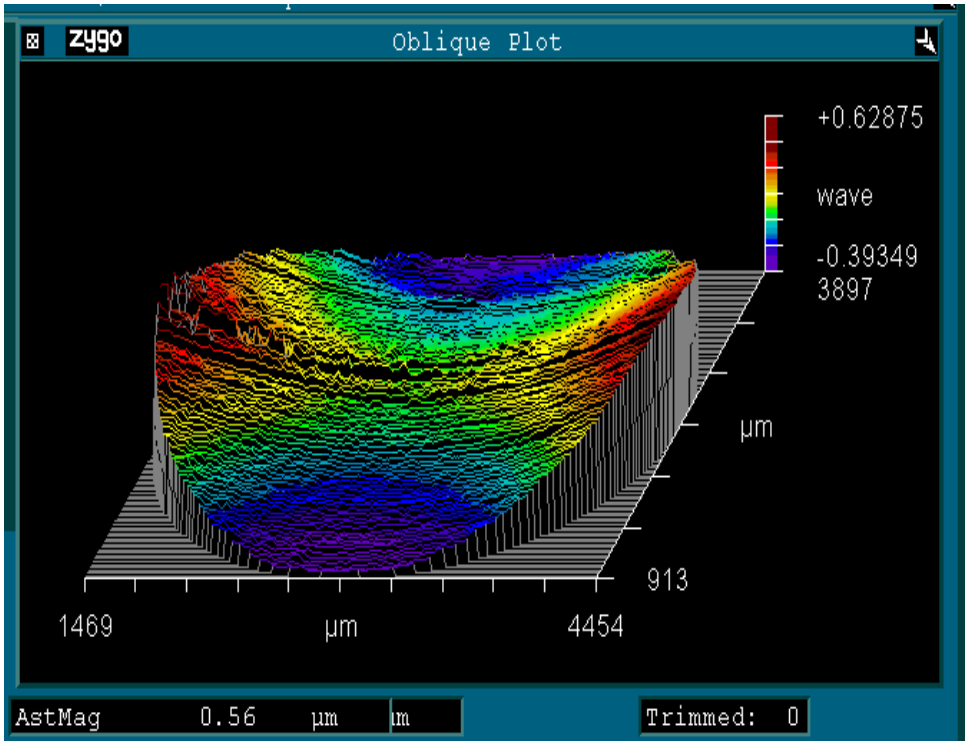

Figure 6. Plot of astigmatic error (magnitude: 0.56 µm) in a part machined with a tool centering of 35 µm.

8.5 RESULTS

Measurement results of the test part in copper are shown in Figures 6 and 7 before and after centering correction. The instrument used was a Zygo GPI XP interferometer with MetroPro analysis software. The interpolation radius was 6.3 mm.

The measured astigmatic magnitude was 0.56 µm, yielding a centering error calculated using Equation 4 of 35 µm on the first sample shown in Figure 6. Figure 6 also shows the radius in the rotational direction identified by cutting tool marks to be larger than the radius in the interpolation direction. This means that the tool is short of the center of rotation and a corresponding shift of the X-axis coordinate of the DTM must be made. The result of this correction is shown in Figure 7. The residual error magnitude is 0.02 µm, yielding a centering error of only 0.3 µm. More improvement than this level is unlikely given that the residual bears little of the irregular saddle shape associated with the astigmatic error. Other machining errors dominate in this case.

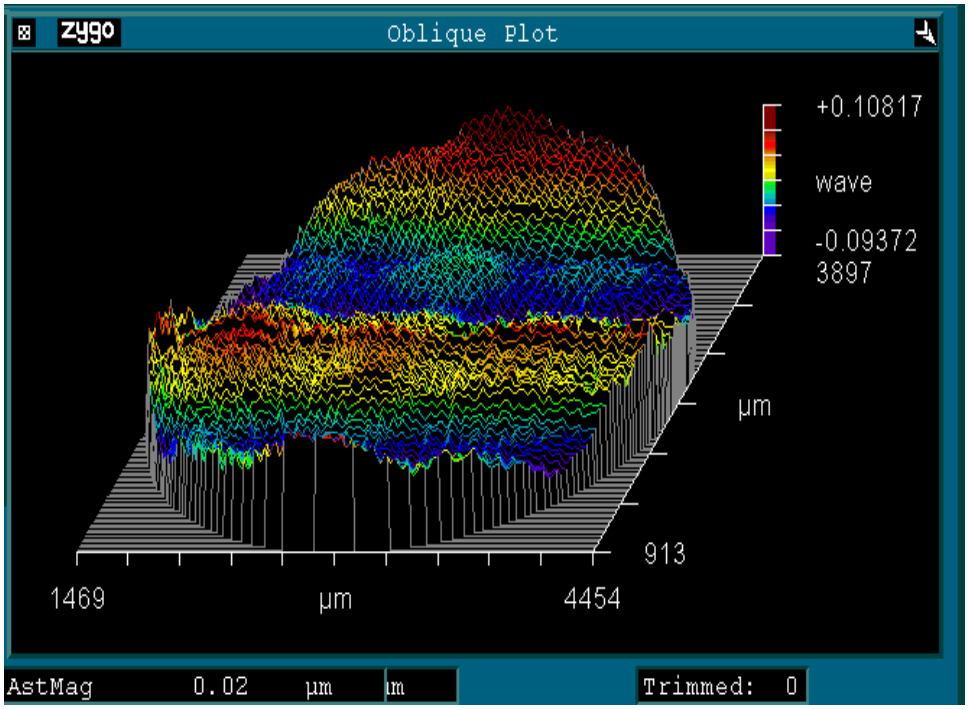

Figure 7. Plot of residual astigmatic error (magnitude: 0.02 µm) after removal of 35 µm centering error determined from the measurement shown in Figure 5. The remaining centering error is 0.3 µm.

8.6 CONCLUSIONS

Machining tests have resulted in confirmation of using the described method in practical use, though an independent means of measuring absolute diameter have not yet been obtained. Use in practice for close-tolerance mechanical parts have, nevertheless, shown that accuracies of 1 µm have been obtained for parts of nominally 25 mm in diameter where interference or loose fit would have resulted from significant error in mating cylindrical parts.

REFERENCES

1. Gerchman, Mark Craig: “Optical Tolerancing for Diamond Turning Ogive Error”, Rank Taylor Hobson, Inc., Keene, NH 03431.
2. Rasnick, W.H. and Yoder, R.C.: “Diamond Turning Setting by Interferogram Analysis”, Oak Ridge Y-12 Plant, Oak Ridge, TN 37830; October 22, 1980.

9 DESIGN OF A MINIATURE PULSEJET ENGINE

John Sayres, Joseph Scroggins, and Scott Steinmetz
Graduate Students
William Roberts and Thomas Dow
Professors
Mechanical and Aerospace Engineering

The goal of this project is to design, fabricate and demonstrate a medium-scale (100 mm length) pulse jet engine. This engine is an intermediate step to create a small scale pulse jet with a length less than 50 mm (2 inches) for a Unmanned Aerial Vehicle (UAV) application. Because the engine must produce significant thrust, it must have an inlet valve to avoid losing energy out the front of the engine. The problem then becomes the control of a high temperature fluid at high frequencies, small size and with low losses. The high temperature environment, high cycle requirements, high speed operation and small size are a challenges to the design, fabrication and motion measurement of the valve. The pulse jet operation is reviewed, computer models of operation are explained and experimental results are discussed.

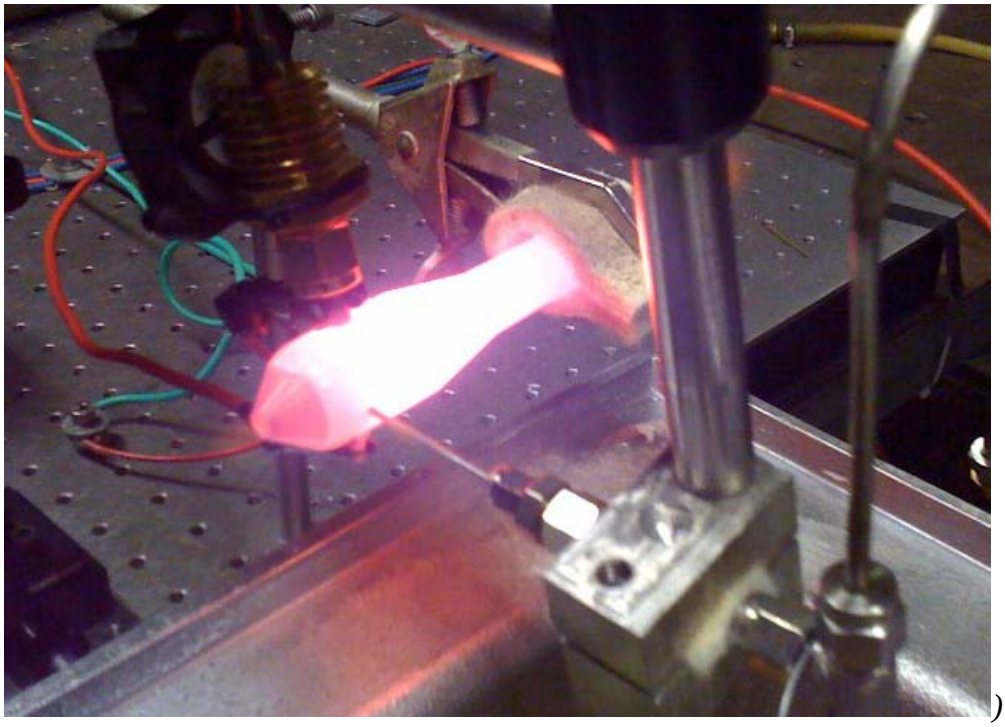

)

9.1 INTRODUCTION

Unmanned aerial vehicles (UAVs) have shown tremendous utility in harsh environments and their role in military and civilian applications will continue to expand. There is also an interest in developing a much smaller and more capable UAV or Micro-Aerial Vehicles (MAVs). . One of the limiting technologies is the propulsion system. To obtain the endurance necessary, these micro-propulsion devices must be air-breathers rather than rocket engines. To date, there has been very little demonstrated success in downsizing turbojet engines to the scale of interest for these small machines. Another possibility, electric motor driving a propeller with batteries, does not have the range required.

Pulse jet engines may be a viable candidate for propulsion of small UAVs. They are relatively simple engines with only a single moving part, the valve. The operation is described below[1]:

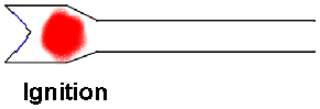

This is the instant that the fuel and air in the pulsejet are ignited. The effect is that a fireball is produced inside the engine which creates a great deal of heat and pressure. The reed valves are held closed by this pressure, effectively leaving the flame and hot gasses only one place to go...

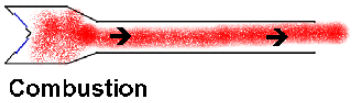

After ignition, the air and fuel continues to burn and expand in a phase called the combustion phase. During this phase the burning gases expand and travel down the tailpipe, exiting at the rear of the engine. The force of the gases leaving the engine in a rearwards direction creates the thrust.

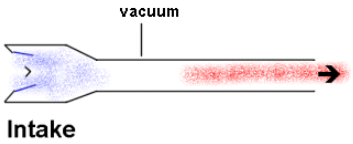

Because gases are have mass, the rapidly exiting exhaust gases have a tendency to keep moving -- even after the pressure inside the engine drops below the pressure outside. This causes a partial vacuum inside the engine that will open and draw air and fuel in through the valves in the front of the engine.

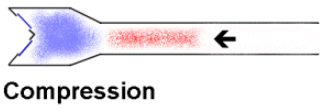

Some of the hot exhaust gases reflect from the open end of the pipe and move back towards the front of the engine by the vacuum. Because they have momentum, the gases in the tailpipe continue to move even after the vacuum is gone. This means that hot gases continue heading towards the front of the engine,

[1] www.aardvark.co.nz/pjet/howtheywork.shtml

compressing the fresh charge of air and fuel that has just been drawn in. The valves close because of the pressure and the hot gases ignite the explosive air/fuel mixture and the process repeats from step one.

The majority of the pulse jet engines in use are for model airplanes. The standard "hobby-sized" pulse jet engine is shown in Figure 1 mounted on a model airplane. This engine is 0.5 meters in length and approximately 50 mm in diameter at the combustion chamber near the front of the engine. It has been available on the market for over 50 years. It is relatively easy to start (put in compressed air and fuel into the front and a temporary spark plug to ignite the mixture and begin the process) and operates at 250 Hz using thin reed valves and liquid fuel pulled into the inlet via a venturi. These types of engines have been studied by Roberts and others.

Figure 1. Hobby-scale, valved pulse jet mounted on a model airplane. Size is about 500 mm long and about 50 mm in diameter at the inlet section on the right. Thrust is about 20 N.

Miniaturizing these engines has also been successfully demonstrated by Roberts [8] and a number of others for overall length scales as small as 40 mm. However, for sizes smaller than the hobby-size, the only successful designs were valveless and produced little thrust. While these valveless pulsejets were able to achieve the necessary scale, the performance was not sufficient for them to be a viable propulsion option for the proposed UAV application. Both their overall thrust and their specific impulse (a measure of the fuel efficiency) were both approximately a factor of two too low to meet the thrust and specific impulse objectives.

Valved pulsejets offer a five-fold increase in performance. The valve has two primary functions: it prevents hot products from leaving through the inlet (which generates negative thrust) and it allows the pressure developed during the heat release phase to reach a maximum value. However, valved pulsejets have only been demonstrated at scales that are ten times larger than desired for the small UAV application. At the target length of 40 mm, these pulsejets will

operate at nearly 3 KHz resonant frequency, with combustion chamber temperatures on the order of 2000° K.

Engine Size	Length, mm	Diameter, mm	Frequency, Hz	Thrust, N
Large – Hobby scale	500	50	250-280 Hz	20
Medium	110	11	1200	1
Small	40	4	3000	0.1

The goals of this project are to develop a valved pulse jet in the medium size range. The particular geometry of the engine is shown in the photograph of Figure 2. Without the head in place it is 115 mm long and has a mass of 100 gm. The design of this engine allows different heads with valves or valveless to be tested with a single body. The photograph on the left shows the engine in operation in a valveless configuration. Note the fuel inlet coming into the engine from the right.

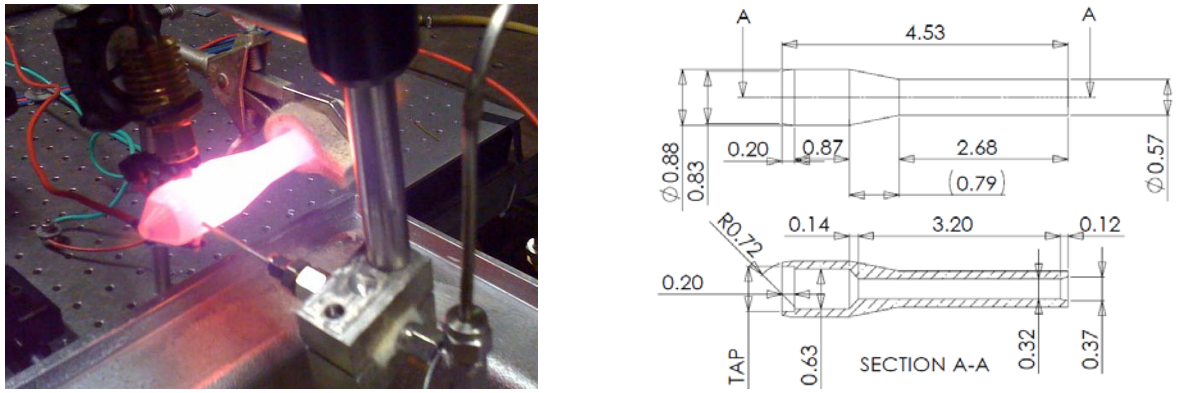

Figure 2. Medium sized pulse jet engine used for development

9.2 DETAILS OF THE PROJECT

The project included four main topics of research related to the smaller engine size:

1. determination of logistically friendly fuel
2. simulation of new valves with computational fluid dynamics model, including chemistry
3. design and evaluation of new valves
4. testing of new valves on appropriately-scaled pulsejet body in a wind tunnel.

These four tasks were not carried out sequentially nor independently from each other, but rather, in a highly coupled manner. The computational modeling effort included both modeling of the flow and combustion processes was intertwined with the experimental work. These four tasks will be described below.

9.2.1 LOGISTICALY-FRIENDLY FUEL

One of the requirements for this project was that the pulsejet must run on a hydrocarbon, preferably one that is storable. While a fuel supplied as a liquie was deemed to be too slow, a fuel that could be stored as a liquid but injected as a gaseous fuel would be ideal. Propane is an obvious choice, but the kinetics of propane are too slow to be viable for a small pulse jet.

Table 1. Candidate fuels investigated for the small pulse jet engine

						Energy density	Laminar flame speed			const. volume			
		density (L)	molar mass	fuel (DIPPR)		fuel	at 25 °C	at 100 °C	T flash	T auto	T adiabatic	T boil	T melt
fuel	formula	g/mL	kg/kmol	DHf, MJ/kmol	LHV, MJ/kg	MJ/L	cm/s	cm/s	°C	°C	°C	°C	°C
acetylene	HC_2H	0.38	26.037	228.20	48.28	18.25	105-155			305	2280		-80.75
butadiene monoxide	C_4H_6O		70.09				36-67	50-81	-50	430		65	-135
DEE	$C_2H_5OC_2H_5$	0.87	74.1	-279.40	33.79	29.36	30-48		-45	180	1981	35	-116
DME	CH_3OCH_3	0.66	46.1	-184.10	28.81	18.92	20-45		-41	350	1955	-24.8	-141.5
ethyl nitrate	$C_2H_5NO_3$	1.10	91.07	-153.97	13.61	14.97		70-86	10			87.6	-112
ethylene	C_2H_4		28.054	52.51	47.17		50-73	50-80	-149.2	450	1950	-103.74	-169.2
ethylene oxide	C_2H_4O	0.87	44.053	-52.63	27.65	23.97	70-90		-55.15	428.9	2138	10.45	-112.5
furfural	$C_5H_4O_2$	1.16	96.08	-201.60	2.48	27.24		60-87	60	315.85		161.7	-36.5
hydrazine	N_2H_4		32.045	95.186	16.00			84-95	38	24-270		113.5	2
hydrogen	H2		2.016		119.95	0.00	102-325			50-571	2210	-253	-259
hydrogen	H2		2.016		119.95	0.00						-253	-259
hydrogen	H2		2.016										
MAPD													
MAPP		0.58							-98	454	2010	-48	-120
propane, liquid	C3H8	0.49	44.097	-103.847	46.35	22.77	35-46		-104	450	1995	-42	-189.7
propargyl alcohol	C_3H_4O	0.97	56.06	51.54	30.60	29.68		77-110	36.1	365		114	-52
propylene oxide-1,2	C_3H_6O	0.82	58.09	-122.6	30.74	25.30	42-67	70-100	-10.5	430	2044	34.5	-97
propylene oxide-1,3	C_3H_6O	0.83	58.09	-104.8	31.01	25.73			-37	449		47.85	-104
propyne	C_3H_4		40.065	192.129	46.33		61-73		-28.15		2025	-23.2	-102.7
syngas	CO + 2H2	0.80	32.042	-238.572	19.93	15.94							

The wide range of fuels shown in Table 1were investigated and they include some rather exotic candidates. As the size of the pulse jet engine drops, the speed of the combustion process must increase and therefore a fuel with a fast flame speed is needed. Hydrogen is by far the fastest fuel but cannot be used because of the problems of storage as a liquid. Acetylene is next but again storage is a problem. The next level down includes Propyne and Ethylene which have similar flame speeds but less than half of the best fuels. Propyne (methyl acetylene) is faster than propane, but can be stored as a liquid at about 90 psi. This fuel was tested to determine if the kinetics were fast enough or if it could be made fast enough by pre-heating. The results of this pre-heating study are shown in Figure 3.

The pulsejet performance for the two fuels was measured from both the operational frequency and the sound pressure level. The preheating bath is shown in the photograph at the right in Figure 3. In the graph at the left, it is clear that as the temperature of Propyne approaches 120 C, the performance approaches that of ethylene. Thus, any pulsejet design that runs on propyne will most likely require preheating of the fuel. This is not an issue because there is ample heat given off by the engine, but the implementation will require careful design to avoid fuel residue clogging the lines.

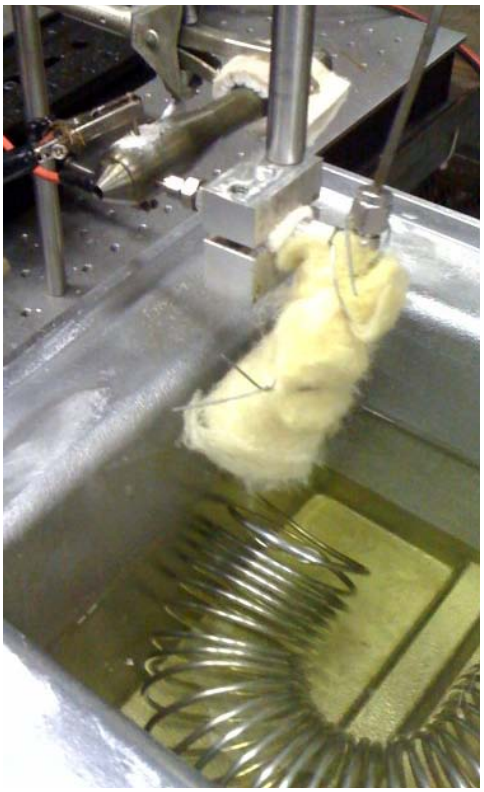

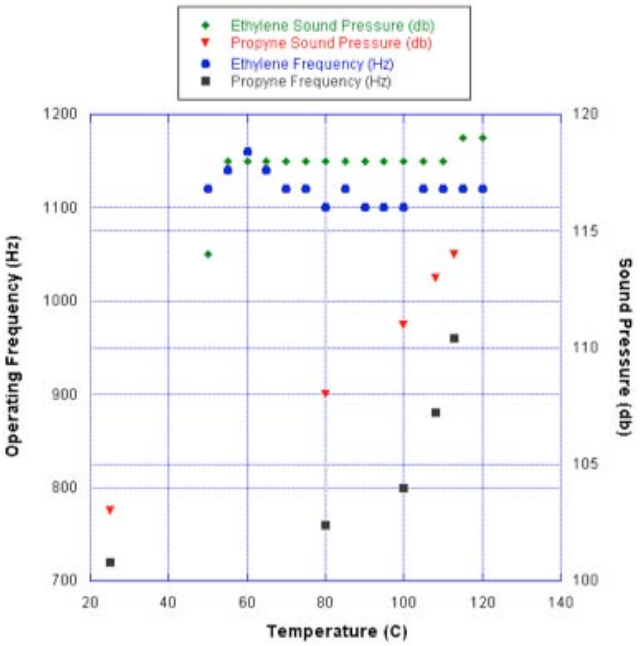

Figure 3. Performance of ethylene and propyne as a function of preheating the fuel

9.2.2 CFD SIMULATIONS

A commercially available CFD software, CFX^{TM} 5.7, was used to model the combustion and flow inside and outside of the pulsejet. Because the pulsejet is symmetric about the axis, the geometry was simplified to two-dimensional axisymmetric to save computational time. The mesh was generated in a 4 degree slice instead of the full 360˚ region. Figure5 shows the computational domain, which includes not only the interior of the pulsejet but also an extended domain to compute the flow field around the pulsejet. Because the boundaries were set far from the pulsejet, effects from pulsejet operation were negligible at the boundaries and the boundary condition was set to temperature T_0 equals to 300K and pressure P_0 equals to10^5 Pa.

A much smaller node distance was used for the flow field inside the pulsejet, shown in Fig. 4, than for the flow field outside the pulsejet, with approximately 18,000 nodes in this model. The code was also tested with a double mesh density case. However, results showed that further increasing the density of nodes does not affect the results. The computations were performed on the NCSU IBM Blade Center utilizing a single 3.0GHz Inter Xeon processor. Typical computational time for one combustion cycle of the pulsejet was about 18 CPU hours.

A k-ε model based on the Reynolds Averaged Navier-Stokes (RANS) equations was used because it offers a good compromise in terms of accuracy and robustness. The Eddy Dissipation Model was chosen as the combustion model. A propane-air five step reaction mechanism (propane oxidation, hydrogen oxidation, CO oxidation and both directions of water-gas shift reaction) provided by CFX 5 was used to simulate the combustion process.

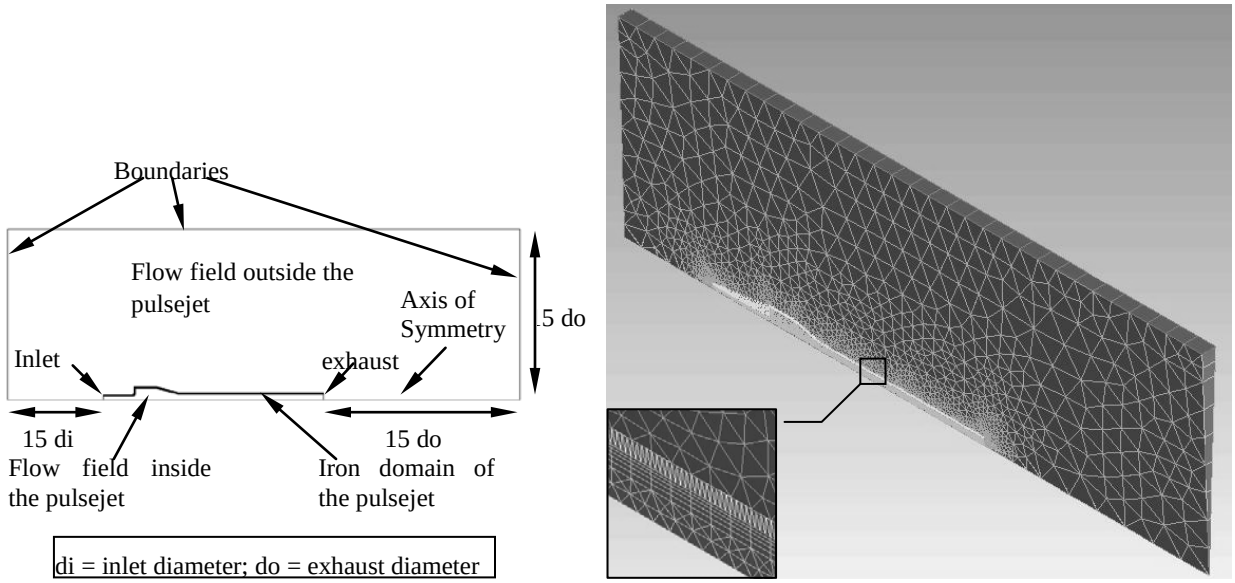

Figure 4. Numerical model for the pulsejet

There is a significant heat flux between the pulsejet walls and fluid inside the pulsejet. However, the frequency is high enough and the thermal inertia is large enough so that the wall temperature distribution can be assumed to be steady. To find the steady temperature distribution, a steady state simulation was performed, where boundary conditions were based on the average gas temperature in a transit simulation. This temperature distribution was further simplified to what is shown in Fig. 5, where the region between two dashed lines represents the combustion chamber, with a constant temperature of 1000 K along the combustion chamber and then an exponential decay toward both the inlet and exit planes, which are at 400° K.

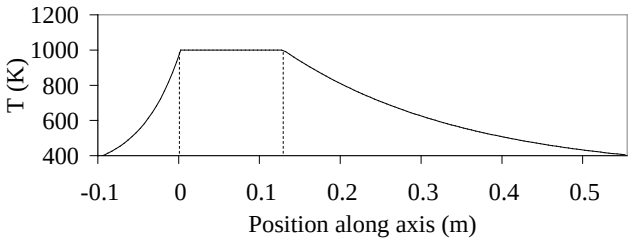

Figure 5. Temperature distribution along the pulsejet wall

The computational procedure for the pulsejet was initiated by setting the velocity to 0 m/s and temperature to 300 K everywhere within the computational domain. A stoichiometric mixture of air and propane was injected into the combustion chamber, ignited and it initiated the pulsed operation of the jet. This process is similar to pulsejet start-up in the analogous experiments.
It was also of interest to understand how the free stream velocities affected the operation of valveless pulsejets. Pulsejets flying at different forward flight speeds were modeled by changing the boundary condition at the inlet of the enclosure flow field. The free stream velocity was varied between zero and 80 m/s.

Monitors for pressure and temperature were set at precisely the same locations as in experiments along the centerline of the pulsejet. Data was acquired at every time step (10^{-5} s) during the simulation. Time-averaged temperature values were calculated by averaging the temperature over a cycle for comparison with experimental (TC) data. Mass flow determined through the valve was determined by a FORTRAN subroutine operating within the CFD model. The valve dynamics are modeled from the jet pressures and valve geometry. The motion of the valve responds to the combustion chamber pressure and opens to allow premixed fuel and air to enter the engine. The chamber pressure and the time steps dictates the mass flow of fuel that enters. The valve size is assumed to be the size of the inlet radius. A sketch of the cross-section of the engine used for the experiments is shown in Figure 6. This engine is the so called "SSP+" size and is 110 mm long with a maximum diameter of 11 mm. The valve dynamics modeled from jet and valve geometry and the results are shown in Table 2.

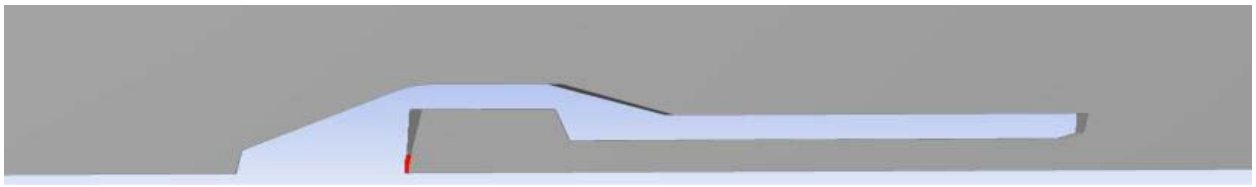

Figure 6. Symmetric model of valved pulse jet engine

Table 2. Model results for valved pulse jet engine

Fuel flow, gm/sec	**0.020**	**0.024**	**0.028**
Thrust, N	.24	.26	.28
ISP, sec	1280	1160	1080
Frequency, Hz	1010	1011	1016
PV Press, psi	4.38	4.62	4.93
Φ theoretical	1.19	1.38	1.50
Total fuel, gm	12	12	12
Flight time, sec	600	600	428

9.2.3 DESIGN AND EVALUATION OF INTAKE VALVES

The valve must passively control the intake of air into the combustion chamber and prevent hot products from escaping out through the inlet. Typically, one side of the valve is exposed to high temperature combustion products, and the other is cooled by the incoming air. In addition, it must operate at a KHz or two for tens of minutes, or millions of cycles. The resistance to opening must be small, as the pressure differential available to open the valve is on the order of a few psi (from previous measurements in an operating valved pulsejet at a larger scale) while there must be enough stiffness in the valve to close rapidly once the pressure differential goes to zero. If the valve is not stiff enough or is too massive, the valve will be open during some portion of the combustion cycle and hot products will be allowed to escape out the inlet. The combination of stiffness and mass produce a natural frequency for the valve. To evaluate the influence of mass and stiffness, an analytical model was produced which models the valves motion based on a prescribed pressure time profile (based on previous operating pressure measurements). In this model, the valve's stiffness and mass were independently varied and the resulting mass flux through the valve was calculated. The stiffness/mass combination that yielded the best mass flux was deemed the most desirable. The result from this simulation is illustrated in Figure 7.

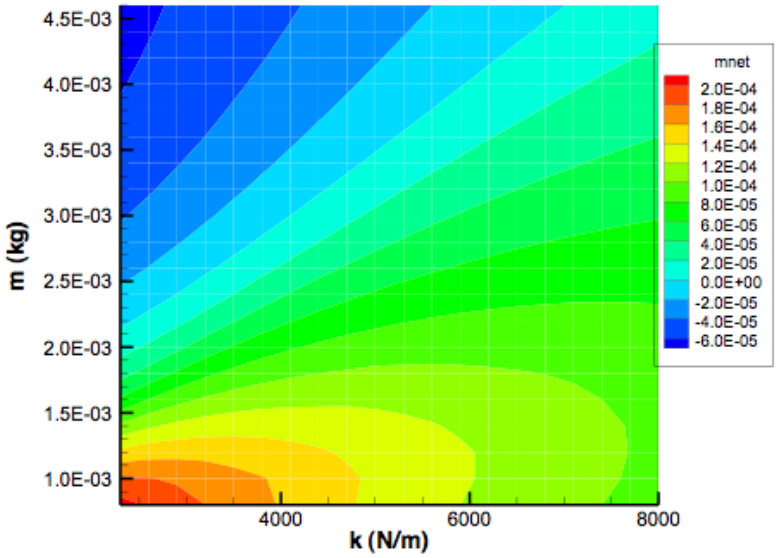

Figure 7. Plot of mass flux through valve as a function of valve mass and valve stiffness, from Matlab simulation using pre-defined pressure-time profile

From this figure, it is clear that to get the most mass flux through the valve, a light, flexible valve is necessary.

With this information in mind, a number of different valves were designed, fabricated and tested. An example of one valve is the flapper valve illustrated in Figure 8. The design of this valve is discussed below from the point of view of material selection, stress, fatigue life and operation. Unfortunately the result was a low pressure during the combustion process and a lack of thrust created. The pulse jet engine operation is influenced by the gas dynamics and combustion process. The timing of the valve and its relationship with the engine operation is difficult to measure since the engine will not operate if the valve is not timed correctly. Additional sensors and potentially control of the spark/ignition will be needed to refine the design of the valve.

Figure 8. Photographs of the flapper valve designed for the small pulse jet engine. The material is heat treated Inconel with a pair of flexures ground to a thickness of 25 µm.

Detail Design of a Flapper Valve

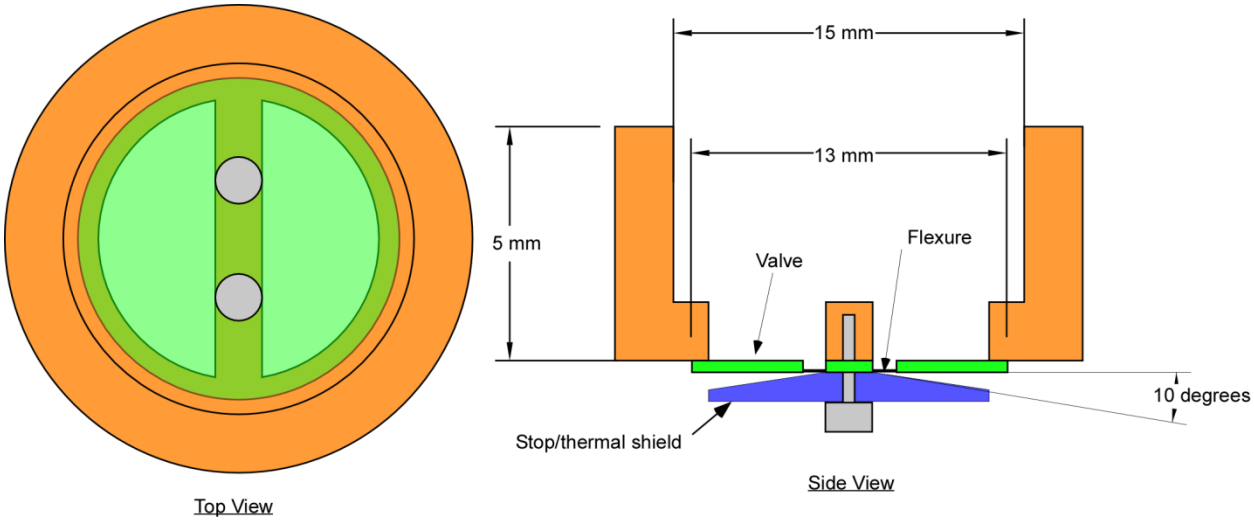

Figure 9. Sketch of the flapper valve with approximate dimensions

Physical Description of the Valve The flapper valve is a circular valve that is attached to the inlet manifold by a pair of screws as shown in Figure 9. It is protected from the hot combustion chamber by a cover that also acts as a valve motion limit. The valve material is Inconel X-750 that has excellent high temperature strength and fatigue properties. In the hardened condition, the yield strength is 190,000 psi (1310 MPa) and the fatigue strength at 1350 F is 47,000 psi (507 MPa). It has been obtained in the annealed state and will be machined and hardened for valve application.

The valve is a thin, flat circular plate with a thinned section that serves as the pivot. This flexure is also the conduit for heat transfer from the valve.

Design Process The valve operates in an extremely harsh environment - exact temperature is not known at this time but estimate is 1200 F and an operating frequency of 1000 Hz. It must operate for 20 minutes at these conditions or about $1x10^6$ cycles. To design the flexure, its size, the mass of the valve, location of the stop and peak stress must be calculated. In addition, the natural frequency should be calculated and compared with the operating frequency.

Valve Geometry The valve is shown in Figure 2. It is a circular shape with thickness (t) and diameter (D). It has two holes along the center line for #2-56 screws and two flat grooves that define the thin flexure regions.

The parameters of interest in this design are the thickness and diameter of the valve, and the size and location of the flexure pivots.

- Flexure thickness = t
- Width of the flexure = w
- Offset of the groove from the center of the valve = *Offset*
- Angle of segment = θ
- Centroid of the valve from flexure = L
- Area of valve segment = A_v

To find these parameters, the following equations have been developed. Figure 10 shows the parameters:

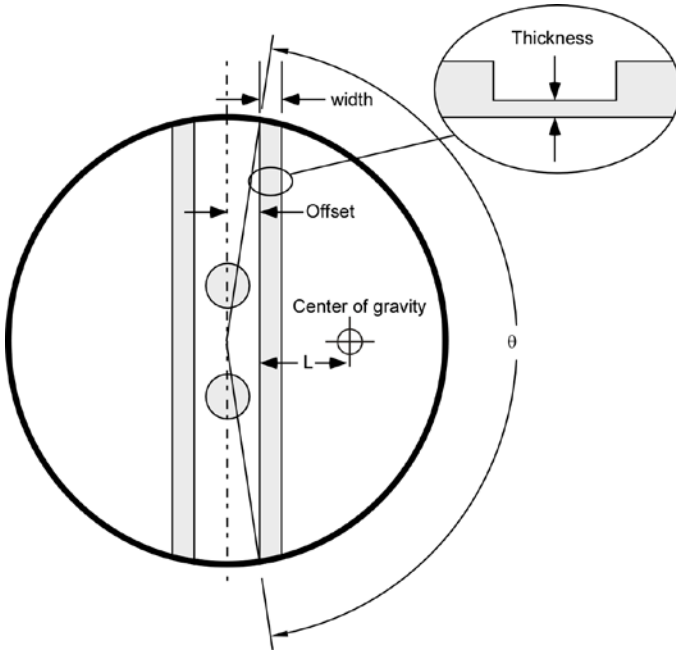

Figure 10. Geometry of the flexure Valve

$$\theta = \pi - 2\sin^{-1}\left(\frac{Offset}{R}\right)$$
$$L = \frac{4R\sin^3\left(\frac{\theta}{2}\right)}{3(\theta - \sin\theta)} \quad (1)$$
$$A_v = \frac{R^2}{2}(\theta - \sin\theta)$$

With these parameter calculated, the loading is needed to determine the deflection and stress in the flexure.

Loading The loading is determined by the vacuum generated by the reflected wave in the combustion process. This has been measured in previous engines and will need to be measured again as the size of the engine decreases.

$$p = pressure = 3psi = 21{,}000Pa$$
$$Force = F = pA_v \quad (2)$$
$$Moment = M = Fy$$

Material Properties The material for the valve must have good high temperature strength as well as fatigue and corrosion resistance. The material chosen is Inconel X-750. This material is mainly Nickel (70%) and Chromium (15%) with a host of other components. No other material has its high strength and fatigue resistance at temperatures up to 1350 F. The material properties are:

- Density = 8.22e-3 gm/mm^3
- Young's Modulus = 2.14e5 N/mm^2
- Yield Strength (room temperature) = 1310 MPa
- Fatigue Strength (1350 F) = 507 MPa

The Inconel X-750 is received in the annealed condition as a sheet material that is 0.010 inch thick. After machining it will be heat treated to achieve maximum performance. The heat treat process precipitation hardening requiring the part to be heated to 1300 F and kept there for 20 hours and then air cooled to room temperature. A heat treat oven is located in the Materials Science Dept at NC State.

Stress Analysis The key parameter is the bending stress at the flexure. This is dependent on the dimensions of the flexure and the load on the valve. Since the flexure is a simple 2D beam, the stress is calculated from beam theory based on the angle of deflection of the valve body, α. The body of the valve is assumed not to deflect. Figure 11 defines the model.

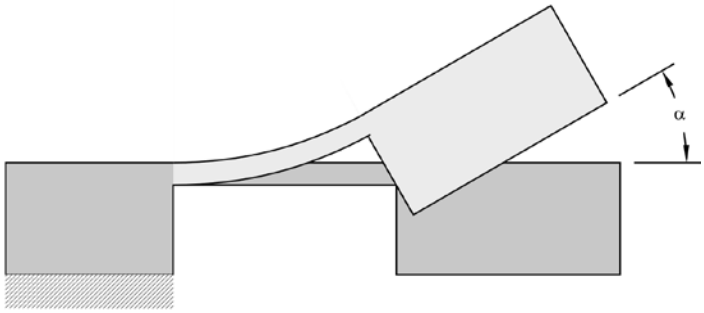

Figure 11. Beam model of flexure

The beam will have a maximum stress at the connection with the fixed part on the left in Figure 3. It will depend on the bending angle and thickness and length of the flexure. The equations for stress vs. deflection are given next where L is the distance to the load.

$$\frac{\partial^2 y}{\partial x^2} = \frac{M(x)}{EI} = \frac{Fx}{EI}$$
$$\frac{\partial y}{\partial x} = \alpha = \frac{1}{EI}\left(FL - \frac{x^2}{2}\right) \tag{3}$$

Equation (3) can be solved for the deflection if the load is known or for the maximum load when the deflection is given. Both have been calculated but to stay within the stress limit of the material the deflection must be limited. The limit has been set to 10 degrees which makes a fully open area of 23 mm^2 or an equivalent diameter of 5.5 mm (0.21 inch). Given the load to produce the desired angle, the stress can be found from the beam equation:

$$\sigma_{max} = \frac{F_\theta L t}{2I} \tag{4}$$

where F_θ is the force at the limit angle (which may be different than the vacuum force on the valve), *L* is the distance to the centroid, *t* is the thickness and *I* is the moment of inertia of the flexure.

Natural Frequency The mass of the valve and the stiffness from the beam analysis can be used to calculate the natural frequency of the valve/flexure assembly in Hz. For the valve designed, the natural frequency is about 500 Hz.

$$\omega_n = \frac{1}{2\pi}\sqrt{\frac{K}{M}} = \frac{1}{2\pi}\sqrt{\frac{\frac{F_\theta}{\theta L}}{M}} \tag{5}$$

Analytical Results The effect of flexure thicknesses and width was investigated using the equations developed above and the results are plotted in Figure 12. The vertical scale is the maximum stress on the flexure which is plotted as a function of the flexure thickness (horizontal scale) and the width of the flexure in the different plots. The fatigue limit at 1350 F is also plotted as the dotted line. Depending on the width of the flexure, a number of thicknesses would

be possible. Unfortunately, these thicknesses are extremely small so the decision was to make the thickness no less than 0.001 inch (0.0254 mm) which resulted in a width of 1.5 mm or (0.060 inch).

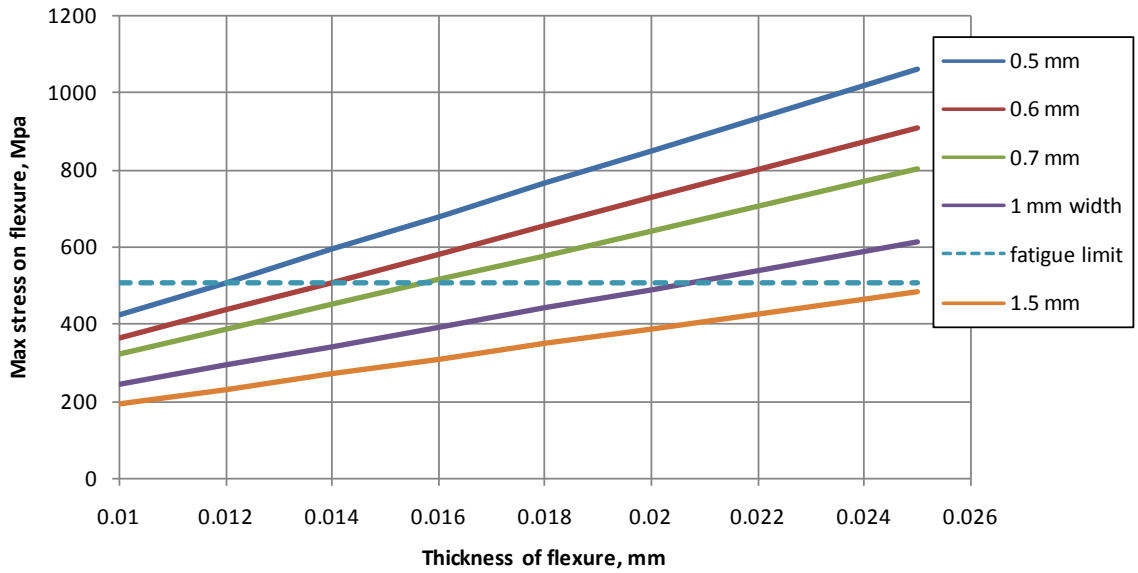

Figure 12. Details of the maximum bending stress for different flexure dimensions

Fatigue Analysis The maximum stress in Figure 4 is the peak stress for the flexure at 10 degrees. For a fatigue analysis, this stress goes from 0 to the peak and can be divided into a mean stress and an alternating stress. For this case where the minimum stress is zero, both the mean and the alternating stress are half of the maximum stress or 250 MPa. The Goodman criteria can be used to assess the factor of safety for this loading on the Inconel X-750 material. The results are shown in Figure 13. The vertical axis is the fatigue limit and the horizontal axis is the ultimate strength of the material. The plot shows the straight line between these two values for temperatures of 1350 F (top) and 1500 F (bottom). The alternating stress is plotted on the vertical axis and the mean stress is plotted on the horizontal axis and the point representing this loading condition is the square on the plot. The distance from the origin to the point can be extended to one of the temperature curves to evaluate the safety factor. For operation at 1350 F for 1,000,000 cycles, the factor of safety is 1.3. Unfortunately at 1500 F, there is no safety factor and the valve will not last the required million cycles. Therefore, it is important to measure the temperature at the flexure for the pulse jet engine. The fact that this valve design will have a thermal barrier built into the stop should keep the temperature below 1350 F.

A flapper valve was designed for the medium-size pulse jet engine design. A material with acceptable thermal properties was identified and purchased. The shape of the valve was finalized with a valve thickness of 0.010 in and a flexure thickness of 0.001 inch and a width of 0.060 inch.

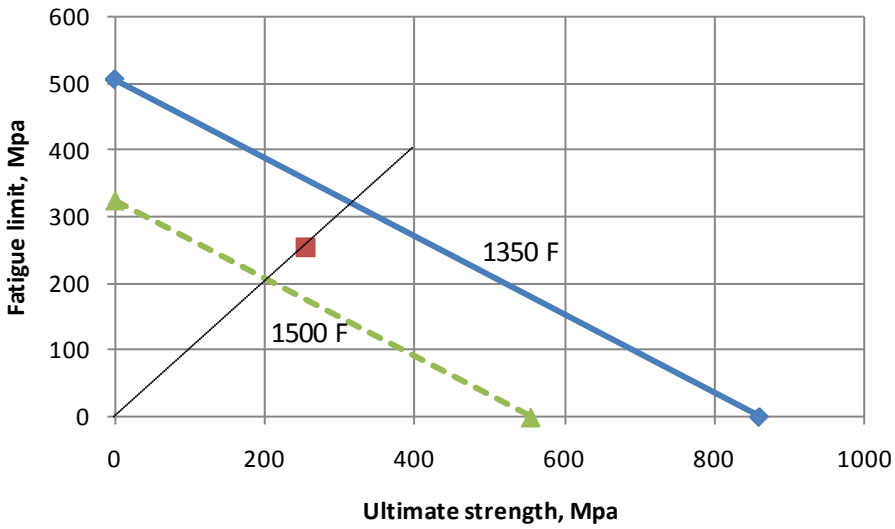

Figure 13. Goodman analysis of the fatigue problem for 1350 and 1500 F operating temperatures.

Valve Fabrication A number of vendors in the Raleigh area were contacted to machine the Inconel valves from 0.25 mm to 0.025 mm. Nobody was interested, in fact the response was "that is impossible". The Higgins Grinding Center of St.Gobain Abrasives in Worchester, Ma agreed to work with us to create the flexure. A fabrication process was jointly developed involving a fixture to hold several valve bodies that had previously been cut to the round shape and screw holes created using water jet machining. A special plastic bond diamond wheel was made for the machining. Two photographs are shown in Figure 14 illustrating the grinding process. The final flexure dimensions were within 10% of the target thickness.

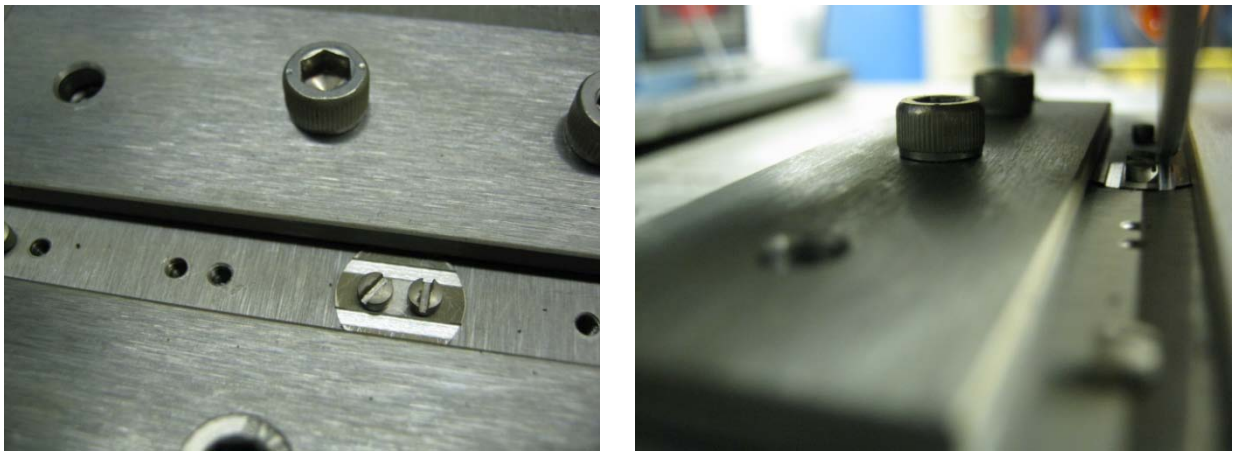

Figure 14. Photographs of the grinding process to create flexures on Inconel valves

Valve Displacement Measurement

The displacement of the valve was measured using a venture to create a vacuum source. It is limited in flow rate but provides an adjustable source to measure the steady state displacement of the valve when subjected to a given vacuum. In addition, an electronic pressure gage was placed in the valve chamber to read the vacuum pressure. The valve head is 14 mm diameter with approximately 0.001" thick flexure. The setup is shown in Figure 15 with a closeup of the valve in Figure 16.

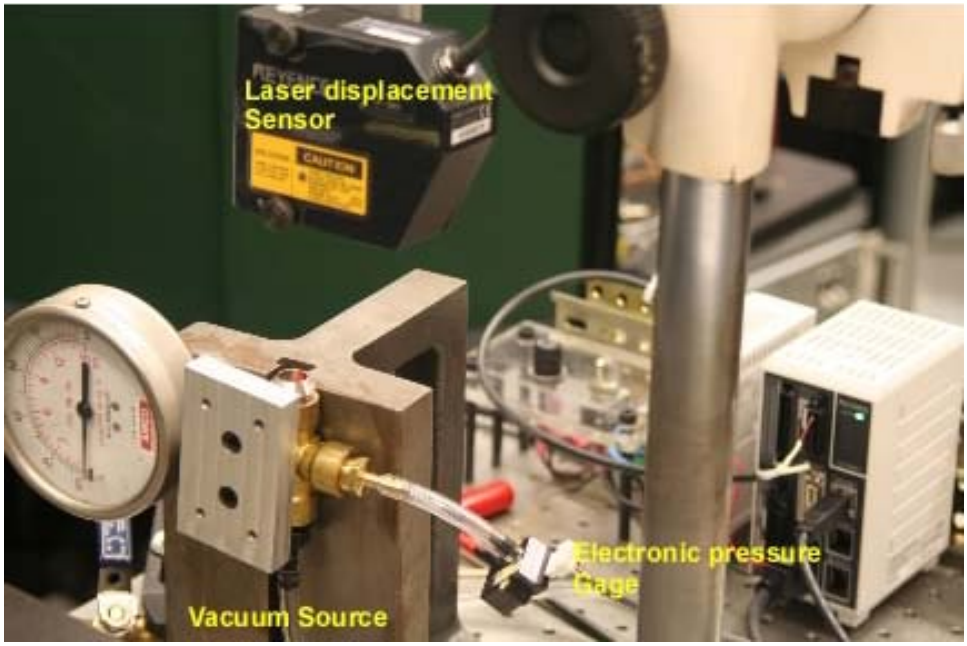

Figure 15. Setup for the displacement and pressure measurements.

Figure 16. Closeup of the valve head showing the location of the laser spot on the valve.

The point of measurement was moved in toward the pivot as shown in Figure 16 to allow the valve to deflect and still capture the measurement beam. It is quite a distance from the maximum deflection on the outer edge but the model can predict the deflection at any point assuming the rigidity of the flap. The model matched the measurements if the thickness of the flexure was changed to 0.0013 inches instead of the nominal 0.001 in. target for the grinding process.

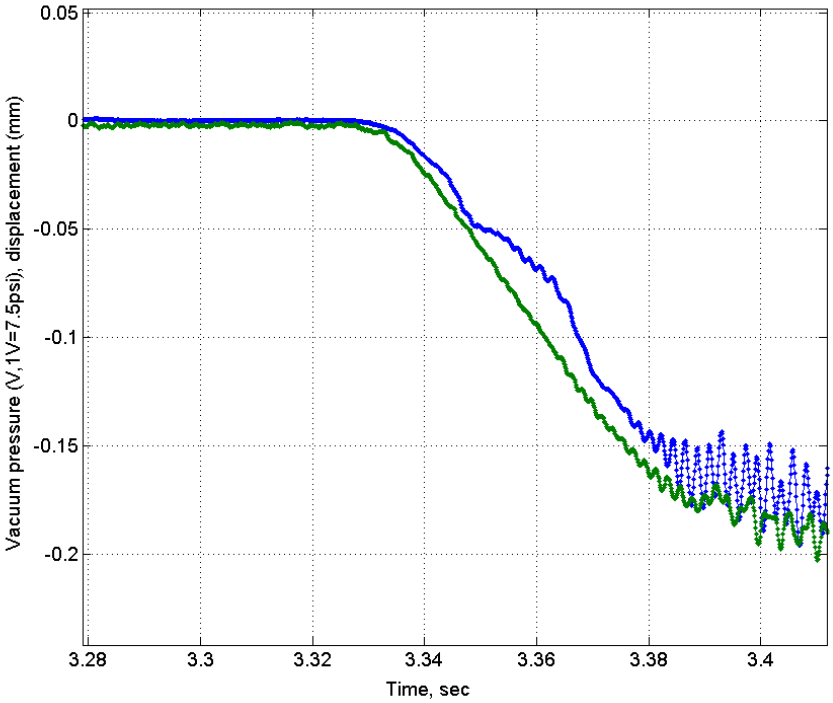

Figure 17. Plot of vacuum pressure (V) and valve displacement (mm)

Figure 17 shows one experiment with the valve displacement represented by the blue (upper) trace and the vacuum represented by the green (lower) trace. The displacement is in mm but the pressure is in V where 1 volt = 7.5 psi. The vacuum in this case is 1.35 psi or 9.5 KPa. The opening at the measured location was 0.175 mm which translates to 0.43 mm at the edge of the head. For this case, the flow rate should be on the order of 1.82 gm/sec or 1.5×10^6 mm^3/sec. This flow is nearly twice the maximum value needed to fill the inlet from the CFD model. Note the vibration on the valve displacement at the 600 Hz natural frequency of the valve.

The thickness of the flexure can be changed by lapping the valve. Both the mass of the valve (currently 0.115 gm for the 0.010 in thick Inconel) and the stiffness of the flexure (currently 1.7 N/mm for the 0.0013 in. thick) can be changed. The back of the valve can be lapped to reduce the flexure thickness and make it less stiff or the front can be lapped to reduce the mass.

Mass Flow through the valve

The mass flow through the valve is determined by the vacuum formed in the combustion chamber and the dynamic response of the valve to that pressure difference. A dynamic model of the valve motion was created in Matlab to see the influence of the valve properties on the lift and inlet flow. A sine wave input was used that is based on measurements made by Roberts using the hobby scale valved engine. If pressure information was available, the response of the valve can be predicted.

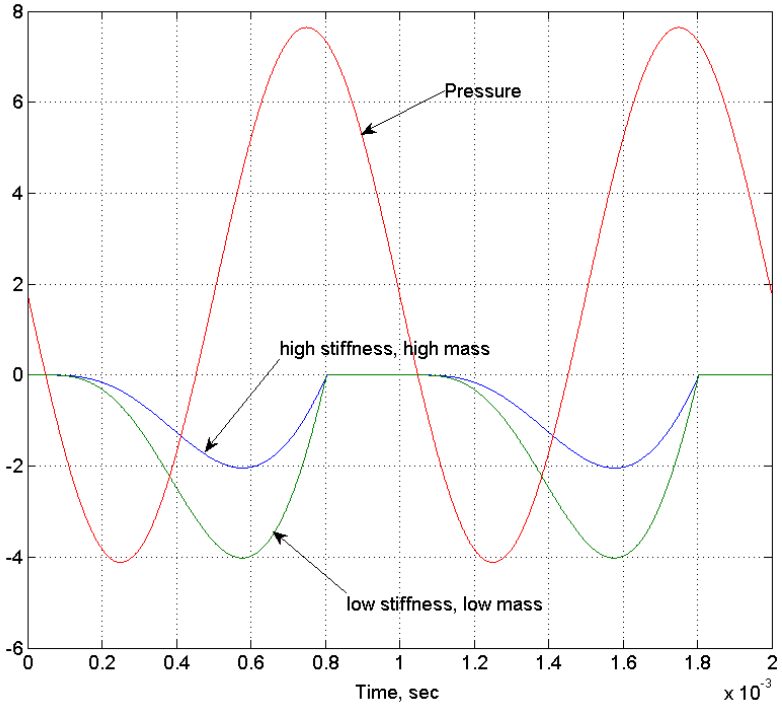

Figure 18. Pressure and valve motion of existing 14 mm valve and reduced stiffness, mass version.

Figure 18 shows the results of the analysis for the 14 mm valve described above. This figure shows the simulated pressure distribution (offset sine wave) and the opening of the valve in response to this pressure. The high stiffness, high mass case is the existing valve (natural frequency 600 Hz) and shows that the valve does not close as the combustion event occurs and the pressure moves through zero. In this case more than 50% of the combustion time, the valve would be open. Changing both the stiffness and the mass allows the valve to open faster and increase the flow rate not change the valve closure problem. Reducing the mass of the valve by lapping the existing valve can increase performance.

Figure 19 shows the results of reducing the mass of the valve to one third its existing value. In this case, the natural frequency was changed from 600 to 1000 Hz. Because the mass is reduced, the amplitude of the opening in response to the pressure is increased substantially. But Figure 19 also shows the effect of the valve stop on the operation of the valve. This stop has several

functions: 1) it limits the maximum opening of the valve to avoid over-stressing the flexure, 2) it controls the maximum motion of the valve from a dynamic standpoint and 3) it serves as a heat shield to reduce the effect of heating from the combustion event and reducing the life of the flexure.

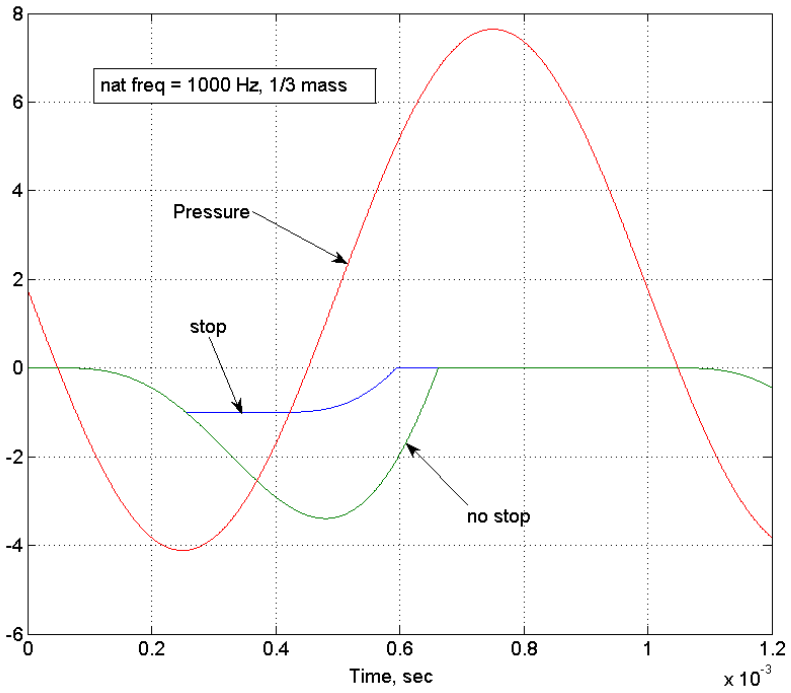

Figure 19. Current 14 mm valve reduced in thickness from 0.010 in to 0.0033 in. to increase the natural frequency to 1000 Hz. Also shown is the effect of the stop on dynamic motion.

When the valve hits the stop, it limits the opening and also reduced the time needed to close the valve. The changes from Figure 18 to 19 should have an important impact on the valve performance. Another idea that could be pursued is to make the stop a stiffer spring that would absorb some energy from the vacuum and assist in closing the valve when the combustion event occurred.

Pulse Jet Engine with Valve Operation

The data generated during operation of the valve is plotted in Figure 20 using the pressure zero (taken from previous tests at 0.4981 V) and a pressure scaling of 14.5 mv/psi as a function of time in seconds. Two conditions are plotted: 1) chopped air pushed into engine inlet at 600 Hz and 2) fired engine with hydrogen fuel supplied at 3.4 lpm with the same chopped air inlet.

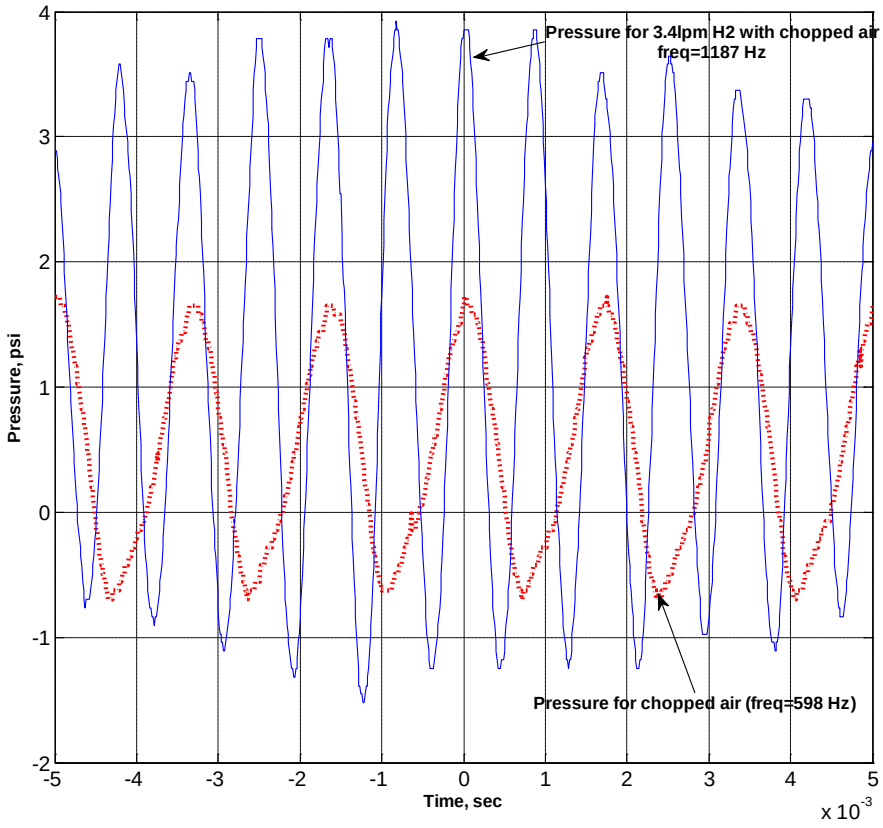

Figure 20. Pressure in pulsejet engine operating on Hydrogen

In this experiment, the engine ran as long at the pulsed pressure was applied. In general, the rational for the pulsed pressure was a startup assist. If the pressure was removed the motor would not remain operating. However, as shown in Figure 20, there was thrust created (more positive pressure than negative pressure) and the engine operating frequency changed from pulsed to fired frequency, meaning the frequency of the air column resonator. Videos of the valve motion at 25,000 frames per second made during operation show the valve moving but the relationship between valve motion and the pressure spikes was not recorded. Additional effort is needed to relate the valve motion, timing and pressure to the engine operation.

9.2.4 WINDTUNNEL TESTING

A high fidelity thrust stand was designed to allow the measurement of very small forces (~1 mN resolution) in a wind tunnel. The design is based on a flexural stage and the final design is shown below in Figure 21. A proximity sensor is used to measure the deflection of the mount, and this is calibrated using a weight before each use. This proved to be very successful. A wind tunnel was designed and built to allow the measurement of both drag and net thrust as a function

of forward flight speed. A pulsejet mounted on the dynamometer is shown below in the wind tunnel.

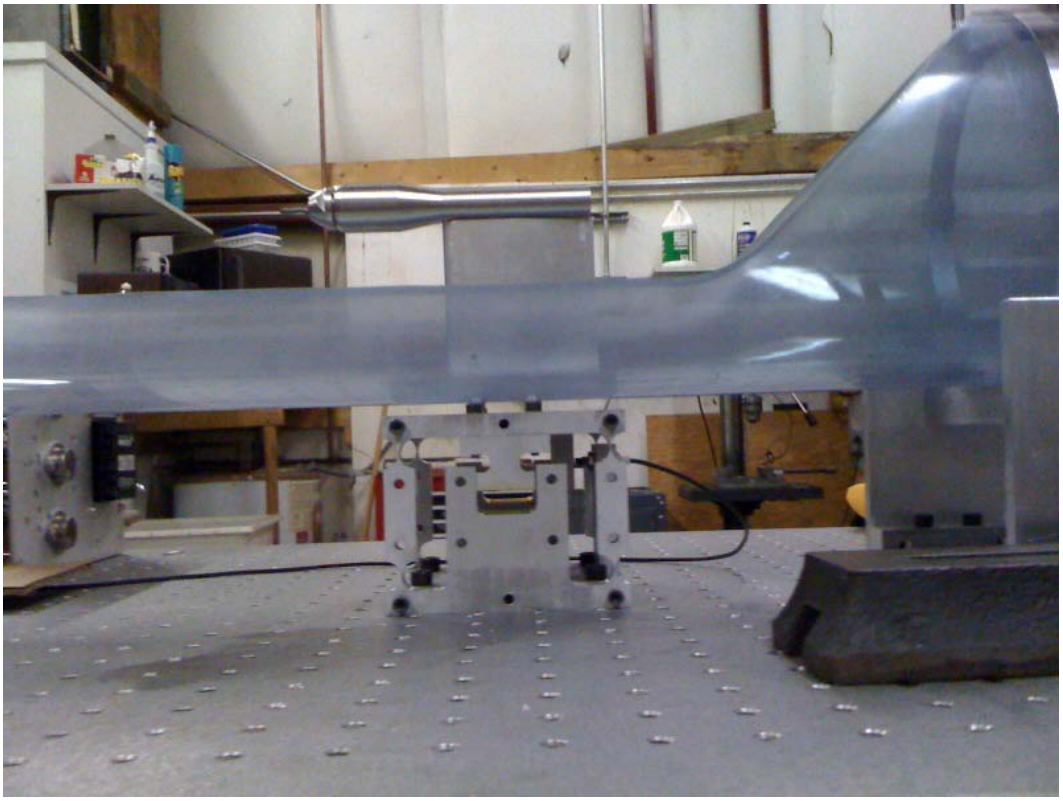

Figure 21. Thrust dynamometer with pulse jet engine mounted on airfoil shaped sting in the wind tunnel with the top of the wind tunnel removed for access to the engine.

The dynamometer was calibrated with the engine in place but not operating and compared to the CFD model of the drag. The results are shown in Figure 22. The drag follows the quadratic shape expected from the relatively blunt body. The drag is on the order of 5% of the theoretical thrust of the motor.

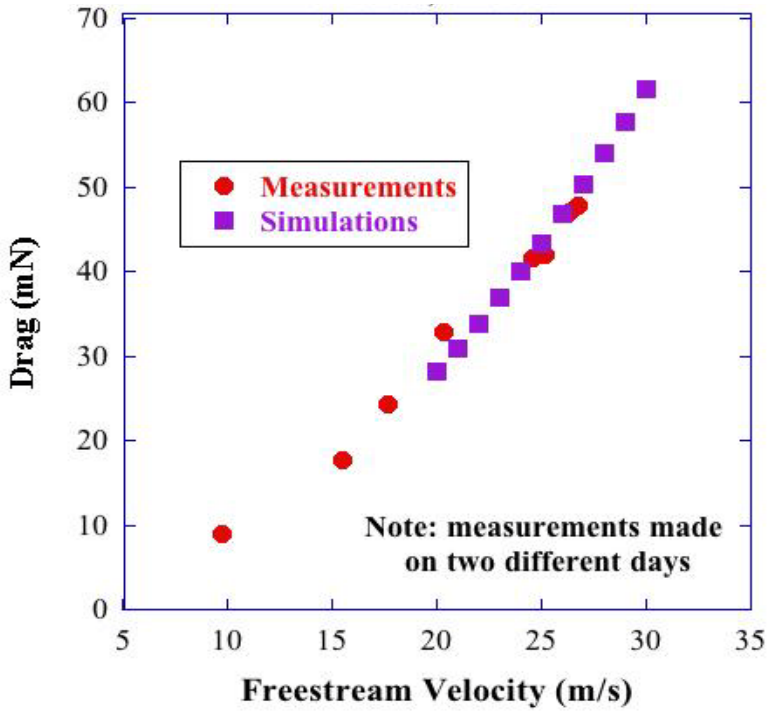

Figure21. Calibration of the wind tunnel dynamometer with the medium sized pulse jet engine on the stand.

9.3 CONCLUSIONS

The valved pulse jet engine in a medium size has not achieved its potential performance most probably due to the valve timing. A number of issues were addressed but question remain to be answered.

Valve Material

The standard material for the hobby-scale pulse jet engines is high-carbon tempered spring steel shown at left from the Beck Technology web page. But this material has a short life even in this low frequency (250 Hz) engine of about 30 minutes. This is equivalent to about half a million cycles. The small scale engines must operate for 20 minutes at frequencies greater than 1 KHz so high strength materials such as Inconel will be required.

Valve Design

A wide range of valve designs have been studied during the past six months with different materials, natural frequencies, motion and geometry. The results lead to a realization of the key role that the valve in the pulse jet operation. The valve is the primary timing device that relates the combustion cycle to the intake process and a more careful approach is needed to collect data on the role of valve for these small engines.

Opening time

The dynamics of the valve is and its role in the timing of the inlet charge plays a crucial role in the engine operation. But the opening must allow sufficient air and fuel into the engine but not too large influence the compression stroke from the reflected pressure wave. Again more careful work is needed to define the to quench the process.

Influence on combustion process

This work is still progressing, and to date we do not have a working valved pulsejet. Current activates include building an apparatus that will simulate the pressure fluctuations in both magnitude and frequency. With this device, the valve motion will be measured, via both a displacement sensor and high speed motion pictures (25,000 frames/sec) to determine if the valves are behaving as expected. Additionally, a higher fidelity CFD model is being developed to simulate the fluid-structure interactions occurring between the valve and the fluid.

REFERENCES

1. T. Geng, D. E. Paxson, F. Zheng, A. V. Kuznetsov, and W. L. Roberts, “Comparison Between Numerically Simulated and Experimentally Measured Flowfield Quantities Behind a Pulsejet”, submitted to Flow, Turbulence and Combustion, March 27, 2009
2. F. Zheng, D.E. Paxson, A.V. Kuznetsov and W.L. Roberts, “Numerical Study of a Pulsejet-Driven Ejector”, 45th AIAA/ASME/SAE/ASEE Joint Propulsion Conference & Exhibit, AIAA 2009-5185, 2009
3. F. Zheng, A. V. Kuznetsov and W. L. Roberts, “Numerical Study of Pulsejet Operation in an Enclosure”, 6th U.S. National Combustion Meeting, 23A2, 2009
4. T. Geng, D. E. Paxson, F. Zheng, A. V. Kuznetsov, and W. L. Roberts, “Comparison Between Numerically Simulated and Experimentally Measured Flowfield Quantities Behind a Pulsejet”, 44th AIAA/ASME/SAE/ASEE Joint Propulsion Conference & Exhibit, AIAA 2008-5046, 2008
5. F. Zheng, R. L. Ordon, T.D. Scharton, A. V. Kuznetsov and W. L. Roberts, “A New Acoustic Model for valveless pulsejets and its application to optimization thrust”, Journal of Engineering for Gas Turbines and Power, 130(4): No. 041501, 2008

6. F. Zheng, T. Geng, A. V. Kuznetsov and W. L. Roberts, “Numerical study of the effect of inlet size and adding inner object on the performance of valveless pulsejets”, AIAA-2007-5056, 2007.
7. T. Geng, F. Zheng, A.V. Kuznetsov, and W.L. Roberts, “Numerical Simulation on the Effect of Starting Vortex Ring on Pulsejet Thrust”, 43rd AIAA/ASME/SAE/ASEE Joint Propulsion Conference & Exhibit, AIAA 2007-5051, 2007
8. T. Geng, F. Zheng, A.P. Kiker, A.V. Kuznetsov, W.L. Roberts, “Experimental and numerical investigation of an 8-cm valveless pulsejet”, Experimental Thermal and Fluid Science, 31, pp. 641–647, 2007

FACULTY

THOMAS A. DOW

Director, Precision Engineering Center
Dean F. Duncan Distinguished University Professor in Mechanical Engineering
Professor, Department of Mechanical and Aerospace Engineering

BS, Mechanical Engineering, Virginia Polytechnical Institute, 1966
MS, Engineering Design, Case Institute of Technology, 1968
PhD, Mechanical Engineering, Northwestern University, 1972

After receiving his PhD degree from Northwestern University in 1972, Dr. Dow joined the Tribology Section of Battelle Columbus Laboratories and worked there for ten years. His research interests were in the areas of friction and wear and included studies on a wide variety of topics from lubrication of cold-rolling mills using oil-in-water emulsions to wet braking effectiveness of bicycle brakes to elastohydrodynamic lubricant film generation in ball and roller bearings. He developed experimental apparatuses, established analytical models, and corroborated those analyses with experimental measurements. Dr. Dow joined the faculty at North Carolina State University in 1982 and was instrumental in developing the academic and research program in precision engineering. His current research interests include the design of precision machining systems, real-time control, and metrology. He was one of the founders of the American Society for Precision Engineering and currently acts as the Executive Director.

JEFFREY W. EISCHEN

Associate Professor
Department of Mechanical and Aerospace Engineering

BS, Mechanical Engineering, UCLA, 1978
MS, Mechanical Engineering, Stanford University, 1981
PhD, Mechanical Engineering, Stanford University, 1986

Dr. Eischen has been with North Carolina State University since 1986 and his research areas of interest include: linear and nonlinear finite element analysis, multi-body kinematics/dynamics/control, fabric mechanics, and stress analysis in microelectronic devices. He teaches undergraduate courses in strength of mechanical components and mechanical design. His graduate courses include fracture mechanics and advanced machine design. He has collaborated with colleagues in the Precision Engineering Center for several years on computer simulation related projects dealing with precision shape control of disk drive read/write heads, stress and deformation analysis of high energy physics equipment, and contact lens mechanics.

RONALD O. SCATTERGOOD

Professor
Materials Science and Engineering Department

BS, Metallurgical Engineering, Lehigh University, 1961
MS, Metallurgy, Massachusetts Institute of Technology, 1963
PhD, Metallurgy, Massachusetts Institute of Technology, 1968

R.O. Scattergood is a Professor in the Department of Materials Science and Engineering. He received BS degrees in Mining Engineering and Metallurgical Engineering from Lehigh University. His MS and PhD degrees were obtained in Metallurgy from M.I.T. In 1968 he became a member of the basic research staff in the Materials Science Division at the Argonne National Laboratory. In 1981, he joined the faculty as a Professor of Materials Engineering at North Carolina State University.

Professor Scattergood's major research interests have been focused on the mechanical behavior of solids. He has worked in the areas of strengthening mechanisms in solids, mechanical testing, fracture, tribology, nanocrystaline materials and precision machining processes. He has expertise in He has published over 200 technical papers, books and reports.

STAFF

KENNETH P. GARRARD

Senior Research Associate
Precision Engineering Center

BS, Computer Science, North Carolina State University, 1979
MS, Computer Studies, North Carolina State University, 1983

As a full-time staff researcher at the Precision Engineering Center, Mr. Garrard's interests and duties have included the development of high performance control systems for ultra-precision machines and software development for custom, multiprocessor computer systems. He participated in the development of the original PEC fast tool servo as well as three other fast tool servo systems that have been delivered to commercial and government sponsors. One of these systems was built specifically for the on-axis turning of off-axis segments of conic surfaces of revolution and another is being used for the fabrication of inertial confinement fusion target mandrels. He has performed numerous prototype fabrication projects that required unique machine configurations and controller software. Mr. Garrard also has a long standing interest in the analysis of scientific data, programming language structures, sorting and searching algorithms, multiprocessor computer architecture and the design and implementation of hard real-time systems.

ALEXANDER SOHN

Research Assistant/Lecturer
Precision Engineering Center

B.S., Physics, University of Texas at Arlington, 1992
M.S., Physics, University of Texas at Arlington, 1994

Mr. Sohn joined the Precision Engineering Center in August, 1997 as a member of the technical staff. His current research interests range from machine design and metrology to the design and fabrication of nonimaging optics. Mr. Sohn's varied research activities began in microwave optics and atomic physics as a student at the University of Texas at Arlington and later progressed to precision machine design, design and fabrication of plastic optics as well as automation and machine vision at Fresnel Technologies, Inc. in Fort Worth, Texas.

PAULA J. KELLEY

Administrative Assistant
Precision Engineering Center

BA, Liberal Arts / Criminal Justice/ University of New Hampshire 1990

Ms. Kelley became a member of the PEC Staff in September 2007. Previously, Ms. Kelley has worked as the book-keeper for Lead Mine Elementary School in Raleigh; office manager for a private non-profit school in New Hampshire; supervisor for a school serving behaviorally challenged teens in Massachusetts and coordinator for a G.E.D. and job training program serving at risk teens. Ms. Kelley provides the overall administrative support for the Center. She left the PEC in the spring of 2009.

MONICA RAMANATH

Administrative Assistant
Precision Engineering Center

BS, Accounting / North Carolina State University, 2001

Ms. Ramanath joined the PEC in September 2009. Previously, Ms. Ramanath worked as an Accounting Technician in the College of Education; book-keeper for 11 branches of the YMCA.

CONSULTANTS

KARL FALTER

Consulting Engineer

BS, Mechanical Engineering, North Carolina State University, 1987
MS, Mechanical Engineering, North Carolina State University, 1989
PhD, Mechanical Engineering, North Carolina State University, 1992

Prior to working as an independent consultant, Dr. Falter was a senior development engineer with Eastman Kodak from 1997 to 2003. He designed and developed electrical and control systems for custom precision machine tools. Dr. Falter also worked for Rank Pneumo from 1994 to 1997.

DAVID YOUDEN

Senior Engineer, Olympic Precision, Inc.
Adjunct Lecturer, Department of Mechanical and Aerospace Engineering

ASME, Central New England College, Worcester, MA, 1965

Prior to joining Olympic Precision's Precision Valley Institute for Advanced Manufacturing in 2006, Mr. Youden was an Applied Research Engineer at Eastman Kodak Company's Manufacturing Systems Technology Division. Between 1984 and 1997 he was Research and Development Manager at Rank Pneumo, a division of Rank Taylor Hobson Inc. Before that, he was Director of Engineering at the Cone Blanchard Machine Company. He has also worked at Ocean Systems, Inc. of Reston, Virginia and the Heald Machine Company, a division of Cincinnati Milacron. During his professional career, Mr. Youden has been granted numerous patents in the field of machine tools, and he has published and presented technical papers on the design and testing of ultra-precision machine tools in the US, Japan, and Germany. In 2006, Mr. Youden received The American Society for Precision Engineering's Lifetime Achievement Award for his contributions to the field of precision engineering.

GRADUATE STUDENTS DURING 2009

DAVID BREHL's extensive industrial career includes a range of design, development, and project engineering roles with AERCO International, BOC Gases, and Babcock & Wilcox. A deepening interest in design of integrated electromechanical systems, along with a desire to focus his career on technology development, led him to pursue a PhD in Mechanical Engineering at NCSU; this follows a recent Master's in ME program at Stevens Institute of Technology (Hoboken, NJ). He joined the PEC in August 2004 and is currently employed at Terrera North America in Charlotte, NC.

QUNYI CHEN first entered NCSU in 1997. He obtained a MSME in 1998 and a MSEE in 1999. After graduation, Qunyi worked at GE Healthcare to design and develop electro-mechanical subsystems for medical diagnostic X-ray equipment. His passion for technology development in precision electro-mechanical engineering led him to return to NCSU in 2005, where he was able to find an ideal match on the PEC's Fast Long Range Actuator project in June 2006. Qunyi was born and raised in Jiangsu, China. There, he received a BSME in 1993 and a MSME in 1996 before coming to the United States.

TIM KENNEDY was born and raised in Chapel Hill, NC. Tim received his BS from NCSU in May 2004. Before working at the PEC, he worked at the Analytical Instrumentation Facility for two years as an undergraduate research assistant. He started working with the PEC August 2004 and currently works for the US Patent and Trademark Office in Washington, DC.

BRANDON LANE joined the PEC in the June, 2008 after graduating with a B.S. in Mechanical Engineering from University of Nevada, Reno. In Reno, he gained engineering experience working as an intern for the Robotics R&D division of Hamilton Company, designing components and technical drawings for automated fluid handling workstations. He also worked as an undergraduate researcher for the UNR Nanocomposites lab where he researched fabrication techniques for carbon nanofiber and nanotube composites. These experiences in R&D sparked his interest in a career that continues higher levels of engineering learning and understanding. His schedule as a graduate student is supplemented by distance running, fishing, and mountain hiking in his free time.

MEIRONG SHI is a graduate student of Department of Material Science and Engineering. She received her MS degree in Microelectronics from East China Normal University in 2007 and joined the PEC in August 2008. The research project Meirong is involved in now is Material Effects and Tool Wear in Vibration-Assisted Machining.

ERIK ZDANOWICZ was raised in Hendersonville, NC. After receiving his BS in mechanical engineering from NCSU in May of 2007, Erik began his MSME degree and worked as a teaching assistant for Statics and Dynamics. Erik joined the PEC in January of 2008 as a research assistant for the redesign of the first generation Fast Long Range Actuator. Upon completion of his MS degree in 2009, Erik hopes to utilize the valuable experience gained at the PEC when he takes his position with Harris Corporation in Melbourne, FL.

GRADUATES OF THE PRECISION ENGINEERING CENTER

Student	Degree	Date	Company/Location
Jeffrey Abler	PhD	December 1994	Lexmark, Inc, Lexington, KY
William Allen	PhD	December 1994	North Carolina State Univ. Raleigh, NC
Kelly Allred	MS	June 1988	
Christopher Arcona	PhD	May 1993	Norton Worcester, MA
Bradford Austin	MS	June 2000	IBM Corporation Fishkill, NY
Markus Bauer	PhD	December 2001	QED, Inc, Rochester, NY
Tom Bifano	PhD	June 1988	Photonics Center, Boston University, Boston, MA
Scott Blackley	MS	May 1990	Motorola Austin, TX
Peter Blake	PhD	December 1988	NASA Goddard Greenbelt, MD
Dave Brehl	PhD	December 2008	Tessera North America Charlotte, NC
Brett Brocato	MS	June 2005	Tessera North America Charlotte, NC
Nathan Buescher	MS	May 2005	Consolidated Diesel Rocky Mount, NC
Mark Cagle	MS	June 1986	NASA-Langley Norfolk, VA

John Carroll	PhD	January 1986	Cummins Engine Co. Columbus, IN
Matthew Cerniway	MS	October 2001	Naval Surface Warfare Ctr West Bethesda, MD
Damon Christenbury	MS	June 1985	Michelin Tire Co. Spartanburg, SC
Stuart Clayton	MS	May 2003	Naval Depot Cherry Point
James Cuttino	PhD	December 1994	UNC – Charlotte Charlotte, NC
Bob Day	PhD	July 1998	Los Alamos National Lab Los Alamos, NM
Joseph Drescher	PhD	May 1992	Pratt & Whitney East Hartford, CT
William Enloe	MS	December 1988	ITT Roanoke, VA
Karl Falter	MS	December 1989	Eastman Kodak Company Raleigh, NC
Peter Falter	PhD	May 1990	Lockheed-Martin Orlando, Florida
John Fasick	MS	May 1998	Kodak Rochester, NY
Steven Fawcett	PhD	June 1991	MicroE Natick, MA
Karalyn Folkert	MS	May 2005	Consolidated Diesel Rocky Mount, NC
Andre Fredette	PhD	May 1993	IBM Research Triangle Park, NC
Karl Freitag	MS	August 2004	Northrop Grumman Baltimore, MD

Stephen Furst	MS	December 2008	NCSU Raleigh, NC
David Gill	PhD	August 2002	Sandia National Laboratories Albuquerque, NM
Jim Gleeson	MS	June 1986	Battelle Columbus Labs Columbus, OH
Mary Smith Golding	MS	May 1990	Harris Corporation Melbourne, FL
David Grigg	PhD	August 1992	Zygo Corporation Middlefield, CT
Hector Gutierrez	PhD	October 1997	Florida Inst. Of Tech. Melbourne, FL.
Christian Haeuber	MS	December 1996	Harris Corporation Melbourne, FL
Simon Halbur	MS	December 2004	
Matias Heinrich	MS	July 2001	Vistakon Jacksonville, FL
Gary Hiatt	PhD	May 1992	Caterpillar Zebulon, NC
David Hood	MS	May 2003	
Peter Hubbel	MS	December 1991	Delco Electronics Kokomo, IN
Konrad Jarausch	PhD	December 1999	Intel Corporation San Jose, CA
Bradley Jared	PhD	December 1999	Sandia National Laboratories Albuquerque, NM

David Kametz	MS	August 2002	Naval Air Warfare Center Aircraft Division Patuxent River, MD
Jerry Kannel	PhD	June 1986	Battelle Columbus Labs Columbus, OH
Tim Kennedy	PhD	May 2008	US Patent and Trademark Office, Washington, DC
Byron Knight	MS	May 1990	US Air Force Washington, DC
Lucas Lamonds	MS	July 2008	Micron Technology Boise, ID
Mark Landy	MS	June 1986	Battelle Columbus Labs Columbus, OH
Mike Loewenthal	MS	December 1988	SVG Norwalk, CT
Michael Long	PhD	June 2000	Eastman Kodak Rochester, NY
Bryan Love	MS	May 2001	Virginia Tech
Michael Hung-Tai Luh	MS	June 1989	Proctor and Gamble Cincinnati, OH
Dan Luttrell	MS	1987	Moore Tool, Inc New Britain, CT
Edward Marino	MS	September 1999	Pratt Whitney Hartford, CT
Edward Miller	MS	December 2000	General Electric Greenville, SC
Michele Miller	PhD	December 1994	Michigan Tech. University Houghton, MI
Paul Minor	MS	September 1998	Hartford, CT

Gary Mitchum	MS	June 1987	Harris Corporation Melbourne, FL
Charles Mooney	MS	December 1994	AIF – NC State University Raleigh, NC
Patrick Morrissey	MS	May 2003	
Larry Mosley	PhD	June 1987	Intel Corporation Chandler, AZ
Patrick Moyer	PhD	May 1993	UNC-Charlotte Charlotte, NC
Nobuhiko Negishi	MS	August 2003	
Ayodele Oyewole	MS	October 1997	Pratt and Whitney East Hartford, CT
Hakan Ozisik	PhD	December 1989	
Witoon Panusittikorn	PhD	December 2004	Fabrinet Kookot, Lumlookka Thailand
John Pellerin	MS	May 1990	Sematech Austin, TX
Travis Randall	MS	August 2004	MBA student NCSU
Ganesh Rao	MS	December 1994	Oak Ridge National Lab Oak Ridge, TN
John Richards	MS	September 1997	Intel Corporation San Jose, CA
Walter Rosenberger	MS	May 1993	The East Group Kinston, NC
Alex Ruxton	MS	December 1996	Pratt &Whitney Palm Beach, Florida
Anthony Santavy	MS	August 1996	Ford Dearborn, MI

Keith Sharp	PhD	May 1998	Morgan Crucible Dunn, NC
Gordon Shedd	PhD	March 1991	Corning , Inc Corning, NY
Wonbo Shim	PhD	May 2000	Seagate Inc. Oklahoma City, OK
Robert Skolnick	MS	September 1997	San Diego, CA
Denise Skroch	MS	May 1989	IBM Corporation Raleigh, NC
Elizabeth Smith	MS	April 1989	
Stanley Smith	PhD	May 1993	
Ronald Sparks	PhD	May 1991	Alcoa Corporation Pittsburg, PA
Brent Stancil	MS	December 1996	Harris Corporation Melbourne, FL
Gene Storz	MS	May 1994	
Anand Tanikella	PhD	August 1996	Norton Industrial Ceramics Northboro, MA
Donna Thaus	MS	May 1996	Northern Telecom Research Triangle Park, NC
John Thornton	MS	December 1993	Digital Instruments Santa Barbara, CA
Michael Tidwell	MS	December 1991	
John Tyner	MS	June 1995	Patuxent Naval Air Station Patuxent River, MD
Nadim Wanna	MS	December 2006	ExxonMobil Corporation Houston, TX

Robert Woodside	MS	December 2006	Harris Corporation Melbourne, FL
Tao Wu	PhD	December 2003	
Yanbo Yin	PhD	October 2007	

ACADEMIC PROGRAM

Problems and limitations associated with precision manufacturing can originate in the machine, the process, or the material. In fact, most problems will probably be caused by a combination of these factors. Therefore, improvement of current processes and development of new manufacturing methods will require knowledge of a multi-disciplinary array of subjects. The educational goal of the Precision Engineering Center is to develop an academic program which will educate scientists and engineers in metrology, control, materials, and the manufacturing methods of precision engineering.

The graduate students involved in the Precision Engineering Center have an annual stipend as research assistants. They can take up to 3 classes each semester while spending about 20 hours per week on their research projects. These students also work in the Center full-time during the summer months.

The Precision Engineering Center began in 1982 with an emphasis on the mechanical engineering problems associated with precision engineering. As a result, the original academic program proposed was biased toward courses related to mechanical design and analysis. However, as the research program has developed, the need for complementary research in sensors, materials, and computers has become obvious. A graduate student capable of making valuable contributions in the computer area, for example, will require a significantly different academic program than in mechanical engineering. For this reason, the Center faculty has set a core curriculum and each student in the program is required to take at least 3 of these core courses. The remainder of the courses for the MS or the PhD degree are determined by the university or department requirements and the faculty committee of the student.

The required courses are:

- MAE 545 Metrology in Precision Manufacturing
- PY 516 Physical Optics
- MAT 700 Modern Concepts in Materials Science
- CSC (ECE) 714 Real Time Computer Systems

PhD DEGREE PROGRAM

The PhD program in Precision Engineering has been set up as a multi-disciplinary program, drawing upon courses throughout the University to provide background and expertise for the students. It should contain required courses to insure solid grounding in the fundamentals plus electives to prepare the student in his area of specialization. Because Precision Engineering is concerned with an integrated manufacturing process, students interested in computer control, materials, machine structure, and measurement and actuation systems are involved in the program. Student research projects include the wide variety of topics addressed in this report. Each student's thesis should have an experimental component because Precision Engineering is basically a hands-on technology.

MS DEGREE PROGRAM

The Master of Science degree will have a higher percentage of application courses than the PhD degree. The emphasis will be to develop the foundation for involvement in precision engineering research and development. A total of 30 credits, including 6 credits for the MS thesis, are required. The thesis, while less comprehensive than the PhD dissertation, will be directed at important problems in Precision Engineering. Typically, the MS program will take four semesters plus one summer.

UNDERGRADUATE PROGRAM

The undergraduate degree broadly prepares an engineering student for industrial activities ranging from product design and engineering sales to production implementation. Because a large share of engineers only have the BS degree, these will be the people who must implement the new technology developed in research programs like the Precision Engineering Center. Therefore, a way must be found to acquaint engineers at the BS level with the techniques, problems, and potential of precision manufacturing.

In most undergraduate degree programs only limited time is available for technical electives. However, these electives offer the student the opportunity to expand his knowledge in many different directions. Beginning graduate courses (such as metrology) can be used as undergraduate electives.

Undergraduate projects and summer employment have also been utilized to include undergraduate students into the research program of the Center. During the 1998-1999 academic year, four undergraduate students in Mechanical Engineering were involved various projects at the PEC.

STUDY PLANS

Study plans for several example students are given below both for the MS and the PhD degree. Because of the breadth of the field and the wide range of thesis topics, few if any study plans will be exactly the same. The plan will depend upon the student's background, his interests, his thesis topic, the department, and the chairman and members of his committee.

PhD PROGRAM IN MECHANICAL ENGINEERING

Major Courses:

- MAE 740 Advanced Machine Design I
- MAE 741 Advanced Machine Design II
- MAE 706 Heat Transfer Theory & Applications
- MAE 713 Principles of Structural Vibration
- MAE 760 Computational Fluid Mechanics and Heat Transfer
- MAE 545 Metrology in Precision Manufacturing
- MAE 715 Nonlinear Vibrations
- MAE 716 Random Vibration
- MAE 714 Analytical Methods in Structural Vibration
- MAE 742 Mechanical Design for Automated Assembly
- MAE 895 Doctoral Dissertation Research

Minor Courses:

- MA 511 Advanced Calculus I
- MA 775 Mathematical Methods in the Physical Sciences I
- CSC 780 Numerical Analysis II
- PY 516 Physical Optics
- ECE 716 System Control Engineering
- MAT 700 Modern Concepts in Materials Science
- ECE 726 Advanced Feedback Control
- ECE 764 Digital Image Processing

PhD PROGRAM IN MATERIALS ENGINEERING

Major Courses:

- MAT 710 Elements of Crystallography and Diffraction
- MAT 700 Modern Concepts in Materials Science
- MAT 556 Composite Materials
- MAT 715 Transmission Electron Microscopy
- MAT 795 Defect Analysis/Advanced Materials Experiments
- MAT 753 Advanced Mechanical Properties of Materials
- MAT 712 Scanning Electron Microscopy
- MAT 895 Doctoral Dissertation Research

Minor Courses:

- PY 414 Electromagnetism I
- ST 502 Experimental Statistics for Engineers I
- MAE 740 Advanced Machine Design I
- MAE 741 Advanced Machine Design II
- MAE 545 Metrology in Precision Manufacturing
- PY 516 Physical Optics
- MA 401 Applied Differential Equations II

PhD PROGRAM IN ME (FOR STUDENT WITH MS DEGREE)

- ECE 716 System Control Engineering
- ECE 791 Gate Array Design
- MAT 700 Modern Concepts in Materials Science
- PY 516 Physical Optics
- MA 502 Advanced Mathematics for Engineers and Scientists II
- MA 775 Mathematical Methods in the Physical Sciences I
- MA 780 Numerical Analysis II
- MAE 732 Fundamentals of Metal Machining Theory
- MAE 740 Advanced Machine Design I
- MAE 741 Advanced Machine Design II

- MAE 545 Metrology in Precision Manufacturing
- MAE 716 Random Vibration

MS PROGRAM FOR ME STUDENT

- MAE 713 Principles of Structural Vibration
- MAE 740 Advanced Machine Design I
- MAE 545 Metrology in Precision Manufacturing
- MAT 700 Modern Concepts in Materials Science
- PY 516 Physical Optics
- MA 501 Advanced Math for Engineers and Scientists I
- MA 502 Advanced Math for Engineers and Scientists II
- MAE 695 Master's Thesis Research

MS PROGRAM FOR COMPUTER SCIENCE STUDENT

- CSC 501 Operating Systems Principles
- CSC 506 Architecture of Parallel Computers
- CSC 512 Compiler Construction
- ECE 521 Computer Design and Technology
- CSC 715 Concurrent Software Systems
- MAE 545 Metrology for Precision Manufacturing
- MAE 789 Digital Control Systems
- ECE 764 Digital Image Processing

MS PROGRAM FOR MATERIALS SCIENCE STUDENT

- MAT 700 Modern Concepts in Material Science
- MAT 710 Elements of Crystallography and Diffraction
- MAT 715 Transmission Electron Microscopy
- MAT 712 Scanning Electron Microscopy
- MAT 722 Advanced Scanning Electron Microscopy and Surface Analysis
- MAE 545 Metrology for Precision Manufacturing
- PY 516 Physical Optics
- ECE 738 IC Technology and Fabrication
- MAT 695 Master's Thesis Research

MS PROGRAM FOR PHYSICS STUDENT

- PY 516 Physical Optics
- PY 552 Introduction to Structure of Solids I
- PY 753 Introduction to Structure of Solids II
- PY 781 Quantum Mechanics I
- PY 782 Quantum Mechanics II
- PY 783 Advanced Classical Mechanics
- PY 785 Advanced Electricity and Magnetism I
- PY 786 Advanced Electricity and Magnetism II
- MAT 700 Modern Concepts in Material Science
- MAE 545 Metrology for Precision Manufacturing
- PY 695 Master's Thesis Research

SHORT COURSES AND TV COURSES

Six graduate level courses: Scanning Electron Microscopy (MAT 712), Advanced SEM Surface Analysis (MAT 722), Modern Concepts in Material Science (MAT 700), Mechanical Properties of Materials (MAT 705), and Metrology (MAE 545) have been offered as video courses nationwide via National Technological University. In a typical year, approximately 120 students from industry and national laboratories participate in these courses. Future plans call for a MS program in Precision Engineering to be offered via the television network.

TECHNICAL REPORTS

Volume 1 - 1983	December 1983	136 pages
Volume 2 - 1984	January 1985	168 pages
Volume 3 - 1985	January 1986	294 pages
Volume 4 - 1986	January 1987	255 pages
Volume 5 - 1987	December 1987	336 pages
Volume 6 - 1988	December 1988	362 pages
Volume 7 - 1989	March 1990	357 pages
Volume 8 - 1990	March 1991	385 pages
Volume 9 - 1991	March 1992	382 pages
Volume 10 - 1992	March 1993	289 pages
Volume 11 - 1993	March 1994	316 pages
Volume 12 - 1994	March 1995	268 pages
Volume 13 - 1995	January 1996	251 pages

Volume 14 - 1996	January 1997	232 pages
Volume 15 - 1997	January 1998	298 pages
Volume 16 – 1998	January 1999	258 pages
Volume 17 – 1999	January 2000	232 pages
Volume 18 – 2000	January 2001	274 pages
Volume 19 – 2001	January 2002	201 pages
Volume 20 – 2002	January 2003	328 pages
Volume 21 - 2003	January 2004	208 pages
Volume 22 – 2004	February 2005	207 pages
Volume 23 – 2005	February 2006	264 pages
Volume 24 – 2006	March 2007	274 pages
Volume 25 – 2007	March 2008	192 pages
Volume 26 – 2008	March 2009	209 pages

PUBLICATIONS IN 2009

1. Q. Chen, T. Dow, K. Garrard, A. Sohn, *Optical and Fiducial Fabrication with a Fast Long Range Actuator (FLORA).* Proceedings of the Twenty-fourth Annual Meeting of the ASPE, Monterey, CA, October 4 - 9, 2009.

2. A. Sohn, K. Garrard, T. Dow, *The Spherical Profilometer Polaris 3D.* Proceedings of the Twenty-fourth Annual Meeting of the ASPE, Monterey, CA, October 4 – 9, 2009.

3. M. Shi, B. Lane, C. Mooney, T. Dow, R. Scattergood, *Diamond tool wear measurement by EBID.* Proceedings of the Twenty-fourth Annual Meeting of the ASPE, Monterey, CA, October 4 – 9, 2009.

4. Lane, B., Shi, M., Dow, T., Scattergood, R. *Study of Tool Wear and Cutting Process of Elliptical Vibration Assisted Machining*. Proceedings of the Twenty-fourth Annual Meeting of the ASPE, Monterey, CA, October 4 – 9, 2009.

5. Sohn, A., *Diamond Tool Centering for Cylindrical Turning*. Proceedings of the Twenty-fourth Annual Meeting of the ASPE, Monterey, CA, October 4 – 9, 2009.

6. Shi, M., Lane, B., Mooney, C., Dow, T., Scattergood, R., *Diamond tool wear measurement by EBID.* Precision Engineering Journal, under review.

7. B. Lane, M. Shi, T. Dow, R. Scattergood, *Diamond tool wear when machining Al6061 and 1215 steel*, WEAR, under review.

8. Dow, T., Eischen, J., Zdanowicz, E., *Design of a Fast Long Range Actuator- FLORA II*, International Journal of Machine Tools and Manufacture, submitted for review.

9. E. Zdanowicz, *Design of a Fast Long Range Actuator*, MS Thesis, Department of Mechanical and Aerospace Engineering, North Carolina State University, Raleigh, NC, 2009.

10. Q. Chen, *Design and Control of a Fast Long Range Actuator for Single Point Diamond Turning*, Ph. D. Thesis, North Carolina State University, Raleigh, NC, 2009.